Optical parametric oscillators and precision optical frequency measurements

by

Dicky Lee

B.A., Physics

University of California at Berkeley

(1987)

Submitted to the Department of Physics

in partial fulfillment of the requirements for the degree of

Doctor of Philosophy in Physics

at the

MASSACHUSETTS INSTITUTE OF TECHNOLOGY

February 1996

Author . .....

Department of Physics

November 2, 1995

Certified by .....

Ngai Chuen Wong

Research Scientist, Research Laboratory of Electronics

Thesis Supervisor

Certified by.. .....

Daniel Kleppner

Professor, Department of Physics

Thesis Supervisor

Accepted by ....

George Koster

Chairman, Departmental Committee on Graduate Students

Optical parametric oscillators and precision optical frequency measurements

by

Dicky Lee

Submitted to the Department of Physics
on November 2, 1995, in partial fulfillment of the
requirements for the degree of
Doctor of Philosophy in Physics

Abstract

We report experimental results of frequency tuning, stabilization, and beat-note phase noise measurements of a type-II phase-matched potassium titanyl phosphate (KTP) doubly resonant optical parametric oscillator (OPO). Three types of OPO cavity design were constructed and experimented for their mechanical stability and frequency tunability. Four tuning elements were employed in our 2-element and 3-element OPOs to control their stability and output frequencies. Discrete frequency tuning of over a range of ~3 THz was obtained by crystal angle tuning and cavity-length scanning. We achieved continuous frequency tuning over a 0.5-GHz range through the use of temperature and electro-optic tuning of the KTP crystal. Using these frequency-control techniques, we phase locked the signal-idler beat frequency to an external microwave frequency source near the frequency degenerate point and at 665 GHz with the use of an optical frequency comb generator. The power spectral density of the residual phase noise of the phase-locked signal-idler beat note was measured to be 0.3 mrad/$\sqrt{\text{Hz}}$. With the ability to tightly phase lock the beat-note frequency, the quadrature spectra of the signal-idler beat-note were experimentally measured for the first time. By amplitude modulating the input pump beam, the pump intensity to quadrature-phase transfer functions were also measured. A linearized quantum mechanical calculation for the OPO beat-note spectra was performed to facilitate a better understanding of the experimental observation. As a foundation for future experiments, we have also constructed and investigated the tuning properties of a dual-cavity OPO (DCOPO). The signal and idler fields were separated internally to resonate in their own respective cavities, thus providing independent cavity-length controls. The DCOPO was continuously tunable over a range of ~1 GHz that was limited by the weak pump resonance. A theoretical model was developed to explain and predict the tuning behavior of our DCOPO.

Thesis Supervisor: Ngai Chuen Wong
Title: Research Scientist, Research Laboratory of Electronics

Thesis Supervisor: Daniel Kleppner
Title: Professor, Department of Physics

To my wife, *Edith*,

my parents, uncle and aunt *Gin*,
for their patience, understanding, and sacrifice.

Acknowledgments

I would like to express my gratitude to Dr. Franco Wong for introducing me to the world of optics and the art of electronics. He taught me everything that I know about optics and more. His willingness to help, generosity with time, insightful advise, and invaluable guidance, make him one of the best advisors that a graduate student can ever ask for. I have enjoyed many of our discussions about Physics, the experiment, and the never-ending issue of Macintosh vs. Intel. It has been my privilege to work for and learn from the best.

I would also like to thank Professor Daniel Kleppner and Professor Wolfgang Ketterle for being my co-advisor and reader, respectively. Their suggestions for my thesis have been most valuable.

Peggy Berkovitz from the Physics Graduate Office is a constant source of help, especially during the last months of my thesis preparation. I can always rely on Peggy to resolve any of the administrative issues so as to not be distracted by the paper work.

I am very fortunate to be blessed with many good friends. To all of them who offered friendship and lent a helping hand along the way, I thank you.

Louis "Reggie" Brothers and Bobby Lai are colleagues and friends. They are always willing to help and to discuss any problems that I might have, not just work-related but sometimes personal ones. Reggie is the person I go to whenever I have a question about electronics, from Op-amp to mixer, and from microwave to Fourier transform. And the time I spent with Bobby, both in and out of the laboratory, has been most enjoyable.

I would like to thank my "Physics Buddies" Hong Jiao, Oliver Bardon and Kevin Lee. Discussing Physics with them is always a learning experience. Hong and I worked for Professor Steiner when we were undergraduates at U. C. Berkeley and I look forward to have the chance to work with Hong again. During the first year of my study at MIT, I spent more time with Oliver and Kevin than with anyone else. We shared many sleepless nights working together as we struggled to survive as first-year

graduate students.

Stephen Cheng, Kinhong "nerd" Kan and Kevin Wong have made all the difference and made life at MIT livable. It would have been impossible to survive the seven years of MIT life without their unfailing friendship and company. We have shared many of life up's and down's, happy and sometimes not-so-happy moments, and not to mention those bottles of Hennessy. I would like to express my gratitude for their help and support over the years.

I am especially grateful to Alaine Young for her help with my thesis and her generosity with time. Without her assistance, comments, and discussions, this thesis would have taken much longer to finish. Alaine is one of the first few friends that I made when I arrived at MIT seven years ago. Her unique point of view during many of our discussions, among Physics and other things, is always stimulating, and her knowledge about good restaurants is immeasurable. More importantly, she has always been a friend.

I am fortunate enough to have Juan Bruno as my suite-mate. Mr. Burno is a fun-loving crazy-kind-of guy. His company and wild stories make life in Ashdown more interesting and enjoyable.

To all of my friends who gave me support during my 12-year journey, I thank you. Especially (in no particular order) Sueanne Chan, Nelson Chau, Larry Cheng, Rebecca Cheong, Ronson Chu, David Hau, Antony Kam and Elaine Chen, Henry Louie, David Tse, and Evaon Wong. A special thank goes to Lisa Li for being a good friend and believing in me for all these years.

To all of my friends, I wish them best of luck.

I would like to thank all of my uncles and aunts in Toronto, Canada for putting up with me during my trips to Toronto. In particular, my whole-hearted appreciation goes to my eldest uncle's family for taking care of my wife during her stay in Canada.

I am forever in debt to uncle and aunt Gin, who took me under their wings when I first arrived in the States. I thank them for their unconditional love and support.

My deepest gratitude goes to my parents. If not for their love and the opportunities that they provided, none of this would have been possible. And let's not forget

my rival sibling, my younger sister Vicky ("Fish"). We did what we were supposed to do as brother and sister while we were growing up, we tormented each other. But I would not have traded her as my sister for the world.

Finally, my gratitude for my wife *Edith*, for her patience, her sacrifice, her understanding, and her love is beyond words.

"One man's noise,

is another man's data."

— anonymous

Contents

List of Figures

List of Tables

Chapter 1

Introduction

In this thesis, we discuss our theoretical and experimental studies of the quantum phase diffusion noise in a type-II phase matched potassium titanyl phosphate (KTP) optical parametric oscillator (OPO). Experimentally, we have developed the necessary frequency tuning and stabilization techniques for a first measurement of the OPO quantum phase noise. A simple theoretical calculation was performed to help us better understand the experimental results. In this chapter, we give a brief introduction of the OPO and outline the purpose of this thesis.

Since its first demonstration by Giordmaine and Miller [18, 19] in 1965, optical parametric oscillators (OPOs) have gained the reputation of being unstable and difficult to operate. However, recent advances in laser stabilization techniques, new crystal growth process and state of the art optical coating technology have sparked renewed interest in continuous-wave (cw) OPO research. There are many different areas of OPO research and application. The OPO has been used to generate tunable radiation from the near infrared (IR) near 1 μm to the mid-IR range [25]. It has also been used in the generation of non-classical light such as in twin-beam intensity correlation experiments [24, 30].

An OPO comprises a nonlinear $\chi^{(2)}$ crystal that is placed inside an optical cavity [7], as sketched in Fig. 1-1. The crystal converts an input pump field (f_p) into two subharmonic outputs, the signal (f_1) and the idler (f_2), via parametric downconversion. The optical cavity provides resonant feedback for the three fields so that when

pumped above threshold, the OPO outputs are intense and coherent. The three fields have to satisfy both the energy and linear momentum conservation conditions,

$$f_p = f_1 + f_2, \tag{1.1}$$

$$\vec{k_p} = \vec{k_1} + \vec{k_2}. \tag{1.2}$$

Not only are the OPO output frequencies constrained by the energy conservation condition (Eq. (1.1)), the sum of the output phases is also constrained by the input pump phase,

$$\phi_p = \phi_1 + \phi_2.$$

However, their phase difference, $\phi_1 - \phi_2$, undergoes a random walk process, known as phase diffusion. The phase diffusion noise of an OPO was first predicted by Graham and Haken [21] in 1968.

The linear momentum conservation is also referred to as the phase matching condition, which determines the output frequencies, f_1 and f_2. Because of the non-resonant nature of the parametric process, the OPO output linewidths are essentially limited by the pump laser linewidth [21, 41]. Its output frequencies are widely tunable and are ultimately limited by the transparency range of the crystal. Because of its wide frequency tuning range, the OPO has many potential applications in the fields of high-resolution spectroscopy and optical frequency metrology. One of our goals is to investigate some of the frequency tuning properties of the cw OPO, such as tunability on a finer scale and output frequencies as functions of external parameters, in the aforementioned applications.

Another OPO application is the use of an OPO as an optical frequency divider as part of a frequency chain to link the optical domain to the cesium (Cs) clock standard, as proposed by Wong [41, 43]. As an optical frequency divider, the OPO output frequency difference is phase locked to a stable microwave reference for exact 2:1 or 3:1 frequency division operations. We have demonstrated in our experiment a 2:1 frequency divider by phasing locking the OPO beat-note frequency to a microwave synthesizer to obtain a very narrow beat-note linewidth. In such high precision mea-

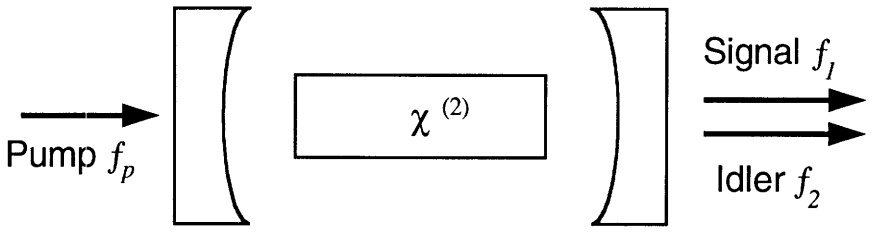

Figure 1-1: Schematic of an optical parametric oscillator. The input pump laser field is labeled as the "pump" (f_p), whereas the outputs fields are labeled as the "signal" (f_1) and the "idler" (f_2).

surements, the phase noise of an OPO can be an important parameter. As the final part of our experiments, the phase noise of the OPO frequency beat note is measured and characterized.

1.1 Beat-Note Phase Noise Measurement

The OPO is also a quantum mechanical device, which can be used to generate non-classical light fields, such as squeezed states and twin-photon beams. These types of non-classical light experiments have been demonstrated by different groups in the past years [8, 40, 45, 22, 29]. However, experimental confirmation of the OPO quantum phase noise is still lacking. The major reason for the lack of experimental work is that the necessary experimental tools for providing systematic OPO frequency tuning, output intensity stabilization and frequency stabilization have not been developed.

In order to fully understand the OPO and exploit its unique properties, we must study every aspect of the OPO device. The purpose of this thesis is to develop experimental techniques for the measurement of the OPO phase noise. The beat-note signal between the signal and the idler fields containing the phase noise can be directly detected using a photodetector. The technical challenges are that the beat frequency must fall within the detection bandwidth of the detector and that the intensity and the frequency of the beat signal must be stable enough for the beat note to be measured.

1.2 Outline of Thesis

To measure the OPO phase noise, we need to be able to systematically tune the OPO output frequencies and intensity, and stabilize its output frequencies. Our approach for achieving tunability and stability was through passive and active control of the OPO cavity, with frequency tuning elements added to the basic OPO system. For intensity stability, we have investigated several OPO cavity designs for their mechanical rigidity. The cavity length was also actively controlled by an intensity servo loop to further reduce the cavity length perturbation.

Four different frequency tuning elements were utilized in our OPO for systematic tunings. The four elements were crystal angle tuning, cavity-length tuning, temperature tuning and electro-optic tuning. Their tuning ranges and coefficients were measured as part of our experiment. We have frequency tuned the OPO output frequencies (δf_1, δf_2) over a range $\sim$3 THz near frequency degeneracy. For stable operation, the beat frequency linewidth was stabilized to mHz level by phase locking it to a stable microwave reference via the electro-optic effect. With our moderately tunable and highly stable OPO, its beat-note phase noise was experimentally measured for the first time.

We have also performed a simple linearized-model calculation to help us better understand our experimental results. Our model includes the pump laser noise contributions so that their effect on the OPO phase noise spectrum can be examined and compared with our observation.

We have also constructed a novel dual-cavity OPO. The dual-cavity OPO design eliminates some of the shortcomings of the usual OPO cavity design, such as limited continuous tuning range and unbalanced signal-idler losses, and provides a foundation for future experiments.

In Chapter 2, we develop the basic theoretical model and framework for our experiments. Our semiclassical calculation consists of two parts: the steady-state mean-field solutions and the small-signal analysis. The mean-field solutions are calculated in the classical regime, whereas the small-signal analysis is of quantum mechanical formu-

lation. Our plane-wave model includes arbitrary signal-idler losses, cavity detuning, and excess pump noise effects.

The krypton ion laser used in our experiment and its associated intensity and frequency stabilization electronics are described in Chapter 3. Chapter 4 discusses the design considerations of OPO cavity construction, the different cavity types, and the nonlinear crystal properties.

The detailed construction and implementation of our OPOs are discussed in Chapter 5. A total of three OPOs were constructed. Their frequency tuning ranges and coefficients are measured. In Chapter 6, the experimental work of beat frequency stabilization is discussed. The beat frequency was stabilized using a phase-locked loop and via the electro-optic effect of the KTP crystal. The phase-locked loop parameters and design considerations are presented.

Chapter 7 discusses the quantum phase noise experiment with a comparison between the experimental results and our theoretical calculation. The detection scheme and the electronic setup are described in detail.

In Chapter 8, we discuss the design, the construction, and the experimental observation of our dual-cavity OPO. The dual-cavity OPO has a much wider cavity-length tuning range than the usual OPO cavity design. The dual-cavity OPO also provides the possibility of varying the signal and the idler cavity parameters independently. This creates new opportunities for OPO study that is otherwise not possible. A theoretical model is developed to describe and predict the tuning behavior of this OPO.

Chapter 9 summarizes our experimental observations and measurements, and discusses some possible future OPO studies using the dual-cavity design OPO.

Chapter 2

Theory

2.1 Introduction

In this chapter, we develop the necessary theory to describe the OPO behavior under steady-state conditions and its fundamental noise characteristics. We consider a cw doubly resonant OPO under a plane-wave approximation. The OPO internal field solutions are calculated in the classical regime for a steady-state mean-field analysis, while the small-signal fluctuation analysis is carried out in the quantum regime, in which vacuum mode fluctuations are included. In the small-signal analysis, the in-phase and quadrature-phase noise power spectra of the beat signal between the two subharmonic outputs are calculated.

There are two contributions to the OPO output noise: OPO-specific noise and technical noise. The OPO-generated noise is caused by the parametric interaction involving the vacuum noise which is quantum mechanical in nature. In the quantum mechanical formalism, losses introduce noise by coupling into the system vacuum noise from the surrounding thermal reservoir. The OPO internal scattering losses and output coupling losses are therefore sources of vacuum noise that is then amplified (or de-amplified in the case of squeezing) by the parametric interaction. The interaction between the vacuum noise and the downconverted output fields causes the phase of the signal-idler beat note to undergo a random walk process, much like the phase diffusion noise of a laser.

Any noise that is not generated via the parametric process is categorized as technical noise. Technical noise include, but not limited to, excess pump laser intensity and phase noise, vibration induced OPO output intensity and frequency noise, and detection electronic noise. The OPO is a phase-sensitive amplifier for both the input pump laser noise and the vacuum noise at the signal and idler frequencies. The transfer characteristics for the amplitude noise and the phase noise of the pump laser are included in the calculation so that their effects on the output spectra can be studied.

2.2 Theoretical Model

Our model is a simple cw doubly-resonant OPO with the signal and the idler fields being resonant with the optical cavity, whereas the pump is of a single-pass configuration. The signal and idler cavities are assumed to have high finesses so that, under cw operations, the output oscillation frequencies (ω_i) are very close to the cavity resonant frequencies (ω_i^c). The cavity detunings

$$\Delta_i = \omega_i - \omega_i^c, \qquad i = 1, 2, \tag{2.1}$$

for the signal and the idler fields are therefore small compared to the free spectral range (FSR) of the cavity. On the other hand, the single-pass pump field "sees" a low finesse cavity so that the pump field detuning can be set $\Delta_p = 0$. Our calculation does not assume frequency degeneracy even though the actual experiment is conducted at a signal-idler beat frequency of 30 MHz.

The total internal fields for the signal and idler are written as the sum of two terms, the steady-state mean fields plus the small fluctuating components. The mean-field solution is a classical calculation and the small-signal fluctuation includes Langevin noise operators. For OPOs with large mean-field outputs, our theoretical model and experimental results are in good agreement [22].

2.3 Mean Field Analysis

The classical internal field equations for three-wave mixing in an OPO are

$$\begin{aligned} \dot{A}_p &= -\kappa_p A_p - \chi A_1 A_2 + \sqrt{2\kappa_p}\, E_p, \\ \dot{A}_1 &= -(\kappa_1 - i\Delta_1) A_1 + \chi A_p A_2^*, \\ \dot{A}_2 &= -(\kappa_2 - i\Delta_2) A_2 + \chi A_p A_1^*, \end{aligned} \tag{2.2}$$

where χ is the positive nonlinear coupling constant, A_i is the internal field mode, and κ_i is the field total loss rate. $E_p = e_p \exp(i\theta_p)$ is the input pump field with e_p^2 being the pump power in photons-per-second unit and θ_p is the pump phase angle. The subscript i refers to the pump (p), signal (1), and idler (2), respectively.

The steady-state mean-field solutions are obtained by writing the internal field A_i in Eq. (2.2) as

$$A_i = r_i \exp(i\phi_i), \tag{2.3}$$

and setting its time derivative to zero ($\dot{A}_i = 0$). The solutions are

$$\tan\theta_\Delta \equiv \Delta_1/\kappa_1 = \Delta_2/\kappa_2, \qquad \pi/2 > \theta_\Delta > -\pi/2, \tag{2.4}$$

$$\theta_\Delta = \phi_1 + \phi_2 - \phi_p, \tag{2.5}$$

$$r_p = \sqrt{\kappa_1\kappa_2 + \Delta_1\Delta_2}\,/\chi, \tag{2.6}$$

$$r_i = C/\sqrt{\kappa_i}, \qquad i = 1, 2, \tag{2.7}$$

$$e_p \cos(\theta_\Delta + \phi_p - \theta_p) = \tilde{e_p}\left(1 + C^2/2\tilde{e_p}^2\right), \tag{2.8}$$

$$e_p \sin(\theta_\Delta + \phi_p - \theta_p) = \tilde{e_p}\,(\Delta_1/\kappa_1), \tag{2.9}$$

where the minimum threshold,

$$\tilde{e_p} = \frac{\sqrt{\kappa_1\kappa_2}}{\chi}\sqrt{\frac{\kappa_p}{2}}, \tag{2.10}$$

is for zero detuning ($\Delta_1 = \Delta_2 = 0$). Furthermore, C is related to the output power

and is given by

$$C^2 = 2\tilde{e_p}^2 \left[\sqrt{F_p - (\Delta_1/\kappa_1)^2} - 1\right], \tag{2.11}$$

where $F_p = (e_p/\tilde{e_p})^2$ is the number of times the OPO is pumped with respect to the zero-detuning threshold. With a field output coupling loss rate of γ_i, the signal and the idler output powers are given by

$$P_1 = 2\frac{\gamma_1}{\kappa_1}C^2 \quad \text{and} \quad P_2 = 2\frac{\gamma_2}{\kappa_2}C^2,$$

and their output power ratio is given by,

$$\frac{P_1}{P_2} = \frac{\gamma_1\kappa_2}{\gamma_2\kappa_1}.$$

The output fields r_1, r_2 are maximum at zero detuning, indicating that the parametric down-conversion process is most efficient when the signal and idler fields are on resonance.

Equations (2.4)–(2.7) describe the conditions for cw OPO operations and deserve closer examination. Equation (2.4) describes the cavity detunings of the signal and idler fields normalized to their respective total loss rates. It imposes a strict condition between their detunings, and hence the output frequencies of the signal and the idler fields. Oscillation cannot occur if Eq. (2.4) is not satisfied. The maximum allowable normalized detuning (Δ_i/κ_i) for a given pump power (F_p) is determined by Eq. (2.11).

The threshold of oscillation (Eq. (2.10)) is directly proportional to the product of the pump, the signal, and the idler loss rates. The threshold can be minimized by resonating the three fields simultaneously thereby lowering their loss rates $\kappa_{p,1,2}$. However, a small loss rate would imply a small detuning range, as evident in Eq. (2.11), and therefore a stringent requirement for the cavity-length stability. The actual OPO design is a compromise between threshold and stability requirements.

Once the external pump power has reached threshold the internal pump field r_p, as shown in Eq. (2.6), is clamped at threshold value. This optical limiting effect was discussed in detail by Leong in Ref. [30] and was not investigated in this study. The

maximum theoretical conversion efficiency is achieved when the OPO is pumped at four (4) times above threshold.

The signal and the idler fields not only have to satisfy the sum-frequency constraint,

$$f_p = f_s + f_i,$$

but the sum of their output phases must also follow that of the input pump laser (Eq. (2.5)). Such a correlation between the two output phases was demonstrated by Nabors *et al.* in Ref. [33]. Since the input phase noise ϕ_p is shared between the two outputs, we have

$$\begin{aligned} \phi_p &= \phi_1 + \phi_2, \\ \langle \phi_1 \rangle &= -\langle \phi_2 \rangle, \end{aligned}$$

assuming that $\langle \phi_p \rangle = 0$. Here, the angular bracket denotes time-averaging for the enclosed variable. It should be noted that only their averaged phases are equal, that their instantaneous phases $\phi_{1,2}$ are not necessarily the same. The phase diffusion noise spectrum is calculated in the following section.

The large-signal steady-state analysis not only provides us the general understandings of OPO behavior and operations, it also establishes the necessary framework for our quantum noise calculation.

2.4 Small Signal Analysis

In the small-signal analysis, we make the transition from classical field variables into quantum mechanical operators by writing A_i as

$$A_i = r_i(1 + a_i)e^{i\phi_i}, \qquad i = 1, 2, p, \tag{2.12}$$

$$= r_i(1 + \mu_i + i\psi_i)e^{i\phi_i}, \tag{2.13}$$

$$\dot{A}_i = r_i(\dot{\mu}_i + i\dot{\psi}_i)e^{i\phi_i}. \tag{2.14}$$

Here, r_i and ϕ_i are the classical mean-field amplitude and phase angle as calculated in Eqs. (2.5)–(2.7), and the quantum mechanical operators μ_i and ψ_i are the normalized amplitude-fluctuation operator and the phase-fluctuation operator, respectively. The μ_i and ψ_i are related to the normalized annihilation and creation operators a_i and $a_i^\dagger$ by

$$\mu_i = \frac{1}{2}\left(a_i + a_i^\dagger\right) \quad \text{and} \quad \psi_i = \frac{1}{2i}\left(a_i - a_i^\dagger\right).$$

The fluctuations are assumed to be much smaller than the mean-field variables.

The set of classical field equations for three-wave mixing (Eq. (2.2)) becomes the quantum Langevin equations

$$\begin{aligned}
\dot{A}_p &= -\kappa_p A_p - \chi A_1 A_2 + \sqrt{2\kappa_p}\, E_p + \sqrt{2\kappa_p}\, u_p, \\
\dot{A}_1 &= -(\kappa_1 - i\Delta_1)A_1 + \chi A_p A_2^\dagger + \sqrt{2\gamma_1}\, u_1 + \sqrt{2(\kappa_1 - \gamma_1)}\, v_1, \\
\dot{A}_2 &= -(\kappa_2 - i\Delta_2)A_2 + \chi A_p A_1^\dagger + \sqrt{2\gamma_2}\, u_2 + \sqrt{2(\kappa_2 - \gamma_2)}\, v_2,
\end{aligned} \tag{2.15}$$

where u_i and v_i are the vacuum input modes associated with the output coupling (γ_i) and internal loss ($\kappa_i - \gamma_i$).

Our calculation is a first order approximation, and we ignore the second and higher order terms of μ_i and ψ_i. The approximation is justified because the amplitude and the phase fluctuations are much smaller than the mean field. To solve for the small-fluctuation terms, we substitute A_i and $\dot{A}_i$ from Eqs. (2.13) and (2.14) into the quantum Langevin equations (Eq. (2.15)). The detailed derivation procedure and algebra are contained in Appendix A.

Since we are interested in the amplitude and phase fluctuation power spectra, it is more convenient to work in the frequency domain than in the time domain. The time-domain equations are therefore Fourier transformed into the frequency domain. The complete set of coupled amplitude and phase fluctuation equations, in the frequency domain, are

$$(\kappa_p - i\omega)\mu_p = -\kappa_p \alpha_r \mu_+ + \kappa_p \alpha_i \psi_+ + R_p, \tag{2.16}$$

$$-i\omega\mu_+ = -\delta\mu_- + \kappa\mu_p + \Delta\psi_p - \Delta\psi_+ + R_+, \tag{2.17}$$

$$(\kappa - i\omega)\mu_- = \delta\mu_p + \beta\psi_p - \beta\psi_+ + R_-, \tag{2.18}$$

$$(\kappa_p - i\omega)\psi_p = -\kappa_p\alpha_r\psi_+ - \kappa_p\alpha_i\mu_+ + \Lambda_p, \tag{2.19}$$

$$(\kappa - i\omega)\psi_+ = \kappa\psi_p + \beta\mu_- - \Delta\mu_p + \Lambda_+, \tag{2.20}$$

$$-i\omega\psi_- = -\delta\psi_+ + \delta\psi_p + \Delta\mu_- - \beta\mu_p + \Lambda_-, \tag{2.21}$$

where we have defined the following variables to simplify the algebra,

$$\kappa = \kappa_1 + \kappa_2, \tag{2.22}$$

$$\delta = \kappa_1 - \kappa_2, \tag{2.23}$$

$$\Delta = \Delta_1 + \Delta_2, \tag{2.24}$$

$$\beta = \Delta_1 - \Delta_2, \tag{2.25}$$

$$\alpha_r = \frac{\sqrt{F_p - (\Delta_1/\kappa_1)^2} - 1}{1 + (\Delta_1/\kappa_1)^2}, \tag{2.26}$$

$$\alpha_i = \frac{\alpha_r\Delta_1}{\kappa_1}. \tag{2.27}$$

It should be noted that because of the normalized-detuning constraint (Eq. (2.4)), the newly defined variables must satisfy

$$\frac{\delta}{\kappa} = \frac{\beta}{\Delta}. \tag{2.28}$$

Also, $\mu_\pm$ are the sum and the difference of the signal-idler amplitude fluctuations defined by

$$\mu_\pm = \mu_1 \pm \mu_2,$$

and $\psi_\pm$ are the sum and the difference of the signal-idler phase fluctuations given by

$$\psi_\pm = \psi_1 \pm \psi_2.$$

There are two advantages in rewriting the variables into $\mu_\pm$ and $\psi_\pm$. The algebra is greatly simplified in our calculation and, more importantly, μ_+ and ψ_- are the quantities that are measured in the experiment.

The $R_{\pm}$ and $\Lambda_{\pm}$ as defined in Eqs. (A.27) are the amplitude and the phase noise operators associated with the vacuum modes $u_{1,2}$ and $v_{1,2}$. Their non-zero correlation relationships are listed in Section A.7.

The R_p and Λ_p as defined in Eqs. (A.19) and (A.20) are the amplitude and the phase noise operators associated with the pump field. Assuming that the intensity and the phase noise of the pump laser are not correlated, R_p and Λ_p have the following nonzero correlation relationships,

$$\langle R_p(\omega)R_p(\omega')\rangle = 2\pi\frac{\kappa_p^2\alpha_r}{2C^2}h^R(\omega)\delta(\omega+\omega'), \tag{2.29}$$

$$\langle \Lambda_p(\omega)\Lambda_p(\omega')\rangle = 2\pi\frac{\kappa_p^2\alpha_r}{2C^2}h^\Lambda(\omega)\delta(\omega+\omega'), \tag{2.30}$$

Here, h^R and h^Λ are the pump intensity and the pump phase noise factors, with h^R and h^Λ equal to one for a shot-noise limited pump, and h^R and h^Λ can be much greater than one for a pump laser with excess noise. The laser noise to OPO output noise transfer functions are found to be frequency dependent, and the amount of contributions depends on both the input noise amplitude and the frequency. By intensity or phase modulating the pump field before it enters the OPO, we can investigate the OPO pump intensity-noise and phase-noise transfer characteristics independently. In our OPO quantum noise experiments, the pump intensity noise effect on the OPO output spectra was investigated and compared with our theoretical calculation.

As we can see from Eqs. (2.16)–(2.21), the intensity and the phase quadratures are coupled through the cavity detunings (β, Δ). If we set Δ_i to zero ($\Delta = \beta = 0$), the set of six coupled equations is reduced to two sets of three coupled equations,

$$(\kappa_p - i\omega)\mu_p = -\kappa_p\alpha_r\mu_+ + \kappa_p\alpha_i\psi_+ + R_p, \tag{2.31}$$

$$-i\omega\mu_+ = -\delta\mu_- + \kappa\mu_p + R_+, \tag{2.32}$$

$$(\kappa - i\omega)\mu_- = \delta\mu_p + R_-, \tag{2.33}$$

and

$$(\kappa_p - i\omega)\psi_p = -\kappa_p\alpha_r\psi_+ - \kappa_p\alpha_i\mu_+ + \Lambda_p, \tag{2.34}$$

$$(\kappa - i\omega)\psi_+ = \kappa\psi_p + \Lambda_+, \tag{2.35}$$

$$-i\omega\psi_- = -\delta\psi_+ + \delta\psi_p + \Lambda_-, \tag{2.36}$$

for the amplitude fluctuation and the phase fluctuations, respectively. The above set of decoupled amplitude-fluctuation equations (Eqs. (2.31)–(2.33)) were obtained by Wong *et al.* in Ref. [44].

Under most experimental conditions, cavity detuning is not zero and therefore, the noise in the two quadratures are mixed. The measured amplitude-quadrature spectrum contains contribution from the phase-quadrature noise, and vice versa. The amount of mixing depends on the degree of detuning; the larger the detuning, the larger the mixing becomes.

2.5 Beat-Note Detection

The following is a general detection procedure used in the experiments. The beat note between the two subharmonic outputs is detected with a high-speed photodetector, and the dc and ac signals from the photodetector are separated with a cross-over network (Fig. 2-1). The ac signal is thus the beat signal between the signal and the idler fields. The beat signal is synchronously demodulated with a local oscillator that has a frequency equal to the beat-note frequency. The amplitude or the phase quadrature of the demodulated signal is obtained by adjusting the phase angle of the local oscillator: the amplitude quadrature is the in-phase quadrature while the phase quadrature is the 90°-out-of-phase quadrature. The demodulated signal is then low-pass filtered and the resulting spectrum is measured with a rf spectrum analyzer. This synchronous homodyne detection scheme (at the rf level) is necessary for separating the in-phase and the quadrature-phase signals; otherwise, the demodulated signal spectrum would be a mix between the two quadratures. Detailed description of the

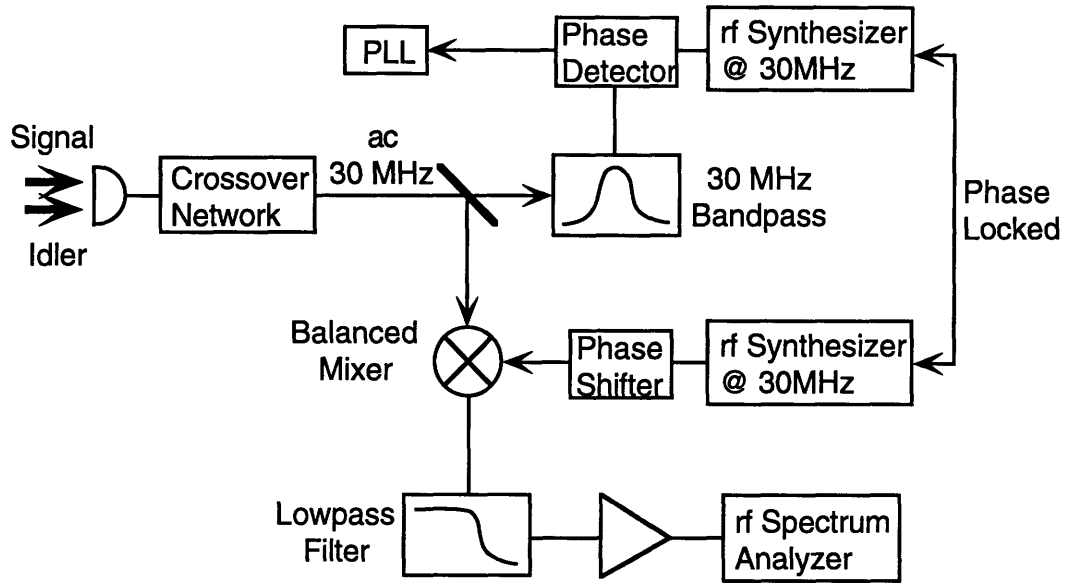

Figure 2-1: Experimental setup for the DRO quantum phase noise measurement.

experimental setup and results are presented in Chapter 6.

The total electric field emerging from the OPO cavity is given by

$$\begin{aligned} E(t) &= \sqrt{2\gamma_1}\, r_1(1+\mu_1+i\psi_1)e^{-i(\omega_1 t+\phi_1)} + \sqrt{2\gamma_2}\, r_2(1+\mu_2+i\psi_2)e^{-i(\omega_2 t+\phi_2)} \\ &\quad - u_1 e^{-i\omega_1 t} - u_2 e^{-i\omega_2 t} - u_3 e^{-i(2\omega_1-\omega_2)t} - u_4 e^{-i(2\omega_2-\omega_1)t}, \end{aligned}$$

where u_3 and u_4 are the image-band vacuum modes. The image-band vacuum modes must be included in the total electric field in order to give the correct shot-noise level [38].

The origin of u_3 and u_4 can be easily understood by referring to Fig. 2-2. The signal at frequency ω_1 and the idler at frequency ω_2 beat to produce a beat-note signal at $\omega_{12} = \omega_1 - \omega_2$, which is the ac signal we detect. The image-band vacuum mode u_3 at frequency $2\omega_1 - \omega_2$ also beat with the signal field to produce a noise signal at ω_{12}, and similarly for u_4 with the idler. We can consider this process as a heterodyne detection: with the signal and the idler fields being the two strong local oscillators and the vacuum modes as the weak signals.

The photocurrent $I(t) = E(t)^\dagger E(t)$ from the photodetector is separated by a cross-

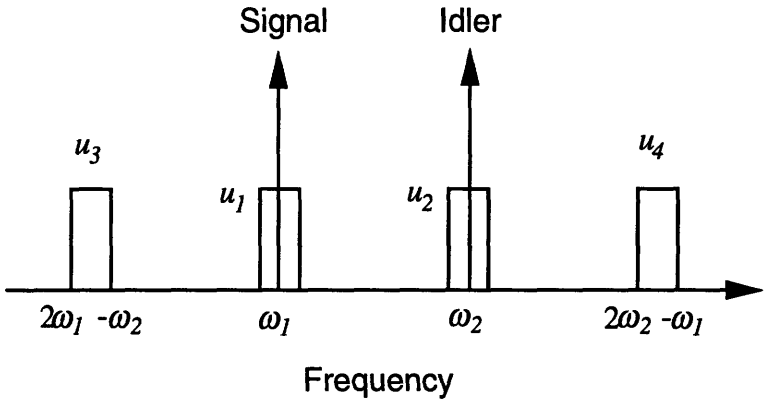

Figure 2-2: Spectral digram showing the signal (ω_1), idler (ω_2) fields and the image-band vacuum modes (u_3, u_4).

over network into ac and dc components. The dc component and the lowpass-filtered ac component of $I(t)$, in first-order approximation, are

$$
\begin{aligned}
I_{dc}(t) &= 2\left(\frac{\gamma_1}{\kappa_1}+\frac{\gamma_2}{\kappa_2}\right)C^2 + 4\left(\frac{\gamma_1}{\kappa_1}\mu_1+\frac{\gamma_2}{\kappa_2}\mu_2\right)C^2 - \sqrt{8}\,C\left(\sqrt{\frac{\kappa_1}{\gamma_1}}\,\mu_1^u + \sqrt{\frac{\kappa_2}{\gamma_2}}\,\mu_2^u\right), \\
I_{ac}(t) &= 2C^2\sqrt{\frac{\gamma_1\gamma_2}{\kappa_1\kappa_2}}\,(1+\mu_+ + i\psi_-)e^{-i(\omega_{12}t-\phi_{12})} \\
&\quad - \sqrt{\frac{2\gamma_1}{\kappa_1}}\,C(\tilde{u}_2^\dagger + \tilde{u}_3)e^{-i(\omega_{12}t-\phi_{12})} - \sqrt{\frac{2\gamma_2}{\kappa_2}}\,C(\tilde{u}_1 + \tilde{u}_4^\dagger)e^{-i(\omega_{12}t-\phi_{12})} \\
&\quad + \text{hermitian conjugate},
\end{aligned}
$$

where we have defined

$$\tilde{u}_3 = u_3 e^{-i(2\phi_1-\phi_2)} \quad \text{and} \quad \tilde{u}_4 = u_4 e^{-i(2\phi_2-\phi_1)}.$$

The quantum efficiency of the photodetector and the electron charge is set to 1 for convenience. The shot-noise power S_0 from the dc photocurrent is given by

$$S_0 = 2\left(\frac{\gamma_1}{\kappa_1}+\frac{\gamma_2}{\kappa_2}\right)C^2. \tag{2.37}$$

The lowpass-filtered in-phase and quadrature-phase of the photocurrent $I_{ac}(t)$ are

obtained from

$$\text{in-phase} : x(t) = \frac{1}{\tau}\int_0^t d\tau\, I_{ac}(\tau)\cos(\omega_{12}\tau - \phi_{12}), \tag{2.38}$$

$$\text{quadrature-phase} : y(t) = \frac{1}{\tau}\int_0^t d\tau\, I_{ac}(\tau)\sin(\omega_{12}\tau - \phi_{12}), \tag{2.39}$$

where the in-phase is the amplitude quadrature and the quadrature-phase is the phase noise of the OPO.

2.6 Quadrature-Phase Noise Spectrum

The first-order quadrature-phase $y(t)$ (Eq. (2.39)) of the photocurrent $I_{ac}(t)$ is calculated to be

$$y(t) = 2C^2\sqrt{\frac{\gamma_1\gamma_2}{\kappa_1\kappa_2}}\,\psi_- + \sqrt{\frac{2\gamma_1}{\kappa_1}}\,(\psi_2^u - \psi_3^u)C + \sqrt{\frac{2\gamma_2}{\kappa_2}}\,(\psi_4^u - \psi_1^u)C,$$

and the power spectrum, normalized to shot-noise level S_0 (Eq. (2.37)), is obtained with

$$\begin{aligned} S_y(\omega) &= \frac{1}{S_0}\int_{-\infty}^{\infty} d\tau\,\langle y(\tau)y(0)\rangle e^{i\omega\tau}, \\ &= \frac{1}{S_0}\int_{-\infty}^{\infty}\frac{d\omega'}{2\pi}\langle Y(\omega)Y(\omega')\rangle, \end{aligned} \tag{2.40}$$

where $Y(\omega)$ is the Fourier transform of $y(t)$, $Y(\omega) = \mathcal{F}\{y(t)\}$. The complete quadrature-phase noise power spectrum as calculated in Appendix A is

$$\begin{aligned} S_y(\omega) = {} & 4\frac{\gamma_1\gamma_2}{\kappa_1\kappa_2}\frac{C^2}{S_0}\Big\{\kappa_p^2\alpha_r\left(h^R|N_{61}|^2 + h^\Lambda|N_{64}|^2\right) \\ & + (\kappa_1^2+\kappa_2^2)\Big(|N_{62}|^2 + |N_{63}|^2 + |N_{65}|^2 + |N_{66}|^2 \\ & \qquad - 2\Im\{N_{62}N_{65}^*\} - 2\Im\{N_{63}N_{66}^*\}\Big) \\ & + 2(\kappa_1^2-\kappa_2^2)\left(\Re\{N_{62}N_{63}^*\} + \Re\{N_{65}N_{66}^*\} - \Im\{N_{62}N_{66}^*\} - \Im\{N_{63}N_{65}^*\}\right)\Big\} \\ & + 2\frac{C^2}{S_0}\left(\frac{\gamma_1}{\kappa_1} + \frac{\gamma_2}{\kappa_2}\right) \end{aligned} \tag{2.41}$$

$$
\begin{aligned}
&- 4\frac{\gamma_1\gamma_2}{\kappa_1\kappa_2}\frac{C^2}{S_0}\kappa_2\left(\Re\{N_{65}-N_{66}\}-\Im\{N_{62}-N_{63}\}\right)\\
&- 4\frac{\gamma_1\gamma_2}{\kappa_1\kappa_2}\frac{C^2}{S_0}\kappa_1\left(\Re\{N_{65}+N_{66}\}-\Im\{N_{62}+N_{63}\}\right),
\end{aligned}
$$

where the matrix element N_{ij} is given by Eq. (A.28), $\Re$ and $\Im$ refer to the real and imaginary part of the relevant quantities.

The complete quadrature-phase noise spectrum equation (Eq. (2.41)) by itself is too complex and little insight can be gained from the complete solution. The only term that we can identify is the frequency-independent shot-noise level,

$$
2\frac{C^2}{S_0}\left(\frac{\gamma_1}{\kappa_1}+\frac{\gamma_2}{\kappa_2}\right)=1,
$$

the fifth line in Eq. (2.41). However, the complete solution can be greatly simplified under special conditions, such as zero detuning and matched losses. We shall discuss these cases in some details so as to gain a better understanding on the noise spectrum.

2.6.1 Zero Detuning

If the signal and the idler fields are on exact resonance ($\Delta_1=\Delta_2=0$), the amplitude and the phase quadratures are then decoupled. The phase-noise spectrum equation, which takes on a much simpler form, can be obtained by either solving Eqs. (2.34)–(2.36) directly or by simplifying Eq. (2.41) using $\Delta_1=\Delta_2=0$.

By solving Eqs. (2.34)–(2.36) directly, we obtain for the phase-noise spectrum

$$
\begin{aligned}
S_y(\omega) \;=\; & 4\frac{\gamma_1\gamma_2}{\kappa_1\kappa_2}\frac{C^2}{S_0}\frac{1}{\omega^2|D|^2}\Big\{\epsilon\kappa_p^2\omega^2\left(\kappa_1-\kappa_2\right)^2 h^R(\omega)+\left(\kappa_1^2+\kappa_2^2\right)\left(|\alpha|^2+|D|^2\right)\\
&-2\left(\kappa_1^2-\kappa_2^2\right)\Re\{\alpha D^*\}\Big\}\\
&+2\left(\frac{\gamma_1}{\kappa_1}+\frac{\gamma_2}{\kappa_2}\right)\frac{C^2}{S_0}\\
&-4\frac{\gamma_1\gamma_2}{\kappa_1\kappa_2}\frac{C^2}{S_0}\frac{1}{\omega|D|^2}\left(\kappa_1-\kappa_2\right)\Im\{\alpha D^*\},
\end{aligned}
$$

$$
\begin{aligned}
\epsilon &= \sqrt{F_p} - 1, \\
\alpha &= (\kappa_1 - \kappa_2)(\kappa_p + \epsilon\kappa_p - i\omega), \\
D &= \epsilon\kappa\kappa_p + (\kappa - i\omega)(\kappa_p - i\omega).
\end{aligned}
$$

Alternatively, by letting $\Delta_1 = \Delta_2 = 0$ the matrix elements N_{61}, N_{62} and N_{63} become zero and the quadrature-phase noise spectrum (Eq. (2.41)) is reduced to

$$
\begin{aligned}
S_y(\omega) &= 4\frac{\gamma_1\gamma_2}{\kappa_1\kappa_2}\frac{C^2}{S_0}\Big\{|N_{64}|^2\kappa_p^2\alpha_r h^{\Lambda} + (\kappa_1^2 + \kappa_2^2)(|N_{65}|^2 + |N_{66}|^2) \\
&\quad + 2(\kappa_1^2 - \kappa_2^2)\Re\{N_{65}N_{66}^*\}\Big\} \\
&\quad - 4\frac{\gamma_1\gamma_2}{\kappa_1\kappa_2}\frac{C^2}{S_0}\left(\kappa_2\Re\{N_{65} - N_{66}\} + \kappa_1\Re\{N_{65} + N_{66}\}\right) \\
&\quad + 2\left(\frac{\gamma_1}{\kappa_1} + \frac{\gamma_2}{\kappa_2}\right)\frac{C^2}{S_0}.
\end{aligned} \tag{2.42}
$$

The pump laser intensity noise contribution (h^R) vanishes from the phase-noise spectrum equation; however, the pump laser phase noise contribution (h^{Λ}) is still a factor. Zero detuning does not suppress the pump laser noise transfer, it only decouples the two quadratures so that the phase-noise spectrum does not contain any pump laser intensity noise. With detuning, the pump laser intensity noise is "leaked" from the in-phase to the quadrature-phase spectrum. The amount of leaking depends on the amount of detuning; the larger the detuning, the larger is the leak, and hence the larger is the pump laser intensity noise contribution in the phase-noise spectrum.

2.6.2 Matched Losses

If the signal and the idler losses are perfectly matched ($\kappa_1 = \kappa_2$), their intensities and phases would be perfectly correlated. As required by the normalized detuning condition (Eq. (2.4)), the signal and idler detunings must be equal ($\Delta_1 = \Delta_2$) when their losses are matched. As a result, the set of internal field equations (Eq. (2.15)) become symmetric in subscripts "1" and "2", the labeling of the signal and idler fields becomes arbitrary (assuming matched output coupling). Since there is no distinction

between the signal and idler fields, the input pump intensity noise and phase noise must be equally shared between the two outputs. In our heterodyne detection, where the phase difference between the signal and idler fields were detected, both the pump laser intensity- and phase-noise contributions vanish from the first-order beat-note spectra. The two quadratures, however, are still coupled through cavity detuning. With $\kappa_1 = \kappa_2$, β (Eq. (2.28)) becomes zero and Eqs. (2.18) and (2.21) reduce to

$$\begin{aligned} (\kappa - i\omega)\mu_- &= R_-, \\ -i\omega\psi_- &= \Delta\mu_- + \Lambda_-, \end{aligned}$$

and give

$$\psi_- = \frac{i}{\omega}\left(\frac{\Delta}{\kappa - i\omega}R_- + \Lambda_-\right). \tag{2.43}$$

The matched-loss phase-noise spectrum can be obtained either by direct calculation using ψ_- from Eq. (2.43), or by letting $\kappa_1 = \kappa_2$ in the matrix element N_{ij}, in which case N_{61}, N_{62}, N_{64}, and N_{65} become zero. With matched losses, the quadrature-phase noise spectrum (Eq. (2.41)) is reduced to

$$\begin{aligned} S_y(\omega) &= 4\frac{\gamma_1\gamma_2}{\kappa_1\kappa_2}\frac{C^2}{S_0}\left\{(\kappa_1^2 + \kappa_2^2)\left(|N_{63}|^2 - 2\Im\{N_{63}N_{66}^*\}\right)\right\} \\ &\quad + 2\frac{C^2}{S_0}\left(\frac{\gamma_1}{\kappa_1} + \frac{\gamma_2}{\kappa_2}\right). \end{aligned} \tag{2.44}$$

Equation (2.44) does not contain any pump laser intensity- or phase-noise factor. Figure 2-3 shows theoretical plots of the phase-noise power (Eq. (2.44)) as a function of cavity detuning at four fixed Fourier frequencies (ω) when the losses are matched. As we can see from Fig. 2-3, the general behavior is that as cavity detuning increases the phase-noise power also increases. However, the relatively small phase-noise power increase indicates that the effect of quadrature coupling is minimal. A summary of the parameter values used in preparing the plots is listed in Table 2.1 for reference.

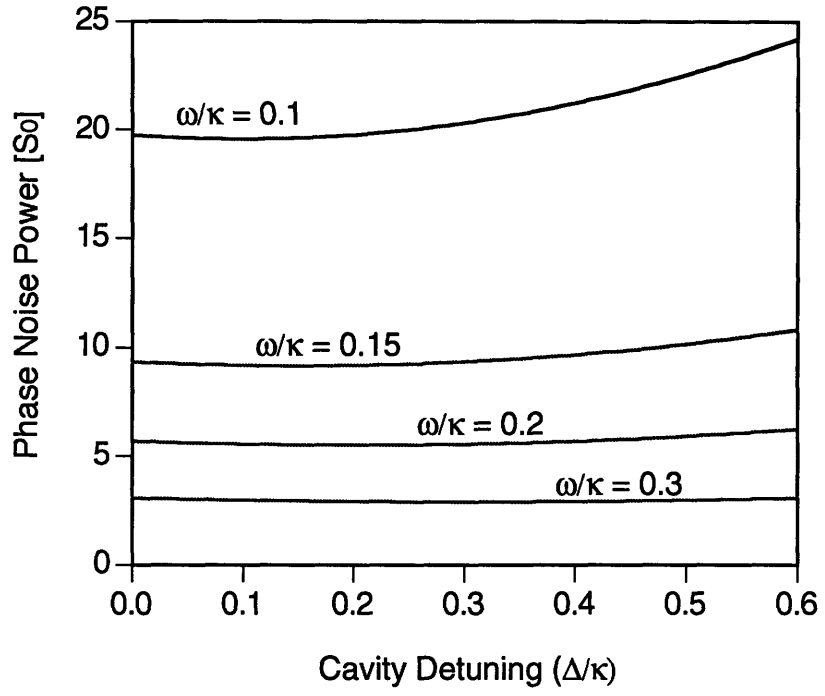

Figure 2-3: Theoretical plots of beat-note quadrature-phase noise power vs. total cavity detunings at four different Fourier frequencies (ω). Noise power is normalized to shot-noise level; cavity detuning Δ and Fourier frequencies ω are normalized to total loss rate κ. (Linear vertical scale in units of S_0, shot-noise level = 1.)

Parameters	Symbol	Typical value [κ]
Signal Total Loss	κ_1	0.4
Idler Total Loss	κ_2	0.6
Combined Total Loss	$\kappa = \kappa_1 + \kappa_2$	1
Differential Total Loss	$\delta = \kappa_1 - \kappa_2$	0.2
Output coupling	$\gamma_{1,2}$	0.1875
Pump Total Loss	κ_p	60
Combined Total Detuning	$\Delta = \Delta_1 + \Delta_2$	0.531
Pump Power/Threshold	F_p	1.4

Table 2.1: Summary of typical OPO parameters used in preparing the theoretical plots.

2.6.3 Matched Losses and Zero Detuning

The noise spectrum Eq. (2.41) can be further simplified if the signal-idler total loss rates are identical ($\kappa_1 = \kappa_2$) and the cavity detuning is zero. At zero detuning, the intensity-quadrature and phase-quadrature noise are decoupled, and with matched losses, the pump laser noise does not contribute to the output spectrum. The resulting expression

$$S_y(\omega) = \frac{\gamma_1 \kappa}{\omega^2} + 1 \tag{2.45}$$

is a Lorentzian that is characteristic of a phase diffusion process, and is a function of the total loss rate and output coupling loss only [15].

The origin of the phase diffusion process of the OPO beat note can be understood by considering the following order of magnitude estimation. Consider an OPO cavity with field total loss rates of κ_1, κ_2 for the signal and idler fields, respectively. The internal circulating signal (P_1) and idler (P_2) power in photon-per-second unit are

$$\begin{aligned} P_1 &= r_1^2 = C^2/\kappa_1, \\ P_2 &= r_2^2 = C^2/\kappa_2, \\ P_T &= r_1^2 + r_2^2, \end{aligned}$$

where r_1, r_2 and C^2 are given by Eqs. (2.7) and (2.11). Within a time period of τ, the number of signal and idler noise photons coupled into the cavity via the loss process are $2\kappa_1\tau$ and $2\kappa_2\tau$, respectively. These noise photons have energies approximately equal to that of the signal and idler fields, but the phase angles of their electric fields are randomly distributed. For each noise photon coupled into the cavity, its noise electric field is added vectorially to the internal coherent signal and idler fields, as illustrated in Fig. 2-4. The addition of $2\kappa_1\tau$ ($2\kappa_2\tau$) noise photons to the internal signal (idler) field is similar to a 2-dimensional random walk process of $2\kappa_1\tau$ ($2\kappa_2\tau$) steps. The standard deviation σ_1 (σ_2) for such a 2-dimensional random walk is $\sqrt{2\kappa_1\tau}$ ($\sqrt{2\kappa_2\tau}$) [36], and therefore the averaged phase angle deviation for the signal and idler

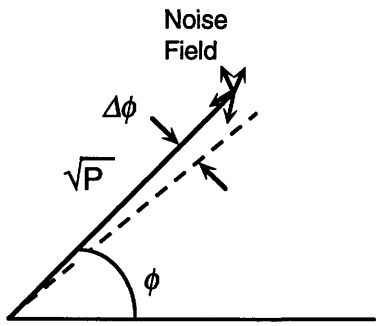

Figure 2-4: OPO internal electric field phasor A with amplitude $P^{1/2}$ and phase angle ϕ. The small noise field causes A to diffuse in phase.

fields are given by

$$\begin{aligned}
\langle \Delta\phi_i^2(\tau) \rangle &= \langle \phi_i^2(\tau) \rangle - \langle \phi_i(\tau) \rangle^2, \\
&= \sigma_i^2/P_i, \qquad\qquad i = 1, 2, \\
&= \frac{2\kappa_i^2}{C^2}\tau.
\end{aligned}$$

Since we are detecting the phase difference of the signal and idler, the averaged signal-idler phase-angle difference deviation is given by

$$\begin{aligned}
\langle \Delta\phi^2(\tau) \rangle &= \langle \Delta(\phi_1 - \phi_2)^2 \rangle, \\
&= \langle (\phi_1 - \phi_2)^2 \rangle - \langle \phi_1 - \phi_2 \rangle^2, \\
&= 2(\kappa_1^2 + \kappa_2^2)\frac{\tau}{C^2}, \\
&= 4\kappa_1^2 \frac{\tau}{C^2}, \qquad\qquad \text{for } \kappa_1 = \kappa_2.
\end{aligned}$$

The diffusion rate D of the OPO internal field is [23, Chap. 20]

$$\begin{aligned}
2D &= \langle \Delta\phi^2(\tau) \rangle / \tau, \\
D &= 2\frac{\kappa_1^2}{C^2}.
\end{aligned}$$

As a result of the phase diffusion, the signal-idler beat note acquires a linewidth.

The linewidth of the beat-note signal $A(t)$ is calculated as follows similar to that of a laser [23, Chap. 20]. Assuming that the effect of the noise photons on the amplitude of the internal field is negligible, we write A as

$$\begin{aligned} A(t) &= \sqrt{r_1 r_2}\exp(-i\phi(t)), \\ &= C(\kappa_1\kappa_2)^{-1/4}\exp(-i\phi(t)). \end{aligned}$$

The power spectrum of $A(t)$ is given by

$$\begin{aligned} S_A &= \frac{1}{2\pi}\int_{-\infty}^{\infty} d\tau \langle A(\tau)A(0)\rangle e^{i\omega\tau}, \\ &= \frac{C^2}{\sqrt{\kappa_1\kappa_2}}\frac{2D}{D^2+\omega^2}, \end{aligned} \tag{2.46}$$

where

$$\langle A(\tau)A(0)\rangle = \frac{C^2}{\sqrt{\kappa_1\kappa_2}}\exp(-D\tau)$$

is the auto-correlation function of A. The linewidth (FWHM) is therefore

$$2D = 4\frac{\kappa_1^2}{C^2}, \qquad \text{for } \kappa_1 = \kappa_2.$$

Our simple order of magnitude estimation yields a diffusion constant D that is four times larger than that obtained in an exact calculation [21, 42]; nonetheless, it provides us with insights into the origin of the phase diffusion noise without detailed calculation. Note that our simple estimate for the beat-note linewidth (Eq. (2.46)) has the same functional dependence (ω^{-2}) of Eq. (2.45). The difference between the two equations is that Eq. (2.46) is the spectrum of the internal electric field, whereas Eq. (2.45) is the spectrum of the phase fluctuation of the output fields.

The noise power of S_y approaches the shot-noise level as ω approaches infinity. The physical meaning is that in very short measurement time interval, the signal-idler phase difference does not have time to diffuse to a different value. The width of the Lorentzian is directly proportional to the product of the total loss rate and the output coupling loss. This should not come as a surprise because losses always

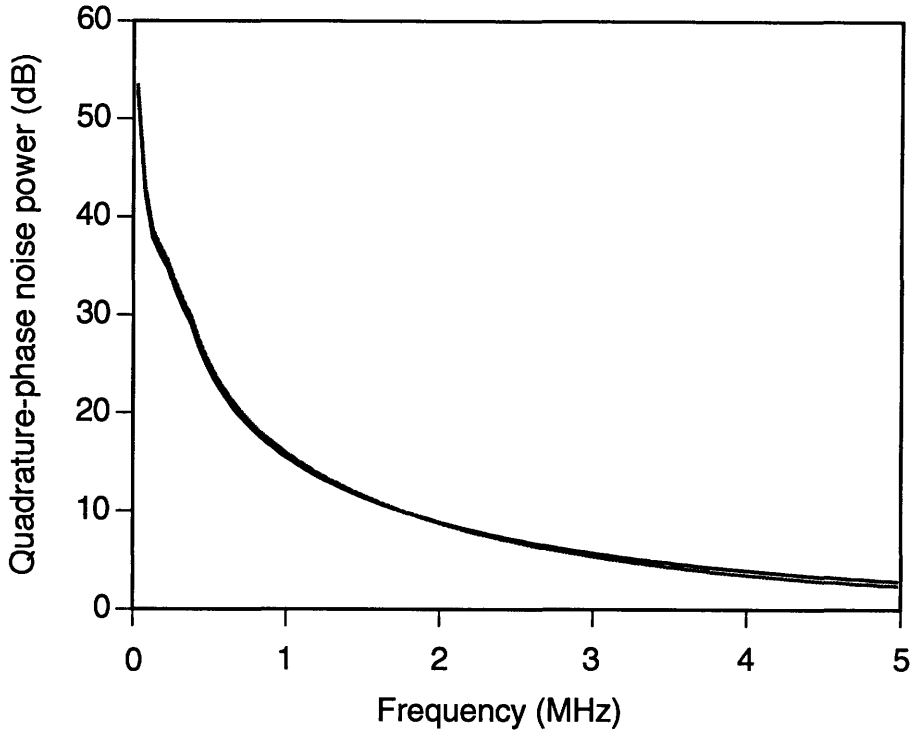

Figure 2-5: Theoretical plots of beat-note quadrature-phase noise power spectra normalized to shot-noise level. (Top) simplified expression (Eq. (2.45)): zero detuning and matched signal-idler losses; (bottom) complete expression (Eq. (2.41)) with shot-noise limited pump. The difference between the traces is negligible. The parameter values used for the plots are listed in Table 2.1.

introduce noise in the quantum mechanical formalism; the greater the loss, the higher is the noise.

The difference between the complete expression (Eq. (2.41)) and the simplified expression (Eq. (2.45)) is very small when the excess pump laser noise is smaller than the phase-noise power, as shown in Fig. 2-5. Equation (2.45) is a good approximation for the complete phase noise expression when the pump laser is shot-noise limited. However, when the pump excess noise is large, the complete solution (Eq. (2.41)) must be used. Equation (2.41) can be used for characterizing the pump laser noise to beat-note noise transfer behavior.

The phase noise power of the quadrature-phase demodulated beat-note signal Eq. (2.41) can be expressed as a power spectral density S_ϕ in units of rad^2/Hz by

using

$$S_\phi = \frac{P_{sn} S_y}{P_c},$$

where P_{sn} is the synchronously demodulated quadrature shot-noise power and P_c is the power of the synchronously demodulated signal-idler beat-note signal.

We can first evaluate a more familiar case of the direct detection of a single beam with the same incident optical power so that the average dc photocurrent is equal to that of the directly detected two-beam scenario. The shot-noise level of the directly detected single-beam dc photocurrent i_{dc} within a detection bandwidth of B is given by the usual expression

$$P_{sn}(\mathrm{dd}) = 2ei_{dc}\mathrm{B}R_L.$$

For the two-beam direct detection, the synchronously demodulated beat-note signal power is given by

$$P_c = \frac{1}{2}\frac{i_{dc}^2}{2}R_L.$$

Here, R_L is the load impedance, and the same demodulation procedure is used as for the phase noise calculations. The photocurrent variance for the synchronously demodulated quadrature has been found (Eq. (2.37)) to be equal to $i_{dc}(= eS_0)$. For a detection bandwidth B (located after synchronous demodulation), the shot-noise power is then given by

$$P_{sn} = 2ei_{dc}\mathrm{B}R_L,$$

which yields a shot-noise power spectral density (B = 1 Hz) of

$$S_{sn} = \frac{8e}{i_{dc}}.$$

This should be compared with the shot-noise power spectral density for the single-beam direct detection result of

$$S_{sn}(\mathrm{dd}) = \frac{2e}{i_{dc}}.$$

The difference of a factor of 4 more in noise in the two-beam heterodyning case [37]

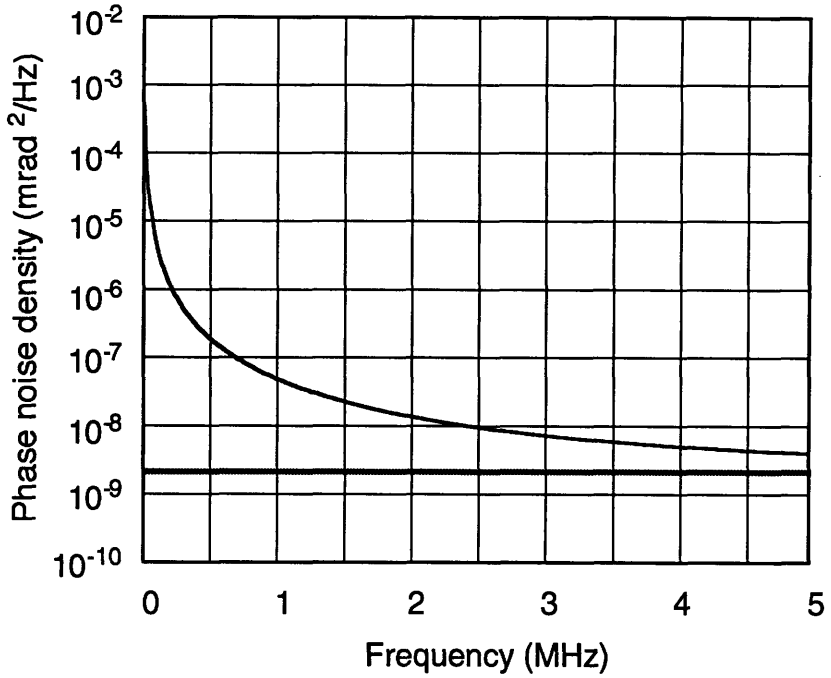

Figure 2-6: Theoretical plots of beat-note quadrature-phase noise power spectral density, assuming a photocurrent of 0.6 mA. The bottom trace near 2×10^{-9} mrad^2/Hz is the shot-noise level.

is due to the fact that heterodyning (two-beam beat signal) reduces the signal-to-noise ratio by a factor of 2 and that the actual noise bandwidth for synchronously demodulated heterodyned signal is twice as much for the same detection bandwidth B (such as that of a lowpass filter.)

Therefore, the phase noise power spectral density is given by

$$S_\phi = \frac{8e}{i_{dc}} S_y.$$

Fig. 2-6 shows the power spectral density and the corresponding shot-noise level converted from Fig. 2-5 for a 0.6-mA detected photocurrent (i_{dc}). At low frequencies, the phase noise power is much larger than the shot-noise level. The phase noise density at 500 kHz, as seen in Fig. 2-6, is about 2×10^{-7} mrad^2/Hz or ~20 dB above shot-noise. It is therefore possible to detect the phase noise even in the presence of technical noises.

2.7 Pump Noise Transfer Characteristics: Cavity Detuning vs. Matched Losses

In previous sections, we have discussed the effects of cavity detuning and signal-idler loss mismatch on the phase-noise spectrum in the absence of excess pump laser noise. We now consider their effects on the phase-noise spectrum in the presence of excess pump noise. As we have discussed in previous sections, signal-idler loss mismatch introduces pump laser noise into the beat-note spectrum, whereas cavity detuning leaks the amplitude-quadrature noise into the phase-noise spectrum. Under typical experimental conditions, the signal-idler losses are not matched and cavity detuning is unavoidable.

The complete quadrature-phase noise spectrum equation (Eq. (2.41)) can be used to predict the relationship between loss mismatch and detuning, and their effects on pump noise transfer. As obtained in Eq. (2.41), the pump laser intensity noise h^R to quadrature-phase noise transfer function H_{AP} is given by

$$\begin{aligned} S_y(\omega) &= H_{AP} h^R, \\ H_{AP}(\omega) &= 4\frac{\gamma_1\gamma_2}{\kappa_1\kappa_2}\frac{C^2}{S_0}\kappa_p^2\alpha_r|N_{61}|^2, \\ &= 2\frac{\gamma_1\gamma_2}{\gamma_1\kappa_2+\gamma_2\kappa_1}\kappa_p^2\alpha_r|N_{61}|^2. \end{aligned} \tag{2.47}$$

Here, we have made use of the definition of S_0 in Eq. (2.37) to obtain the final Equation (2.47).

The magnitude-squared of the matrix element N_{61} in Eq. (2.41) is the pump laser intensity noise to quadrature-phase spectrum transfer function. This noise transfer function was measured as part of our OPO quantum noise experiment. The pump intensity was modulated with a modulator before it entered the OPO. A strong modulation ensured $h^R \gg 1$ so that the input modulation dominates over all other noise terms. By having a known amount of pump modulation, we were able to measure $|N_{61}|^2$ directly on a spectrum analyzer.

The transfer function H_{AP} is a function of three variables, namely the Fourier

frequency ω, cavity detuning Δ, and signal-idler loss mismatch δ (Eq. (2.23)). The noise transfer behavior is studied by plotting H_{AP} as a function of two of the variables while holding the third one fixed. We normalize the variables in units of total loss rate κ and use the signal loss rate κ_1 as the loss-mismatch variable instead of δ for convenience. The signal and the idler losses are identical when

$$\begin{aligned} \frac{\kappa_1}{\kappa} &= \frac{\kappa_1}{\kappa_1 + \kappa_2} \\ &= \frac{\kappa_1}{2\kappa_1} \\ &= 0.5, \end{aligned}$$

and the cavity is on exact resonance when $\Delta/\kappa = 0$.

In Fig. 2-7, H_{AP} is plotted against ω and Δ at two κ_1/κ values: 0.6 and 0.7. H_{AP} is zero when the two quadratures are decoupled at zero detuning. For a given value of loss mismatch (κ_1), the coupling between the quadratures increases with increasing detuning (Δ). As a result, the pump intensity to quadrature-phase transfer (H_{AP}) increases with increasing coupling. In Fig. 2-8, H_{AP} is plotted against ω and κ_1 at two Δ/κ values: 0.3 and 0.5. Again, H_{AP} is zero at matched losses, and increases with loss mismatch at any given detuning.

Figure 2-9 and 2-10 shows theoretical plots of the pump intensity noise to beat-note quadrature-phase ($|N_{61}|^2$) and pump phase noise to beat-note quadrature-phase ($|N_{64}|^2$) transfer functions, using typical experimental parameter values listed in Table 2.1. The plots show the transfer functions at three different values of total detuning (Δ). As shown in Fig. 2-9 and 2-10, the pump laser noise are attenuated as the Fourier frequency increases even when the signal and the idler total loss rates are not well matched ($\kappa_1/\kappa = 0.4$, $\kappa_2/\kappa = 0.6$), and the noise attenuation factors decrease as cavity detuning increases. It is, therefore, preferable to operate the OPO close to zero detuning so as to reduce the pump noise effect.

The plots also show that the suppression for the pump phase noise is much larger than the suppression for the pump intensity noise. The difference in the amount of suppression between the pump intensity noise to beat-note quadrature-phase transfer

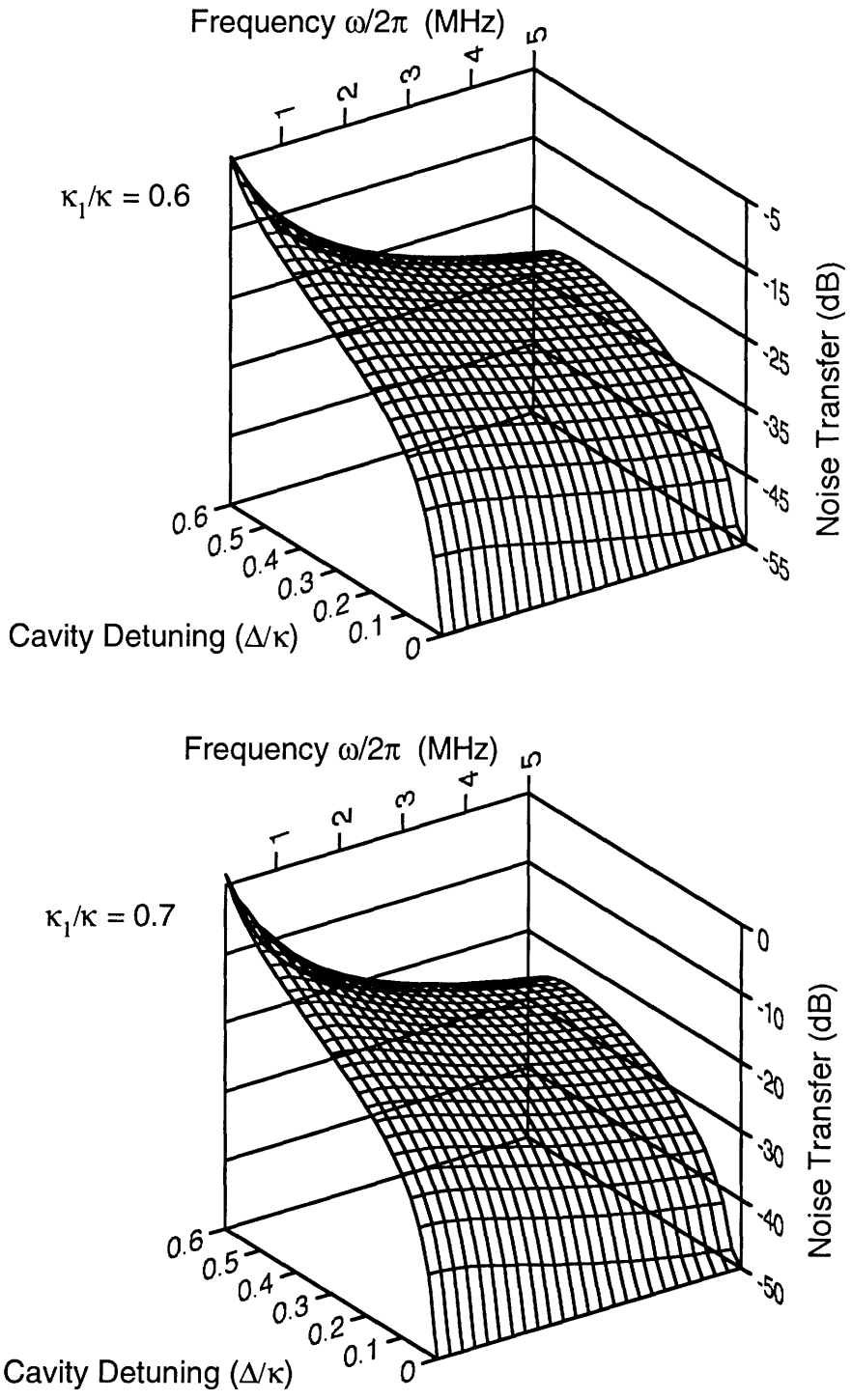

Figure 2-7: Theoretical 3-D plots of pump laser intensity to quadrature-phase noise transfer as a function of Fourier frequency (ω) and detuning (Δ/κ) at two loss mismatch values: $\kappa_1/\kappa = 0.6$ and 0.7. Note the different vertical scale of the two plots.

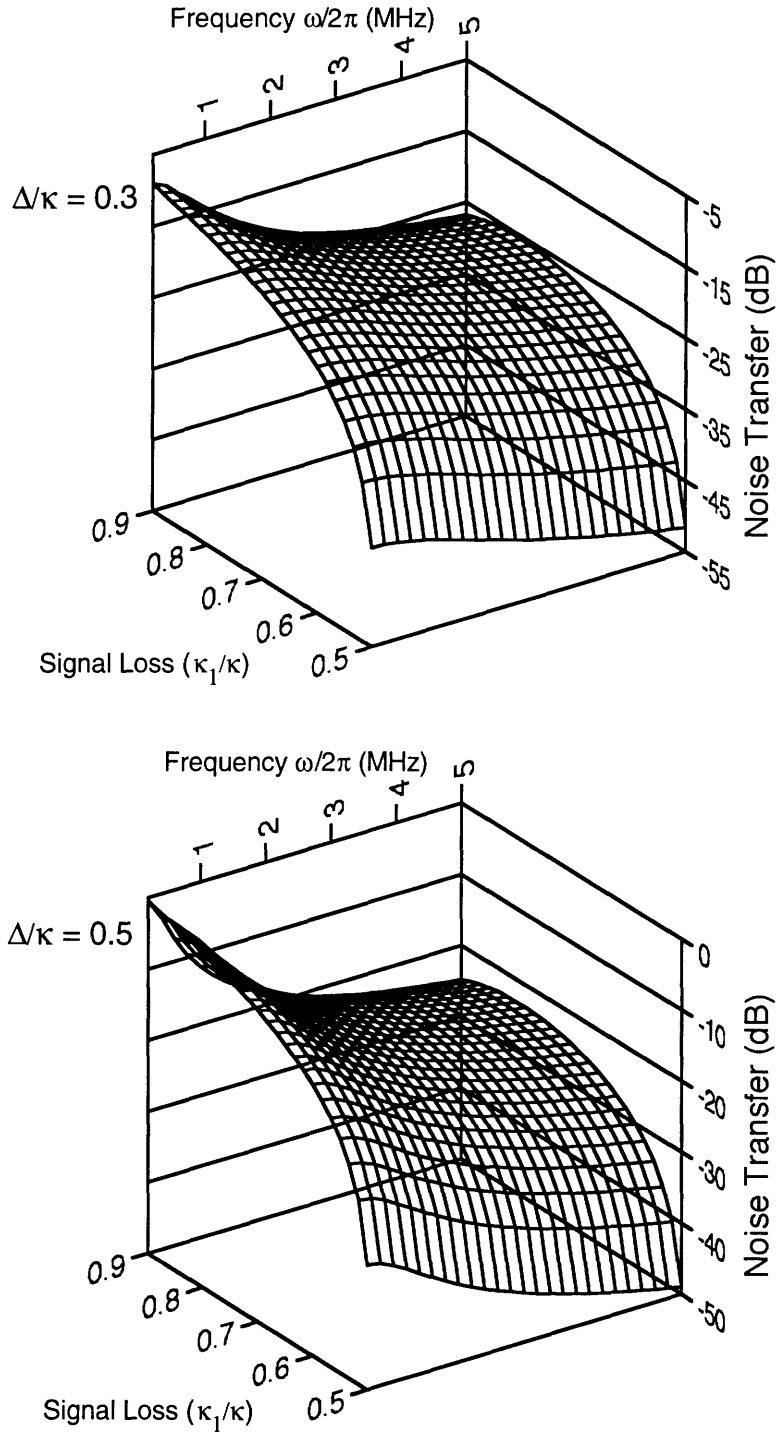

Figure 2-8: Theoretical 3-D plots of pump laser intensity to quadrature-phase noise transfer as a function of Fourier frequency (ω) and loss mismatch (κ_1/κ) at two detuning values $\Delta/\kappa = 0.3$ and 0.5.

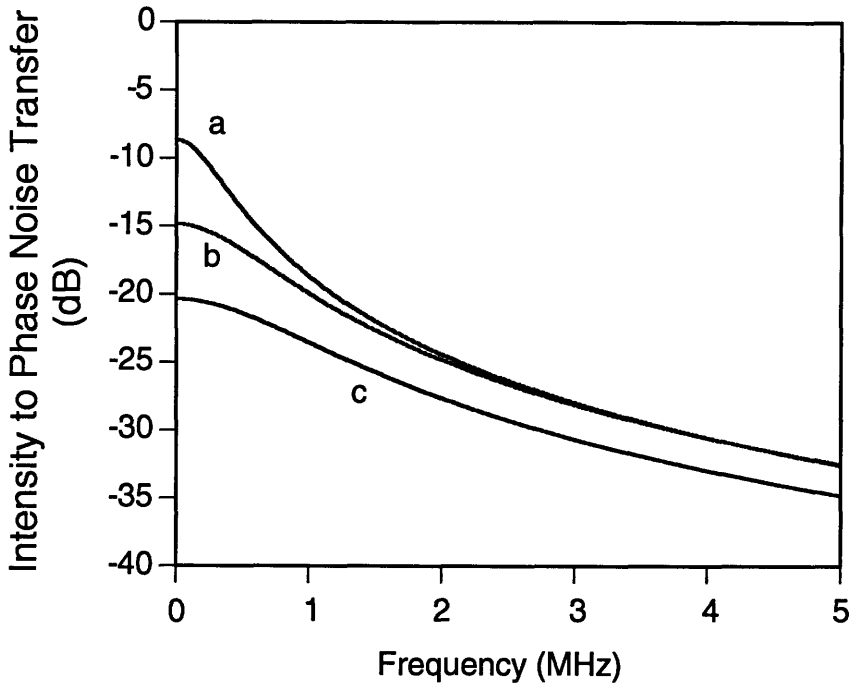

Figure 2-9: Theoretical plots of pump laser intensity to quadrature-phase noise transfer function at different normalized detunings (Δ/κ): (a) 0.4; (b) 0.3; (c) 0.2 ($\kappa_1 = 0.4$). The parameter values used for the plots are listed in Table 2.1.

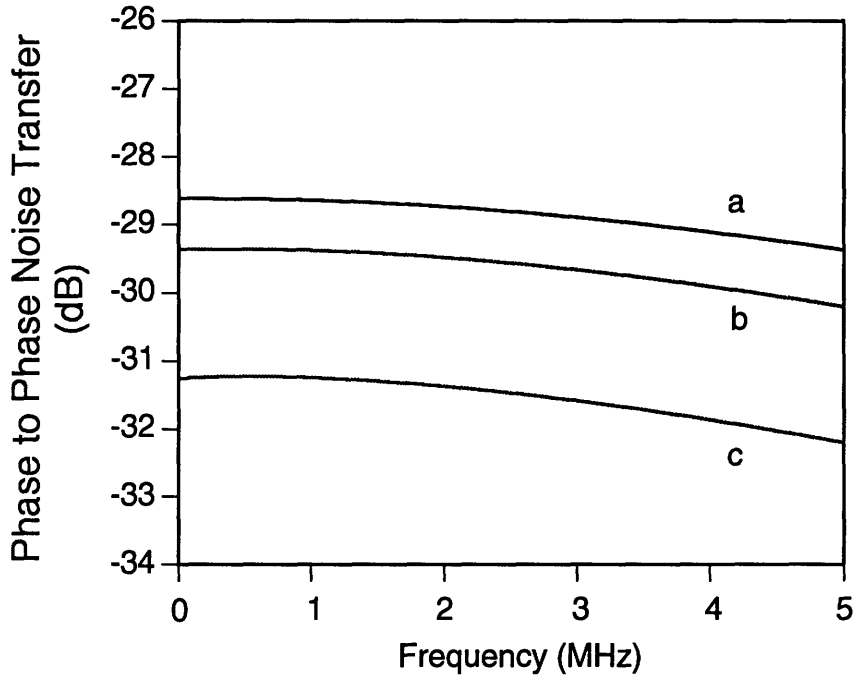

Figure 2-10: Theoretical plots of pump laser phase noise to quadrature-phase transfer function at different normalized detunings (Δ/κ): (a) 0.4; (b) 0.3; (c) 0.2 ($\kappa_1 = 0.4$). The parameter values used for the plots are listed in Table 2.1.

(H_{AP}) and the pump phase noise to quadrature-phase transfer can be attributed to the difference-frequency detection scheme. Since the sum of the OPO output phases follow that of the input pump field (Eq. (2.5)), when their difference is detected, as in our experiment, a high degree of correlation can be achieved if the signal-idler losses are well matched. On the other hand, our difference-frequency detection scheme also detects the output sum intensity, not their difference, therefore we do not expect a large amount of common-mode suppression in the pump laser intensity noise. This can be compared with an intensity correlation measurement in a twin beam experiment in which the difference-intensity is measured and the laser pump intensity noise is suppressed due to common-mode suppression.

In general, H_{AP} increases with increasing detuning and loss mismatch. The beat-note phase noise can be more precisely measured by either reducing the detuning or by better matching the signal and idler losses. If the losses are matched, the pump laser noise, both intensity and phase noise, do not contribute and the effect of detuning is negligible (Eq. (2.44)). Therefore, the signal-idler losses should be matched as closely as possible in order to have a more precise phase noise measurement. However, it can be difficult to match the two losses, and residual pump noise may leak through.

An easier alternative is to operate the OPO at zero detuning. At zero detuning the two quadratures are decoupled, and the pump intensity-noise contribution to the quadrature-phase spectrum is removed. The pump intensity noise to quadrature-phase transfer can be significant at low frequencies as we can see from Fig. 2-9. On the other hand, the pump phase-noise contribution to the quadrature-phase spectrum is largely suppressed by the heterodyne detection scheme (Fig. 2-10) and the impact is less significant. It is therefore preferable to operate as close to zero detuning as possible.

2.8 In-Phase Noise Spectrum

The in-phase signal of the demodulated photocurrent $x(t)$ (Eq. (2.38)) is given by

$$x(t) = 2C^2\sqrt{\frac{\gamma_1\gamma_2}{\kappa_1\kappa_2}}\,(1+\mu_+) - \sqrt{\frac{2\gamma_1}{\kappa_1}}\,(\mu_2^u+\mu_3^u)C - \sqrt{\frac{2\gamma_2}{\kappa_2}}\,(\mu_4^u+\mu_1^u)C.$$

Since we are interested in the noise spectrum, we only need to consider the fluctuating terms of the in-phase photocurrent,

$$\Delta x(t) = 2C^2\sqrt{\frac{\gamma_1\gamma_2}{\kappa_1\kappa_2}}\,\mu_+ - \sqrt{\frac{2\gamma_1}{\kappa_1}}\,(\mu_2^u+\mu_3^u)C - \sqrt{\frac{2\gamma_2}{\kappa_2}}\,(\mu_4^u+\mu_1^u)C. \tag{2.48}$$

The algebra is much simplified in the special case of zero detuning ($\Delta_1 = \Delta_2 = 0$). The correlations needed to calculate the in-phase spectrum were worked out by Wong *et al.* in Ref. [44]. With reference to their calculation, the in-phase noise power spectrum is calculated as

$$\begin{aligned}
S_x(\omega) &= \frac{1}{S_0}\int_{-\infty}^{\infty}\frac{d\omega'}{2\pi}\langle\Delta X(\omega)\Delta X(\omega')\rangle \\
S_x(\omega) &= 4\frac{C^2}{S_0}\left\{\frac{\gamma_1\gamma_2}{\kappa_1\kappa_2}\frac{1}{|D|^2}\left[(\kappa_p^2+\omega^2)\left((\kappa^2+\delta^2)(\kappa^2+\delta^2+\omega^2)-4\kappa^2\delta^2\right)\right.\right. \\
&\qquad \left.\left. + 2\epsilon\kappa_p^2 h^R(\omega)|\kappa^2-\delta^2-i\kappa\omega|^2\right]\right. \\
&\quad \left. + \left(\frac{\gamma_1}{\kappa_1}+\frac{\gamma_2}{\kappa_2}\right)\right. \\
&\quad \left. - 2\frac{\gamma_1\gamma_2}{\kappa_1\kappa_2}\Re\left\{\frac{(\kappa_p-i\omega)(\kappa^2-\delta^2-i\kappa\omega)}{D}\right\}\right\},
\end{aligned} \tag{2.49}$$

$$\begin{aligned}
\epsilon &= \sqrt{F_p}-1, \\
D &= (\kappa^2-\delta^2)\kappa_p\epsilon - \omega^2(\kappa_p+\kappa) - i\omega\left[\kappa\kappa_p(\epsilon+1)-\omega^2\right].
\end{aligned}$$

Figure 2-11 shows a theoretical plot of the in-phase noise spectrum for a shot-noise limited pump and the noise spectrum is normalized to the shot-noise level of the OPO

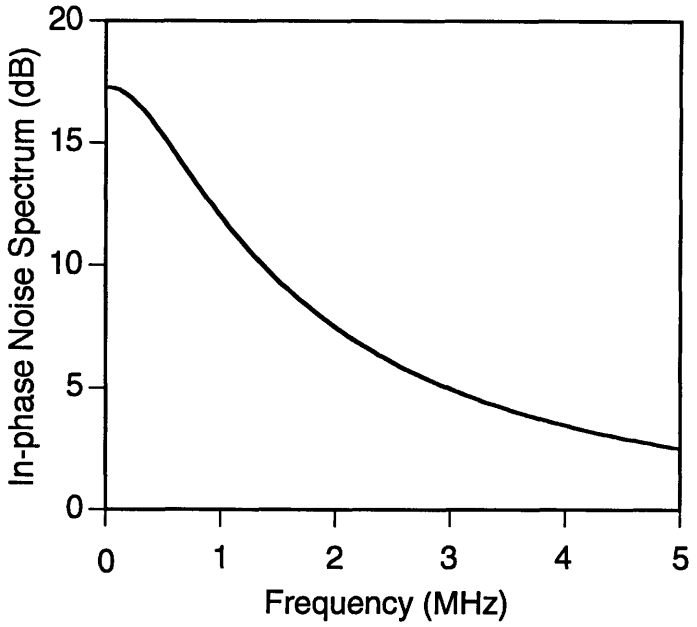

Figure 2-11: Theoretical plot of beat-note in-phase noise power spectrum (S_x) with a shot-noise limited pump laser. The power spectrum is normalized to shot-noise level (0 dB) of the OPO output dc power (zero detuning). The parameter values used for the plots are listed in Table 2.1.

output power. The pump intensity noise to in-phase noise transfer function (H_{AA}),

$$\begin{aligned} S_x(\omega) &= H_{AA} h^R(\omega), \\ H_{AA} &= \frac{\gamma_1}{\kappa} \frac{4}{|D|^2} \epsilon \kappa_p^2 |\kappa^2 - \delta^2 - i\kappa\omega|^2, \qquad \text{for } \gamma_1 = \gamma_2, \end{aligned}$$

is shown in Fig. 2-12, where S_x and the excess pump intensity noise h^R are normalized to their respective shot-noise levels. The transfer function H_{AA} relates h^R to the fractional in-phase noise S_x and it is pump power dependent (F_p). The larger than 0 dB transfer at low frequencies in Fig. 2-12 does not imply a gain in the in-phase noise but rather a small OPO output power. The in-phase noise spectrum difference between low frequencies and high frequencies is about 10 dB, which is much smaller than the 40-dB difference in the quadrature-phase spectrum.

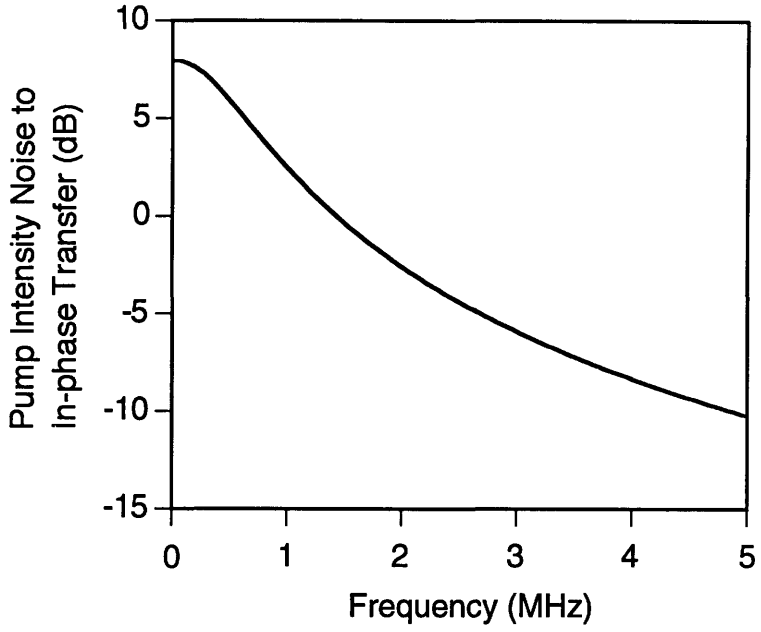

Figure 2-12: Theoretical plot of pump laser intensity noise to in-phase noise transfer function (H_{AA}) (zero detuning). The parameter values used for the plots are listed in Table 2.1.

2.9 Intensity Noise Spectrum

The detected signal-idler signal can be separated into dc and ac components. The synchronously demodulated ac components give the in-phase and quadrature-phase signals, whereas the dc component gives the intensity noise of the combined beam. The dc component is given by

$$\begin{aligned} \Delta I_{dc} &= 4C^2\left(\frac{\gamma_1}{\kappa_1}\mu_1 + \frac{\gamma_2}{\kappa_2}\mu_2\right) - \sqrt{8}\,C\left(\sqrt{\frac{\kappa_1}{\gamma_1}}\,\mu_1^u + \sqrt{\frac{\kappa_2}{\gamma_2}}\,\mu_2^u\right), \\ &= 4C^2\left(\Gamma\mu_+ + g\mu_-\right) - \sqrt{8}\,C\left(R_1^u + R_2^u\right), \end{aligned} \tag{2.50}$$

$$\begin{aligned} \Gamma &= \frac{1}{2}\left(\frac{\gamma_1}{\kappa_1} + \frac{\gamma_2}{\kappa_2}\right), \\ g &= \frac{1}{2}\left(\frac{\gamma_1}{\kappa_1} - \frac{\gamma_2}{\kappa_2}\right). \end{aligned}$$

Comparing Eq. (2.50) with Eq. (2.48), we see that the dc-intensity fluctuation

(Eq. (2.50)) and the demodulated in-phase signal (Eq. (2.48)) are not identical. The in-phase signal contains only the sum-intensity fluctuation (μ_+), whereas the dc-intensity signal contains both the sum-intensity (μ_+) and the difference-intensity fluctuations (μ_-). If the signal and the idler losses are matched, g becomes zero and the two equations would give the same result.

2.10 Summary

We discuss in this chapter the model and the results of our theoretical study of OPO characteristics. The simple plane-wave model used in the calculation provides general understanding of OPO behavior under steady-state conditions. The intensity and phase quadrature power spectra are calculated using the linearized quantum Langevin equations. In the spectra calculations, we allow arbitrary losses and detuning for the signal and the idler fields for more realistic modeling of experimental conditions. Furthermore, the effects of excess pump laser intensity noise and phase noise are also included in the calculation to enable us to study the laser noise transfer functions of the OPO.

Our calculation shows that detuning mixes the intensity-quadrature and the phase-quadrature noise for the beat-note signal between the signal and the idler fields. The amount of mixing depends on the degree of detuning, with complete separation between the two quadratures at zero detuning. On the other hand, loss mismatch is responsible for the transfer of pump laser noise to the signal-idler beat signal. When the losses of the two fields are perfectly matched, the correlations between the two fields are also perfect. The pump laser noise are evenly split between the signal and the idler so that the noise contribution is canceled when the difference is detected.

Detuning and loss mismatch do not significantly affect the phase noise spectrum in the absence of excess pump noise, as shown in Fig. 2-5. However, with excess pump noise, the impact of cavity detuning can be more significant than loss mismatch. In order to have a precise measurement, loss mismatch and cavity detuning should both be minimized.

We shall discuss the experimental work of the phase noise measurements in Chapter 6, where the theoretical predictions and experimental results are compared.

Chapter 3

Pump Laser System

3.1 Introduction

In this chapter we describe the pump laser system that was used in all of our OPO experiments and we shall refer to this chapter for pump laser characteristics.

The doubly resonant condition of the OPO places very stringent requirements on the intensity and frequency stability of the input pump laser. Any intensity or frequency fluctuation in the input field is transferred to the OPO outputs. Moreover, because of mixing of the intensity noise and frequency noise in the OPO, it is important to reduce both intensity and frequency noise in the pump.

In an OPO the signal-idler frequency difference is, to zeroth order, immune to the pump frequency noise. That implies that the individual signal and idler frequency undergoes a frequency deviation that is equal to half of the input pump frequency deviation. Since the OPO cold-cavity IR linewidth is approximately 5 MHz, any pump frequency fluctuation that is larger than 10 MHz can prevent the OPO from sustaining a cw oscillation. Therefore, the laser frequency's jitter has to be minimized in order to have stable cw OPO operations.

The pump laser system in our experiments was an intensity and frequency stabilized krypton ion laser that could yield 500 mW of power at the input port of the OPO. Figure 3-1 shows a schematic of our pump laser system, the Kr^+ laser, the intensity-servo loop and the frequency-servo loop. In the following sections, we

will discuss the pump laser that was used in our experiments and its intensity and frequency stabilization servo systems.

3.2 Pump Laser

The pump laser was a Coherent INNOVA 200 krypton ion (Kr^+) laser operating at a wavelength of 530.9 nm with a single transverse and longitudinal mode. The choice of 530.9 nm as the pump wavelength was primarily determined by the large volume of experimental data on KTP at the wavelength of 532.1 nm of the frequency-doubled 1064 nm and by our interest in operating the OPO near frequency degeneracy. There have been numerous experiments on the second harmonic generation (SHG) of 1.064 μm using potassium titanyl phosphate (KTP) crystal as the nonlinear medium and the SHG phase-matching angle for KTP at 1064 nm has been well established for both flux grown and hydrothermally grown crystals. The phase match angle for 530.9 nm is approximately $\sim$1.8° larger than that for 532.1 nm, which is at $\theta = 90°$, $\phi = 23.8°$ for a flux grown KTP crystal.

Our Kr^+ laser had a maximum output power of about 850 mW at 531 nm. However, usable power at the OPO input port after the Faraday isolator and the intensity servo was only about 500 mW, a 40% reduction. The Faraday isolator had a measured 10% insertion loss at 531 nm and an extinction ratio of more than 40 dB, which was adequate for our experiment.

The laser exhibits a significant amount of intensity and frequency noise at low frequencies around 400 Hz that was caused by the laser's plasma tube structural vibrations, which in turn was induced by the flow of water coolant inside the laser. Under free running conditions, the laser peak-to-peak intensity noise was $\sim$2.6% at 500 mW with an estimated frequency jitter of $>$ 40 MHz. Table 3.1 summarizes some of the properties of the krypton ion laser.

A frequency-doubled diode-pumped YAG laser has excellent intensity and frequency noise characteristics and is an alternative pump source, but its output power is usually limited to $\sim$50–60 % of the fundamental power at 1064 μm. This diode-

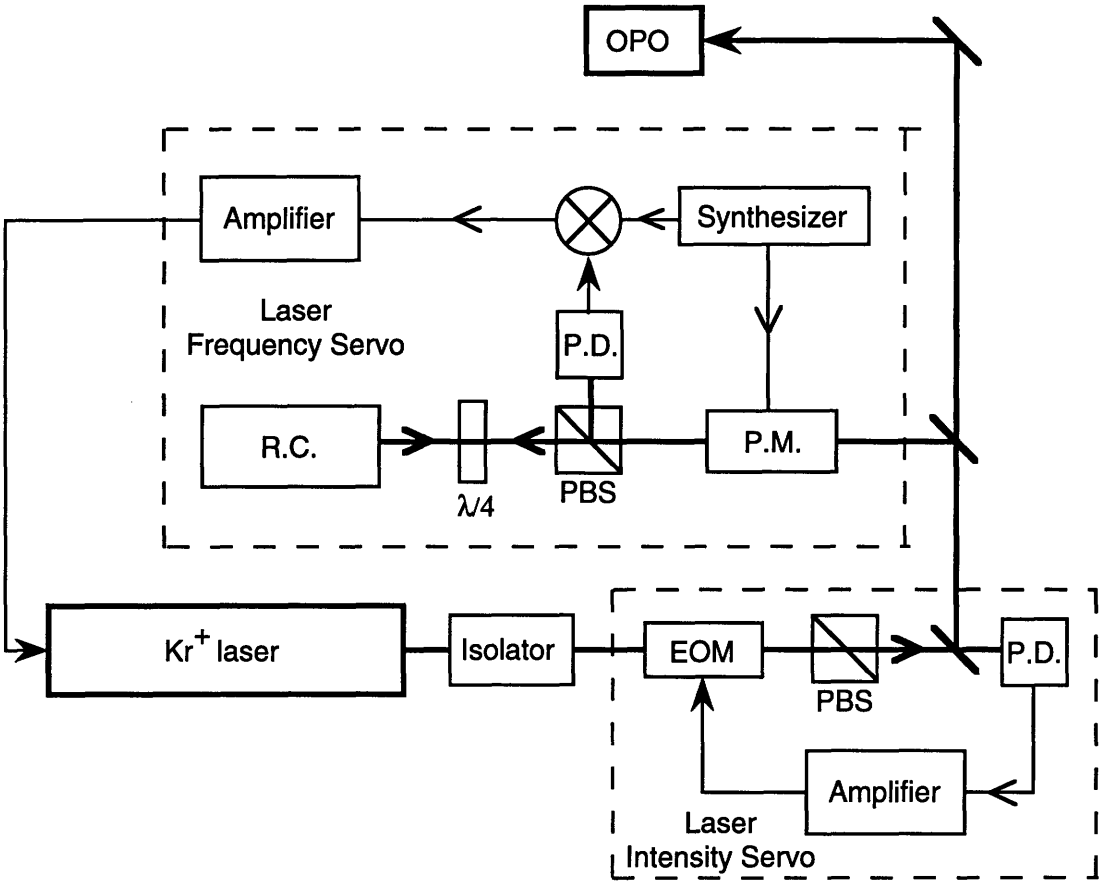

Figure 3-1: Schematic of pump laser system showing the Kr^+ laser, the intensity-servo loop, and the frequency-servo loop. (PBS: polarizing beam splitter; P.D.: photodetector; EOM: electro-optic modulator; PM: phase modulator; RC: reference cavity.)

Single frequency line	530.9 nm
Beam quality	TEM_{00}
Cavity configuration	15-m output coupler; Flat back high reflector with prism and etalon
Cavity length	1.95 m
Max. power (single line)	850 mW
Free spectral range	76 MHz
Intensity noise	$\sim 2.6\%$ at 500 mW of output
Frequency jitter	$> \pm 20$ MHz

Table 3.1: Summary of krypton ion laser output properties.

pumped source is an obvious replacement for the large-frame krypton ion laser in the future.

3.3 Intensity Stabilization

The laser intensity was actively controlled by a feedback servo loop to reduce the intensity noise and to allow for adjustment of the incident power at the OPO input port. The intensity servo consisted of an electro-optic modulator (EOM; Quantum Technology model 28), a photodetector, a polarizing beam splitter (PBS), and an amplifier for error signal conditioning (Fig. 3-1).

The laser intensity fluctuation detected by the photodetector was compared to a quiet dc reference to generate the error signal for feedback. The dc level was not only a reference for the noise fluctuation, but it also controlled the amount of optical output power. The error signal was integrated and amplified by the signal-conditioning electronics before it was input to the EOM. A test-input port was included in the amplifier circuit to permit the test-input signal and the intensity error signal to be summed before the EOM, thus providing a means for pump laser amplitude modulation. In response to the error signal, the EOM rotated the polarization of the incoming linearly polarized laser field. Together with the PBS, which acted as a polarization analyzer, the combination reduced the intensity fluctuation of the input field and controlled the amount of optical power transmitted through the EOM-PBS unit.

The intensity servo loop had a measured unity-gain bandwidth of 1 MHz, which was adequate for our experiments. The dc reference level and the over-all loop gain were user adjustable and could be easily changed during the experiment.

Figure 3-2 shows the time traces of the pump laser intensity fluctuations under free-running and servo-locked conditions, and Figure 3-3 shows the corresponding spectra in the frequency domain. The peak-to-peak intensity noise was measured to be 2.6% at 500 mW of usable power under free-running conditions and was reduced to 0.53% under servo-locked conditions. From Fig. 3-3, the intensity spectra show a

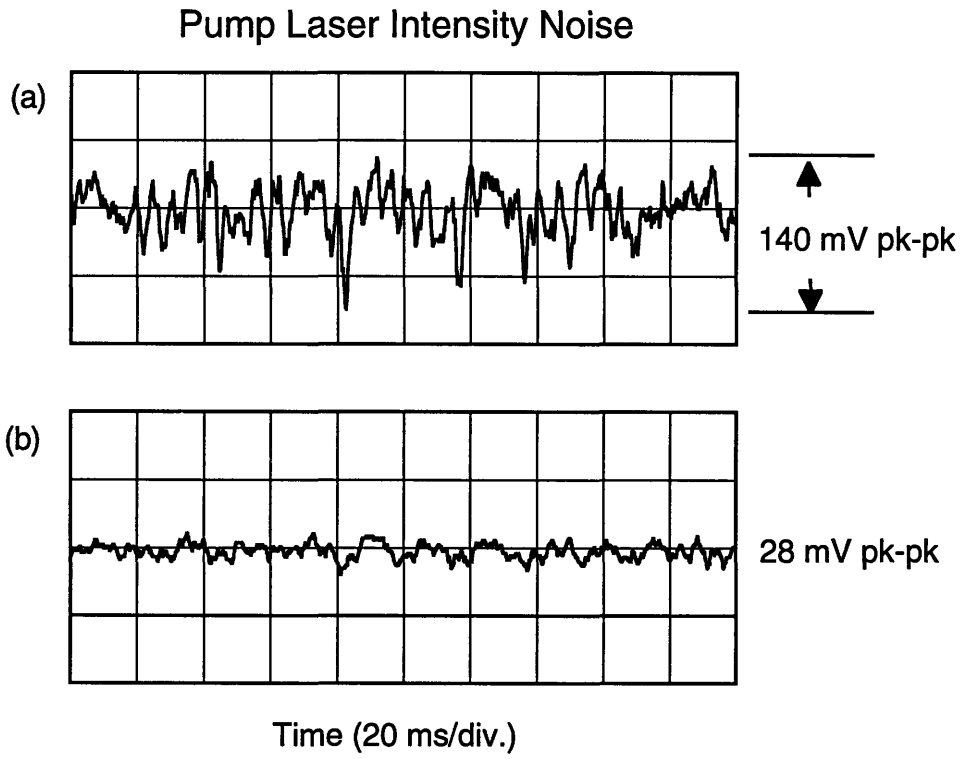

Figure 3-2: Time traces of pump laser intensity noise under (a) free-running (peak-to-peak intensity noise is 2.6% at 500 mW), and (b) servo-locked (peak-to-peak noise 0.53%) conditions. Averaged dc intensity voltage is 5.3 V. (Vertical scale 50 mV/div.; horizontal scale 20 ms/div.)

noise suppression of more than 20 dB at low frequencies and the intensity become shot nose limited at 2.5 MHz. The slight rise in noise level between 1.5–3 MHz in Fig. 3-3b was caused by excess intensity-loop gain.

3.4 Frequency Stabilization

The laser frequency was actively stabilized with the Pound-Drever [12] stabilization system to less than ± 25 kHz. The free-running laser frequency jitter was estimated to have a peak-to-peak deviation of > 40 MHz (mostly at 400 Hz due to water induced vibrations).

The detailed workings of the Pound-Drever technique will not be discussed here, only the result and some of the specific implementations are described. The major

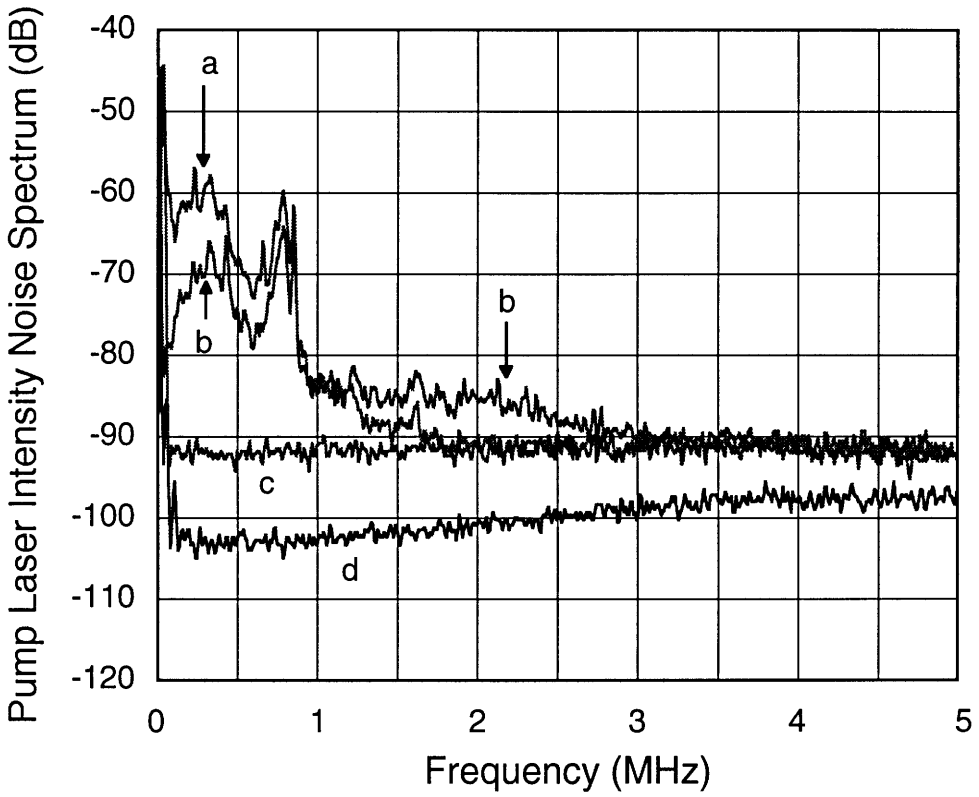

Figure 3-3: Traces of pump laser intensity noise spectra under (a) free-running conditions and (b) intensity-locked conditions. (c) Trace of shot-noise level. (d) Trace of photodetector electronic noise level obtained when incident light is blocked. The rise in noise level between 1.5–3 MHz in (b) is caused by excess intensity-loop gain.

components of the laser frequency stabilization loop consisted of a phase modulator (PM), a Zerodur reference cavity (RC), a high speed photodetector (PD), a rf synthesizer, a PZT-mirror actuator, and the signal-conditioning electronics (Fig. 3-1). The modulation frequency for the laser sidebands was 15 MHz with a modulation index β of 0.6. The single-ended reference cavity's free spectral range (FSR) was 725 MHz with a measured finesse of 743, yielding a cavity linewidth (FWHM) of 975 kHz. To improve isolation from vibrations that were transmitted through the table, the reference cavity was placed on top of Sobrothene absorbers, a soft damping material. The actuator of the frequency stabilization loop was the laser-cavity back-mirror that was attached to a stack of two piezoelectric transducers (PZT). The bandwidth of the laser-frequency loop was estimated from Fig. 7-2 to be 25 kHz and was limited by the bandwidth of the PZT's stack.

Figure 3-4 shows a time trace of the detected pump power obtained in transmission through the reference cavity. From the 20 mV peak-to-peak deviation in Fig. 3-4, the residual frequency jitter was estimated ($2 \times 20/860 \times 975$ kHz) to be ± 25 kHz, compared to 40 MHz peak-to-peak under free-running conditions. The laser frequency/phase noise is further discussed in Section 7.2.4.

3.5 Summary

In this chapter, we have discussed the pump laser system including the intensity and frequency stabilization servos. Table 3.5 summarizes the relevant operating properties of the pump laser field at the OPO input port:

Wavelength	Single frequency at 530.9 nm
Max. power at OPO input	400 mW
Intensity noise	0.5%
Shot-noise limited frequency	above 2.5 MHz
Frequency jitter	~50 kHz

Table 3.2: Summary of pump laser operating properties at the input port of the OPO.

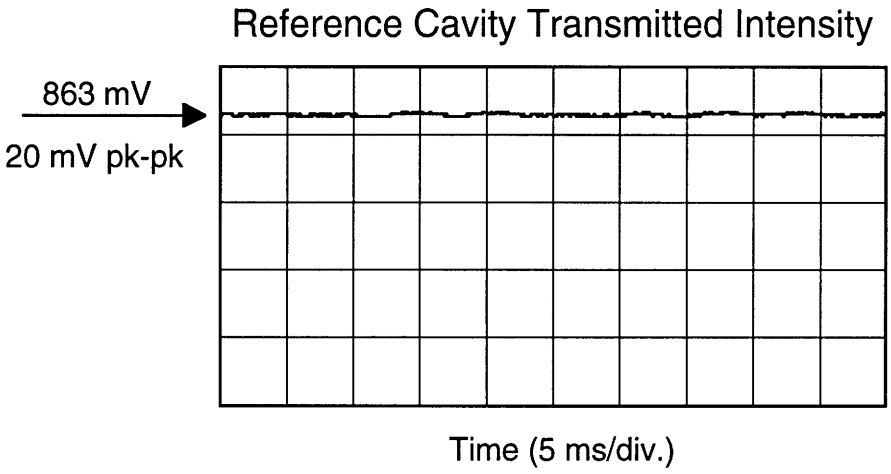

Figure 3-4: Time trace of transmitted pump intensity behind the reference cavity. The small amount of peak-to-peak deviation (20 mV) indicates that the laser frequency is locked to the reference cavity. The residual frequency jitter is estimated to be 50 kHz. (Vertical scale, 20 mV/div.; horizontal scale, 5 ms/div.)

Chapter 4

OPO Cavity Design

4.1 Introduction

There are two major design requirements for our OPO quantum noise experiment: stability and tunability of the OPO. The OPO output intensity and frequency stabilities affect the accuracy of our measurement directly. The intensity and frequency noise are mixed via the parametric process Any fluctuation would affect the stability of the frequency difference that contains the phase noise information we are trying to measure. Stable OPO operation is only part of the requirements, detecting the signal and idler beat-note signal is not as trivial as it may seem. Before we can conduct any OPO phase noise experiment, the OPO output frequencies must be tuned to around the frequency degenerate point so that their frequency difference falls within the detection bandwidth of the experiment. It is therefore necessary to have a systematic procedure for continuously tuning the output frequencies to any desired operating point, including near frequency degeneracy.

Since the signal that we are trying to measure may be only a few dB above the shot-noise level, excess noise in the OPO system must be reduced to near the shot-noise level. The smaller the OPO intensity and frequency fluctuations, the more accurately we are able to measure the quantum noise characteristics. Furthermore, as the noise signal is obtained from the phase difference between the two OPO outputs, their frequency difference must be stable during the course of the measurement.

Our goal for the OPO frequency tuning capability is not limited to smooth, continuous tuning over a narrow range of just a few ten's or hundred's of MHz. It is also of interest to develop a widely tunable (> THz) and highly stable OPO as a tunable optical frequency source. Such a frequency source may have potential applications in precision measurements.

In the past, a wide tuning capability and a highly stable operation for an OPO imply conflicting design requirements. After carefully studying various designs, we have combined the flexibility needed for a wide tuning capability and the rigidity needed for a highly stable operation into a single OPO cavity design. The level of tunability and stability achieved is unprecedented. In this chapter, we discuss some of the design considerations for achieving excellent stability and tunability in a single design of the OPO cavity.

4.2 Background

An OPO consists of a nonlinear $\chi^{(2)}$ medium placed inside an optical cavity. In a parametric down-conversion process, the nonlinear medium converts an input pump field into two subharmonic output fields, called the signal and the idler. The optical cavity provides a positive feedback for the three fields to enhance the three-wave mixing interaction. Above the pump threshold, where the parametric gain equals the total loss [39, p.122], parametric oscillation occurs.

In the down-conversion process, energy and linear momentum are conserved,

$$f_p = f_1 + f_2, \tag{4.1}$$

$$\vec{k_p} = \vec{k_1} + \vec{k_2}, \tag{4.2}$$

where f is the frequency, $\vec{k}$ is the wave vector, and the indices p, 1, 2 denote pump, signal and idler, respectively. The linear momentum relationship (Eq. (4.2)) is also known as the phase-matching condition.

The signal and idler output frequencies are determined by the phase-matching

condition and the cavity resonance frequencies. Coarse frequency tuning (> 100 GHz) can be achieved by changing the phase-matching condition (Eq. (4.2)) while fine tuning (< 100 GHz) can be achieved by changing the cavity resonance frequencies (cavity length). The phase-matching condition can be varied by changing the refractive indices of the nonlinear medium at the three wavelengths. By projecting the $\vec{k}$ vectors onto the propagation axis the phase matching condition becomes

$$\frac{n_p}{\lambda_p} = \frac{n_1}{\lambda_1} + \frac{n_2}{\lambda_2}. \tag{4.3}$$

If the refractive indices n_1 and n_2 were varied, the two output wavelengths λ_1 and λ_2 would have to follow accordingly in order to satisfy Eq. (4.3).

The above simple discussion on the OPO and frequency tuning are provided as an introductory reference for the following sections on OPO cavity design considerations. Detailed discussion for various means of coarse and fine tunings is presented in Section 5.2.

4.3 Design Considerations

We now turn our attention to the two OPO design criteria for the quantum noise experiment: stability and tunability.

4.3.1 Stability

The doubly resonant OPO (DRO), in which both the signal and the idler fields are simultaneously resonant with the optical cavity, places a very stringent requirement on the cavity-length stability. The requirement is determined by the DRO cavity's finesse and free spectral range (FSR), as is illustrated in the following example. Consider a DRO with a FSR of 4.5 GHz and a finesse of 600, the cold-cavity linewidth is 7.5 MHz. Above threshold the double-resonance condition is satisfied, and the DRO cavity can be thought of as two cavities in series, so that it has a double Lorentzian line shape. This leads to a DRO cavity linewidth equal to $(\sqrt{2}-1)^{1/2}$ times the cold-

cavity linewidth, or 4.8 MHz. The corresponding cavity-length tolerance is $\sim$0.56 nm for stable cw outputs [39, p.122].

Poor mechanical stability of cavities, coupled with the crystal's absorption-induced thermal problems and the lack of narrow-linewidth pump lasers have contributed to the DRO's reputation of being highly unstable and difficult to tune. Recent advances in crystal quality, laser source and stabilization technique have overcome some of the technical difficulties. However, factors such as the pump laser noise, mechanical vibrations of the OPO cavity, and operation near the frequency degenerate point, still need to be addressed.

The most effective way to improve mechanical stability is the use of a properly designed OPO cavity. One example is the novel design of a monolithic ring DRO cavity [33, 32], which has shown dramatic improvement in OPO output stability. Our design goal is to minimize the DRO intensity and frequency noise through passive and active controls. The DRO's were constructed as mechanically rigid as possible with a minimum of movable parts and as compact as possible. For better isolation, a sheet of thick rubber was placed between the optical table and the DRO to reduce the effect of mechanical vibrations transmitted through the table. With the proper cavity design and isolation, most of the vibrations could be eliminated. The DRO cavity length was actively stabilized by an intensity servo loop to reduce the residual noise.

Because of the finite detection bandwidth of the experimental setup, the OPO was operated around its frequency degeneracy. A type-II phase-matching geometry was chosen for its stable operation near the degenerate point. There are two types of phase matching, type-I and type-II. In type-I phase matching, the signal and the idler fields are co-polarized so that they are truly degenerate at frequency degeneracy. It has been demonstrated by Eckardt *et al.* that a type-I phase-matched OPO was not stable near degeneracy and it would easily mode hop to different operating points within the phase-matching bandwidth [14]. In type-II phase matching, the signal and the idler fields are never truly degenerate because they are orthogonally polarized. Their orthogonal polarizations means that at degenerate frequency, their refractive indices are different, thus permitting stable operation of the OPO [28]. We have

used potassium titanyl phosphate (KTP) as the nonlinear material for its type-II phase-matching, among other favorable characteristics.

4.3.2 Tunability

Systematic and continuous frequency tuning at the operating point of near frequency degeneracy is essential for our experiment. Since we are also interested in using the OPO as a tunable optical frequency source, our requirements for tunability include broad tuning range, ease of tuning, and high precision.

Since KTP is a biaxial crystal, the phase-matching condition, and hence the output frequencies (Eq. (4.3)) can be changed by varying the incident angle between the pump beam and the nonlinear crystal. In our type-II phase-matched KTP OPO, coarse tuning of the output frequencies was achieved by angle tuning the input pump beam orientation relative to the crystal. This angle tuning could be accomplished in two ways: by adjusting the pump beam relative to the crystal or by adjusting the crystal relative to a fixed pump beam. We used both methods on different OPOs and found that the second method was experimentally easier for tuning the output frequencies. In theory, the output frequency range of the parametric downconversion process is limited by the phase-matching condition and the transparency range of the nonlinear medium. But in practice, the output frequency range is limited by the available pump power as the oscillation threshold increased due to walk off of the three fields as the phase-matching angle is tuned away from the optical axis. In our KTP OPO experiments, the angle-tuning range was primarily limited by the physical size of the nonlinear crystal.

In addition to the coarse angle tuning, there were three other tuning elements built into each OPO for fine tuning. They were PZT[1]-mirror cavity-length tuning, temperature tuning and electro-optic tuning. One of the cavity mirrors was bonded to a stack of PZTs to control the cavity length. The KTP crystal temperature was controlled through a thermo-electric (TE) cooler. For the electro-optic effect, a pair of

[1]Piezoelectric transducer.

electrodes was placed across the crystal's z-axis to provided fast electric-field (E-field) tuning. The OPO frequency tuning experiment is discussed in more details later in Section 5.2.

4.4 Parametric Medium

We chose potassium titanyl phosphate (KTP) as the nonlinear medium in our experiments because of its type-II phase matching, large nonlinear coefficients, low absorption, large temperature and angular tolerances, and good optical quality.

Since KTP is a biaxial crystal, the orthogonally polarized signal and idler waves "see" different refractive indices in a type-II phase-matching geometry. The type-II phase matching permitted smooth tuning near the frequency degenerate point, where our OPO's were designed to operate. The crystals' cut was specified such that the propagation axis was 25.3° from the x axis toward the y axis in the xy plane ($\theta = 90°, \phi = 25.3°$). This was $\sim 1.8°$ greater than the usual angle for YAG frequency doubling [47]. The effective nonlinear coefficient[2] (YAG doubling) at this angle was $d_{eff} = 3.18$ pm/V compared to $d_{36} = 0.38$ pm/V for KDP and $d_{eff} = 1.94$ pm/V for BBO [13].

The wide temperature bandwidth of 25°C [2] of KTP simplified the operation of our OPOs. An oven was not required to stabilize the crystal's temperature, and yet temperature tuning range of several GHz was still possible. With a large angular tolerance, more frequency modes were accessible at any particular angular setting between the pump beam and the crystal, thus simplifying the tuning procedure. Commercial availability of KTP crystals along with state-of-the-art optical polishing and coating were also factors in our choice of KTP.

The following table summarizes some of the physical properties of KTP crystals [2, 4, 13].

Crystal system : Orthorhombic

[2]Exact values for KTP nonlinear coefficients are active areas of research. The most recent publication from *Boulanger et al.* [4] measured d_{eff} to be ~2.43 pm/V.

Point group : mm^2

Cell parameters : $a = 1.28$ nm, $b = 0.640$ nm, $c = 1.059$ nm

Refractive indices	532 nm	1064 nm
n_x	1.7785	1.7381
n_y	1.7892	1.7458
n_z	1.8894	1.8302

Nonlinear coefficient	
at 532 nm [4] [pm/V]	$d_{15} = 1.4$
	$d_{24} = 2.65$
	$d_{33} = 10.7$

Electro-optic coefficient	pm/V
r_{13}	9.5
r_{23}	15.7
r_{33}	36.3
r_{51}	7.3
r_{42}	9.3

Temperature coefficients	$\Delta n_x = 1.1 \times 10^{-5}$
of refractive index (K^{-1})	$\Delta n_y = 1.3 \times 10^{-5}$
	$\Delta n_z = 1.6 \times 10^{-5}$
Thermal expansion	$\alpha_1 = 11 \times 10^{-6}$
coefficients (K^{-1})	$\alpha_2 = 9 \times 10^{-6}$
	$\alpha_3 = 0.6 \times 10^{-6}$
Thermal conductivity (W/cm K)	$k_1 = 2.0 \times 10^{-2}$
	$k_2 = 3.0 \times 10^{-2}$
	$k_3 = 3.3 \times 10^{-2}$
Phase-matching angle	$\theta = 90°$
$\omega = 532$ nm, $2\omega = 1064$ nm	$\phi = 24.3°$
Transparency range	350–3000 nm
Temperature bandwidth	25° C
Density	2.945 g/cm^3
Specific heat	0.724 J/g K
Damage threshold	500 MW/cm^2
(10 ns pulse, 1064 nm)	

4.5 Configurations

OPO cavity configurations can be classified by the types of resonant cavity and by their mechanical designs. In this section, we discuss the advantages and disadvantages of various configurations.

4.5.1 Ring vs. Linear Cavity

A ring cavity has the advantage of having a traveling wave inside the cavity and avoids setting up high-field intensity nodes inside the crystal, thereby minimizing

photo-refractive damage. On the other hand, a ring cavity is more difficult to align than a linear cavity.

In our experiment, all of the OPOs were of linear cavity design with a double-pass pump configuration. The combination of a linear cavity and a double-pass pump configuration has a major advantage over other designs in that, under the optimal condition, the parametric interaction length is effectively doubled [11]. The optimal condition is when the three fields (pump, signal and idler) reflect off the mirror surfaces without any extra relative phase shifts induced by reflection. If such a condition is met, the effective length of the medium is doubled and the threshold is reduced by a factor of 4 compared to a ring cavity. Even under the worst case situation, when the three fields reflect off the mirrors with a π phase shift, the OPO would self-adjust the phase-matching condition [11] so that the threshold would still be reduced by a factor of 2. The OPO always picks the lowest threshold signal and idler mode pair for oscillation. Given the same nonlinear crystal length, a double-pass pump linear cavity configuration has a threshold that is 2 to 4 times lower than that of a ring cavity, provided the losses are equal in both cases.

4.5.2 Singly to Triply Resonant Cavity

An OPO can be further classified as singly, doubly and triply resonant. Using different mirror coatings, we can selectively choose to resonate any one, or two, or all three interacting fields. As the name implies, a singly resonant OPO (SRO) resonates only one of the three fields, a doubly resonant OPO (DRO) resonates only two and so on.

The threshold of oscillation, given by

$$\frac{\kappa_1 \kappa_2 \kappa_p}{2\chi^2},$$

is related to the product of the total loss of the three fields. The threshold decreases as one goes from singly to doubly, to triply resonant. For comparison, Yang *et al.* has recently demonstrated a cw singly resonant KTP OPO with a threshold of 1.4 W, while a similarly configured DRO has a threshold of around 20 mW [46]. On the

other hand, the requirement on cavity length stability increases from singly to triply resonant as more constraints on the cavity length are imposed on the oscillation conditions. We chose the doubly resonant design in our experiments as a compromise between threshold and stability requirements.

4.5.3 Construction

The three basic types of OPO configurations: monolithic, 2-element and 3-element, are shown in Figure 4-1. They all share the same simple concept: a nonlinear crystal placed between two reflecting surface. They differ in their implementation of the two cavity mirrors.

Monolithic Design

The monolithic design has the simplest form. Both ends of the crystal surfaces are polished and coated to form the reflecting mirrors. The monolithic OPO has the best mechanical stability and the lowest threshold because it has no movable parts and minimum scattering losses. Nabors *et al.* was the first to demonstrate wideband tunability and stable free-running operation in a monolithic lithium niobate ($LiNbO_3$) DRO [32].

However, the monolithic DRO's disadvantages out-weigh its advantages to make it an impractical design. Its fabrication process is more complex than the other designs and it has a low tolerance for error in polishing. Once the cavity is formed, it lacks any flexibility in changing the cavity parameters, such as the output coupling and the confocal parameter. There is no easy implementation for fast cavity-length adjustment to compensate for any external perturbation, except with electro-optics tuning, in which a high electric field ($\sim$ 500 V/mm) is required to scan a free spectral range of the cavity. The high field that is required is known to cause grey-track damage [3]. Another cavity-length control is to make use of the slow thermal expansion of the crystal with the use of a TE cooler. Finally, the most serious problem with a monolithic linear DRO is that there is only one propagation path that can support

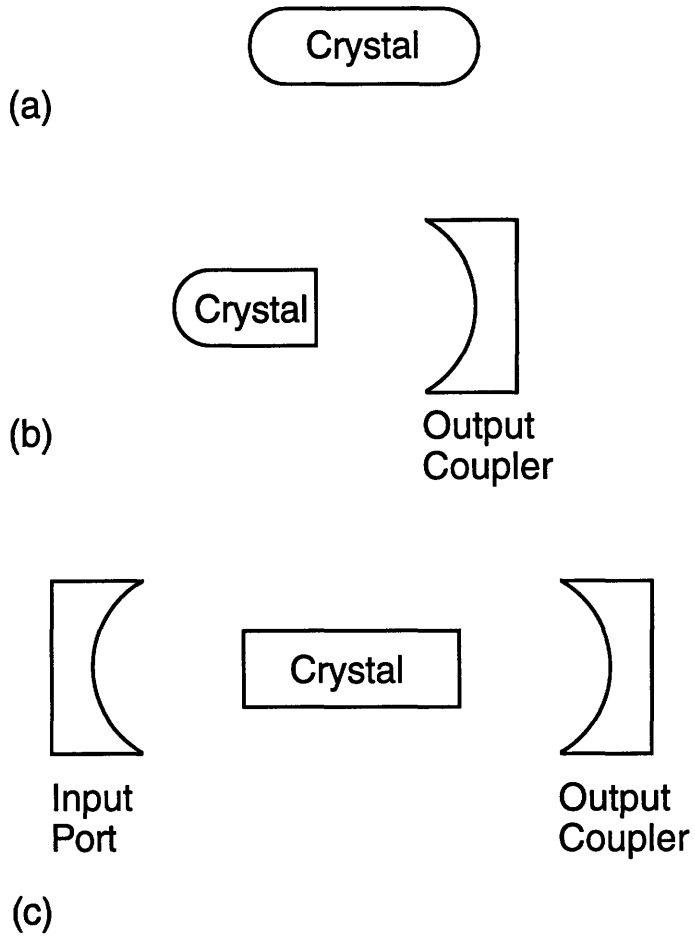

Figure 4-1: Three different cavity configurations of OPOs, (a) monolithic, (b) 2-element, and (c) 3-element.

stable oscillation, as determined by the two curved mirrors. With only one propagation path, the monolithic DRO cannot be angle tuned and the output frequencies are predetermined by the propagation path. Furthermore, the DRO would stop oscillation if that path is damaged for any reason, such as caused by photorefractive or coating damage.

Advantages	Disadvantages
Low threshold	Complex fabrication
Stable operation	Lack of flexibility
Compact	Lack of fast tuning
	Lack of angle tuning
	Only one propagation path

Table 4.1: Summary of monolithic linear DRO cavity design advantages and disadvantages.

Multi-Element Design

In a multi-element design, one or both of the reflective surfaces are replaced with mirrors, and the corresponding crystal surfaces are polished flat and AR coated to minimize reflective losses. A two-element DRO comprises a crystal and one mirror, and a three-element design consists of a crystal and two mirrors.

The 3-element OPO is the easiest to construct and most flexible in changing cavity parameters. One of the external mirrors is mounted on PZT stacks to provide fast cavity-length control. If there were localized damage to the crystal, it could be translated to allow cw operations on a new spot on the crystal surface. The main drawback in the 3-element OPO, however, is its high threshold due to its two air-crystal interfaces. It is also perceived to be the least mechanically stable configuration. A multi-element design is inherently more susceptible to environmental vibration than the monolithic design. It is therefore necessary to eliminate any spring-loaded mount from the design and the cavity elements should be fixed in position by attaching them rigidly to a common platform. Our 3-element OPO, with its highly stable construction in which the mirrors were attached to aluminum plates and bolted onto

a spacer block, was as stable as the monolithic cavity.

Finally, the 2-element OPO is a compromise between the monolithic and the 3-element design. It is easier to construct and more flexible than the monolithic design in changing cavity parameters after fabrication. It has an intermediate threshold level and it incorporates a fast PZT cavity-length control. However, mechanical stability may still be a concern as in the 3-element design. Careful design consideration is still needed to achieve the desired mechanical stability.

Advantages	Disadvantages
Easy fabrication	Higher threshold than monolithic cavity
Flexible	Mechanical stability is a concern
Wideband angle tuning	
Fast cavity-length tuning	

Table 4.2: Summary of multi-element DRO cavity design advantages and disadvantages.

4.6 Summary

We discussed, in this chapter, the OPO stability and tunability requirements for our quantum noise experiment, and how to incorporate these requirements into the cavity design. The advantages and disadvantages of various OPO design configurations were also discussed.

After careful consideration, type-II phase-matched KTP crystals were chosen as the nonlinear medium in our doubly resonant OPOs (DROs). We tried all three different mechanical configurations for our DROs, each with tunability and stability as the highest priorities. Four frequency tuning elements were integrated into each DRO construction, with the exception of the monolithic cavity. Our experimental results with these DROs are presented in the following chapters.

Chapter 5

Frequency Tuning Experiments

5.1 Introduction

In Chapter 4, the stability and tunability requirements for the OPO quantum noise experiment were discussed in detail. We now proceed to discuss our series of experiments on the tunability of various OPO cavity configurations. Since we were also interested in developing the OPO as a tunable frequency source, our experiments were not confined to limited tunability around the frequency degenerate point, as was required in the quantum noise measurements.

Three different DROs were fabricated and studied in our experiments. They were the monolithic cavity, the 2-element cavity, and the 3-element cavity. Each DRO included four different frequency tuning schemes, from coarse, discrete tuning to fine, continuous tuning. The four tuning elements were the crystal's angle, the PZT[1]-actuated-cavity-length, the crystal's temperature, and the crystal's electro-optic effect. Their frequency tuning ranges and coefficients were measured in our experiments. In particular, our best results were obtained from the 3-element DRO where the output intensity was stabilized to 0.6% rms and the output frequency difference (f_d) was discretely tuned to span over ± 3 THz. Furthermore, continuous tuning in f_d using the temperature control and the electro-optic effect were also achieved

[1]Piezoelectric transducer.

with respective ranges of ~0.5 GHz and 40 MHz.

In this chapter, we first discuss the working principles of the four tuning elements, followed by a brief description of the high-speed difference-frequency detection system, and finally the experimental observations for the tunability of our DROs. The experiments on the stabilization of the DRO output frequencies are discussed in Chapter 6.

5.2 Frequency Tuning Schemes

Systematic frequency tuning in our DROs was critical for our quantum noise experiment, as well as for any tunable optical frequency source application. Four different frequency tuning capabilities were implemented in our DROs to control the output frequencies, as stated in the introduction. Each element employed a different scheme and covered a different frequency span. They were the coarse but wide-span angle tuning, the fast but narrow-span electro-optic tuning, and the intermediate-span PZT-length and temperature tunings. These four elements allowed us to access any frequency within the phase-matching bandwidth that was limited by the crystal's physical size.

The signal and idler output frequencies were determined by the phase-matching condition and the cavity resonance frequency. The phase-matching condition established a frequency bandwidth within which the DRO could oscillate. However, it was the cavity resonance that determined the actual oscillation frequency. Therefore, frequency tuning was achieved by changing either the phase-matching condition or the cavity resonant frequency, depending on the required tuning range.

Of the four tuning elements, only angle tuning changed the phase-matching condition, whereas the other tuning elements affected the effective optical length, and hence the cavity resonance frequency. Except for the PZT-length tuning, the temperature and electro-optic tuning elements modified the refractive indices by different amounts. However, the small modification of the refractive indices had negligible effects on the phase-matching condition.

The PZT-cavity-length control, on the other hand, changed the cavity resonance frequency by changing the common-mode intra-cavity spacing without affecting the crystal.

5.2.1 Angle Tuning

Angle tuning was used to provide coarse frequency tuning with the widest tuning range (> THz). By changing the relative orientation between the pump beam and the crystal, the phase-matching condition could be varied to provide frequency tuning. The phase-matching condition, when projected onto the propagation axis, becomes

$$\frac{n_p}{\lambda_p} = \frac{n_1}{\lambda_1} + \frac{n_2}{\lambda_2}. \tag{5.1}$$

If the refractive indices n_1 and n_2 are changed, the two output wavelengths λ_1 and λ_2 would have to change accordingly in order to satisfy Eq. (5.1).

In a type-II phase-matched KTP crystal, the x, y, and z components of the wave vector $\vec{k}$ have to satisfy the following equations [47]

$$\begin{aligned}
\frac{k_x^2}{n_\omega^{-2} - n_{x,\omega}^{-2}} + \frac{k_y^2}{n_\omega^{-2} - n_{y,\omega}^{-2}} + \frac{k_z^2}{n_\omega^{-2} - n_{z,\omega}^{-2}} &= 0, \\
\frac{k_x^2}{n_{2\omega}^{-2} - n_{x,2\omega}^{-2}} + \frac{k_y^2}{n_{2\omega}^{-2} - n_{y,2\omega}^{-2}} + \frac{k_z^2}{n_{2\omega}^{-2} - n_{z,2\omega}^{-2}} &= 0,
\end{aligned}$$

$$\begin{aligned}
k_x &= \sin\theta\cos\phi, \\
k_y &= \sin\theta\sin\phi, \\
k_z &= \cos\theta,
\end{aligned}$$

where $n_{2\omega}$ and n_ω are the refractive indices for the fundamental and the subharmonic waves, respectively. Here, θ is angle between the propagation direction and the z axis and ϕ is the angle from the x-axis toward the y-axis in the xy plane, as illustrated in Fig. 5-1.

For our OPO, the ordinary subharmonic ray (vertical polarization, along the crys-

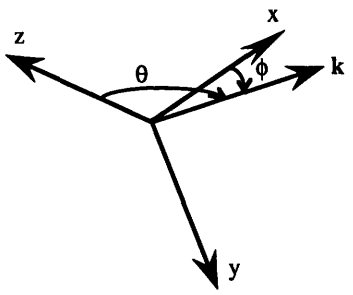

Figure 5-1: Sketch of the crystal's optical axes and the propagation direction $\vec{k}$. θ is the angle from the z-axis and ϕ is the angle from the x-axis toward the y-axis in the xy plane.

tal's z axis) propagating in the xy plane ($\theta = 90°$) saw an effective refractive index n_o given by

$$\frac{1}{n_o^2(\omega)} = \frac{\cos^2\phi}{n_y^2(\omega)} + \frac{\sin^2\phi}{n_x^2(\omega)},$$

and the extra-ordinary ray (horizontal polarization) saw a refractive index of

$$n_e(\omega) = n_z(\omega),$$

where ϕ was the phase-matching angle, and n_x, n_y, n_z were the refractive indices along the principal axes. Therefore, this phase-matching condition, and hence the output frequencies, could be varied by changing the pump-crystal angle. The values of the refractive indices n_x, n_y at various frequencies could be estimated using the Sellmeier equations for KTP [2, 47, 16].

In practice, the phase matching condition (Eq. (5.1)) does not have to be satisfied exactly for OPO oscillation. Slight mismatch in the phase-matching equation can exist. There is a tolerance, or bandwidth, in the phase-matching condition

$$\Delta\vec{k} \equiv \vec{k_p} - \vec{k_1} - \vec{k_2},$$

within which the DRO generates outputs. The phase mismatch ($\Delta\vec{k}$) does not affect the operation or the behavior of the DRO, except the oscillation threshold [11]. The

threshold of a DRO is modified by the phase mismatch factor given by

$$\text{threshold} \sim \left(\frac{\sin(\frac{\Delta kd}{2})}{(\frac{\Delta kd}{2})} \right)^{-2}, \tag{5.2}$$

where d is the crystal length. Minimum threshold is attained at zero phase mismatch.

The bandwidth of the signal-idler frequency difference (f_d) allowable by the phase mismatch ($\Delta kd = 2\pi$), assuming no dispersion can be estimated by

$$\text{bandwidth}(\Delta f_d) = \frac{2c}{d(n_2 - n_1)},$$

where c is the speed of light, and n_1, n_2 are the signal and idler refractive indices, respectively. A quick calculation for a 8-mm long crystal gives a bandwidth of 890 GHz.[2] The phase matching bandwidth was utilized for obtaining continuous frequency tuning in our DRO.

5.2.2 PZT-Length Tuning

The output coupler of the DRO was mounted on a stack of two PZTs for cavity length control. Besides acting as the actuator of the DRO intensity stabilization loop, the PZT-mounted mirror also provides output frequencies tuning capability. There are two different modes of PZT tuning: discrete medium range (~10 GHz) tuning and continuous fine (< 10 MHz) tuning.

Discrete Tuning

DRO oscillation occurs only when the double resonance condition was satisfied. As the cavity length was scanned, there existed more than one PZT position at which the double resonance condition was satisfied. At each of these PZT positions, the DRO output was referred to as a frequency mode. Between each adjacent mode, the signal and idler output frequencies, as well as their wave numbers (number of half wavelengths) were different. These changes in the frequencies and the wave

[2]With $n_1 = 1.746$ and $n_2 = 1.830$

numbers were necessary to compensate for the difference in refractive indices seen by the orthogonally polarized signal and idler fields.

We have developed a simple theoretical model to explain the PZT tuning behavior and to predict the frequency difference of each adjacent modes. As calculated in Appendix D, the signal-idler frequency difference changed (Δf_d) between each adjacent mode was twice the nominal free spectral range of the cavity, and the spacing between these PZT positions was determined by the cavity's geometry.

As an numerical example, consider a typical DRO cavity with a physical mirror separation of $l = 38$ mm and a $d = 8$-mm long KTP crystal placed between the mirrors. The nominal free spectral range of the cavity is 3.4 GHz. Therefore, between each adjacent mode, the frequency difference f_d changes by 6.4 GHz and the cavity-length spacing between modes is ≈ 4 nm.

Continuous Tuning

Continuous frequency tuning was achieved by adjusting the cavity length while the DRO was above threshold. The cavity-length adjustment was small enough so that it would not stop the DRO from oscillation. We can estimate the change in the signal-idler frequency difference (Δf_d) as a function of cavity-length change (δl) by considering the normalized cavity-detuning equation (Eq. (2.4)),

$$\frac{f_1 - f_1^c}{\kappa_1} = \frac{f_2 - f_2^c}{\kappa_2}, \tag{5.3}$$

where $f_{1,(2)}$ is the signal (idler) frequency, $f_{1,(2)}^c$ is the signal-cavity (idler-cavity) resonance frequency, and $\kappa_{1,(2)}$ is its total loss rate. By using the frequency difference definition,

$$f_d = f_1 - f_2,$$

the sum-frequency constraint,

$$f_p = f_1 + f_2,$$

and Equation (5.3), one obtains the difference frequency equation,

$$f_d = \frac{\kappa_1 - \kappa_2}{\kappa_1 + \kappa_2} f_p + \frac{2c}{\kappa_1 + \kappa_2} \left(\frac{\kappa_2}{\lambda_1^c} - \frac{\kappa_1}{\lambda_2^c} \right). \tag{5.4}$$

By using

$$\delta \frac{1}{\lambda_i^c} = -\frac{1}{\lambda_i^c} \frac{\delta l_1}{L_1},$$

the change in frequencies difference (Δf_d) is then given by

$$\Delta f_d = \frac{-2}{\kappa_1 + \kappa_2} \left(\kappa_2 f_1^c \frac{\delta l_1}{L_1} - \kappa_1 f_2^c \frac{\delta l_2}{L_2} \right), \tag{5.5}$$

where

$$L_{1,2} = l + d(n_{1,2} - 1)$$

is the effective signal-cavity (idler) optical length. Here, l is the physical separation between the two mirrors and d is the crystal length. As a first order approximation, we replace the cavity resonant frequencies ($f_{1,2}^c$) by half the pump frequency ($f_1^c \approx f_2^c \approx f_p/2$). Equation (5.5) then becomes

$$\Delta f_d \approx \frac{-f_p}{\kappa_1 + \kappa_2} \left(\kappa_2 \frac{\delta l_1}{L_1} - \kappa_1 \frac{\delta l_2}{L_2} \right). \tag{5.6}$$

As we can see from Eq. (5.6), frequency tuning depends on the difference of the optical path lengths ($L_{1,2}$) as seen by the signal and the idler fields.

In the case of PZT-length tuning, where the cavity-length change for the signal and the idler fields are identical ($\delta l_1 = \delta l_2$), the PZT-length tuning effect on frequency tuning is minimal. Using the same numerical example of $l = 38$ mm and $d = 8$ mm, PZT-length tuning has an estimated coefficient of $\Delta f_d = 2.6$ MHz/nm.

The utility of Eq. (5.6) is not limited to PZT-length tuning, it can also be used to estimate temperature and electro-optic tunings, where δl_1 and δl_2 are functions of temperature and the voltage across the electrodes.

5.2.3 Temperature Tuning

Temperature tuning was used to provide continuous frequency tuning with a tuning range of ~0.5 GHz. By placing the crystal on top of a TE cooler the KTP crystal's temperature could be tuned. The temperature adjustment (ΔT) affected the crystal in two ways: through the refractive index temperature dependence and thermal expansion of the crystal. The differential index change was responsible for the frequency tuning, while the common-mode index change was compensated by the PZT dc bias.

The change in the optical-path length (Δl_n) from the refractive index temperature dependence (Δn) is given by

$$\Delta l_n = d\Delta n \Delta T,$$

and the change in crystal length (Δl_T) from the thermal expansion (α) of the crystal is given by

$$\Delta l_T = n\alpha d\Delta T.$$

Using the α and Δn values[3] listed in Chapter 4, the length changes per degree Kelvin for a 8-mm long crystal are estimated to be:

	refractive index (mm/K)	thermal expansion (mm/K)	total (mm/K)
signal (1)	9.6×10^{-5}	14.0×10^{-5}	2.36×10^{-4}
idler (2)	12.8×10^{-5}	14.6×10^{-5}	2.74×10^{-4}

The corresponding temperature tuning range for a $l = 38$ mm and $d = 8$ mm cavity with matched signal and idler losses is estimated to be $\Delta f_d \approx 220$ MHz/K.

5.2.4 Electro-Optic Tuning

Electro-optic tuning was achieved by applying an electric field (E-field) across the crystal's z axis. The refractive indices for the ordinary (vertical, $n_o(E)$) and the extra-ordinary (horizontal, $n_e(E)$) rays as a function of the externally applied E-field

[3] $\alpha_1 = 10 \times 10^{-6}; \Delta n_1 = 1.2 \times 10^{-5}, \Delta n_2(\Delta n_z) = 1.6 \times 10^{-5}$.

(E) are

$$n_o(E) = \left(\frac{\cos^2\phi}{n_y^2}(1 + n_y^2 r_{13}E) + \frac{\sin^2\phi}{n_x^2}(1 + n_x^2 r_{23}E)\right)^{-\frac{1}{2}},$$

and

$$n_e(E) = n_z(1 + n_z^2 r_{33}E)^{-\frac{1}{2}},$$

where r_{13}, r_{23}, and r_{33} are the electro-optic coefficients.

Using the electro-optic coefficients and refractive indices values[4] listed in Chapter 4, the change in $n_o(E)$ and $n_e(E)(n_z)$ per volt for a 3-mm thick crystal are estimated to be -1.2×10^{-7} and -3.7×10^{-8}, respectively. The E-field tuning coefficient is about 5 MHz/V, following our numerical example.

This fast E-field tuning capability is essential for phase locking the signal and idler beat frequency in our phase noise experiments, without which a free-running beat note would not be stable enough for the measurement.

5.3 Detection System

In our frequency tuning experiment, we tried to characterize the tuning ranges and coefficients of various DRO tuning parameters. The DROs was pumped by the same krypton ion laser system as described in Chapter 3. The pump laser was intensity stabilized to 0.5% rms noise and frequency stabilized to a peak-to-peak jitter of ~50 kHz. The setup of the experiment can be divided into two functional blocks: the intensity-servo loop and the beat frequency diagnostics, as shown in Fig. 5-2.

The beam emerging from the DRO was first collimated and divided into two parts by a beam splitter. About 1/4 of the combined signal and idler power was focussed onto photodetector D1 for intensity stabilization. Detector D1 consisted of a EG&G YAG-100 photodiode and a LM6361 operational amplifier, configured as a transimpedance amplifier with a 1-kΩ feedback. The intensity error signal that was generated by comparing the photodetector D1 output and a stable dc reference voltage was used to stabilize the DRO cavity length and hence the output intensity.

[4] r_{13} = 9.5 pm/V, r_{23} = 15.7 pm/V, r_{33} = 36.3 pm/V; n_x = 1.7381, n_y = 1.7458, n_z = 1.8302.

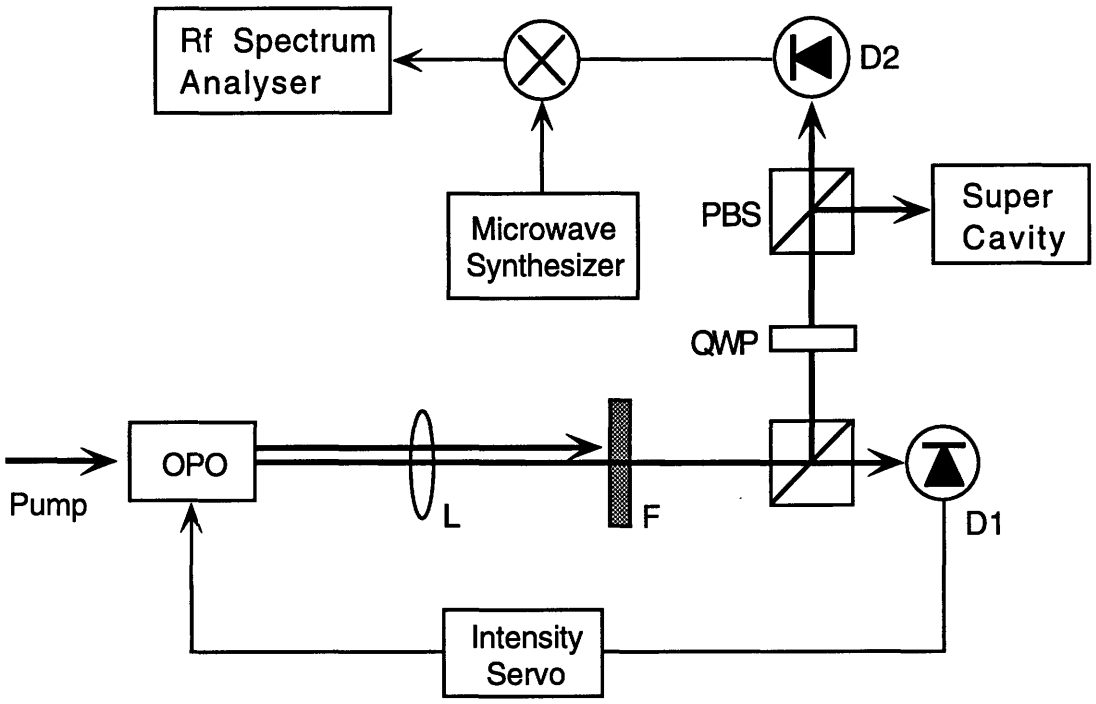

Figure 5-2: Schematic of the experimental setup for signal-idler beat signal detection. (L, focusing lens; F, green block filter; D1, low-speed EG&G photodetector; D2, high-speed BT&D photodetector; QWP, $\lambda/4$ waveplate; PBS, polarizing beam splitter.)

The overall intensity loop unity gain frequency was estimated to be ~3 kHz.

The second part of the output from the beam splitter was focused onto a high-speed BT&D photodiode (D2) with a detection bandwidth of 26 GHz. The two output fields were also monitored on an 8-THz optical spectrum analyzer whose transverse modes spacing was 25 GHz. While being monitored on the optical spectrum analyzer, the output frequencies were tuned to within the high-speed photodiode detection bandwidth for beat frequency measurements.

The signal-idler beat-note signal that was detected by the high-speed photodetector was demodulated with a microwave synthesizer and a mixer to below 2-GHz range. The demodulated signal was then monitored on a wideband rf spectrum analyzer for measuring the change in the difference frequency (Δf_d) when the DRO was tuned.

5.4 Experimental Observations

We investigated three different DRO configurations in our experiments for their tunability and stability. Our first DRO was a 2-element design, the second one was a monolithic design and the third was a 3-element configuration. We first present the experimental observations for the 2-element DRO, followed by the 3-element and finally by the monolithic cavity. All of our DROs have similar coating requirements for their input port and output coupling. The input port was coated for high reflection for the signal and idler fields and for maximum transmission for the pump. The output coupler was coated for maximum reflection for the pump and with less than 1% output coupling for the subharmonic waves. Therefore, the cavities were single ended for the signal and the idler, and it was a double-pass pump configuration that effectively doubled the interaction length.

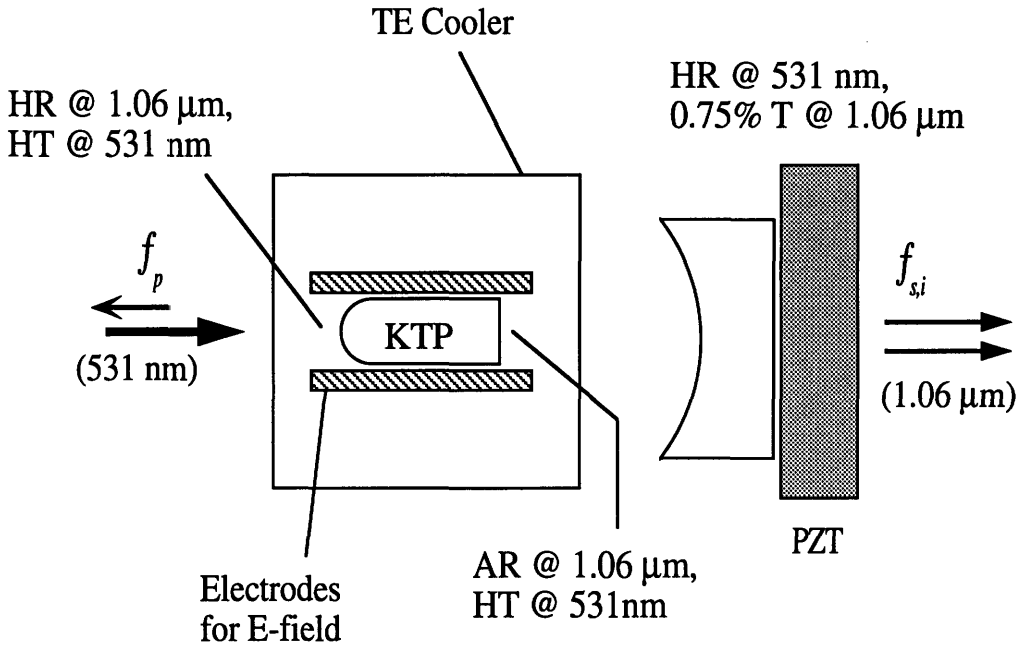

Figure 5-3: Schematic of the 2-element DRO cavity design. The DRO was mounted using a single mirror mount for improved mechanical stability.

5.4.1 2-Element DRO

DRO Cavity Setup

The 2-element DRO [28] consisted of a 25-mm-radius mirror and a 8-mm-long flux-grown KTP crystal (Fig. 5-3). The crystal was cut for 90° noncritical phase matching with the propagation axis set at 25.3° from the x axis toward the y axis in the x-y plane. One end of the crystal was anti-reflection (AR) coated at 1.06 μm with ~15% reflectivity at 531 nm. The other end, which served as the input port, had a 40-mm radius of curvature and a coating of maximum reflection at 1.06 μm and ~80% transmission at 531 nm. The output mirror, coated for maximum reflection at 531 nm and 0.75% transmission at 1.06 μm was located ~21 mm from the flat side of the crystal. The nominal free spectral range of the optical cavity was ~4.3 GHz and the nominal confocal parameter was ~35 mm.

Threshold

The DRO had a minimum threshold of 22 mW for a signal-idler frequency difference of ~800 GHz and a total conversion efficiency of ~30% over a large range of pumping levels of as much as 5 times above threshold. For the phase-locking experiment, as is discussed in Chapter 6, the DRO was operated close to frequency degeneracy with $f_d < 100$ GHz and had a threshold of 40 mW. The 2-element DRO crystal was gray-track damaged during the experiment (Appendix E.2). As a result, its cold-cavity finesse and absorption losses were not measured because the damage would have yielded higher losses than the undamaged crystal.

Angle Tuning

The compact 2-element DRO was mounted in a single mirror mount for improved mechanical stability. The incident angle of the pump beam relative to the crystal was varied to accomplish crystal angle tuning. The output coupler was realigned to maintain cavity resonance. We were able to tune the output frequency separation f_d over a range of 900 GHz near frequency degeneracy at 1.0617 μm. The full angle tuning range for our DRO was expected to be ~1.5 THz, limited only by the 3 mm $\times$ 3 mm cross section of our KTP crystal and its input curvature of 40 mm.

PZT-Length Scan/Tuning

At each pump beam angle setting we scanned the cavity length using the PZT-attached output mirror to excite a set of ~10–20 signal-idler mode pairs (Fig. 5-4). At certain PZT positions the double-resonance condition was satisfied, and IR outputs were observed over a PZT scanning distance of ~ 0.5 nm. Unlike the usual cavity scanning, the resonance peaks occurred at a separation of ~4.7 nm. We used a PZT intensity servo to lock the DRO output power to the side of a resonance mode and thereby obtained stable cw DRO signal and idler outputs. The signal and idler frequencies were monitored with an 8-THz super-cavity optical spectrum analyzer. By adjusting the bias of the PZT driving voltage to access difference mode pairs, we

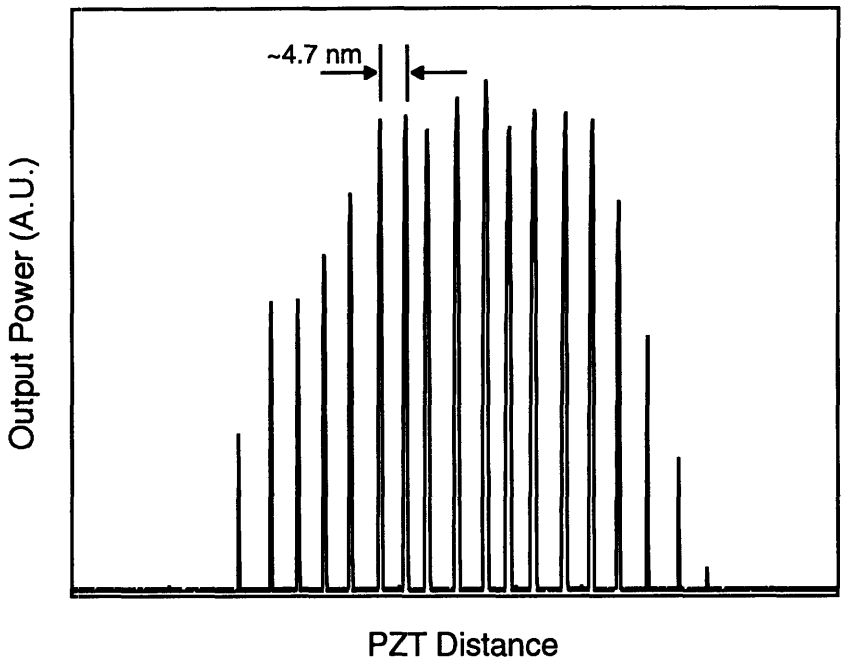

Figure 5-4: PZT cavity-length scanning trace of 2-element DRO output power when pumped at 2.2× threshold. Cavity-length spacing is ~4.7 nm between resonance peaks.

were able to lock to approximately half of the resonance modes. Figure 5-5 shows a typical time trace of the 2-element DRO output intensity under intensity servo-locked conditions. The peak-to-peak output intensity noise was about 16% of the total output power.

As we scanned and locked the DRO to different resonance modes, we observed that the signal frequency of an adjacent mode pair increased by one free spectral range while the idler frequency decreased by one, or vice versa. As shown in Appendix D, this change in frequency was accompanied by an increase or decrease of unity in the signal and idler mode numbers. These changes in the mode numbers and the output frequencies were necessary to compensate for the difference in refractive indices seen by the orthogonally polarized signal and idler waves. Therefore, when the DRO was tuned from one resonance mode to the next with a cavity spacing of ~5 nm, the signal-idler frequency difference f_d changed by, ~8.6 GHz, or twice the nominal FSR.

The set of 10–20 resonance modes in a PZT scan comprised a small number of

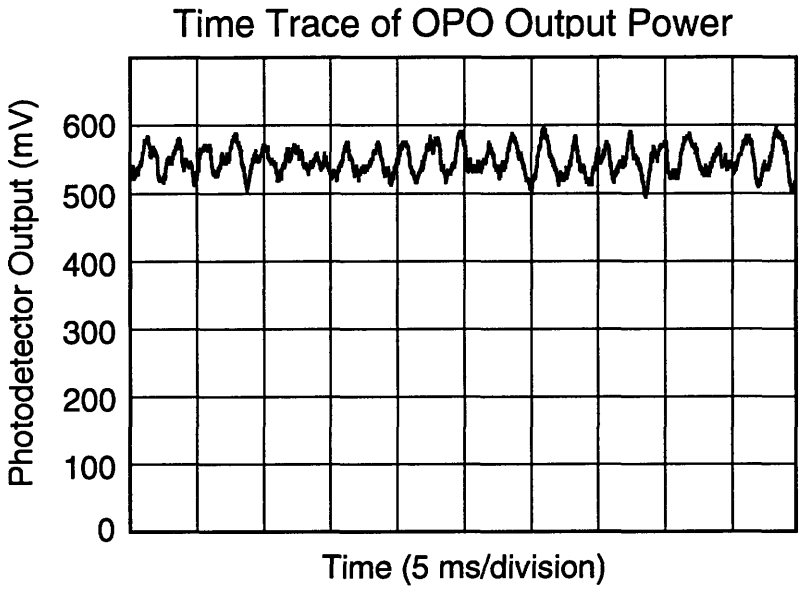

Figure 5-5: Typical time trace of the 2-element DRO output intensity under servo-locked conditions showing major noise contribution at around 400 Hz and a peak-to-peak deviation of ~16% (vertical scale, 100 mV/division; horizontal scale, 5 ms/division).

subsets, each with ~3–10 modes. Within each subset, the above tuning pattern applied. The tuning patterns of the subsets were approximately the same, so that nearly identical signal and idler outputs (with different output powers) could be obtained from more than one subset of modes. However, the number of modes in each subset varied, and there was usually one preferred subset with the largest tuning range, whose truncated versions were associated with the other subsets. Typically the tuning range spanned by the largest subset was ~50–100 GHz, limited by the spectral bandwidth of the KTP crystal and the pumping level. As a result, at each angle setting we were able to obtain systematic tuning over a discrete PZT range, Δf_d ~50–100 GHz.

Using Fig. 5-4 as an example, the first seven leftmost modes formed a subset in which the signal-idler frequency difference f_d of adjacent modes differed by two free spectral ranges. The eighth through the tenth modes formed a second subset. We have observed that as we scanned the cavity the intensities of the modes within

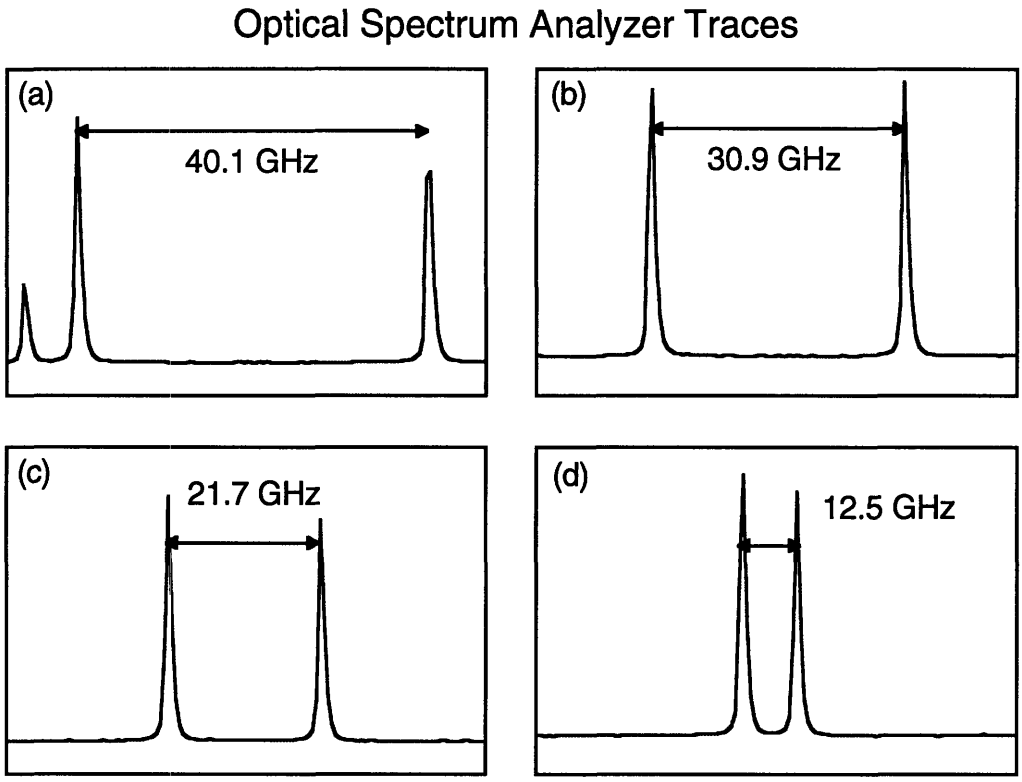

Figure 5-6: Typical optical spectrum analyzer traces of signal and idler outputs as the DRO was scanned and locked to adjacent resonance modes of a mode subset. The free spectral range for this series was ~4.6 GHz.

a subset would increase (or decrease) monotonically, as in the first subset of seven modes in Fig. 5-4. The break in this monotonic increase in intensity usually signified a new subset of modes. Figure 5-6 shows a series of four typical optical spectrum analyzer traces of the signal and the idler frequency outputs of the intensity-locked DRO. In this series the signal-idler frequency spacing decreased by ~9.2 GHz, or approximately twice the nominal free spectral range, as the DRO cavity was scanned and locked to four adjacent resonance modes of a mode subset.

Temperature Tuning

With angle tuning and PZT scanning, together with our intensity servo, we were able to operate the cw DRO stably with discrete but systematic frequency tuning over ~ 1 THz. Continuous tuning was obtained by varying the temperature of the

crystal with a Peltier thermoelectric (TE) cooler. The servo-locked DRO could be temperature tuned over a range Δf_d ~0.5 GHz, and we measured a temperature tuning coefficient of $\Delta f_d(T)$ ~300 MHz/K. A larger tuning range could be obtained by unlocking the intensity servo first, changing the temperature, and then relocking the intensity servo. A possible explanation for the limited 0.5-GHz temperature tuning range was that the intensity servo ran out of dynamic range while compensating for the common-mode cavity length changed. In general the thermal response was slow and accurate frequency control could be obtained only when the signal-idler beat was monitored with a high-speed detection system.

E-Field Tuning

Continuous frequency tuning was also achieved by applying an electric field across the crystal's z axis. The crystal's surfaces perpendicular to the z axis were coated with a conductive silver paste to which electrodes were attached. We obtained fast narrow-band E-field tuning capability with a tuning coefficient of $\Delta f_d(E) \sim 0.15$ MHz/V.

The E-field tuning range Δf_d was ~40 MHz, limited by the possibility of gray-track damage. The E-field tuning capability was essential for phase locking the signal-idler beat frequency and for precision tuning. We note that, using published results of KTP's electro-optic coefficients, that the effective E-field tuning coefficient $\Delta f_d(E)$ should be ~0.8–0.9 MHz/V. The discrepancy between measured and expected values was probably due to the high ion conductivity of the flux growth crystal. High mobility of the ions, caused by its high conductivity, provided a partial shield to the applied electric field, thus effectively reducing its field strengths in the crystal. The tuning ranges and coefficients of the four tuning elements are summarized in Table 5.1.

Pump Resonance Side Effect

Due to the imperfect coating of our DRO input coupler, the pump field was weakly resonated and the OPO was quasi-triply resonant. The cluster modes occurred at and around the pump resonance position, as the internal pump intensity was enhanced

Parameter	Mode	Range	Coefficients
Angle	Discrete	$\sim$ 1.5 THz	-
PZT	Discrete	$\sim$ 100 GHz	-
Temperature	Continuous	$\sim$ 0.5 GHz	$\sim$ 300 MHz/K
E-field	Continuous	$\sim$ 40 MHz	$\sim$ 0.15 MHz/V

Table 5.1: Tuning ranges and coefficients of signal-idler difference frequency f_d of 2-element flux-grown KTP DRO

by the resonance. The cavity-length spacing between two sets of cluster modes was 265 nm, or half the pump field wavelength. Figure 5-7 shows the two different sets of cluster modes in one PZT-length scan. The two sets of modes observed were different, as predicted by Debuisschert *et al.* [11]. The output frequencies of the two sets were offset by one free spectral range of the cavity, ~4.6 GHz. Using Figure 5-7 as an example, the smallest frequency difference f_d for the first set of cluster modes was $<$ 500 MHz and the adjacent mode's f_d was two free spectral range apart (Fig. 5-7d and e). For the second set of cluster modes, the smallest f_d was one free spectral range. In Figure 5-7b and c, the signal and the idler frequencies switched their positions in the optical spectrum analyzer outputs, as they were tuned past the frequency degenerate point.

5.5 3-Element DRO

DRO Cavity Setup

The 3-element DRO cavity was composed of two mirrors and a 3 mm $\times$ 3 mm $\times$ 8 mm hydrothermally grown KTP crystal (Fig. 5-8). The two mirrors were rigidly fixed to their respective attachment plates, which were then bolted to the sides of an aluminum spacer block. To compensate for the lack of mirror adjustments, the crystal, electrodes and TE cooler assembly were mounted on a modified mirror mount with a built-in rotation stage. The modified mirror mount was in turn attached to the spacer block from underneath, without touching other supporting structures. This

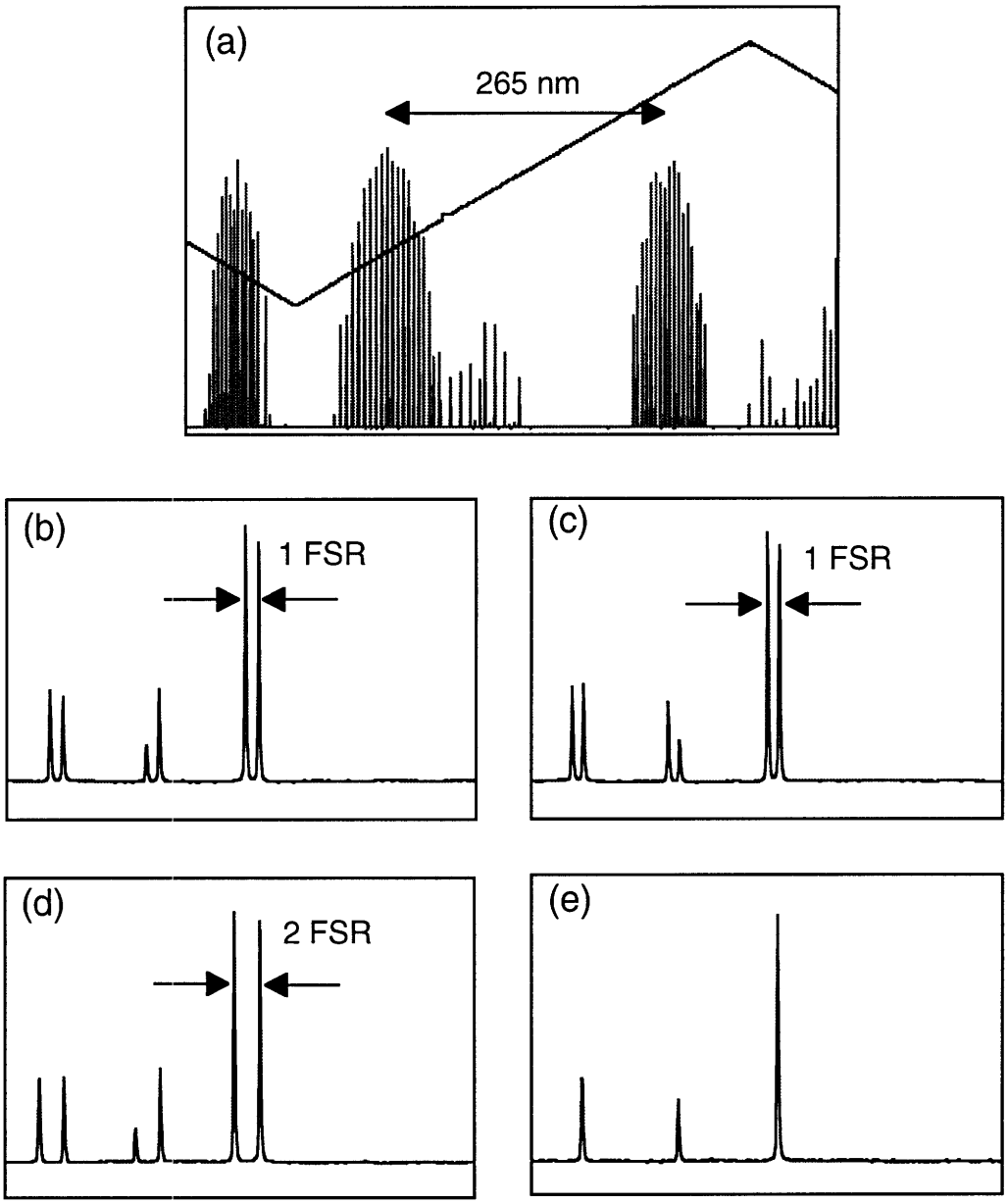

Figure 5-7: (a) PZT scan showing two different sets of cluster modes. The cavity spacing between the centers of the sets was 265 nm. (b) & (c): Optical spectrum analyzer traces of two adjacent modes from the same set of cluster modes in (a). The signal-idler frequency difference was one free spectral range in both traces. (d) & (e): Optical spectrum analyzer traces of two adjacent modes from the second set of cluster modes in (a). (d): Signal-idler frequency was two free spectral ranges apart. (e): Signal-idler frequency difference was within resolution bandwidth of the spectrum analyzer, and appears as one single peak. The smaller peaks in (b)–(e) were non-TEM_{00} transverse modes of the optical spectrum analyzer.

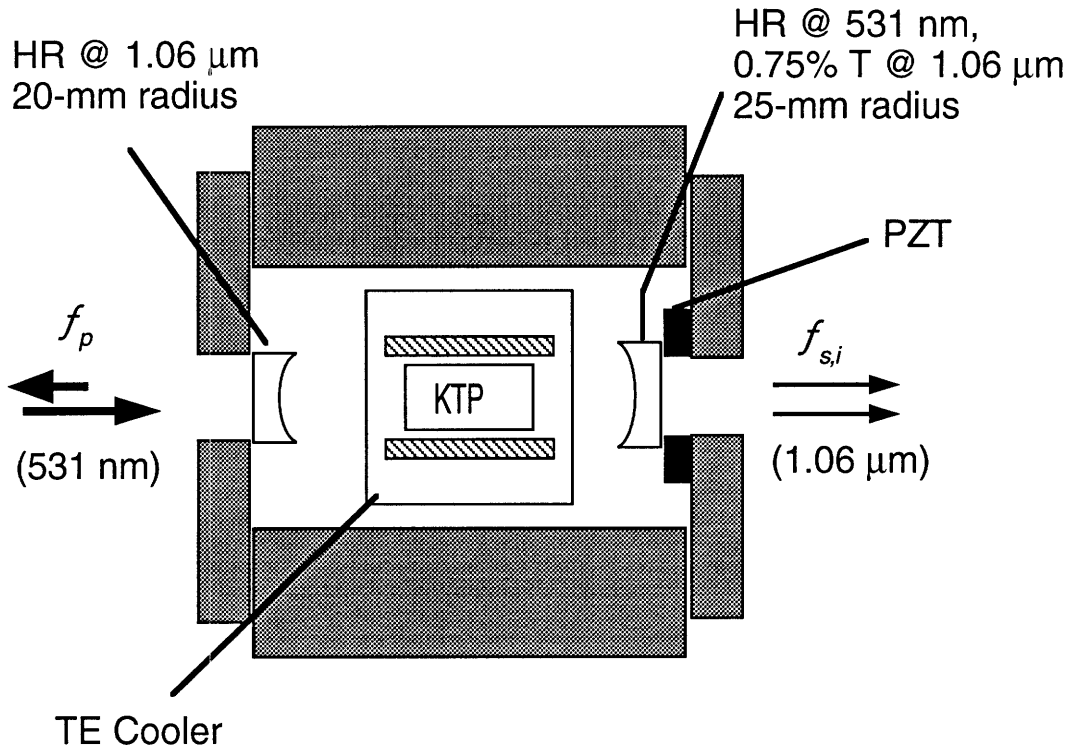

Figure 5-8: Schematic of the 3-element DRO cavity design. The mirrors were rigidly fixed to an aluminum spacer block, and the crystal was attached to a rotation stage and a mirror mount for angle tuning.

design provided excellent isolation of vibration and at the same time permitted full adjustment of the crystal's orientation for angle tuning.

The crystal was polished flat and antireflection coated on both sides. The input mirror had a 20-mm radius of curvature and was coated for maximum reflection at 1.06 μm with a measured reflectivity of $\sim$10% at 531 nm. The 25-mm-radius 0.75% output coupler was bonded to a PZT stack for cavity scanning. The physical separation between the two mirrors was $\sim$38.7 mm giving a nominal free spectral range of 3.4 GHz. Like the 2-element DRO, this 3-element DRO cavity also used a double-pass pump configuration.

Angle Tuning

For coarse alignment, the attachment plates could be moved by ± 2 mm in the plane perpendicular to the propagation axis. Final cavity alignment was achieved by adjusting the pump beam angle relative to the cavity and by adjusting the crystal orientation inside the cavity. We have tuned the KTP crystal over a range of $\Delta f_d \sim \pm 1.5$ THz, with an expected range of more than 6 THz.

Temperature and E-Field Tuning

The PZT scanning and temperature tuning characteristics were similar to those of the 2-element DRO, except that the temperature tuning coefficient was smaller, as expected from a larger mirror separation than the 2-element cavity. We have measured slightly different values for the temperature tuning coefficient at two different f_d's in separate experiments (Table 5.2). The difference was possibly due to insufficient thermal contact between the crystal and the TE cooler.

For E-field tuning, the crystal's z faces were gold plated for better electrical contact. In an early experiment, we have measured an E-field tuning coefficient of 0.85 MHz/V. But at a later date, the same crystal yielded a smaller E-field tuning coefficient of 0.52 MHz/V indicating possible photorefractive or gray-track damages. In order to avoid further gray-track damage, the applied voltage range was reduced while an adequate beat-frequency tuning range was retained. The tuning ranges and coefficients of the 3-element DRO are summarized in Table 5.2.[5]

Cavity Losses and Threshold

From cold-cavity finesse measurements, we estimated the round-trip losses at 1.06 μm at two different phase-matching angles, around frequency degeneracy and around minimum threshold. Table 5.3 summaries the measured finesses and losses for the ordinary ray (vertical) and the extra-ordinary ray (horizontal). The difference in the round-trip losses could be caused by a number of factors, such as different crystal

[5]See Chapter 6 for the detection scheme of the 665 GHz beat-note signal.

Parameter	Mode	Range	Coefficients
Angle	Discrete	$\sim$ 6 THz	-
PZT	Discrete	$\sim$ 100 GHz	-
Temperature	Continuous	$\sim$ 0.5 GHz	$\sim$ 210 MHz/K (f_d = 230 MHz) $\sim$ 188 MHz/K (f_d = 665 GHz)
E-field	Continuous	$\sim$ 40 MHz	$\sim$ 0.85 MHz/V (on 9/11/92; at f_d $\sim$20 GHz) $\sim$ 0.52 MHz/V (on 11/22/94; at f_d $\sim$230 MHz)

Table 5.2: Tuning ranges and coefficients of signal-idler difference frequency f_d of 3-element hydrothermally grown KTP DRO. Note the different f_d's for the two temperature coefficients. The OPO was operated near frequency degeneracy when the two E-field coefficients were measured.

	Ordinary ray (Total loss[%]/Finesse)	Extra-ordinary ray (Total loss[%]/Finesse)
Empty cavity	0.82 / 765	0.82 / 765
Minimum threshold	1.12 / 557	1.35 / 463
Near degeneracy	1.61 / 387	2.42/ 256

Table 5.3: Summary of 3-element DRO measured total losses and finesse for two phase-matching angles: minimum threshold and near degeneracy.

absorption coefficients for the two polarizations and different reflection coefficients for the antireflection coating on the biaxial crystal. As shown in Table 5.3, the losses increased when tuned to the frequency degenerate point, as reflection losses increased at the crystal's surfaces. The minimum threshold at f_d $\sim$1.5 THz was $\sim$40 mW. Near frequency degeneracy, $f_d \leq$ 100 GHz, the threshold was $\sim$90 mW. Figure 5-9 shows a plot of the 3-element DRO's conversion efficiency as a function of pump power.

Stability

We observed that the mechanical stability of this 3-element DRO approached that of a monolithic cavity. Stable cw outputs were obtained for several minutes under free running conditions, with $\sim$16% peak-to-peak intensity noise (Fig. 5-10). This intensity

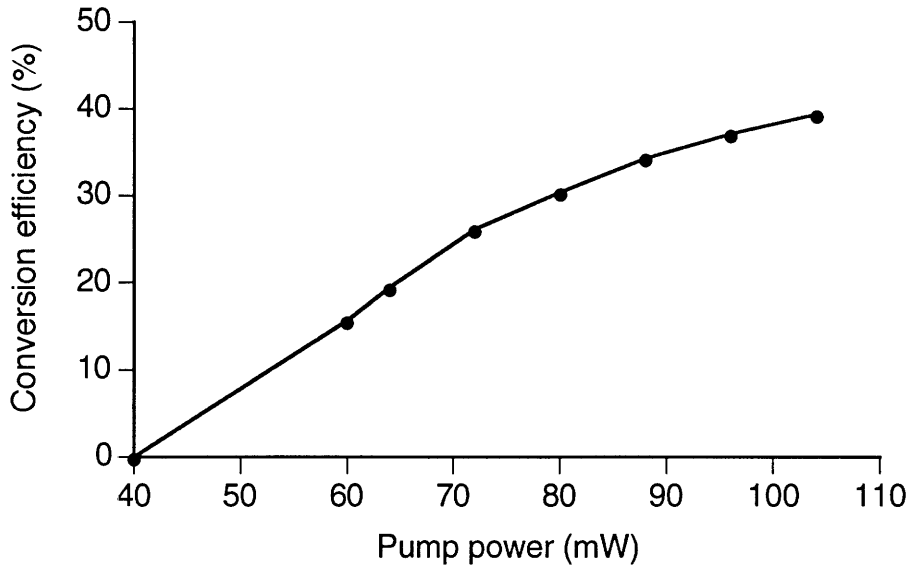

Figure 5-9: Plot of 3-element DRO's conversion efficiency. DRO threshold was 40 mW. Conversion efficiency was ~39% when pumping ~ 2.6× threshold.

noise was caused by residual frequency jitter of the pump laser and absorption-induced thermal fluctuation. With an intensity servo loop, the output residual intensity noise was stabilized to ~ 0.6% rms (Fig. 5-11). Under servo-locked conditions stable outputs without any mode hopping could be maintained for longer than 1 hour, limited only by accidental perturbations such as gas filling of the pump laser.

Because of its superior construction, the 3-element DRO was mechanically more stable than the 2-element DRO. As a result, it was easier to acquire an intensity lock for the 3-element DRO and the lock was less susceptible to environmental perturbation than the 2-element DRO. The beat frequency jitter of the 3-element DRO (±200 kHz) was also less than that of the 2-element DRO (±1.5 MHz).

5.6 Monolithic DRO

DRO Cavity Setup

The monolithic DRO was of a linear-cavity design with both ends polished to a radius of curvature of 10 mm (Fig. 4-1a). The input port was high reflection coated for 1.06

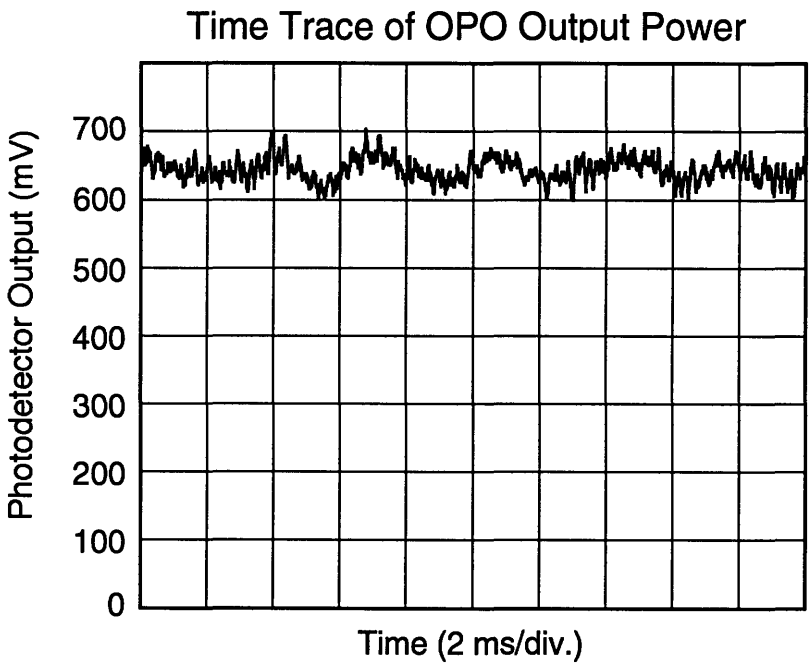

Figure 5-10: Typical time trace of 3-element DRO output intensity under free-running conditions. The 3-element DRO was highly stable with peak-to-peak intensity noise of ~16%. The residual intensity noise was at around 400 Hz.

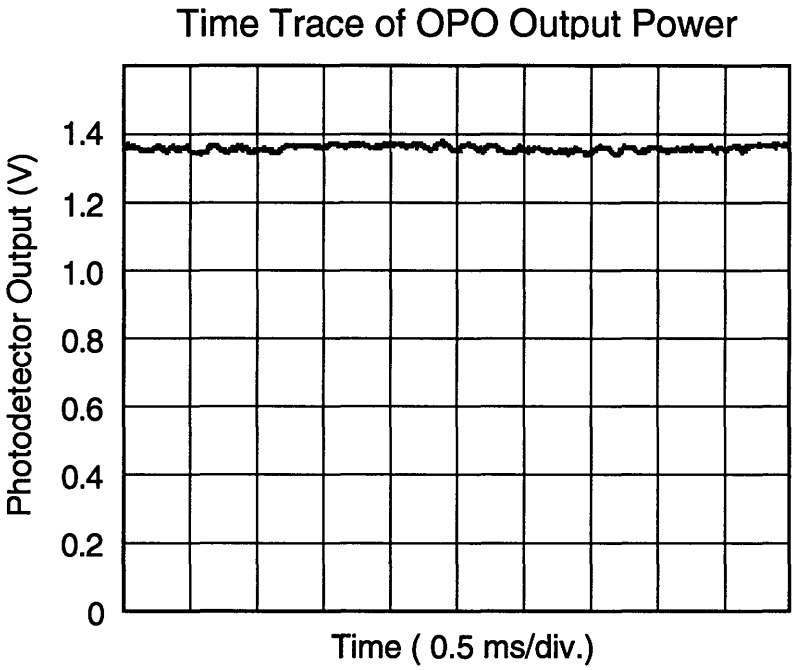

Figure 5-11: Time trace of 3-element DRO output intensity under servo-locked conditions. The residual intensity noise is only 0.6% rms.

μm and maximum transmission coated for 531 nm. The output end was maximum reflection coated for 531 nm with 0.5% output coupling for the signal and idler fields. As in the 2-element and 3-element DRO, the monolithic DRO was double-pass pump configured.

There were only two tuning elements available to our monolithic DRO. They were the slow temperature tuning, controlled by a TE cooler, and the fast electro-optic tuning. However, the electro-optic tuning was not implemented in our experiment. By virtue of the linear-cavity design, angle tuning was not available because there was only one propagation path that could support oscillation. If the pump beam incident angle were changed, the propagation path would deviate from the optimum path and the DRO would cease to operate.

Threshold

From cold cavity measurements, the total losses at 1.06 μm were measured to be $\sim$ 1.2% and $\sim$ 1.4% for the vertical and horizontal polarizations, respectively. The minimum threshold was $\sim$15 mW and the DRO was typically pumped at 35 mW. The monolithic DRO output intensity was very stable, with a minimum output intensity fluctuation of $\sim$10% peak-to-peak under free-running conditions.

Bistable Behavior

Because of the small confocal parameter ($b \approx 10$ mm), there was severe localized IR absorption. We observed thermally induced instability and bistability [31] in the monolithic DRO. Figure 5-12 shows a time trace of the monolithic DRO output intensity showing the bistable behavior. The output frequencies were monitored on an 8-THz optical spectrum analyzer at the same time when Fig. 5-12 was taken. The optical spectrum analyzer shows that the DRO was oscillating between two different signal-idler mode pairs and the signal (idler) frequencies of the two different mode pairs were 2–3 GHz apart. The oscillation period was 0.05 ms and the onset of bistability was not predictable.

Additional studies could not be performed because the crystal's coatings were damaged and the DRO stopped working. The performance of our first generation monolithic DRO design was not optimized.

5.7 Summary

In this chapter, we have discussed the experimental observations of our various DRO configurations. We have shown that type-II phase-matched KTP DRO operating near frequency degeneracy could be stabilized and tuned systematically. With our 3-element DRO, we have demonstrated that the stability and tunability requirements can be satisfied simultaneously in a DRO cavity design. With the four different tuning elements, our 2-element and 3-element DROs signal-idler difference frequencies were tuned discretely over a range of $\sim$1–3 THz and continuously over a $\sim$0.5-GHz range.

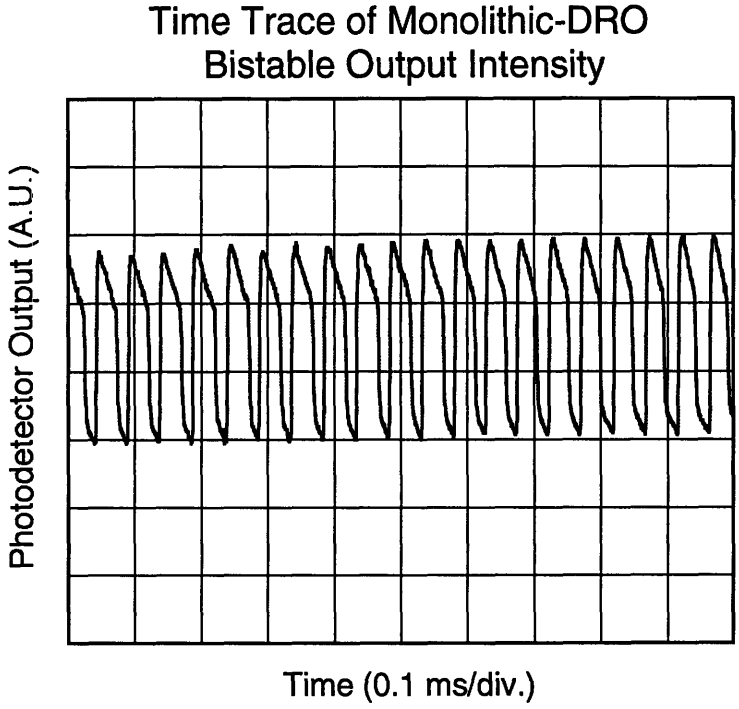

Figure 5-12: Time trace of monolithic-DRO unstable output power showing the bistable behavior. The DRO outputs oscillated between two different signal-idler mode pairs. The oscillation period was ~0.05 ms and the frequency difference between the mode pairs was 2–3 GHz. (Threshold, 19 mW; pump power, 35 mW.)

With the ability to frequency tune and operate stably near frequency degeneracy, we proceeded to stabilize the beat-note frequency as the final requirement in our quantum phase noise experiment. Our phase-locking experiment which used the electro-optic effect to frequency stabilize the signal and idler beat-note is discussed in the next chapter.

Chapter 6

Phase-Locked DRO Frequency Division

6.1 Introduction

In this chapter, we discuss our DRO frequency stabilization experiment with the use of a phase-locked loop (PLL). The beat-note signal of the DRO outputs was detected with a high-speed photodiode and was phase locked to a microwave synthesizer using the electro-optic effect of the KTP crystal. We were able to determine the beat-note linewidth at the mHz level when the beat frequency itself was in the 10's of GHz range. However, our detection bandwidth was limited by the bandwidth of the high-speed photodiode. To extend the detection bandwidth up to a few THz, a wide-band optical frequency comb generator (OFCG) was added to extend the bandwidth beyond the photodiode bandwidth [5].

In the following sections, we discuss in more details the PLL design considerations, the experimental setup, and results. Details of the OFCG experiment is discussed in Section 6.6.

6.2 Optical Frequency Division

Traditionally, it is very difficult to determine precisely the output frequencies of the DRO, even if the input pump frequency is exactly known. But in applications of optical frequency metrology and high-resolution spectroscopy, the DRO output frequency must be precisely tunable. In the case of near-degeneracy operation, Wong has suggested that by measuring the beat frequency between the signal and idler outputs, the output frequencies can be precisely determined [41]. This is known as optical parametric division.

The basic concept of optical parametric division is as follows (Fig. 6-1): since the pump (f_p), the signal (f_1), and the idler frequencies (f_2) must satisfy the energy conservation relation,

$$f_p = f_1 + f_2,$$

a measurement of the output frequency difference,

$$f_d = f_1 - f_2,$$

would determine precisely the signal and the idler output frequencies [41]

$$f_{1,2} = \frac{1}{2}(f_p \pm f_d).$$

The precision of $f_{1,2}$ depends on a precise measurement of f_d, assuming that f_p is known. If the DRO is operated near frequency degeneracy such that f_d is in the microwave range, then f_d can be measured on a rf spectrum analyzer and can even be stabilized to a microwave reference.

6.3 PLL Design Considerations

A phase-locked loop (PLL) consists of three basic components: a phase detector, a low-pass filter, and a voltage controlled oscillator (VCO). The phase detector, digital or analog, generates an output voltage that is proportional to the phase difference of

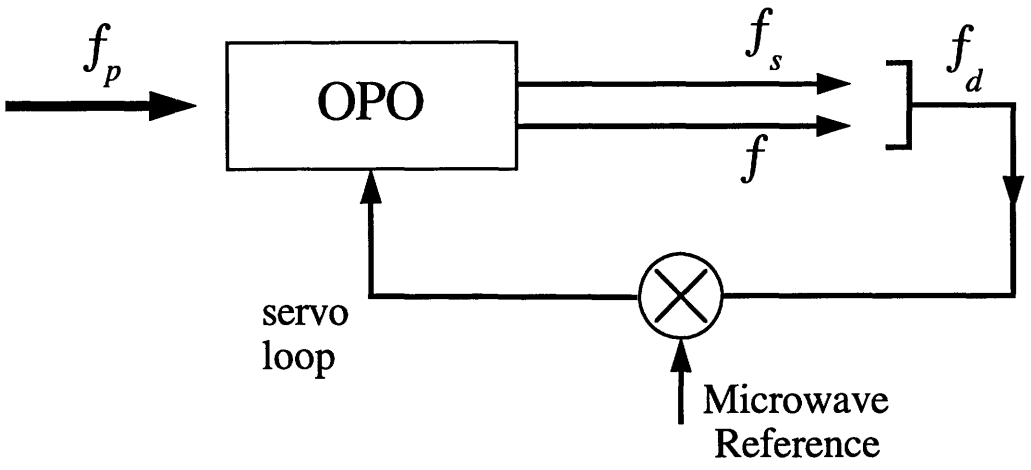

Figure 6-1: Conceptual diagram of signal-idler beat-note measurement and feedback stabilization.

the two inputs. For the phase detector, its two inputs are the DRO beat-note signal and the microwave reference which is to be utilized for stabilizing the DRO output beat frequency. The VCO is the DRO, with its output frequencies controlled by the electro-optic effect of the KTP crystal. The low-pass filter is the most critical part of the PLL, because it determines the overall loop characteristics and response.

In general, the filter is configured as a proportional gain stage plus an integrator (Fig. 6-4). The filter has two time constants τ_1, τ_2 associated with its bandwidth with

$$\tau_1 = R_1 C, \quad \text{and} \quad \tau_2 = R_2 C,$$

where R and C are the resistance and capacitance values used in the filter. The values of R_1, R_2 and C determine the overall loop behavior of the PLL and must be chosen carefully for the desired loop characteristics. There are two considerations [1, 17] for the loop performance; first, the rate of beat-note frequency shift under free-running conditions, and secondly, the transient response of the loop.

The averaged rate of beat-note frequency shift ($\Delta\dot{\omega}$) can be estimated using

$$\Delta\dot{\omega} = 2\pi(2f_j)\nu,$$

where f_j is the peak-to-peak deviation (in units of Hz) of the beat-note frequency jitter, and ν is the frequency (in units of Hz) at which the jitter is occurring. For example, if the beat-note frequency is jittering (ν) at a rate of 400 Hz with a peak-to-peak deviation (f_j) of 3 MHz, then the averaged rate of beat-note frequency shift ($\Delta\dot{\omega}$) is 1.5×10^{10} rad/s^2. The natural frequency squared (ω_n^2) of the PLL should be larger than $\Delta\dot{\omega}$ so that the loop is fast enough to track the beat-note jittering. In other words, with ω_n being related to the overall-loop gain, a large loop gain is required to track a fast moving signal. On the other hand, the overall gain of the loop should not be too high, otherwise loop stability might become an issue, as with any feedback system.

The transient response is governed by the damping factor ξ of the PLL. As suggested by Best [1], under most applications $\xi = 0.702$ is a suitable choice.

In addition to $\Delta\dot{\omega}$ and ξ we also need to know the overall-loop gain K before we can calculate the time constants ($\tau_{1,2}$) for the loop. The overall-loop gain K is defined by

$$K = K_\phi K_{vco} K_A,$$

where K_ϕ is the gain constant of the phase detector, K_{vco} is the E-field tuning coefficient of the DRO, and K_A is any amplifier voltage gain that is inserted into the loop. The values of $R_{1,2}$ and C, and hence τ_1, τ_2 (Fig. 6-4) are then calculated using

$$\tau_1 = R_1 C = \frac{K}{\omega_n^2},$$

and

$$\frac{R_2}{R_1} = \frac{2\xi\omega_n}{K}.$$

The unity gain frequency, ω_0, of the PLL can be obtained by solving

$$1 = \frac{K(1 + i\omega_0\tau_2)}{\omega_0^2\tau_1}.$$

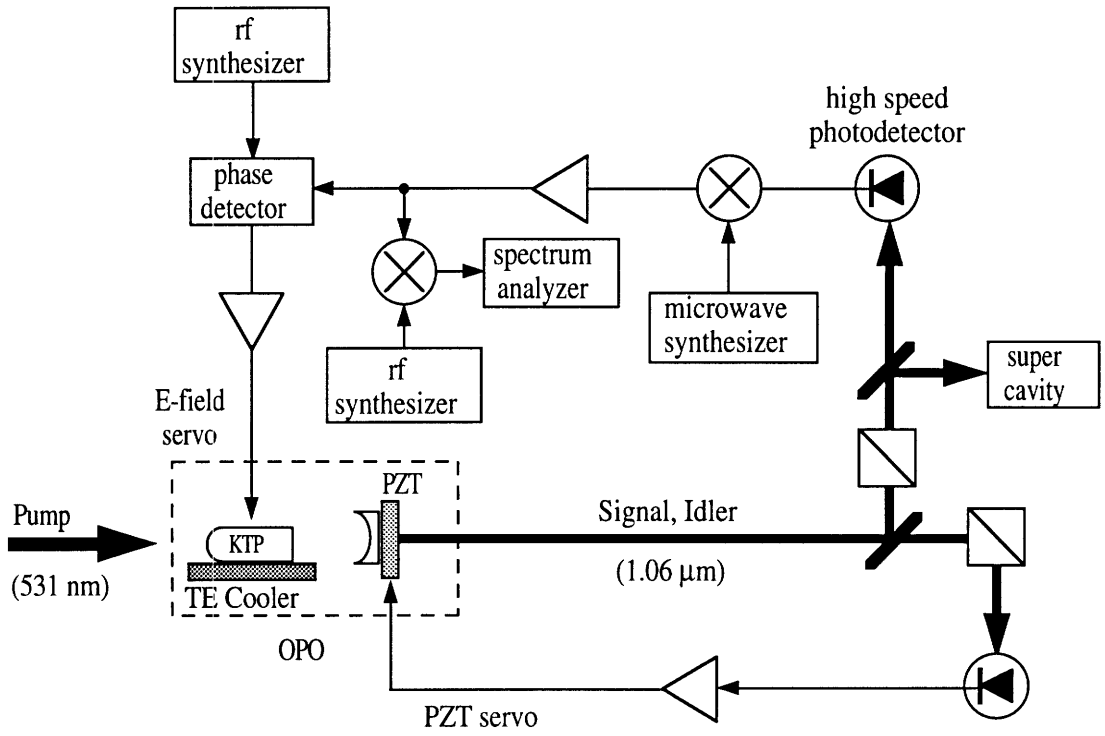

Figure 6-2: Experimental setup for phase locking the signal-idler beat frequency of the DRO's to a microwave synthesizer, shown with the PZT intensity servo and E-field phase-locked loop.

6.4 Experimental Setup

The setup of the phase-locking experiment can be divided into two functional blocks: a high-speed frequency diagnostic system and the phase-locking servo. Figure 6-2 shows a schematic of the experimental setup with the DRO intensity servo, the frequency diagnostic system, and the phase-locking servo.

6.4.1 High-Speed Frequency Diagnostic System

The high-speed frequency diagnostic system allowed us to measure the beat signal with high precision. The high-speed beat note detection electronics consisted of a InGaAs/InP photodiode, microwave synthesizers, mixers and a rf spectrum analyzer. The detection bandwidth was limited by the high-speed photodiode (BT&D PDC 4304-30), which had a 3-dB bandwidth of 25 GHz and a responsivity of 0.75 A/W.

The OPO was first tuned to near frequency degeneracy such that the signal-idler frequency difference was within the detection bandwidth. The orthogonally polarized outputs were projected onto a common polarization axis by a polarizing beam splitter and focused onto the high-speed photodiode. Typically, the optical power was attenuated to yield a dc photocurrent of $\sim$ 300 μA. The ac signal from the photodiode was separated by a bias tee and demodulated in a microwave double balanced mixer whose local oscillator was derived from a HP microwave synthesizer (model 8679G). The mixer output at $\sim$ 40 MHz was further amplified with a low noise, 500-MHz bandwidth, 40-dB gain amplifier (Trontek). Half of the amplified signal was input into a phase detector for phase locking the beat frequency at 40 MHz, and the second half was measured with a wideband rf (1.8 GHz) spectrum analyzer (Tektronix 496P) for beat frequency measurement.

For higher precision, the amplified signal was further demodulated using a second rf synthesizer (HP 3325A) to a range of less than 1 MHz for higher-resolution analysis. All the synthesizers were phase-locked to each other to eliminate relative drifts among them. Under phase-locked conditions, the beat frequency was measured down to kHz range, limited by the resolution of the synthesizers, and the beat-note linewidth was measured down to mHz level, limited by the resolution of the spectrum analyzer. The accuracy of the measurement was ultimately limited by the accuracy of the synthesizer chain.

6.4.2 Phase-Locked Loop

Our implementation of the PLL consisted of a band-pass filter, a digital phase detector, and an active low-pass filter, as sketched in Fig. 6-3. The down-converted beat note at $\sim$40 MHz was filtered with a band-pass filter (BPF) of 40-MHz center frequency and 3-MHz bandwidth. The band-pass filtered beat note was then input to a digital phase detector whose output error signal was used to phase lock the DRO's beat note.

We improved the signal-to-noise ratio and narrowed the linewidth of our 3-element DRO's beat note with the insertion of the BPF before the phase detector. The BPF

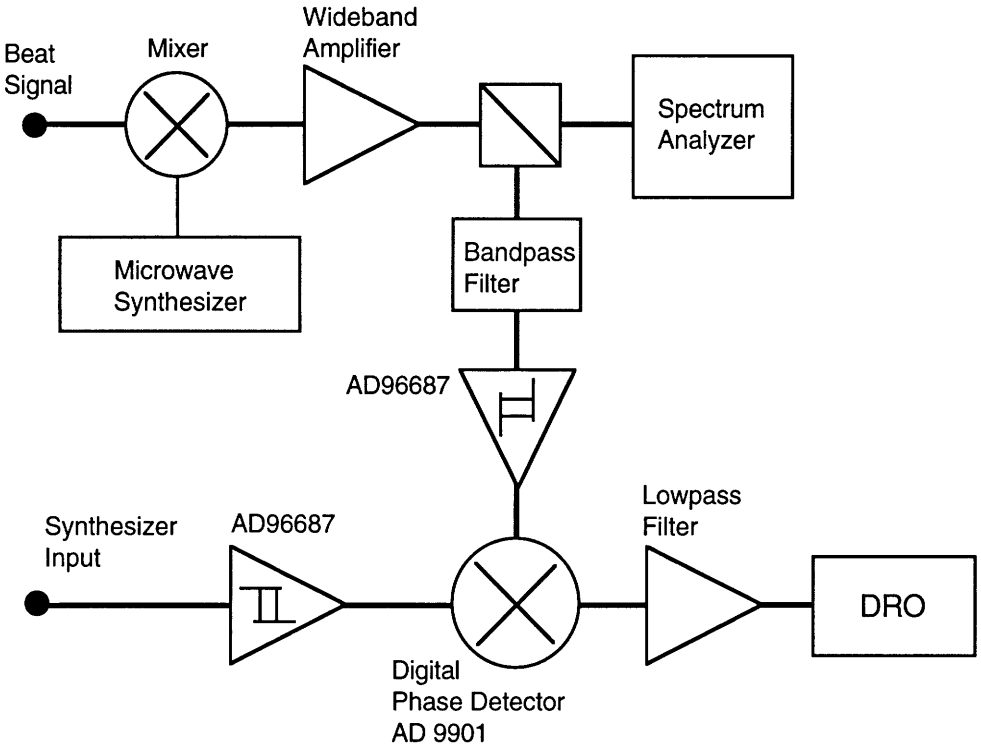

Figure 6-3: Schematic of phase detector circuit.

worked by cutting down the noise interference from other frequencies so that the phase detector only saw the desired 40-MHz signal. The disadvantage, however, was that it limited the capture range of the PLL to the bandwidth of the BPF.

The band-pass filtered beat note and the synthesizer reference were input into two separate high-speed comparators (Analog Device 96687) to convert the analog signals into emitter collector logic (ECL) digital waveforms. The phase difference between the two ECL waveforms was compared with a digital phase detector chip (Analog Device 9901), which has a gain constant of $K_\phi = 0.285\text{V/rad}$. The output from the AD 9901 was also in ECL digital format whose duty cycle was proportional to the phase difference. Since an ECL waveform was not centered around zero volt, a summing amplifier was required to bias the phase detector output to be symmetric around zero volt.

An active filter composed of an operational amplifier then filtered out any high frequency components in the phase detector output (Fig. 6-4). The filtered output was the phase error signal which was fed to the crystal E-field tuning electrodes for phase locking the DRO.

In the 2-element DRO a high voltage amplifier with ten times gain ($K_A = 10$) was needed to amplify the phase error signal and to increase the dynamic range of the PLL. But no amplifier was required ($K_A = 1$) for the 3-element DRO because of a higher E-field tuning coefficient for the hydrothermally grown KTP crystal (as compared with a smaller coefficient for the flux grown KTP used in the 2-element DRO (Tables 5.1 and 5.2)).

6.5 Experimental Results

We have phase locked both the 2- and 3-element DRO's to an external microwave synthesizer to obtain very narrow beat-note linewidth. The 2-element DRO was not studied as extensively as the 3-element DRO because it was accidentally damaged during the experiment.

Without any phase locking, the beat note had a jitter of $\sim \pm 250$ kHz in the 3-

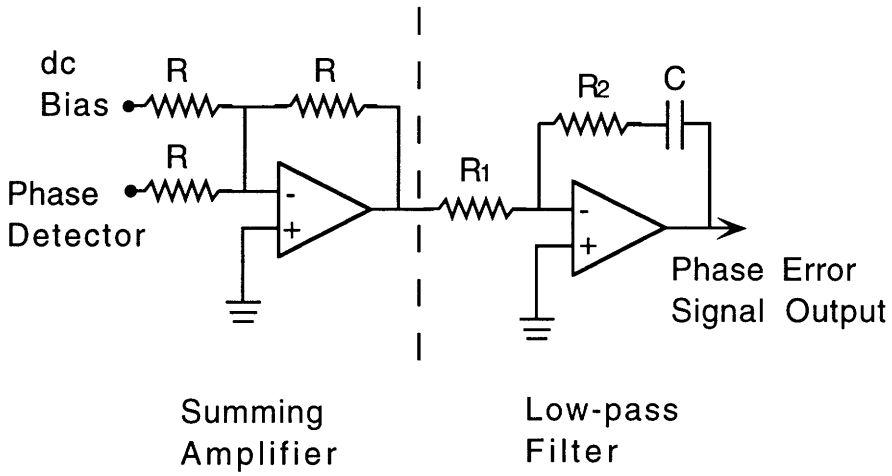

Figure 6-4: Schematic diagram of summing amplifier and active low-pass filter.

element DRO and a jitter of $\sim$ 3 MHz in the 2-element DRO. The 3-element DRO had a smaller frequency jitter because of its superior design and mechanical construction in which no spring-loaded mirror mounts were used. The amount of jittering was also affected by residual laser frequency jitter, mechanical vibration of the DRO, residual DRO intensity noise, and jitter in the pump laser beam pointing direction. In general, the smaller the residual noises were in the system, the smaller the beat-note jittering was. Furthermore, we believe that output frequency instability was also caused by the crystal's thermal cycling as it absorbed circulating IR power.

We should point out that under phase-locked conditions when the signal-idler beat note was stabilized, the signal and the idler frequencies themselves were not stable. The signal and the idler frequencies jitters followed that of the pump laser frequency jitter.

6.5.1 2-Element DRO

Our 2-element DRO was to our knowledge the first externally phase-locked DRO[1]. The experimental conditions were described in previous sections, except that the band-pass filter (BPF) was not in place and the signal-idler beat note was demodulated to 50 MHz instead of 40 MHz.

We phase locked the 2-element DRO at a beat frequency of ~9.4 GHz, as reported in Ref. [28]. The phase-locked 50-MHz beat note was measured with a Tektronix 496P rf spectrum analyzer to have a 3-dB linewidth (FWHM) of ~33 Hz, as shown in Fig. 6-5. The resolution bandwidth of the spectrum analyzer was 30 Hz, suggesting that beat-note linewidth was substantially less than 30 Hz. Without the phase locking servo the beat frequency had a 3–5 MHz jitter. The unity-gain frequency of the PLL was estimated to be 45 kHz.

Power Spectral Density

When a signal is tightly phase locked to its reference, it is more appropriate to quantify the locking with its power spectral density instead of its linewidth. The power spectral density of the phase noise is given by

$$S_\phi(\omega) = \frac{P_s(\omega_0 + \omega)}{P_c(\omega_0)B},$$

where P_c is the carrier power at frequency ω_0, P_s is the noise sideband power at a frequency ω from the carrier ω_0, and B is the bandwidth of the measurement system.

In Figure 6-5 the phase noise level at 200–400 Hz from the carrier is approximately -42 dBc, which yields a power spectral density of ~2.1 mrad/$\sqrt{\text{Hz}}$.

6.5.2 3-Element DRO

The 3-element DRO was phase locked at a beat frequency of 12.3 GHz and demodulated to 40 MHz for the phase-locking electronics. We improved the signal-to-noise

[1]Self-phase locking in a type-I monolithic DRO at frequency degeneracy was reported by Nabors *et al.* at Stanford University in 1990 [33].

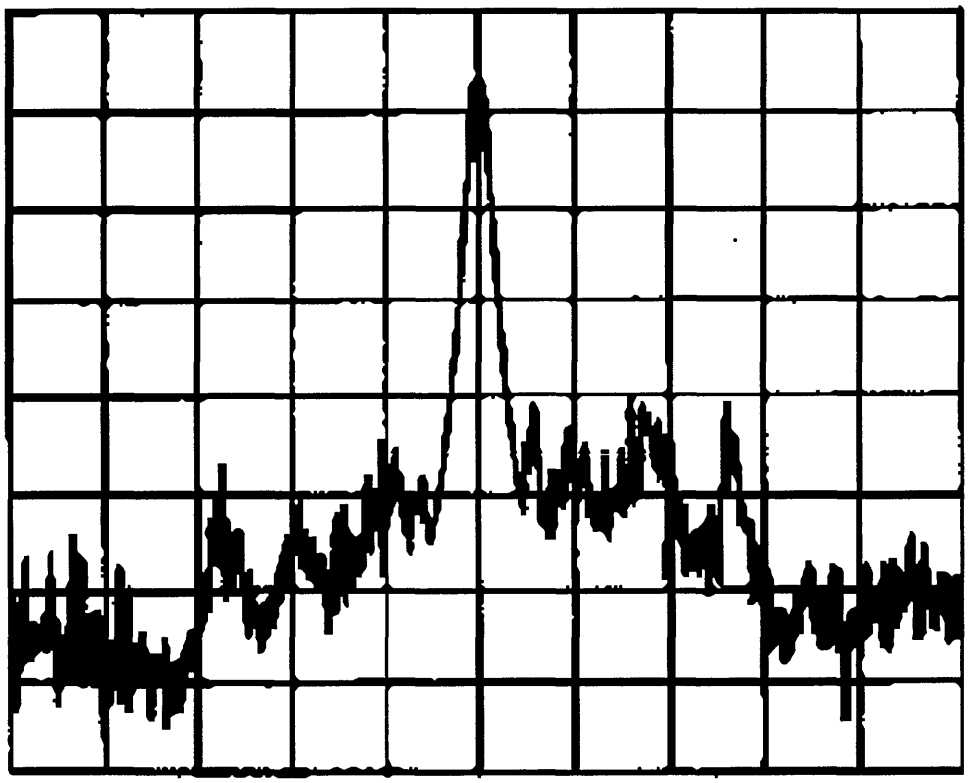

Figure 6-5: Trace of demodulated signal-idler beat-note spectrum of the 2-element OPO showing a 3-dB width (FWHM) that was limited by the 30-Hz resolution bandwidth of the rf spectrum analyzer (vertical scale, 10 dB/div.; horizontal scale, 200 Hz/div.; center frequency, 50 MHz; sweep time, 50 s).

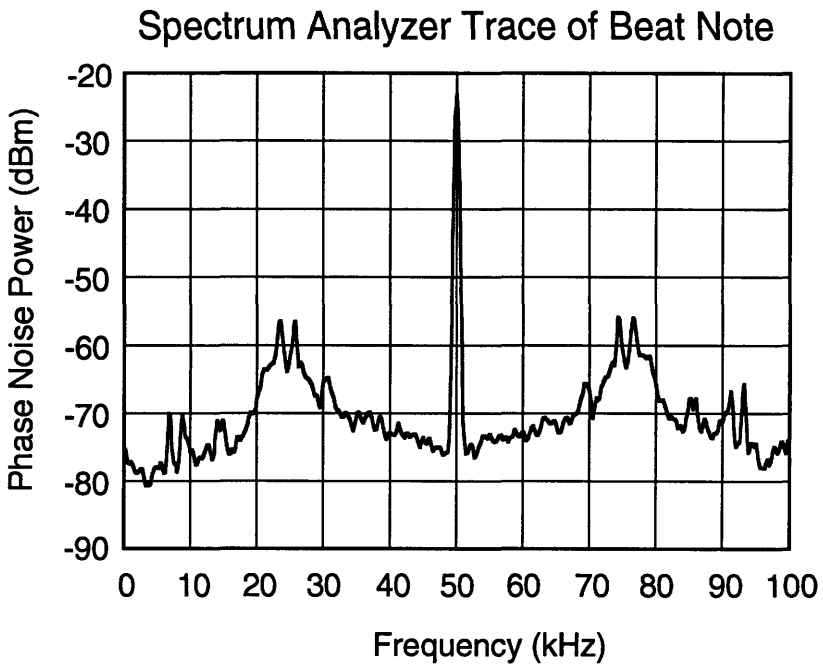

Figure 6-6: FFT spectrum analyzer trace of the demodulated signal-idler beat note of the 3-element OPO. The rise in the phase noise at around 25 kHz from the center frequency agreed with the calculated unity-gain bandwidth of the phase-locked loop (resolution bandwidth, 500 Hz).

ratio and narrowed the beat-note linewidth in our 3-element DRO with the 40-MHz BPF. Since the beat frequency jitter of the 3-element DRO was only ~250 kHz without phase-locking servo, a smaller unity gain bandwidth could be used. The unity gain frequency of our PLL was 25 kHz.

The demodulated 40-MHz signal was further downconverted to 50 kHz with a second synthesizer. A high-resolution FFT spectrum analyzer (Stanford Research SR760) was used to examine the demodulated beat signal. Figure 6-6 shows the FFT spectrum analyzer trace of the down-converted 50 kHz signal-idler beat note, at a frequency span of 100 kHz and a resolution bandwidth of 500 Hz. The phase noise of the DRO rose as the loop gain diminished beyond the unity gain bandwidth of the PLL.

We expanded the scale of the FFT spectrum analyzer for higher resolution measurements, as shown in Fig. 6-7. The trace was taken with a span of 12 Hz and

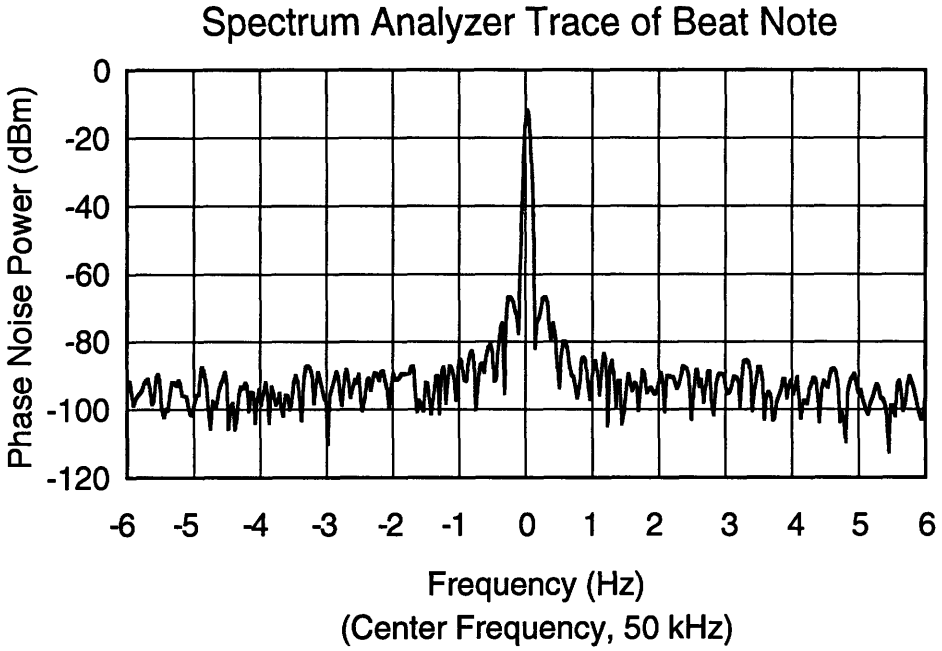

Figure 6-7: FFT spectrum analyzer trace of the demodulated signal-idler beat note of the 3-element OPO showing a 3-dB width (FWHM) that is limited by the 60-mHz resolution bandwidth of the FFT spectrum analyzer (sweep time, 33 s).

a resolution bandwidth of 60 mHz. The 3-dB linewidth (FWHM) of the peak was ~60 mHz, suggesting that the signal-idler beat note was tightly phase locked to the microwave reference signal.

Power Spectral Density

In Figure 6-7 the phase noise level at 1–6 Hz from the carrier is approximately −83 dBc, which yields a power spectral density of $\sim$ 0.3 mrad/$\sqrt{\text{Hz}}$, as is in Fig. 6-6 at low frequencies.

Our detection electronics was not shot-noise limited with the electronic noise level about −103 dB from the peak of the beat-note signal in Fig. 6-7. The corresponding shot-noise level for the detected 300 μA dc power was about −160 dB from the peak of the beat-note signal. The amount of noise suppression in any servo-loop system would only be as good as the reference. In the case of a phase-locked OPO, the residual phase noise of the beat-note would only be as good as the combined phase

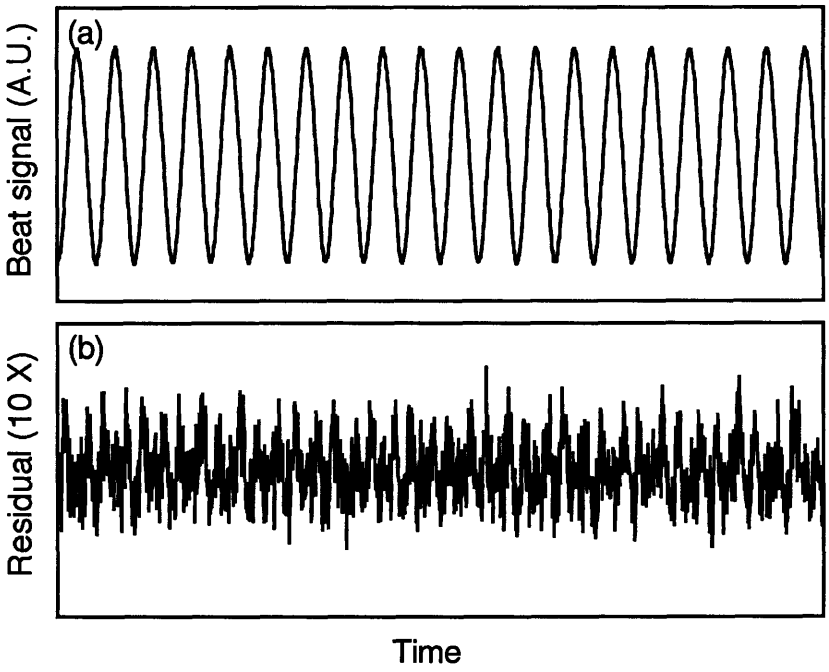

Figure 6-8: (a) Time trace of a 12.3-GHz signal-idler beat note demodulated to 1 Hz signal. Low-pass filter: 10 Hz. (b) Residual of a fit to trace (a) with a 1-Hz sine wave, magnification 10×. Rms phase noise is $\sim$ 28 mrad (horizontal span, 20 s).

noise of the synthesizer chain.

We also demodulated the phase-locked 40-MHz downconverted signal to 1 Hz, which was then low-pass filtered with a 10-Hz lowpass filter. Figure 6-8a shows the 1-Hz demodulated beat signal trace taken over a period of 20 s, indicating that the signal-idler beat frequency was phase continuous with respect to the microwave synthesized signal. The residual of a fit to the beat signal with a 1-Hz sine wave is shown in Fig. 6-8b at a 10× vertical magnification. If we assume that the residual is entirely due to phase noise, thus ignoring any contribution from amplitude modulation noise, the rms phase noise is calculated from Fig. 6-8b to be ~28 mrad. As a comparison with Figure 6-7, this yields an average power spectral density of ~6.3 mrad/$\sqrt{\text{Hz}}$ over the 20-Hz bandwidth, which is much higher than that obtained from Figure 6-7. Note that in this comparison we use the actual noise bandwidth at base band that is twice the filter bandwidth.

The larger phase noise in Figure 6-8 was caused by two factors in the measurement setup. Approximately half of the noise variance was the result of the diode nonlinearity of the double balance mixer, which generated harmonics of the 1-Hz signal, and the other half was caused by the noisy 10-Hz lowpass active filter. This was confirmed by a test measurement that used two phase-locked rf synthesized signals as inputs to the mixer under the same operating conditions. We obtained a phase noise of ~ 28 mrad, as in the experimental trace of Figure 6-8. When the test signal was first amplified by 20 dB before filtering, the noise variance was reduced by half. In the future the use of a low-noise filter and a beat frequency higher than the filter bandwidth should eliminate the discrepancy between the frequency-domain and the time-domain analyses.

6.6 Wideband Phase Locking using a Frequency Comb Generator

The beat frequency detection range of our experiment was limited by the bandwidth of our electronics, in particular the high-speed photodiode. A way to increase the detection bandwidth without using even higher speed electronics was to employ an optical frequency comb generator (OFCG) in our experiment. An OFCG generates precisely spaced sidebands from the input optical field to span over a wide frequency range [26, 27, 20]. The span of the frequency comb is determined by the number of sidebands and their frequency spacing, which in turn is determined by the microwave modulation frequency.

6.6.1 Experimental Setup

The setup was to input the idler field from the DRO into the OFCG to generate a wideband frequency comb, as sketched in Fig. 6-9. The beat signal between the signal field and one of the idler sidebands was detected using a photodetector and used for phase-locking the DRO. The OFCG in our phase locking experiment was developed in our laboratory by L.R. Brothers, as reported in Ref. [5]. Our OFCG was a phase modulator designed for 1.06 μm with optical feedback for the carrier and the sideband fields. The cavity resonant enhancement increased the number of sidebands and lowered the modulation frequency power requirement for a given frequency span for the comb. The $LiNbO_3$-based OFCG had a total span of $\sim$3 THz when modulated with 1 W of cw microwave power at a modulation frequency (f_m) of 17.05 GHz.

The rest of the experimental setup was similar to the 3-element DRO phase-locking experiment, only that an OFCG was inserted into the output beam path to generate a frequency comb. Also, the 25-GHz photodiode was replaced with a New Focus 1-GHz photodetector. There were two reasons to replace the 25 GHz photodiode with a lower speed detector. First, the New Focus photodetector could operate with a

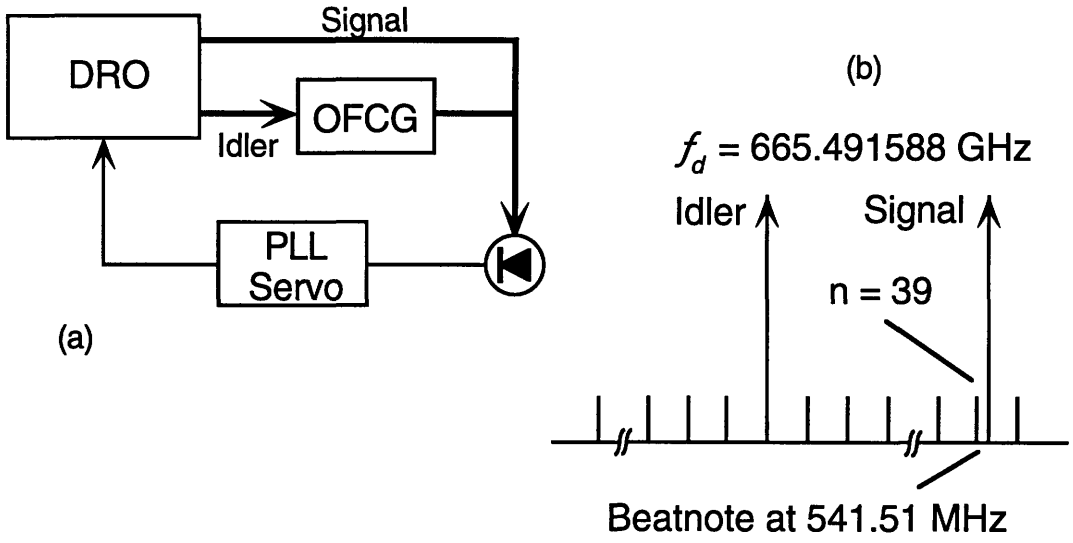

Figure 6-9: (a) Block diagram of phase-locking DRO experiment with frequency comb generator inserted in the beam path. (b) Frequency spectral diagram showing the generated frequency comb and the position of the signal relative to the sidebands.

much higher optical input power. In the 3-element DRO experiment, the signal and idler powers impinging on the photodiode were approximately equal; therefore, the ac signal was as strong as the dc signal. In the OFCG experiment, the sideband power decayed exponentially as the sideband order increased. The sideband (idler) power from the OFCG was much weaker than the signal power from the DRO, with the signal serving as the local oscillator in the heterodyne measurement. The ac signal power from the detector was therefore much weaker than the dc signal, which was mostly due to the strong local oscillator power. As a result, it was necessary to use a higher power detector for the dc signal. Secondly, the photodetector bandwidth should be less than half of the modulation frequency of the OFCG. Otherwise, the detector would detect more than one signal from the beat of the local oscillator and the sidebands.

In our experiment, the 3-element DRO was initially angle tuned so that the signal-idler frequency difference was within 50 GHz of our target frequency of 665 GHz. The DRO was pumped at 1.8 times above threshold (threshold $\approx$ 60 mW) with an output power of $\sim$ 4.7 mW in each of the signal and the idler output beams. The

orthogonally polarized outputs were separated with a polarizer, and ~4 mW of the lower-frequency idler beam was input into the OFCG. The modulated idler output and the signal were recombined and detected with the 1-GHz photodetector. A dc photocurrent of 1 mA was generated by the incident 1.5 mW signal. The DRO was tuned so that the beat between the signal and the nearest sideband of the comb was less than 1 GHz. The beat was amplified and then down-converted to ~40 MHz by a double balanced mixer. The 40-MHz beat was input into the phase detector for phase locking and monitoring.

6.6.2 Experimental Results

In our experiment the DRO was tuned so that the signal was near the 39th sideband of the modulated idler. We determined the sideband order k by dithering the 17-GHz modulation frequency f_m by 1 MHz and measuring the change in the beat frequency of k MHz. Moreover, by observing the sign of the beat frequency change relative to that of the dither, we determined that the frequency of the signal was higher than that of the sideband. The exact signal-idler frequency difference of the phase-locked DRO was 665.491588 GHz, with the frequency precision limited by the microwave source. We should point out that f_d had a jitter of $\pm$250 kHz when the DRO was not phase locked, and hence there was no uncertainty in the determination of the sideband order.

Figure 6-10 is the spectrum analyzer trace of the down-converted beat-note signal after various stages of amplifier gain and demodulation. The over-all effective gain of the detection electronics after the photodetector was 41 dB. The noise floor of the measurement (combined shot noise and electronic noise) was -95 dBm, or about 62 dBc. With ~1.3 mA of photocurrent, the electronic-noise level was 1 dBm smaller than the combined noise level. From the 47-dB of signal-to-noise ratio at low frequencies and a resolution bandwidth of 1 kHz, the residual phase-noise spectral density is calculated to be 0.2 mrad/$\sqrt{\text{Hz}}$, which is comparable with our previous measurement of 0.3 mrad/$\sqrt{\text{Hz}}$ from the 3-element DRO experiment in Section 6.5.2. The comparable phase-noise spectral densities in the two cases suggest that it should

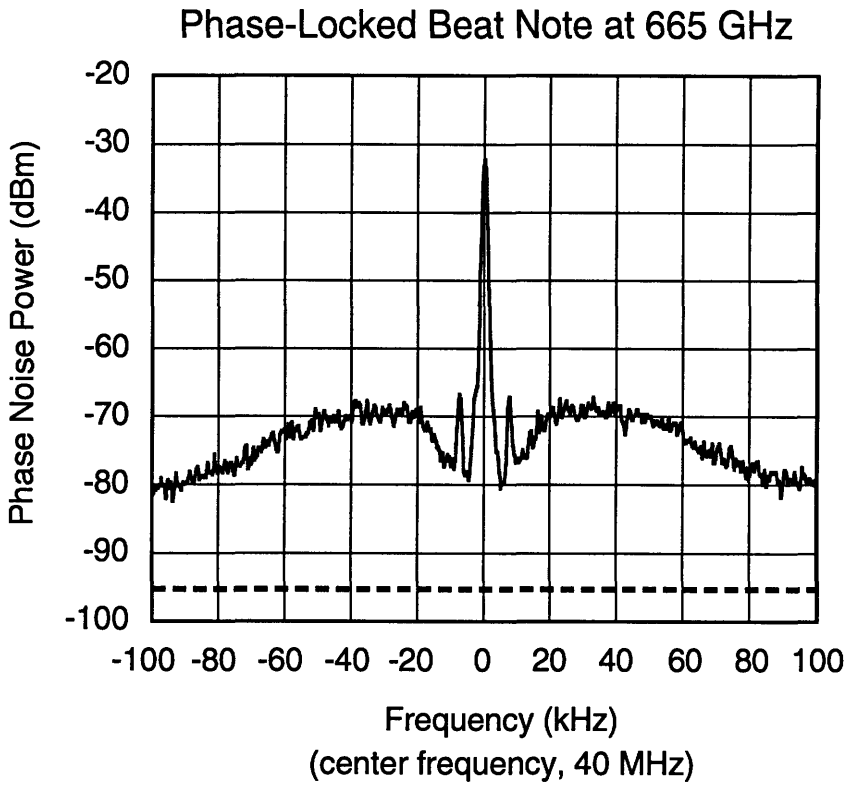

Figure 6-10: Spectrum analyzer output of phase-locked DRO beat note using an optical frequency comb generator at 665 GHz (analyzer bandwidth, 1 kHz). Dotted line: combined shot noise and electronic noise floor. The two sidebands at ±6 kHz are due to dithering of the cavity mirror for servo locking the modulator cavity.

be possible to phase lock the DRO at an even higher frequency difference, limited eventually by the phase noise of the higher-order sideband.

6.7 Summary

We have demonstrated for the first time optical frequency division by phase locking the output difference frequency of a DRO to a microwave reference. The 2- and 3-element DROs were phase locked to yield very narrow linewidths with the measurement essentially limited by the resolution of the spectrum analyzer. From the signal-to-noise ratio, we calculated the phase noise power spectral density of our phase-locked beat note to be $\sim$0.3 mrad/$\sqrt{\text{Hz}}$. Furthermore, we extended our de-

tection range beyond the photodiode bandwidth by using an optical frequency comb generator. The measured phase noise power spectral densities of the phase-locked 3-element DRO at 12.3 GHz and 665 GHz were essential the same, suggesting that it should be possible to phase lock the DRO at a much higher signal-idler frequency difference.

With the ability to stabilize the signal-idler beat-note signal, we were ready to perform the OPO quantum noise spectra measurement. The experimental setup and results are discussed in the next chapter.

Chapter 7

OPO Quantum Noise Experiments

7.1 Introduction

In this chapter, we discuss the experimental setup and results of our OPO noise experiments. Two different types of OPO noise characteristics were studied. The first type was the inherent quantum noise that was generated by the OPO, and the second type was the input-to-output noise transfer characteristics.

The OPO quantum noise originates from the interaction between the vacuum modes and the internal fields via the parametric down-conversion process. The vacuum modes are coupled into the OPO three-wave mixing equations through the scattering losses and output coupling losses. In a quantum mechanical formulation, loss introduces vacuum noise. OPO experiments that exhibit sub-shot-noise behavior have been demonstrated by different groups around the world, such as twin beams intensity correlation, squeezed amplification, and generation of squeezed states, just to name a few [24, 30, 45, 34]. However, there has not been any experiment on the phase noise characteristic of an OPO.

The vacuum modes interact with the phase-quadrature of the signal and idler fields to generate phase noise. The phase difference between the signal and idler fields undergoes a random walk process, much like the phase diffusion in a laser. The OPO phase diffusion noise is quantum mechanical in nature and was first predicted by Graham and Haken in their classic paper on OPOs [21]. Other groups have also

calculated the phase diffusion noise spectrum [15, 35], but experimental confirmation has been lacking. In order to observe and measure the OPO phase noise spectrum, the signal-idler beat note must be stable during the measurement. Only with recent advances in OPO stabilization techniques has such an experiment become feasible [28]. To the best of our knowledge, we have experimentally measured the OPO phase noise for the first time.

The input-to-output noise transfer characteristics in an OPO form the second part of our OPO noise studies. Through the parametric downconversion process, any excess noise in the input pump field is transferred to the signal-idler outputs. The transfer process does not arise from the vacuum interaction. It is found to be frequency dependent and is a function of pump power, cavity detunings, and total loss rates.

7.2 Background

Before we start the discussion on our experimental results, we consider what is to be expected from our experiments.

7.2.1 OPO Intensity Spectrum

As discussed in Chapter 2, the OPO intensity and beat-note in-phase fluctuations are almost identical. We, therefore, expect the IR intensity and the beat-note in-phase signals to exhibit identical behavior, not only in their spectra but also in their input amplitude noise transfer functions. It is also not surprising that the two spectra should follow the input pump laser intensity noise spectrum. Any intensity noise in the pump laser beam would be transferred to the outputs via the down-conversion process. The experimental observation of intensity noise spectrum, in-phase noise spectrum, and the transfer function are presented later in this chapter.

7.2.2 In-Phase and Quadrature-Phase Coupling

The in-phase and the quadrature-phase components of the beat-note signal are coupled through the non-zero cavity detuning. The amount of coupling depends on the amount of detuning: the larger the detuning, the greater is the coupling. Because of the side-locking scheme we employed in the intensity stabilization, a small amount of detuning was unavoidable. From the pumping power and the OPO output power, we estimate the "normalized" detuning factor, Δ/κ, was about 0.531. However, the actual amount of in-phase noise leaking into the quadrature-phase also depended on the total loss mismatch between the signal and the idler fields. If the signal and idler losses were perfectly matched the two quadratures would then be decoupled. If, on the other hand, the losses were not matched and the pump laser was shot-noise limited, the addition of in-phase noise to the quadrature-phase would also be minimal.

7.2.3 Second Order Effect

From the theoretical calculation of the quadrature-phase noise spectrum, we find that the noise power spans a range of more than 40 dB. Our first-order calculation of the OPO quantum noise is a good approximation under normal experimental conditions, but would break down when we strongly modulate the input pump field in our OPO noise transfer measurements. Second order terms must be included in order to account for our experimental observations.

The quadrature-phase signal $y(t)$ (Eq. (A.31)), including the second-order terms, can be written as

$$y(t) = 2C^2\sqrt{\frac{\gamma_1\gamma_2}{\kappa_1\kappa_2}}\,(\psi_- - \mu_1\psi_2 + \psi_1\mu_2) + \cdots \tag{7.1}$$

$$= 2C^2\sqrt{\frac{\gamma_1\gamma_2}{\kappa_1\kappa_2}}\left((1+\frac{1}{2}\mu_+)\psi_- - \frac{1}{2}\mu_-\psi_+\right) + \cdots \tag{7.2}$$

The quadrature-phase spectrum $y(t)$ is modified by the second-order terms to include the signal-idler sum-intensity (difference-intensity) fluctuation μ_+ (μ_-). Because of common-mode cancellation, the magnitude of μ_- is smaller than that of μ_+; we

therefore ignore the second term of Eq. (7.2) and approximate the beat-note phase noise as

$$(1+\frac{1}{2}\mu_+)\psi_-.$$

If the input pump field is amplitude modulated at a modulation frequency of ω_m, the modulation would be transferred to the signal-idler output fields at the same frequency. The amplitude modulation contained in μ_+ would be transferred to the quadrature-phase spectrum S_y via the second-order term $\mu_+\psi_-$, even at zero detuning. This second order effect produces a pump-induced quadrature-phase spectrum that is frequency upshifted by an amount equal to the modulation frequency, ω_m, but with a smaller noise power.

This second-order pump-induced effect can be understood by considering the following situation. Assuming that the pump intensity is strongly modulated at the modulation frequency ω_m so that the modulation dominates over other noise term, hence a classical calculation suffices. The signal-idler sum-intensity then takes on the form

$$\mu_+ = me^{-i\omega_m t},$$

where $m \ll 1$ is the modulation index. The quadrature-phase signal (Eq. (7.2)) becomes

$$\begin{aligned} y(t) &\sim (1+\frac{1}{2}\mu_+)\psi_- \\ &\sim (1+\frac{1}{2}me^{-i\omega_m t})\psi_-, \end{aligned}$$

and the quadrature-phase power spectrum S_y is calculated from the Fourier transform ($\mathcal{F}$) of the auto-correlation function of $y(t)$,

$$\begin{aligned} S_y(\omega) &= \mathcal{F}\{\langle y(\tau)y(0)\rangle\} \\ &\sim \mathcal{F}\{\langle \psi_-(\tau)\psi_-(0)\rangle\} + \frac{m}{2}\mathcal{F}\left\{\langle e^{-i\omega_m\tau}\psi_-(\tau)\psi_-(0)\rangle\right\} \\ &\sim S_y^0(\omega) + \frac{m}{2}S_y^0(\omega-\omega_m), \end{aligned} \tag{7.3}$$

$$S_y^0 = \mathcal{F}\{\langle \psi_-(\tau)\psi_-(0)\rangle\}.$$

Here, we have made use of the attenuation property of Fourier transforms [6, Chap. 7],

$$\begin{aligned} \mathcal{F}\left\{f(t)e^{at}\right\} &= F(\omega - ai), \\ \text{where} \qquad \mathcal{F}\{f(t)\} &= F(\omega), \end{aligned}$$

to obtain Eq. (7.3)).

As we can see from Eq. (7.3), S_y consists of two terms: a modulation-independent (first) term and a modulation-dependent (second; m) term. The quadrature-phase power at the modulation frequency ω_m is given by

$$S_y(\omega_m) \sim S_y^0(\omega_m) + \frac{m}{2} S_y^0(0). \tag{7.4}$$

The second term of Eq. (7.4) gives the pump-induced frequency upshifted spectrum and it is smaller in power by an order of m. At low frequencies, the quadrature-phase noise power ($S_y(\omega_m)$) is much larger than the shifted pump-induced spectrum power and, therefore, the quadrature-phase spectrum dominates. At high frequencies, the quadrature-phase power at ω_m is lower by 40 dB compared to the low frequency range, and the shifted pump-induced spectrum dominates. The shifted-spectrum is only observable when the shifted-spectrum noise power is larger than the original spectrum power at the modulation frequency i.e., for $mS_y^0(0) > S_y^0(\omega_m)$ for large ω_m. Since the quadrature-phase spectrum is a monotonously decreasing function, there exist a cross-over frequency at which the shifted-spectrum power is larger than that of the quadrature-phase spectrum. The cross-over frequency is approximately located at the point where the shifted-spectrum power equal to the original spectrum power, and is estimated to be 2 MHz from Fig. 7-16.

The pump intensity to quadrature-phase transfer function H_{AP} is obtained by dividing the quadrature-phase spectrum (Eq. (7.4)) by the input pump intensity spec-

trum h^R, which is proportional to the modulation index m,

$$\begin{aligned} H_{AP} &= \frac{S_y(\omega_m)}{h^R(\omega_m)} \\ &\sim \frac{S_y(\omega_m)}{m} \\ &\sim \frac{S_y^0(\omega_m)}{m} + \frac{1}{2}S_y^0(0). \end{aligned} \tag{7.5}$$

H_{AP} consists of a frequency-dependent (first) term and a constant (second) term. At frequencies below the cross-over frequency, the first term of H_{AP} dominates; whereas at frequencies above the cross-over frequency, the constant term of H_{AP} dominates.

7.2.4 Pump Laser Noise

The pump laser intensity and frequency stabilization systems have been presented in Chapter 3. We now further characterize the noise from the pump laser, both intensity and phase noise, in more detail before we present the OPO noise measurements.

Intensity Noise

The pump laser intensity noise was easily measured with a photodetector and a rf spectrum analyzer. The incident power on the photodetector was attenuated from 250 mW at the OPO input port to ~1.5 mW to within the power handling capability of the detector. Figure 3-3 shows the pump laser intensity noise spectra under free-running and intensity-locked conditions. When the pump laser was under intensity-locked conditions (Fig. 3-3b), the intensity noise at low frequencies was reduced by as much as 20 dB from that under free-running conditions (Fig. 3-3a). The pump laser has a large amount of excess noise below 1 MHz and was shot-noise limited above 2.5 MHz. At the input port of the OPO, the excess pump intensity noise power was (S_{full}) estimated from the 25 dB of excess noise (at 400 kHz) in Fig. 3-3 using

$$S_{obs} = \eta S_{full} + (1 - \eta) \tag{7.6}$$

to be ~47 dB above shot-noise level. Here, η is the attenuation factor ($\eta = 1.5/250 = 0.006 = -22$ dB), S_{full} (47 dB) is the full noise power without attenuation, and S_{obs} (25 dB) is the observed noise power after attenuation. The slight rise in noise level between 1.5 to 2.5 MHz was caused by excess intensity-loop gain.

To study the effects of excess pump intensity noise on the quadrature-phase spectrum, we modeled the pump noise with a simple straight-line model (Fig. 7-1a) and calculated the in-phase and quadrature-phase spectral responses (Fig. 7-1b and c). The in-phase spectrum was calculated using the simplified zero-detuning equation (Eq. (2.49)), whereas the quadrature-phase spectrum was calculated using the complete equation (Eq. (2.41)). For a first-order approximation, Eq. (2.41) gives the qualitative behavior without having to calculate the more complex second-order terms. Since detuning only couples the two quadratures, the use of zero-detuning in-phase spectrum equation does not affect the pump intensity to in-phase noise transfer. As shown in Figure 7-1, the in-phase and quadrature-phase spectra show the same pump intensity profile in the frequency range 0.2–2 MHz, suggesting the presence of coupling between the two quadratures. Furthermore, the in-phase noise power is about 10 dB larger than that of the quadrature-phase indicating intensity noise suppression in the quadrature-phase spectrum.

Frequency/Phase Noise

The pump laser frequency/phase noise spectrum was obtained from the error signal of the laser frequency stabilization servo. In a Pound-Drever frequency stabilization system, a high finesse Fabry-Perot cavity is used as a frequency discriminator to convert frequency deviations into error signal voltages (v). Here, the error signal is the heterodyne signal between the reflected sidebands and the cavity-leakage pump field. Cheng *et al.* has shown that the error signal is proportional to the laser frequency-noise amplitude S_f when the noise frequency f_n is within the Fabry-Perot cavity linewidth (980 kHz) [9]. For f_n that is much larger than the cavity linewidth, the error signal is proportional to the laser phase-noise amplitude S_ϕ, with $S_f = S_\phi f_n$. At frequencies (f_n) outside the servo-loop bandwidth (25 kHz), the error-signal noise

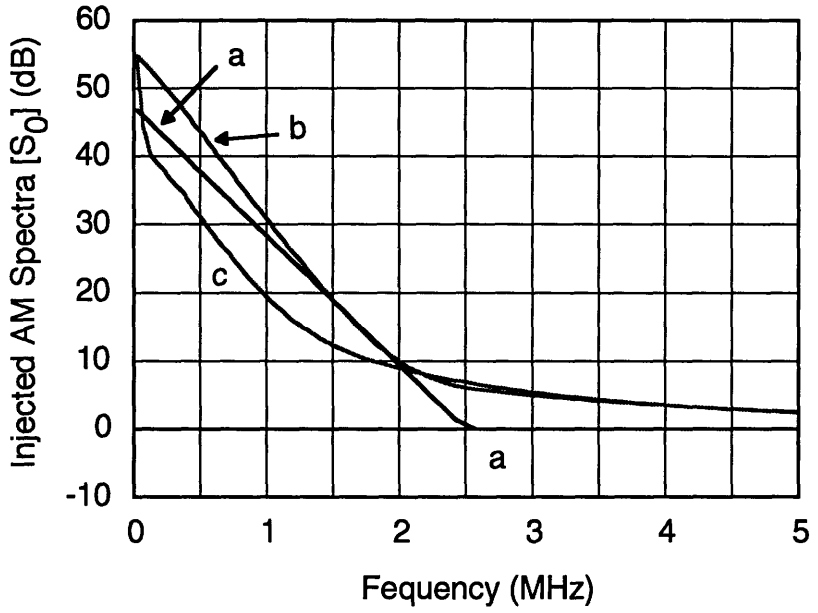

Figure 7-1: Theoretical plots of the quadrature-phase spectra showing coupling with the in-phase spectrum. (a) Simple straight-line excess noise model for the input pump field. (b) In-phase spectrum (Eq. (2.49)) showing the same noise profile as the input pump noise spectrum. (c) Quadrature-phase spectrum (Eq. (2.41)) showing the excess pump noise between 0.5–1.5 MHz caused by cavity detuning. All traces are normalized to their respective shot-noise levels (0 dB).

power density S_v^2 and the pump laser phase-noise power density S_f^2 are related by

$$\begin{aligned} S_v &= CJ_0(\frac{S_f}{f_n})J_1(\frac{S_f}{f_n})\chi(f_n) \\ &\approx C\chi(f_n)\frac{S_f}{2f_n}, \end{aligned} \tag{7.7}$$

$$\begin{aligned} C &= 8J_0(\beta)J_1(\beta)V_m, \\ \chi^2(f_n) &= r^2(f_n) - 2r(f_n)r(f_p)\cos\theta(f_n) + r^2(f_0), \\ r(f_n)e^{i\theta(f_n)} &= \frac{r_1 - r_2\exp(-i2\pi f_n/FSR)}{1 - r_1r_2\exp(-i2\pi f_n/FSR)}, \end{aligned}$$

where $\beta = 0.6$ is the phase modulation index by the phase modulator used in the Pound-Drever system, $V_m = 0.24V$ is the error voltage at the mixer output, $r_1^2 = 99.25\%$ and $r_2^2 = 99.9\%$ are the power reflectivities of the Fabry-Perot cavity front and back mirrors, FSR is the free spectral range (725 MHz) of the cavity, J_0 and J_1 are Bessel functions [9]. Note that Eq. (7.7) only applies for the reflected signal from the reference cavity and not for the transmitted signal, as the reflected and transmitted pump fields have very different cavity transfer functions.

Figure 7-2 shows the detected error signal spectra S_v^2 at two frequency spans, 2 MHz and 500 kHz. The pump laser phase-noise power spectral density was obtained from Fig. 7-2 and Eq. (7.7) to give Fig. 7-3. From Figs. 7.7 and 7-3, we see that the pump laser had a large amount of excess frequency/phase noise below 2 MHz, as in the intensity noise, and for frequencies above 2 MHz, electronic noise of the servo-loop dominated.

The pump laser had a large amount of excess intensity and phase noise between the frequency range of 0.5–2.5 MHz. Above 2.5 MHz, the pump laser was very close to shot-noise level and its contribution to the OPO output noise was much reduced. The frequency windows for phase noise measurements would be between 2.5–5 MHz and below 0.5 MHz.

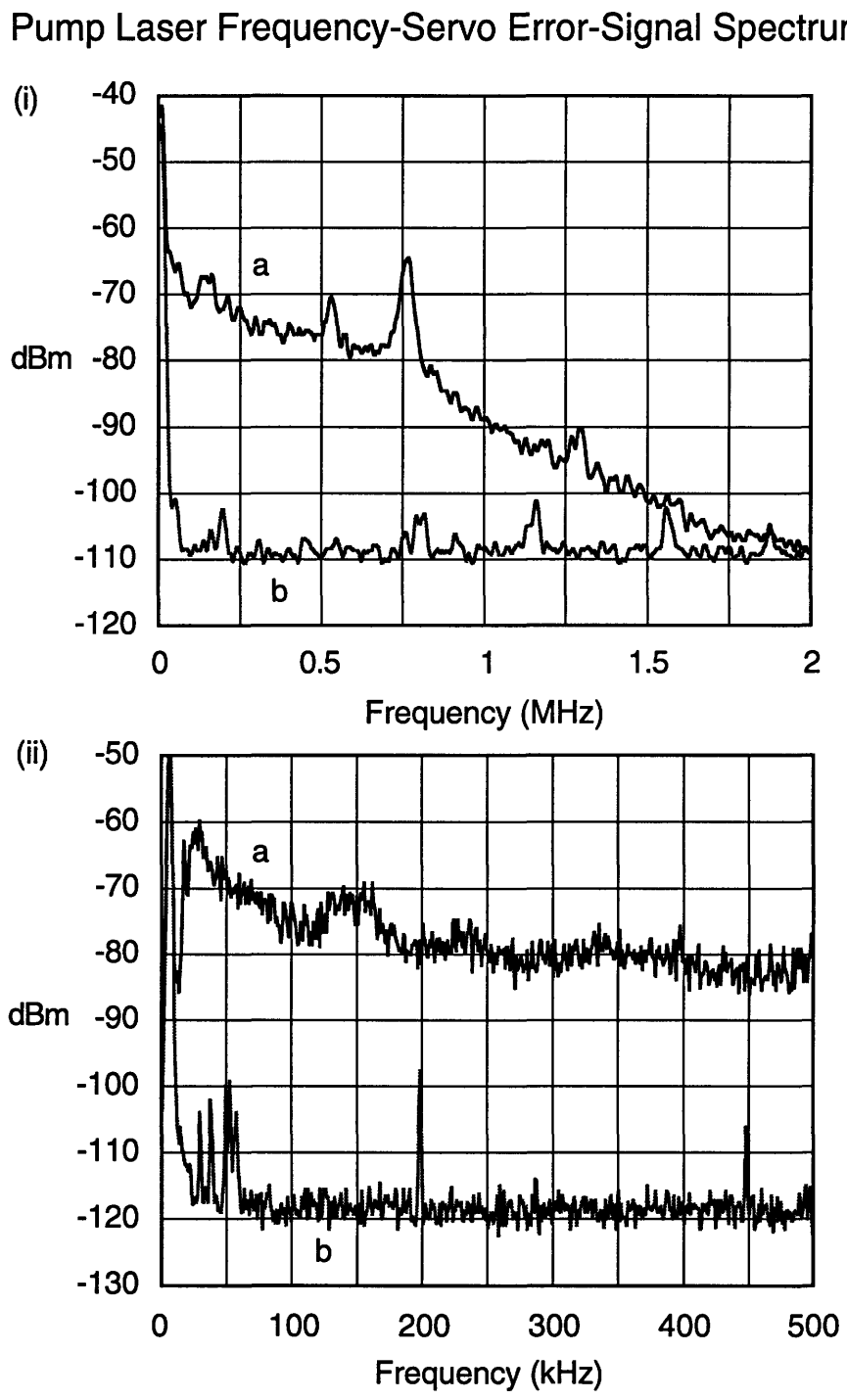

Figure 7-2: (i) : Trace (a) shows the spectrum of laser frequency stabilization servo error signal; Trace (b) shows the detector electronic-noise level (bandwidth, 30 kHz). (ii) Zoom-in trace of (a): note the difference in both the vertical and horizontal scale (bandwidth, 3 kHz). Shot-noise level was estimated to be (a) -110 dBm; (b) -120 dBm.

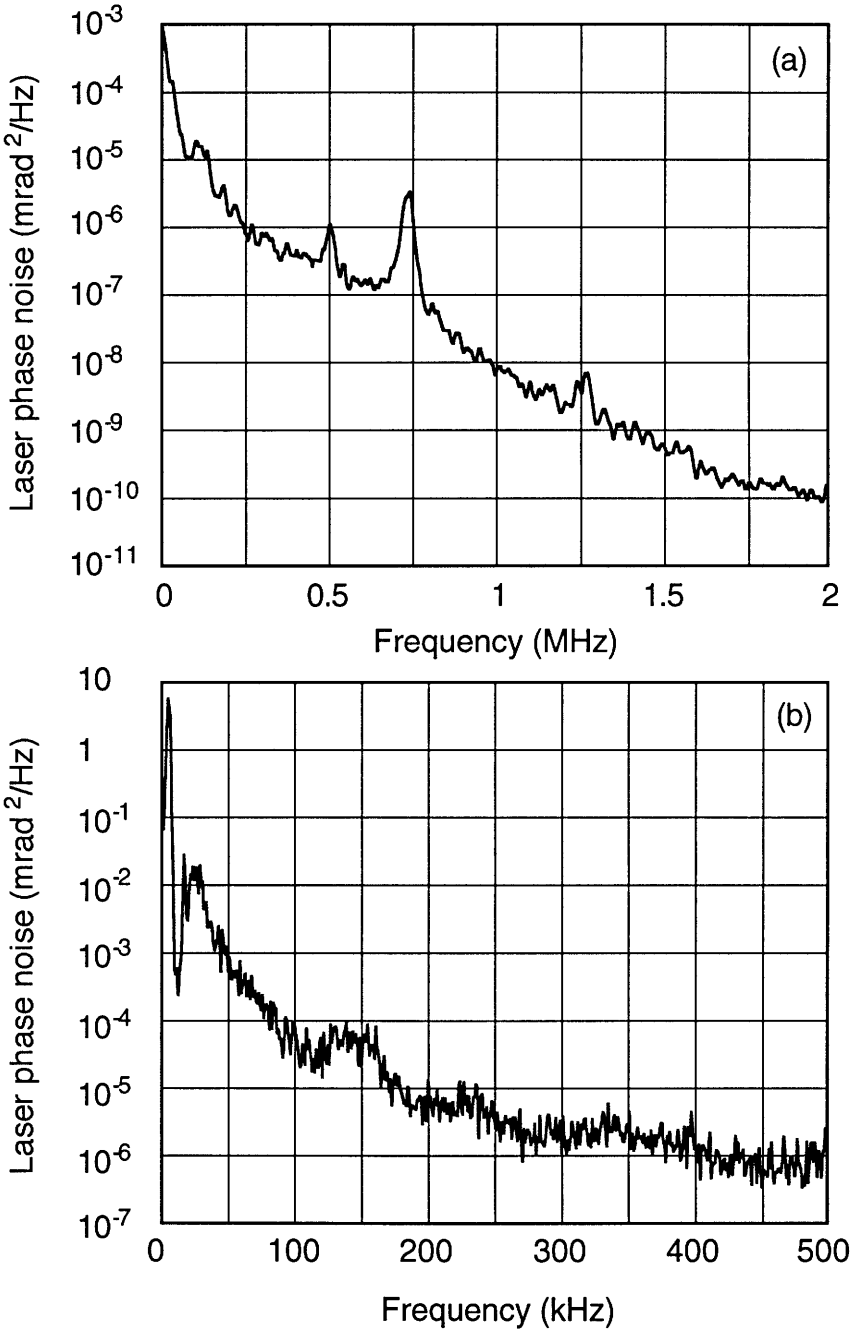

Figure 7-3: Pump laser phase-noise power spectral density obtained from Fig. 7-2 at two frequency spans: (a) 2 MHz, (b) 500 kHz. Shot-noise level was estimated to be 10^{-10} mrad^2/Hz.

7.2.5 Amplitude Modulation of the Pump

To study the effects of excess pump noise, we modulated the input pump intensity and monitored the resultant in-phase and quadrature-phase spectra. Amplitude modulation of the input pump field was accomplished by applying a rf signal to the test port of the laser intensity stabilization servo. The rf signal from the test port was summed with the laser intensity error signal before being sent to the electro-optic modulator. The pump laser intensity loop response was then measured by detecting the pump laser intensity noise with a spectrum analyzer while sweeping the rf modulation frequency.

Two different sources of modulation signals were used in the noise transfer experiment. The first one was from a signal synthesizer producing a pure sine wave at one frequency. A single-frequency modulation allowed us to concentrate the study on a narrow frequency span and examine the spectrum on a finer scale. The second signal source was a broadband tracking frequency sweep provided by the rf spectrum analyzer. The frequency sweep was synchronized to the internal local oscillator of the spectrum analyzer so that transfer functions could be easily measured over the span of the analyzer. Figure 7-4 shows the broadband amplitude-modulated pump intensity spectrum at the input port of the OPO, normalized to shot-noise power.

7.3 Experimental Setup

The theoretical background for OPO noise calculations has been covered in Chapter 2. We now proceed to discuss the experimental aspects of our noise studies. The following is a general detection procedure used in the experiment. The experimental technique of the phase noise measurement is very similar to the phase-locking experiment that is described in Chapter 4.

The phase noise experiment was conducted with the signal-idler beat note phase locked at a frequency of 30 MHz. The beat-note signal was directly detected with a photodetector and demodulated with a local oscillator (at 30 MHz) that in turn was phase locked to the rf synthesizer used for phase locking the OPO. By varying

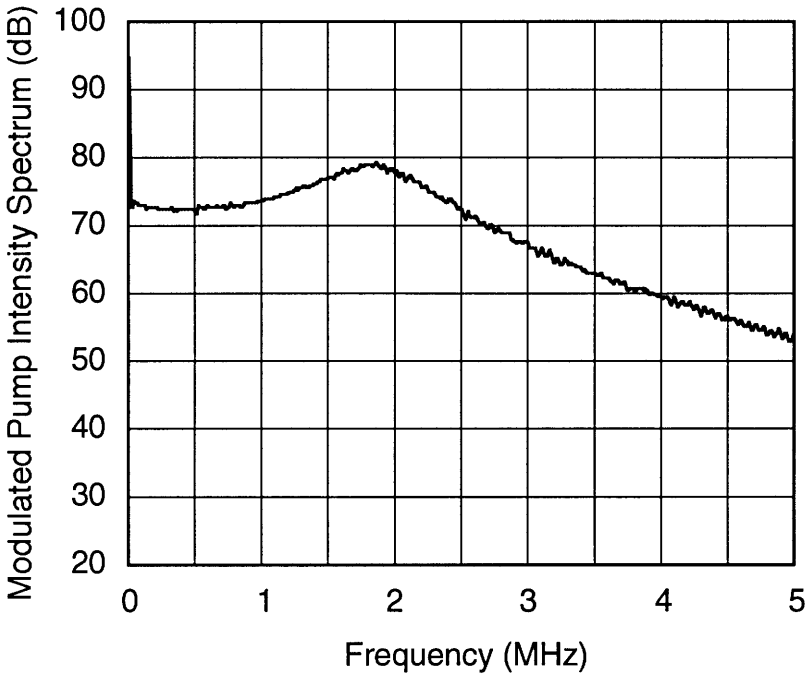

Figure 7-4: Trace of amplitude modulated pump laser intensity spectrum normalized to shot-noise power. The trace was taken at the input port of the OPO with a pump power of 250 mW and the modulation power at the test input port of the intensity servo was −40 dBm. The roll off at 2 MHz shows the laser intensity servo bandwidth (bandwidth, 30 kHz).

the relative phase between the two rf synthesizers, the in-phase and the quadrature-phase components of the photocurrent were obtained. The noise power spectra of the two quadratures were then measured with a rf spectrum analyzer. In the second part of our experiment, the pump laser intensity was amplitude modulated to investigate three different types of OPO noise transfers characteristics: pump intensity to output intensity noise transfer, and pump intensity to beat-note signal in-phase and quadrature-phase transfers.

7.3.1 Pump System

In this experiment, we used the same krypton ion laser pump system that was employed in the frequency tuning and the phase-locking experiments. A full description of the laser operation can be found in Chapter 3.

7.3.2 OPO

The OPO used in the quantum noise experiment was the same 3-element OPO used in the frequency-tuning and phase-locking experiments as described in Chapters 5 and 6. Here, we summarize the important operating parameters for the 3-element OPO.

The operating threshold of the OPO near frequency degeneracy was about 180 mW and typical pump input power was 250 mW, at $\sim$ 1.4 times threshold value. The nominal free spectral range of the cavity was 3.4 GHz including the 8-mm long potassium titanyl phosphate (KTP) crystal inside the cavity. From cold cavity finesse measurements the total losses of the OPO cavity at 1.064 μm were measured to be 1.6% for the vertical polarization, and 2.4% for the horizontal polarization. The output coupling loss for either polarization was 0.75%.

For cw OPO operations, we servo locked the output intensity of the OPO to the side of a cavity resonance mode. Typical locking-point was at the half power point of the cavity mode, and a total output power of 15 mW was obtained. The residual peak-to-peak intensity noise was about 2%. Unfortunately, the use of a side-locking

Parameters	Symbol	Measured Power Loss	Normalized to $[\kappa]$
Signal total loss	κ_1	1.6%	0.4
Idler total loss	κ_2	2.4%	0.6
Combined total loss	$\kappa = \kappa_1 + \kappa_2$	4%	1
Differential total loss	$\delta = \kappa_1 - \kappa_2$	0.8%	0.2
Output coupling	$\gamma_{1,2}$	0.75 %	0.1875
Pump total loss	κ_p	90%	60
Combined total detuning	$\Delta = \Delta_1 + \Delta_2$	-	0.531
Pump Power/Threshold	F_p	1.4	-

Table 7.1: Summary of various measured loss rates and operating parameters for the 3-element OPO under typical experimental conditions.

scheme means that the cavity detuning was non-zero, which led to the mixing of the in-phase and the quadrature-phase noise. Further discussion on quadrature couplings and experiments will be presented later in this chapter. Table 7.1 summarizes various measured loss rates and operating parameters for the 3-element OPO under typical experimental conditions.

7.3.3 Optics

Figure 7-5 shows the schematic of the optical setup for the OPO quantum noise experiment. The outputs from the OPO were first divided into two parts by a beam splitter whose splitting ratio was 1:4. The first part, about 20% of the total power (3 mW), was detected by the OPO intensity-servo to provide cw operations with less then 1% peak-to-peak intensity noise. The remaining portion of the output beams (12 mW) went through a quarter waveplate and a polarizing beam splitter (PBS1) so as to project the two orthogonally polarized beams onto a common polarization axis. The waveplate and PBS combination not only further divided the beam into two portions, but it also allowed us to adjust the power ratio between the signal and the idler fields.

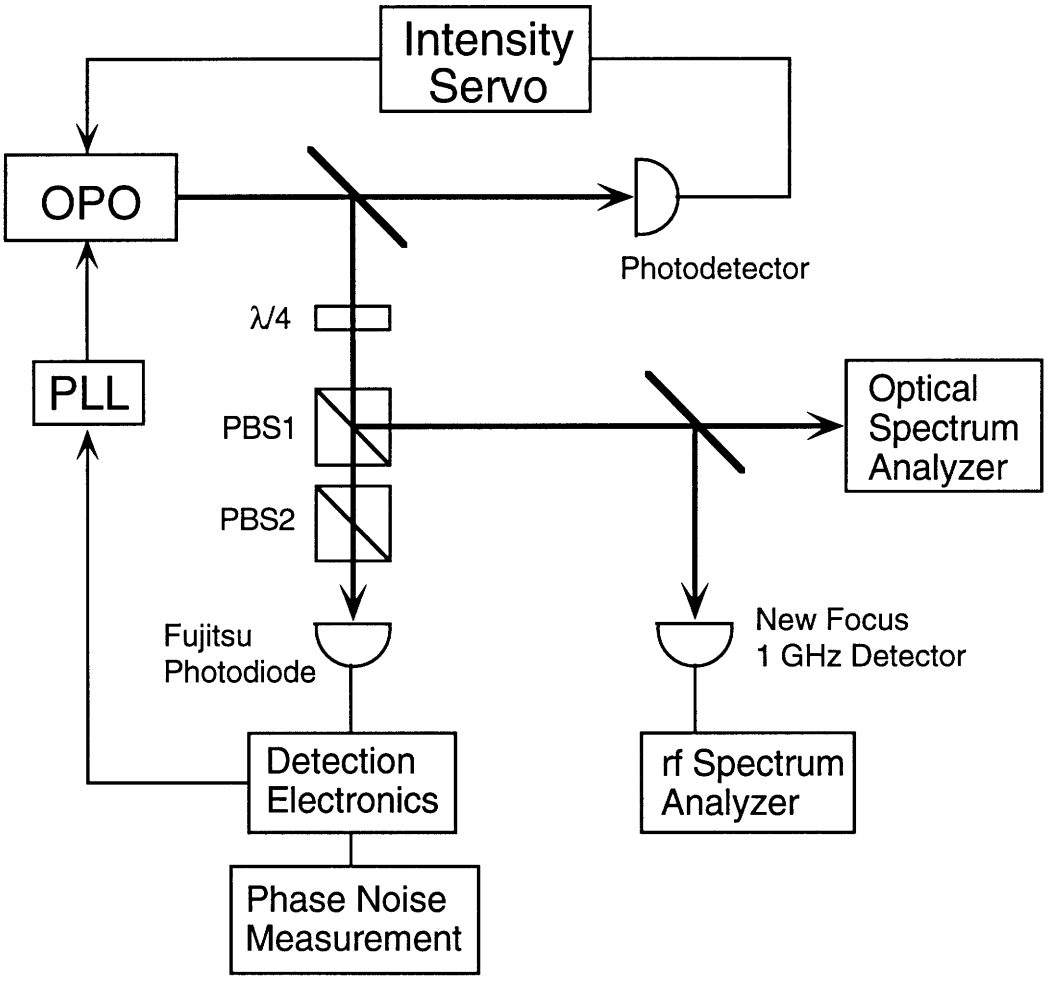

Figure 7-5: Schematic of the optical setup for the quantum noise experiment.

Optical Diagnostic

The first portion from the polarizing beam splitter (PBS1) was input into a diagnostic system for determining the exact frequency difference between the signal and the idler fields. The diagnostic system consisted of a 8-THz Super-Cavity optical spectrum analyzer and a 1-GHz photodetector connected to a 2-GHz wideband rf spectrum analyzer. The diagnostic system allowed us to monitor the signal-idler frequency difference while we tuned the OPO. The frequency difference was monitored on the Super-Cavity while we angle tuned and PZT tuned[1] the output frequencies to within a few hundreds of MHz. The Super-Cavity could resolve a signal-idler frequency separation to as small as 50 MHz. While monitoring on the rf spectrum analyzer, we then adjusted the OPO's crystal temperature to bring the beat frequency to within the capture range of the PLL for frequency stabilization. Since the capture range of the PLL was only 1 MHz peak-to-peak, it was therefore necessary to have a fast real-time and high resolution diagnostic system for frequency monitoring. The width of the PLL capture range was determined by the bandwidth of the 30 MHz bandpass filter and the dynamic range of the PLL electronics.

The remaining portion from the polarizing beam splitter (PBS1) went through a second polarizing beam splitter (PBS2) before it was focused onto a low-noise photodetector for noise measurement and phase locking[2]. PBS2 allowed us to continuously adjust the incident power for optimal signal-to-noise ratio. The incident power on the photodetector was typically attenuated to ~0.8 mW to within the power handling capability of the photodetector.

7.3.4 Detection Electronics

The quantum noise detection electronic system could be divided into two functional blocks: a phase-locked loop to phase lock the beat-note frequency to a rf source, and an in-phase and quadrature-phase detection system (Fig. 7-6). The input sig-

[1]See Chapter 5 for detailed descriptions of various tuning elements and their ranges.
[2]See Chapter 6 for a detailed description of the phase-locking servo.

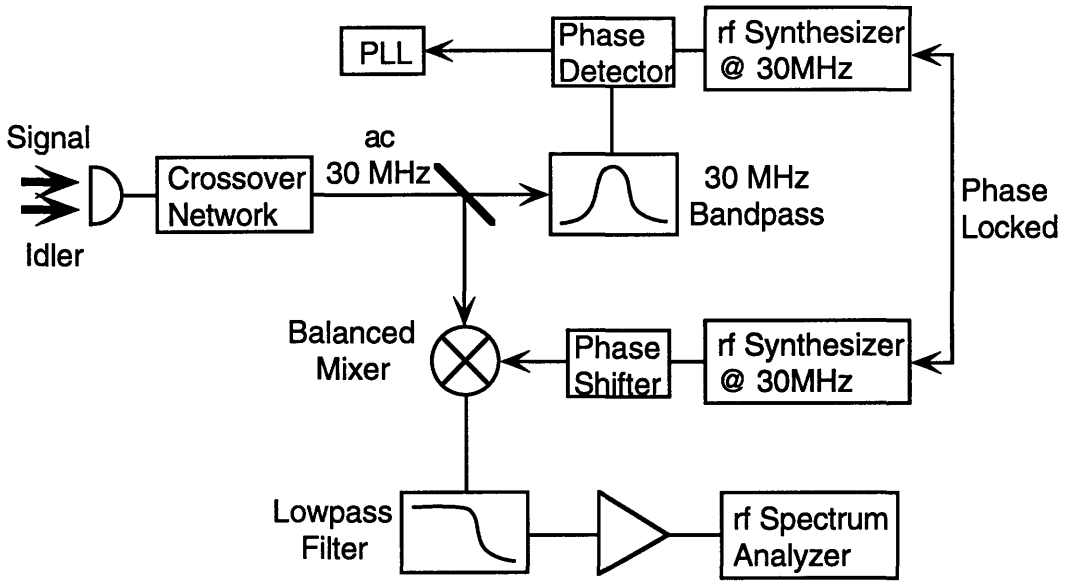

Figure 7-6: Schematic of electronic detection system for the quantum noise experiment.

nals for the two blocks were derived from the photocurrent of a low-noise 50-MHz-bandwidth photodetector. The photodetector consisted of a Fujitsu InGaAs photodiode (FID13S32WS) and a Comlinear operational amplifier (CLC-425) configured as a transimpedance amplifier with a feedback resistance of 2 kΩ. The responsivity of the Fujitsu photodiode was nominally 0.75 A/W. Typical dc output voltage was 1.3 V, with 0.8 mW of optical incident power. The output signal was separated into dc and ac components by a cross-over network whose cross-over frequency was 470 kHz. The ac component contained the beat-note frequency and phase information and the dc component was monitored to set the initial incident optical power.

The ac signal was divided into two equal parts with a power splitter (Mini-Circuit ZSC-2-1W) after the cross-over network. The first part was used for phase locking the beat note and the second part was for spectral analysis. As in the phase-locking experiment, the signal-idler beat frequency was tightly phase-locked to a synthesizer reference. The unity gain bandwidth of the PLL in this experiment was lowered to 20 kHz from 25 kHz in the phase-locking experiment. The slightly smaller bandwidth was chosen because we wanted to reduce the electronic noise effect due to the PLL,

while still being able to maintain a stable beat frequency. The phase-locking reference frequency was also switched from 40 MHz to 30 MHz because of the availability of rf synthesizers.

In-Phase and Quadrature-Phase Detection System

The remaining ac signal from the power splitter went into the in-phase and quadrature-phase detection system for power spectral measurements. The beat-note signal was demodulated to base band with a double-balanced mixer (Mini-Circuit ZLW-2) whose local oscillator reference was from a rf synthesizer (HP 8565A) at 30 MHz. The local oscillator signal and the PLL reference were phase locked together to eliminate any systematic phase drifts. It was also necessary for adjusting the phase angle of the local oscillator so as to yield the in-phase or the quadrature-phase components of the beat-note signal. To determine the correct local oscillator phase angle, the demodulated signal was monitored on an oscilloscope while the local oscillator phase angle was adjusted. When the average voltage on the oscilloscope was zero, the phase angle corresponded to the quadrature-phase setting, and when the average voltage was maximized it corresponded to the in-phase setting. The two phase angle settings were found to be 90° apart, as expected. The output of the mixer was then low-pass filtered and amplified by 20 dB (HP 8447A pre-amplifier) before it was input into a rf spectrum analyzer for analysis. The measurement bandwidth of our experiment was limited by the 5-MHz span of the analyzer (Tektronix model 7L5).

Measurement Limits

The accuracy of our measurement is determined by the overall electronic noise of our detection system and the resolution/accuracy of the Tektronix spectrum analyzer. The sensitivity of the measurement was determined by the electronic-noise level of the detection system; the smaller the electronic noise, the smaller the signal that could be detected. The electronic-noise level (Fig. 7-7a) was experimentally measured on the rf spectrum analyzer by blocking any optical input into the Fujitsu InGaAs photodiode.

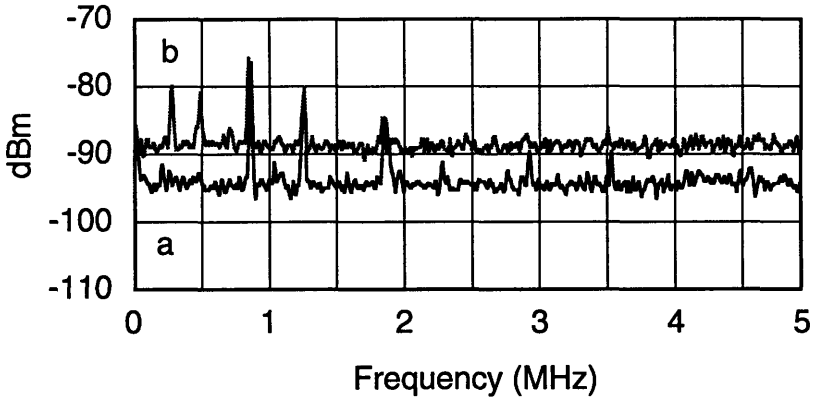

Figure 7-7: (a) Detection system electronic-noise level, P_{en}. (b) Measured shot-noise level (P'_{sn}) when 1 V of optical power was detected at the Fujitsu-Comlinear photodetector (bandwidth, 30 kHz). The measured noise level (combined shot noise and electronic noise) in trace (a) agreed with the expected value calculated from the 1 V photodetector output.

The minimum signal-idler optical power required for the experiment was determined by the detection system electronic-noise level. The shot-noise power from the signal and idler fields should be larger than the electronic-noise level so that the system was "shot-noise limited". The shot-noise level (Fig. 7-7b) was obtained using the signal and idler fields as input to the photodiode, but with the signal and idler frequency difference (> 7 GHz) much larger than the system detection bandwidth (50 MHz). In our experimental setup, the shot-noise level was ~5.5 dB (3.5×) larger than the electronic-noise power. The total ac signal power, and hence the shot-noise power, that was available was limited by the power handling capability of the Fujitsu-Comlinear photodetector. Since the measured shot-noise power (P'_{sn}) was only 3.5× of the electronic-noise power (P_{en}), the electronic-noise must be subtracted from the measured shot-noise level in order to obtain the true shot-noise power (P_{sn}),

$$P_{sn} = 10^{P'_{sn}/10} - 10^{P_{en}/10}. \tag{7.8}$$

The accuracy of our experiment is determined by the resolution/accuracy of the Tektronix spectrum analyzer. The specifications for the spectrum analyzer specified

a maximum 2-dB error when used in the vertical Log-10-dB/div. mode. This measurement uncertainty was experimentally verified using a broadband white spectrum as an test input signal. The test signal was a shot-noise spectrum generated with a thermal light source (a light bulb) focussed onto the Fujitsu-Comlinear photodetector. Two spectrum analyzer traces were taken as one set of data, with one of the traces being the white spectrum without any attenuation and the second trace being the spectrum attenuated by 6 dB. Different sets of data were taken over a period of time to determine the uncertainty. The relative noise power of the two traces (attenuated and unattenuated) was compared between each set of data, rather than their absolute powers, so as to eliminate possible drifts in the input signal.

Figure 7-8(i) and (ii) shows two sets of attenuated and unattenuated spectra showing the measurement uncertainty of the spectrum analyzer. The relative power differences for Fig. 7-8(i) and (ii) were 5.9 dB and 4.2 dB, respectively. The two sets of traces were taken 40 mins. apart with identical experimental conditions. This simple calibration measurement of the spectrum analyzer demonstrated the large measurement error of the analyzer. The inaccuracy of the analyzer was most likely caused by the old age of the equipment.

Since we expected the OPO spectral power to span over a 30-dB range, the 2-dB uncertainly in the spectrum analyzer would not significantly affect our experimental measurements. Moreover, some of the OPO operating parameters, such as detuning and excess pump noise power were only estimates, thus further contributing to our measurement uncertainty. Therefore, we were concerned mostly with the general shape and slope of the OPO spectra than with their absolute values.

7.4 Experimental Results

7.4.1 OPO Intensity Noise

Figure 7-9 shows the directly detected OPO outputs sum-intensity noise spectrum. The OPO intensity spectrum had similar spectral profile as the pump laser intensity

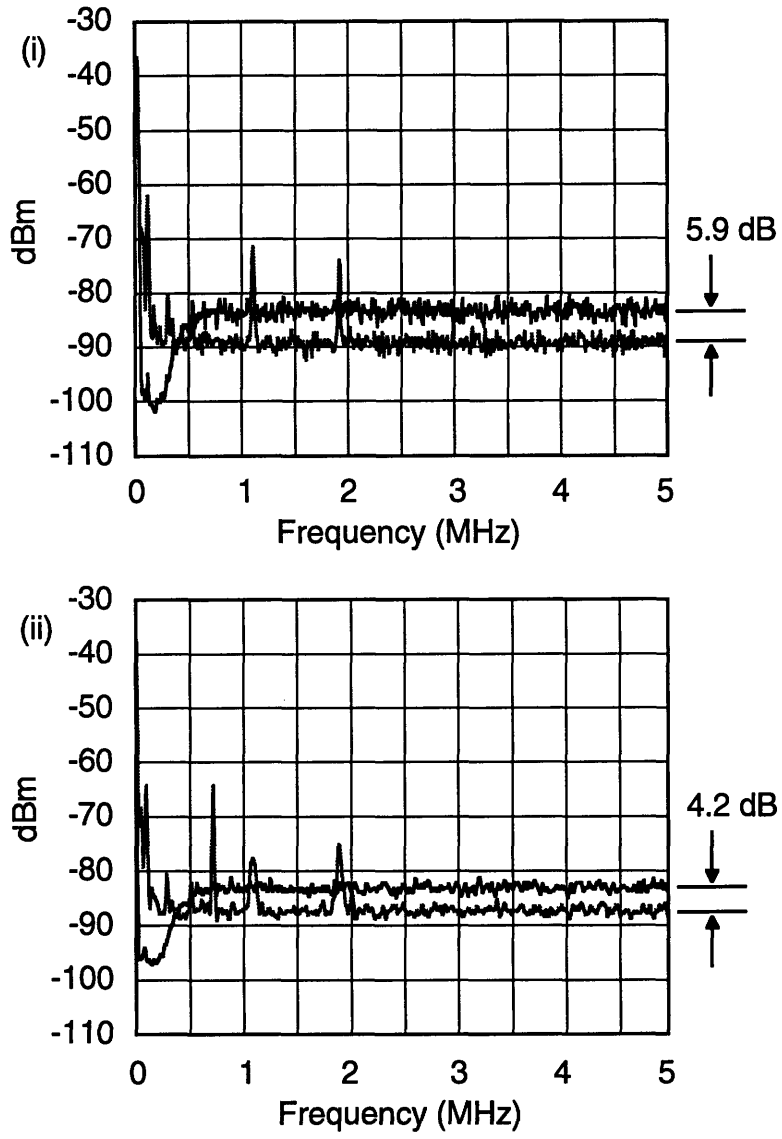

Figure 7-8: Spectrum analyzer traces of the test white-noise spectrum showing the measurement uncertainty. (i) and (ii) were taken 40 mins. apart and the relative power difference between the attenuated and unattenuated spectra should be about 6 dB (bandwidth, 30 kHz).

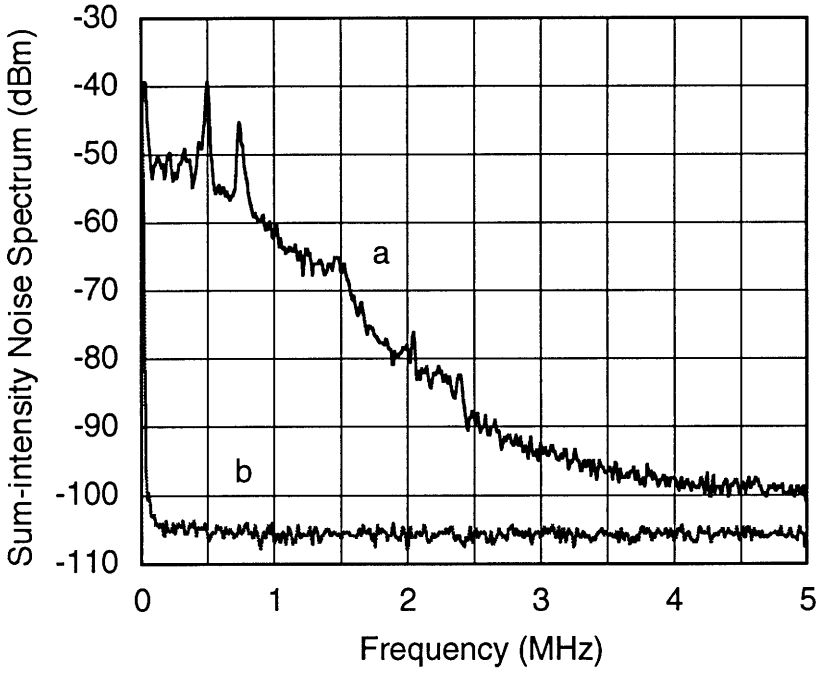

Figure 7-9: (a) OPO outputs sum-intensity noise spectrum showing the same spectral profile as the pump laser intensity noise. (b) Electronic noise level of photodetector (bandwidth, 30 kHz).

noise (Fig. 3-3b), as discussed in Section 7.2. The experimental and theoretical plots of the pump intensity to OPO sum-intensity noise transfer function are shown in Fig. 7-10. The calculated trace and the experimental trace agreed well even with the uncertainties in a few of the parameters, such as cavity detuning and excess pump noise power. However, only the slope and the general shape of the two traces should be compared, but not their absolute values. The absolute value of the experimental curve was only an estimate with error margin of ± 5 dBm. A summary of various measured experimental parameters used in preparing the theoretical plots is listed in Table 7.1 for reference.

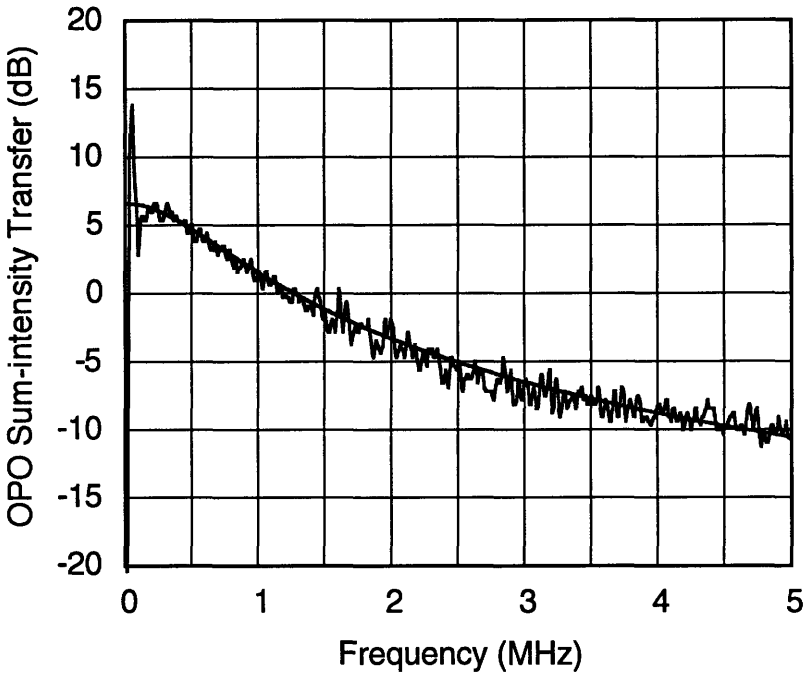

Figure 7-10: Experimental and theoretical plots of the pump intensity to OPO sum-intensity noise transfer function normalized to shot-noise level. ($\Delta/\kappa = 0.446$; bandwidth, 30 kHz.)

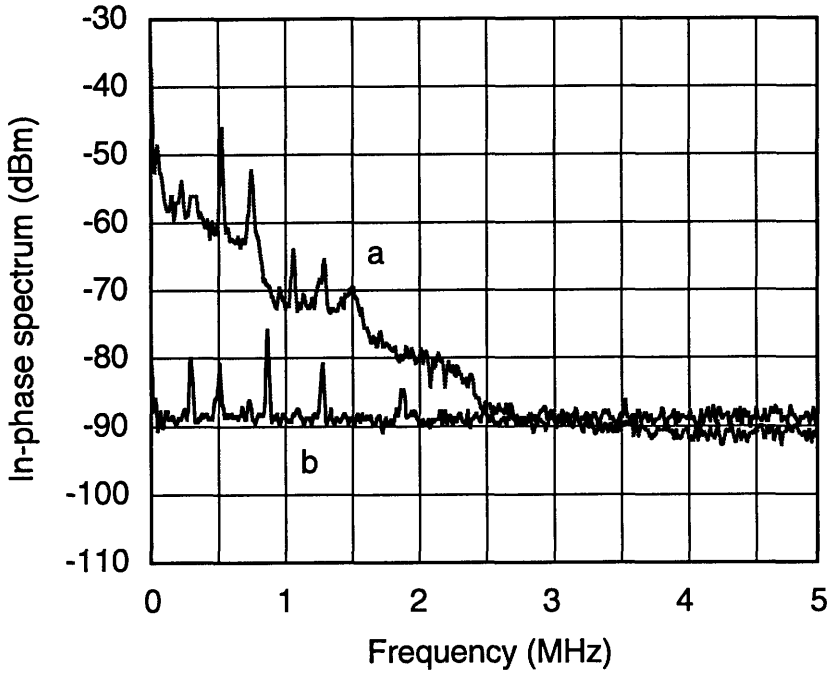

Figure 7-11: Experimental traces of (a) in-phase spectrum and the corresponding (b) shot-noise level (bandwidth, 30 kHz).

7.4.2 In-Phase and Quadrature-Phase Spectra

In-Phase

The in-phase spectrum was obtained from the demodulated signal as discussed in Section 7.3.4. Figure 7-11 shows the spectrum analyzer traces of the in-phase and the shot-noise spectra obtained directly from the analyzer during one particular run. As with the OPO sum-intensity noise spectrum, the in-phase spectrum had similar spectral profile as the pump laser intensity noise (Fig. 3-3b). The two large spikes at frequencies 500 kHz and 750 kHz on trace (a) were due to excess pump laser noise (Fig. (3-3)). The frequency peaks on trace (b) were originated from the noise of the digital synthesizer that had leaked through the detection system.

The drop of in-phase noise power at high frequencies (Fig. 7-11a) to below shot-noise level (Fig. 7-11b) was caused by the systematic measurement uncertainty in our detection system. The noise power difference at high frequencies between the

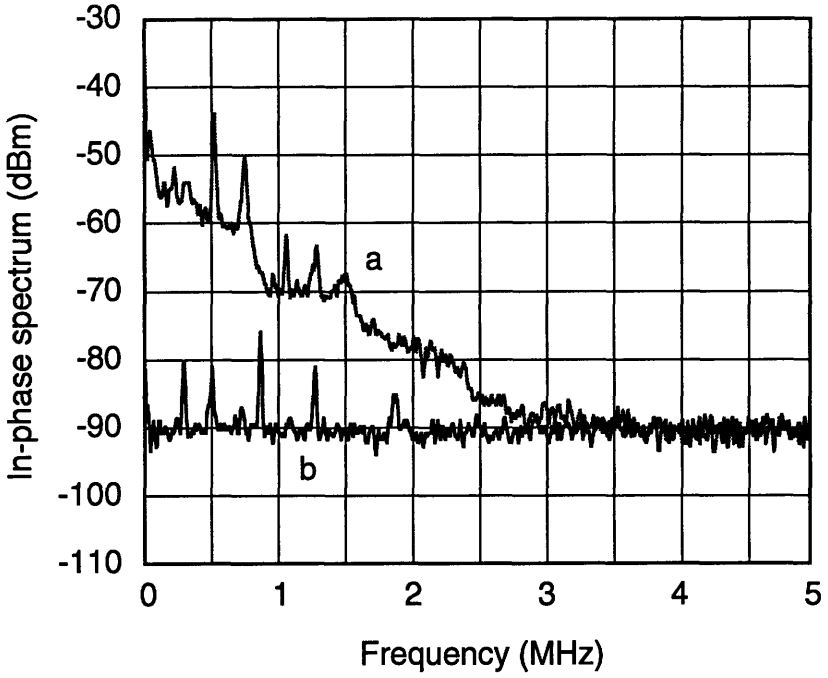

Figure 7-12: Experimental traces of (a) in-phase spectrum and the corresponding (b) shot-noise level after corrected for electronic noise level. (Vertical scale, 10 dB/div.; horizontal scale, 500 kHz/div.; bandwidth, 30 kHz.)

two traces was 2 dB, within the measurement uncertainty of the analyzer. We would like to point out that during other runs of the experiment the in-phase spectrum did not drop below the shot-noise level, unfortunately such traces were not recorded. Figure 7-12 shows the in-phase spectrum and the shot-noise level after corrected for the measurement uncertainty of the analyzer and electronic noise level (Eq. (7.8)).

From the measured 47-dB excess pump intensity noise (at 0.5 MHz; Sect. 7.2.4) and the pump intensity to in-phase transfer function (4 dB; Fig. 7-1b), we expected about 51 dB (47 dB + 4 dB) of excess intensity noise in the in-phase spectrum. The measured in-phase noise power in Fig. 7-12 was about 30 dB above shot noise. After using Eq. (7.6) for power attenuation correction ($\eta = 0.053 = -13$ dB), the in-phase noise power was about 43 dB (30 dB + 13 dB) above shot-noise level, in reasonable agreement with the expected value.

For comparison, the in-phase (a) and the sum-intensity (b) spectra are shown side-by-side in Figure 7-13. As expected from theory, the in-phase and the sum-intensity

spectra are almost identical.

Quadrature-Phase

The quadrature-phase spectrum (Fig. 7-14a) was obtained from the demodulated signal-idler beat-note signal when the averaged signal voltage was zero. However, since the in-phase and quadrature-phase spectra were mixed via cavity detuning, the quadrature-phase spectrum might be affected by the excess pump intensity noise (Eq. (7.2)).

Figure 7-14 shows the experimentally measured quadrature-phase spectrum (a) and the corresponding shot-noise level (b) after being corrected for electronic noise contribution. The two large peaks at frequencies 500 kHz and 750 kHz on trace (a) were due to excess pump laser noise (Fig. (3-3)) and the frequency peaks on trace (b) were electronic noise from the synthesizer. The theoretical plot of the quadrature-phase spectrum including the attenuation factor (Eq. (7.6)), η (0.8/15 = 0.053 = −13 dB), is shown in Fig. 7-14c for comparison. The corresponding quadrature-phase noise power spectral density S_ϕ in units of mrad^2/Hz obtained from Fig. 7-14 using

$$S_\phi = \frac{S_y(\omega)}{P_c B}$$

is shown in Fig. 7-15. Here, P_c (11 dBm) was the carrier power at 40 MHz at the input of the rf spectrum analyzer and B (30 kHz) was the detection bandwidth of the analyzer.

The measured quadrature-phase power was much larger than the calculated value. For example, the difference between the observed and calculated noise power at 1 MHz was about 15 dB. The disagreement was caused by the large amount of excess pump laser noise in our system. As we can see from Fig. 7-3, the pump laser excess phase noise spanned a range of ~50 dB between dc to 1 MHz. Similarly, the quadrature-phase power range (Fig. 7-15) was ~45 dB, in the same frequency range, suggesting a correlation between the pump phase noise and the quadrature-phase noise. Moreover, the heights of the frequency peaks at 750 kHz in Figs. 7-3 and 7-15 were both about

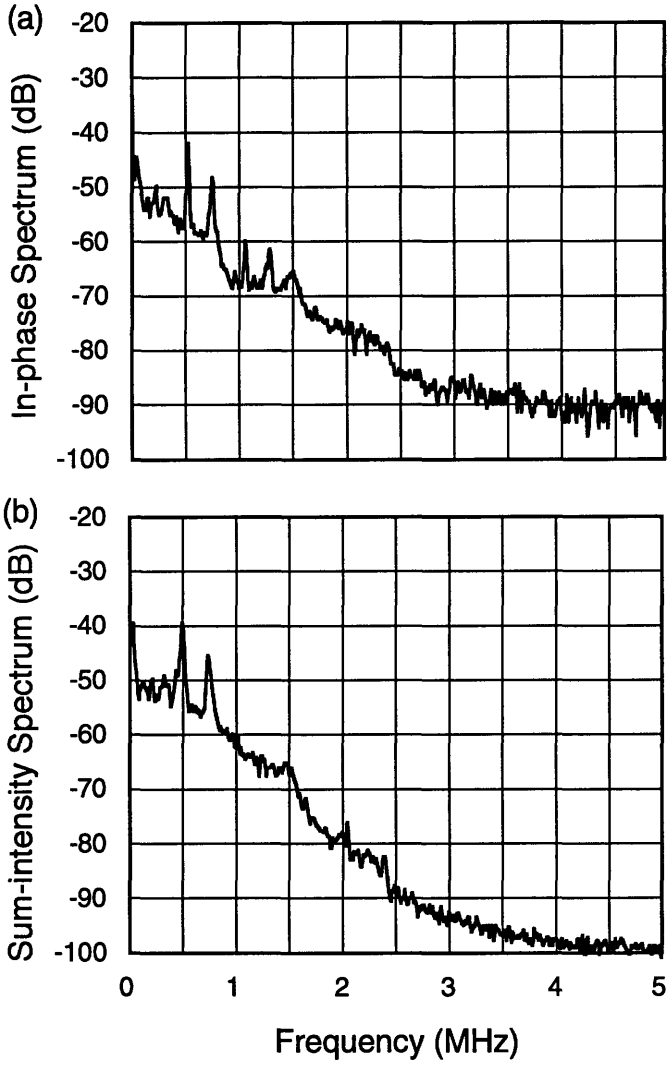

Figure 7-13: Experimental traces of (a) in-phase and (b) OPO intensity noise spectra (bandwidth, 30 kHz). The two traces have similar profiles in the 0.5–2.5 MHz frequency range as predicted by our theory (Chap 2).

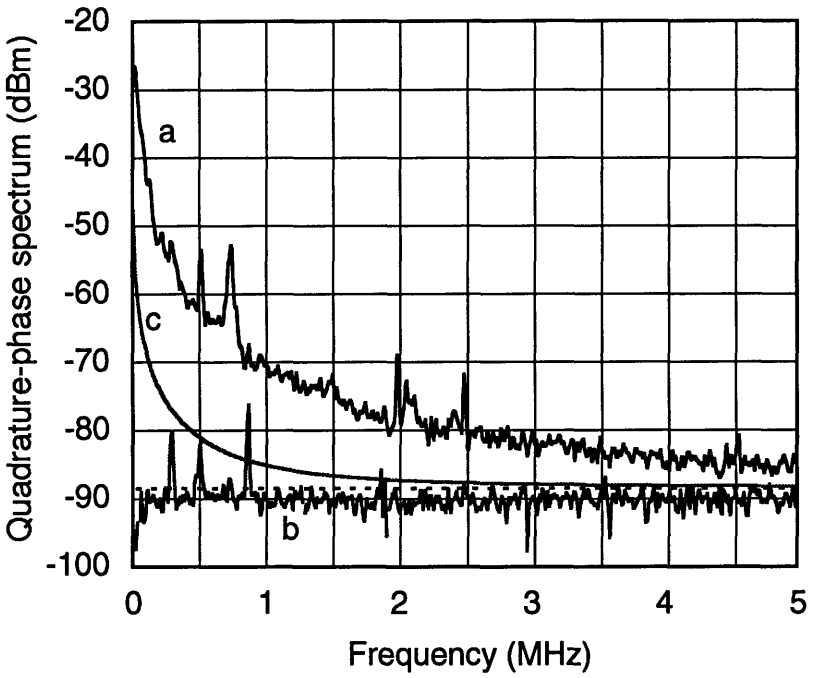

Figure 7-14: (a) Experimental trace of quadrature-phase noise spectrum (bandwidth, 30 kHz). (b) Trace of shot-noise level with local oscillator noise leaking through (frequency peaks). (c) Theoretical trace of quadrature-phase noise spectrum. Dotted-line is the shot-noise power calculated from the 0.65-mA photocurrent. The two experimental traces (a) and (b) have been corrected for electronic noise contribution.

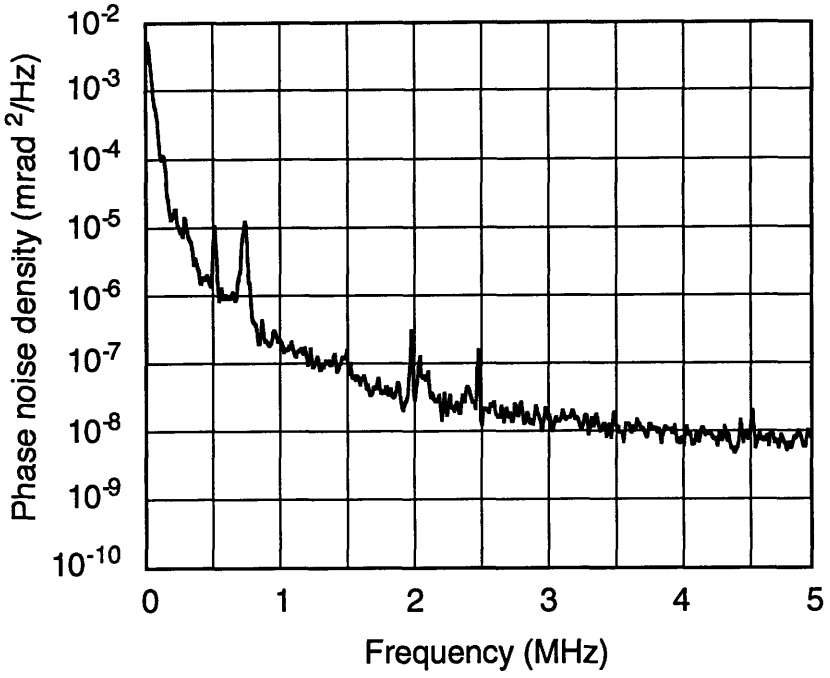

Figure 7-15: Trace of quadrature-phase noise power spectral density obtained from Fig. 7-14.

16 dB above the surrounding, further indicating that the pump phase noise was the dominating factor in the quadrature-phase spectrum.

Since our measurement was dominated by excess pump laser phase noise, we were only measuring the beat-note phase noise spectrum and not the phase diffusion noise of the OPO.

7.4.3 Noise Transfer Characteristics

Pump Intensity to Quadrature-Phase Transfers

The input pump field was amplitude modulated with two different signal sources: a synthesizer providing single frequency sine waves and a rf spectrum analyzer providing a broadband frequency sweep. We first modulated the pump field at two discreet frequencies, 400 kHz and 3 MHz. The observed in-phase and quadrature-phase spectra in Fig. 7-16 show intensity noise suppression in the quadrature-phase spectrum. Because of the nonzero cavity detuning, the two quadratures were coupled and the

intensity noise suppression in the quadrature-phase was not complete. The suppression of the frequency peaks in the quadrature-phase from the in-phase were 15 dB at 400 kHz and 22 dB at 3 MHz. However, a closer look at the quadrature-phase spectrum at 3 MHz revealed that the suppression was more than 22 dB. The residual peak at 3 MHz was caused by the pump field amplitude modulation (Eq. (7.4)), as discussed in Sect. 7.2.3. Figure 7-16d shows the 3 MHz residual peak on an expanded scale (200 kHz span) showing the pump-induced frequency upshifted amplitude-phase spectrum.

The pump field was also amplitude modulated with a broadband frequency sweep. Figure 7-17 shows the quadrature-phase spectrum (a) under broadband pump intensity modulation, and the resulting pump intensity to quadrature-phase transfer function (b). The transfer function, (Fig. 7-17(b)), consisted of two regions. The quadrature-phase noise power dominated at frequencies below the cross-over frequency of 2 MHz, and the pump-induced frequency-shifted-spectrum dominated at frequencies above the cross-over frequency. Note that the slope of the transfer function in Fig. 7-17(b) was relatively flat at high frequencies, as predicted by Eq (7.5).

Unlike the sum-intensity and the in-phase transfer functions, the theory again disagreed with the experimental result in the quadrature-phase measurement. Figure 7-18 shows traces of theoretical quadrature-phase intensity transfer functions calculated from equations (Eq. (2.47)) at different values of detunings. Eq. (2.47) is a first-order approximation where second order and higher orders terms are ignored. As seen from the two Figs. 7-17 and 7-18, the calculated slope was about 6 dB/octave compared to 10 dB/octave obtained experimentally. We tried to account for the discrepancy. The most likely explanation was the breakdown of our first-order theoretical calculation under such extreme strong pump-intensity modulation conditions. When the intensity fluctuation (μ_+) caused by the excess pump laser noise was not small, our first-order approximation was no longer valid. The same type of disagreement occurred when we measured the pump intensity to quadrature-phase transfer function, as to be discussed in the next section. Moreover, it was also likely that the excess pump laser phase noise (Fig. 7-3) played a significant role in the excess

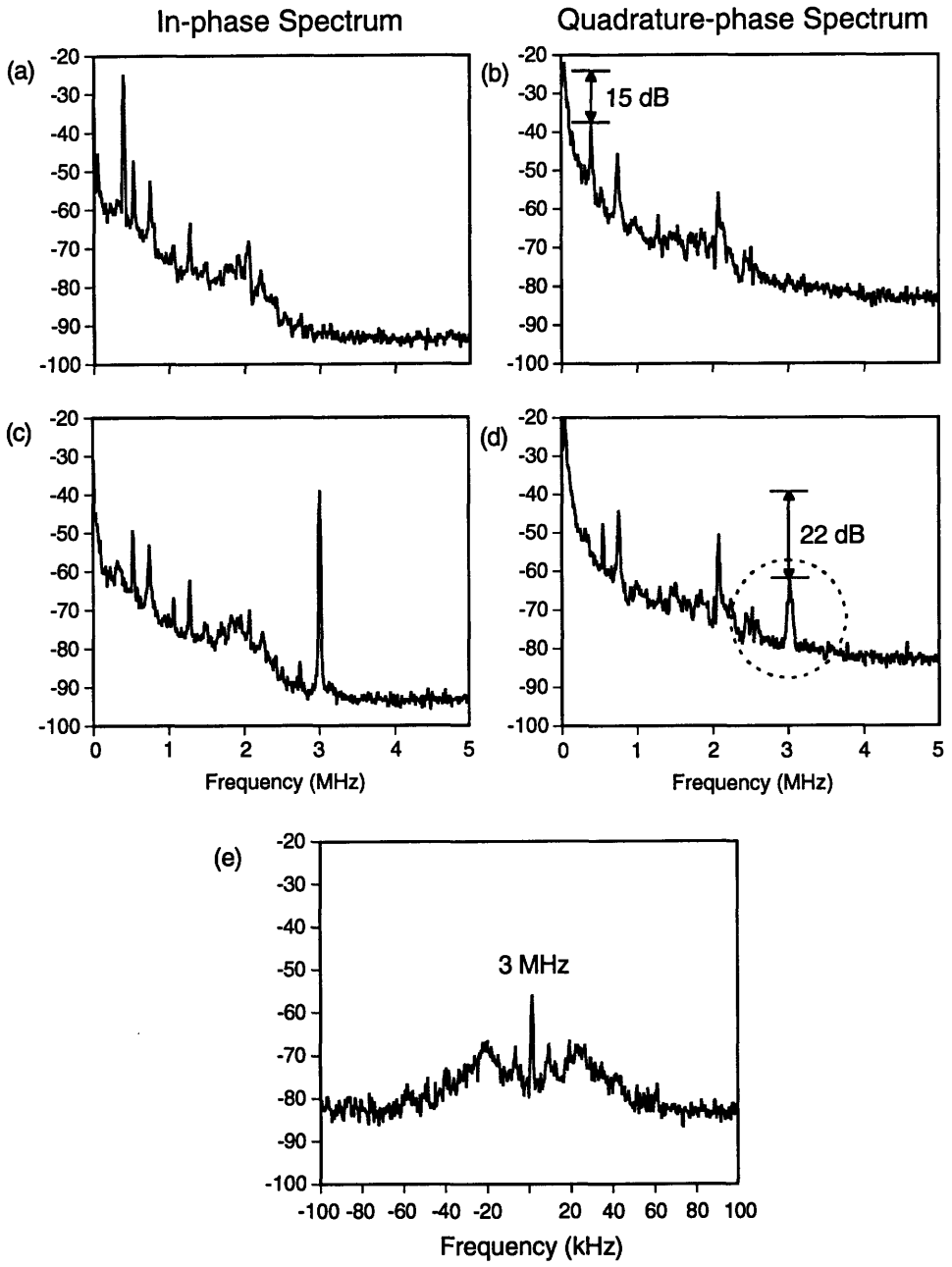

Figure 7-16: (a) In-phase spectrum showing the modulation signal at 400 kHz. (b) Quadrature-phase spectrum with residual modulation signal at 400 kHz. (c) In-phase spectrum with modulation signal at 3 MHz. (d) Quadrature-phase spectrum with residual signal at 3 MHz. (e) Expanded scale of (d) at 3 MHz showing the pump-induced frequency-shifted phase spectrum. Note the characteristic phase-locked loop noise within ± 20 kHz of the 3 MHz noise peak (See Fig. 6-6 of Chap 6). (Bandwidth, (a)–(d): 30 kHz, (e): 1 kHz.)

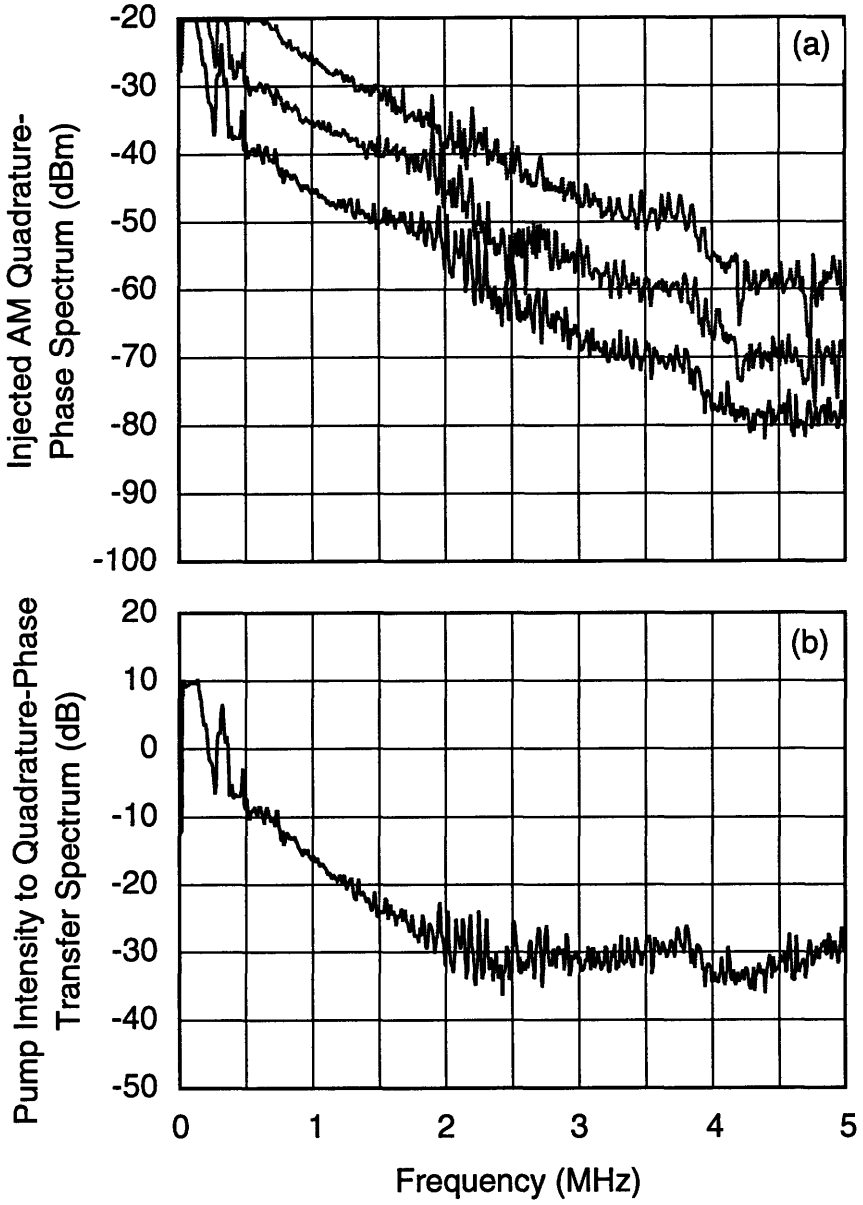

Figure 7-17: (a) Traces of quadrature-phase spectra with broadband amplitude modulated pump input field. The modulation power between each trace was increased by 10 dBm. (b) Trace of quadrature-phase transfer function spectrum obtained by dividing the spectra in (a) by the input pump spectrum (bandwidth, 30 kHz).

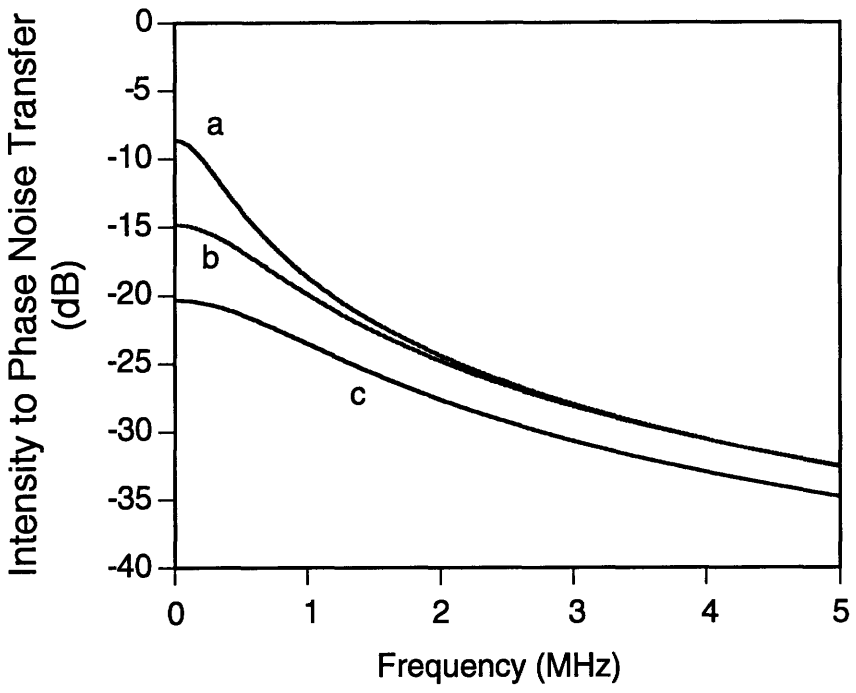

Figure 7-18: Theoretical plots of pump laser intensity noise to quadrature-phase noise transfer functions calculated using our linearized first-order equations at different normalized detunings (κ/Δ) : (a) 0.4; (b) 0.3; (c) 0.2.

quadrature-phase power.

As a confirmation to our quantum mechanical calculation, we performed a first order classical calculation for the same OPO with an amplitude modulated pump input field. The classical and quantum mechanical calculations predicted the same intensity noise to quadrature-phase transfer characteristics, as expected. The disagreement between our calculation and experimental result suggests that a better theoretical model is needed. For example, a numerical simulations using the complete first-order nonlinear differential equations may be required to predict a correct transfer spectrum.

Pump Intensity to In-Phase Transfers

Similarly, the pump intensity to in-phase transfer function spectrum was obtained by modulating the input pump laser. Figure 7-19 shows the resultant pump intensity to

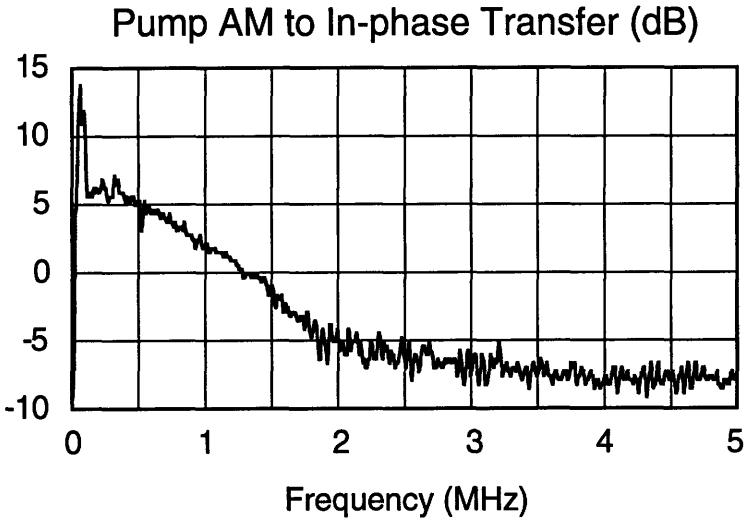

Figure 7-19: Experimental trace pump intensity to in-phase transfer function spectrum.

in-phase transfer function. Again, the in-phase and sum-intensity characteristics are identical, as expected.

7.5 Summary

We have, for the first time to our knowledge, experimentally measured the in-phase and quadrature-phase noise spectra of the signal-idler beat note of an OPO. The pump amplitude modulation to quadrature transfers were also studied in the experiment.

As expected from our calculation, the OPO sum-intensity and in-phase characteristics were very similar. Their spectra and intensity noise transfer functions were found to be almost identical with our theoretical calculations. In the presence of large excess pump intensity noise, the sum-intensity and in-phase spectral profiles were dictated by the input pump laser intensity noise characteristics.

For the quadrature-phase component, the observed spectrum had a significant amount of noise power at low frequencies and a noise level that approached the shot-noise level at high frequencies. However, the observed quadrature-phase spectral power was much larger than the calculated value at all frequencies. The disagreement

between the observed and the calculated spectra was caused by the large amount of excess pump noise power. In any future experiment, it will be necessary to suppress the pump laser noise before we can accurately measure the phase diffusion noise of the OPO.

In our pump intensity to quadrature-phase noise transfer study, we found that the pump intensity noise was partially suppressed in the quadrature phase. However the suppression was not complete because of the nonzero cavity detuning and the observed intensity transfer function also had a steeper slope than the calculated function.

A possible explanation for the discrepancy between the observed and calculated transfer functions was the breakdown of our first-order approximation in the presence of large excess pump noise or when the pump intensity was strongly modulated. Our assumption was no longer valid when the sum-intensity fluctuation μ_+ was not small and higher-order term contributions might by significant. Our theory is a good approximation when the pump laser excess noise is small compared with the spectral power that we are trying to measured. However, when the pump laser excess noise is large a more complicated and complete calculation is required to gain further understanding of the OPO phase noise characteristics.

Chapter 8

Dual-Cavity DRO

8.1 Introduction

In previous chapters, we have discussed the designs and experiments with our doubly resonant optical parametric oscillators (DRO). We have demonstrated excellent stability and tunability in our DROs. With four tuning elements, a procedure was devised to systematically tune the output frequencies of the DROs to any frequency within the phase-matching bandwidth (~6 THz) that was limited by the crystal's physical size. With these characteristics, the DRO beat-note phase noise was for the first time experimentally observed since its prediction of more than 20 years ago.

The usual design of a DRO is of a single-cavity design, in which both the signal and idler fields are resonated in a common cavity. The drawback of a single-cavity design is that it is over constrained. The doubly resonance condition can only be maintained over a cavity-length change of ~1 nm, or about 10 MHz in our DRO cavities. To achieve a wider continuous frequency tuning range, we employed crystal temperature tuning. However, temperature tuning was slow and it can be difficult to maintain precise frequency control due to its long response time. A new dual-cavity DRO (DCDRO) design was investigated for its frequency tunability. We found that this new DRO design has a much broader frequency tuning range than the usual DRO design and the increase in threshold was minimal.

We have observed in our dual-cavity DRO a minimum threshold of 66 mW and a

continuous PZT-tuning range of ~1 GHz. The 1 GHz tuning range was much wider than the PZT-tuning range of a single-cavity DRO (SCDRO) of a few MHz, but it was much smaller than our expectation of a few tens of GHz. A theoretical model was developed to explain the limited tuning range and to predict the tuning behavior of our DCDRO. Factors considered in our model are pump resonance, finite polarization isolation of the polarizer, and polarization axis misalignment between the crystal and the polarizer. Our plane-wave calculation agrees with the experimentally observed tuning range to within 10%.

In this chapter, we discuss our experiments with the DCDRO and the theoretical analysis of its tuning behavior. The DCDRO and experimental setup are first presented, followed by experimental observations and the theoretical calculation. Finally, we discuss possible future experiments with the DCDRO, how it can be used in the quantum noise experiment, and its potential applications as a widely tunable optical frequency source.

8.2 Background

In this section, we discuss how the limitation of a single-cavity design can be removed by the addition of a second cavity, that is a dual-cavity DRO, and the advantages we gain from such a design. We shall label a DRO that has two independent optical cavities for the two output fields a dual-cavity DRO (DCDRO). Whereas, the usual DRO design with a single cavity for both outputs is labeled as a single-cavity DRO (SCDRO).

The first DCDRO was reported by Colville *et al.* at the University of St. Andrews, Scotland [10]. They have demonstrated a type-II phase-matched lithium triborate (LBO) DCDRO with non-degenerate operation at signal and idler frequencies of 502 nm and 1.32 μm. Their DCDRO was continuously tunable over a range of 0.4 GHz with PZT-tuning.

Inspired by their results, we have converted our 2-element type-II phase-matched KTP SCDRO into a DCDRO design by adding a polarizing beam splitter (PBS)

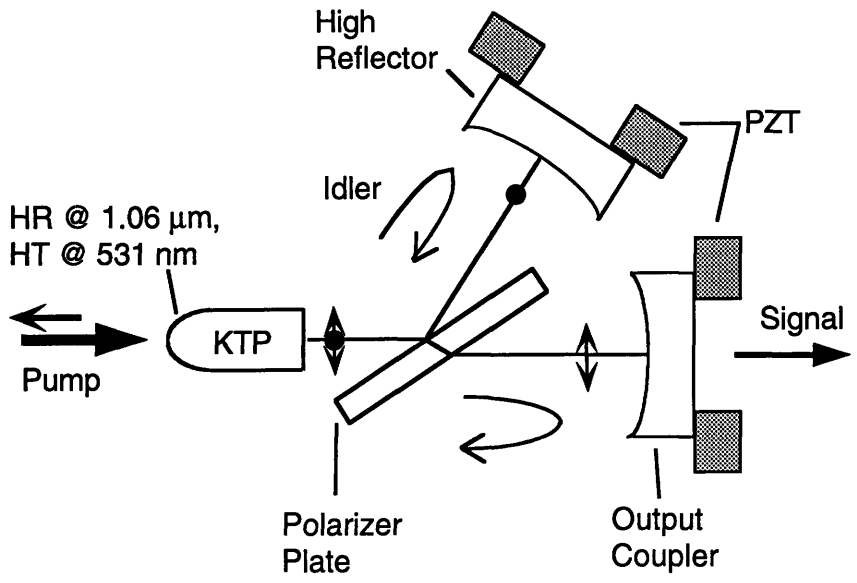

Figure 8-1: Dual-cavity DRO cavity design. The polarizer plate is attached to a mini-rotation stage for minimum threshold adjustment.

inside the optical cavity and by adding a second PZT-mounted mirror, as shown in Fig. 8-1.

8.2.1 Quantum Noise Experiment

In our quantum noise experiment, the measurement accuracy was limited by the excess noise of our pump laser. For more accurate measurements, the pump laser noise contribution need to be suppressed. There are three ways to reduce, or even eliminate, the pump laser noise contributions from the beat-note quadrature spectrum. The amount of pump noise to beat-note transfer is a function of three factors: excess pump noise, cavity detuning, and total-loss mismatch, as discussed in Chapter 2. The first and the most obvious solution is to reduce the pump noise. For example, the use of a diode-pumped YAG and its second-harmonic, coupled with a narrowband optical filter cavity, can significantly improve the pump noise characteristic.

The second approach is to operate the DRO at zero cavity detuning. At zero cavity detuning, the in-phase and the quadrature-phase of the beat-note signal are

decoupled. Therefore, the pump laser amplitude noise and phase noise are contained within their respective quadratures, thus eliminating the intensity-noise contribution from the quadrature-phase spectrum and the phase-noise contribution from the in-phase spectrum. Since the pump intensity to OPO beat-note phase noise transfer is significant (Chap. 2), zero detuning reduces the pump-induced phase noise. This, however, is an imperfect solution because the issue of the pump-laser phase noise has not been addressed, as the quadrature-phase spectrum still contains the pump-laser phase noise contribution. Furthermore, maintaining stable operations with minimum DRO intensity fluctuations at the peak of a resonance mode can be technically challenging.

Since the pump noise contribution is related to the difference of the two cavities losses(Eq. (2.41)), the third and the best solution is to match the signal and the idler total internal losses so that both the pump laser amplitude noise and phase noise contributions are eliminated from the quadrature spectra. One way to better match the two internal losses is to insert a polarization-sensitive lossy element inside the DRO optical cavity to introduce extra loss for one of the polarizations. However, there is not a perfect polarization-sensitive element that would only affect one polarization. Moreover, the usual design of a DRO, such as the 2 and 3-element designs that we discussed in Chapter 5 consists of one single optical cavity for both the signal and idler fields. Therefore, the disadvantage is that there is no independent adjustment for the two field losses.

For independent loss controls of the two cavities, one can separate the signal and idler cavities so that they become independent of each other. With the two fields resonating separately in their own respective cavity, a Brewster plate can be add to one of the cavities to introduce losses without affecting the other. The total loss of the cavity with the Brewster place can be varied continuously by adjusting the angle of the plate. By using a dual-cavity system, a perfect match between the two cavity losses becomes feasible.

8.2.2 Tunable Optical Frequency Source

The SCDRO design is over constrained because both the signal and idler cavity lengths are changed by the same amount and in the same direction. There are no independent adjustments for the two cavities. The doubly resonant condition can only be maintained over a ~0.5 nm range in cavity-length change which corresponds to a few MHz in the output frequencies. The continuous tuning of a SCDRO is therefore significantly smaller than one free spectral range of the OPO cavity. In our DRO frequency tuning experiments, as described in Chapter 5, a 500 MHz continuous tuning range was obtained for our SCDROs by using temperature tuning. However, this temperature tuning was slow (10's of seconds) and was limited by the over-constraint of the doubly resonant condition and not by the ~100 GHz phase-matching bandwidth.

A DCDRO removes the constraint and extends the continuous tuning range that is expected to be eventually limited by the phase-matching bandwidth of the crystal. With the addition of a second cavity, we gain independent signal and idler cavity-length controls. This additional degree of freedom removes the constraint of the doubly resonance condition so that DRO oscillation can be maintained over a much wider frequency range.

8.2.3 PZT-Tuning Characteristics of a DCDRO

The DCDRO is expected to have a much wider PZT-tuning range than a SCDRO. Its tuning behavior can be understood by considering the following argument. Consider that at certain signal and idler cavity-length positions, the double resonance condition is satisfied and the output power is detected. The DCDRO can be tuned by decreasing the signal-cavity length (Fig. 8-2), which causes the signal frequency to increase. By the sum-frequency constraint, the double resonance is maintained only if the idler frequency is decreased, which can be accomplished by increasing the idler-cavity length.

This PZT-tuning coefficient can be estimated using Eq. (5.6),

$$\Delta f_d \approx \frac{-f_p}{\kappa_1 + \kappa_2}\left(\kappa_2 \frac{\delta l_1}{L_1} - \kappa_1 \frac{\delta l_2}{L_2}\right). \tag{8.1}$$

Because of the independent cavity-length controls capability, the signal and the idler cavity lengths can be varied in opposite directions so that

$$\delta l_1 = -\delta l_2 = \delta l.$$

If we further assume that the two cavity optical paths are approximately equal, $L_1 \approx L_2$, Eq. (8.1) is then reduced to

$$\frac{\Delta f_d}{\mathcal{F}} = -\frac{\Delta l}{\lambda/2}, \tag{8.2}$$

where $\mathcal{F}$ is the free spectral range and λ is the subharmonic wavelength, assuming near degeneracy. The frequency tuning range can therefore be estimated from cavity-length changes. As an numerical example, for a DCDRO cavity with a free spectral range $\mathcal{F} = 3.7$ GHz, the PZT-tuning coefficient (Δf_d/nm) is 7 MHz/nm.

With one of the cavities scanning and the other cavity length being fixed, the cavity length separation between adjacent modes for a DCDRO is different from that of the SCDRO. The cavity-length separation can be estimated by considering the sum-frequency constraint,

$$\frac{1}{\lambda_1} + \frac{1}{\lambda_2} = \frac{1}{\lambda_1'} + \frac{1}{\lambda_2'}, \tag{8.3}$$

where $\lambda_{1,2}$ and $\lambda'_{1,2}$ are the signal (subscript 1) and the idler (subscript 2) wavelengths of two adjacent modes. The λ_i and the cavity length L_i are related by,

$$\frac{1}{\lambda_i} = \frac{m_i}{2L_i}, \qquad \text{and} \qquad \frac{1}{\lambda_i'} = \frac{m_i + \Delta m_i}{2L_i'}, \tag{8.4}$$

where m_i is the wave number (number of half wavelengths) and Δm_i is the change in wave number between adjacent modes. The sum-frequency constraint (Eq. (8.3))

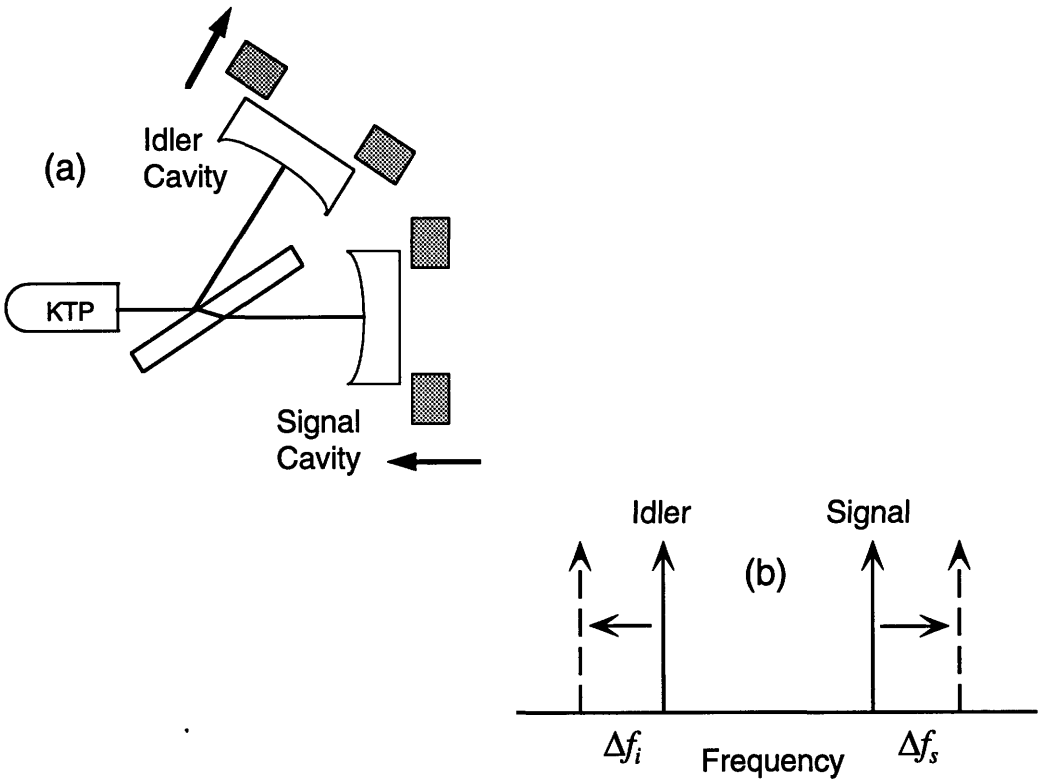

Figure 8-2: Diagrams showing the relationship between DCDRO cavity-length change and the output frequencies. (a) The signal cavity-length decreases while the idler cavity-length increases, with the corresponding (b) signal frequency increases and the idler frequency decreases as a result of the cavity length change.

becomes,

$$\frac{1}{\lambda_1/2}\frac{\delta l_1}{L_1} + \frac{1}{\lambda_2/2}\frac{\delta l_2}{L_2} = \frac{\Delta m_1}{L_1} + \frac{\Delta m_2}{L_2}, \tag{8.5}$$

with the use of Eq. (8.4). In the case of the DCDRO, with one cavity length being fixed ($\delta l_2 = 0$) and $\Delta m_1 = -\Delta m_2 = 1$, Eq. (8.5) reduces to,

$$\delta l_1 = \frac{\lambda_1}{2}\left(1 - \frac{L_1}{L_2}\right). \tag{8.6}$$

For $L_1 = 41.4$ mm, $L_2 = 40.6$ mm, $\lambda_1 \approx 1062$ nm, the cavity-length spacing for a resonance mode jump is $\delta l_1 \approx 10.2$ nm. The corresponding SCDRO mode spacing, with $\delta l_1 = \delta l_2 = \delta l$, is $\delta l = 5.2$ nm.

8.3 Experimental Setup

8.3.1 Detection System

The DCDRO was pumped by the same krypton ion laser used in our frequency tuning experiments. The output intensity servo for the DCDRO was also the same as in our frequency tuning experiments, as described in Chapter 3 and 5. Figure 8-3 shows a schematic of the setup of the DCDRO frequency tuning experiment.

By the design of the DCDRO, there was only one main output from the 0.5% output coupler, namely, the horizontally polarized signal. The output from the high reflector of the idler cavity was usually very weak and was not utilized. It was possible to monitor the internal fields by detecting the signal field that was reflected off the back surface of the polarizer plate and the idler field that was transmitted through the plate. It turned out that by monitoring this auxiliary output, we were able to measure some of the characteristics of the DCDRO.

KTP Crystal

The DCDRO was fabricated with a 3 mm × 3 mm × 9.5 mm KTP crystal, a polarizer plate, and two 25-mm-radius mirrors, as sketched in Fig. 8-1. The type-II phase-

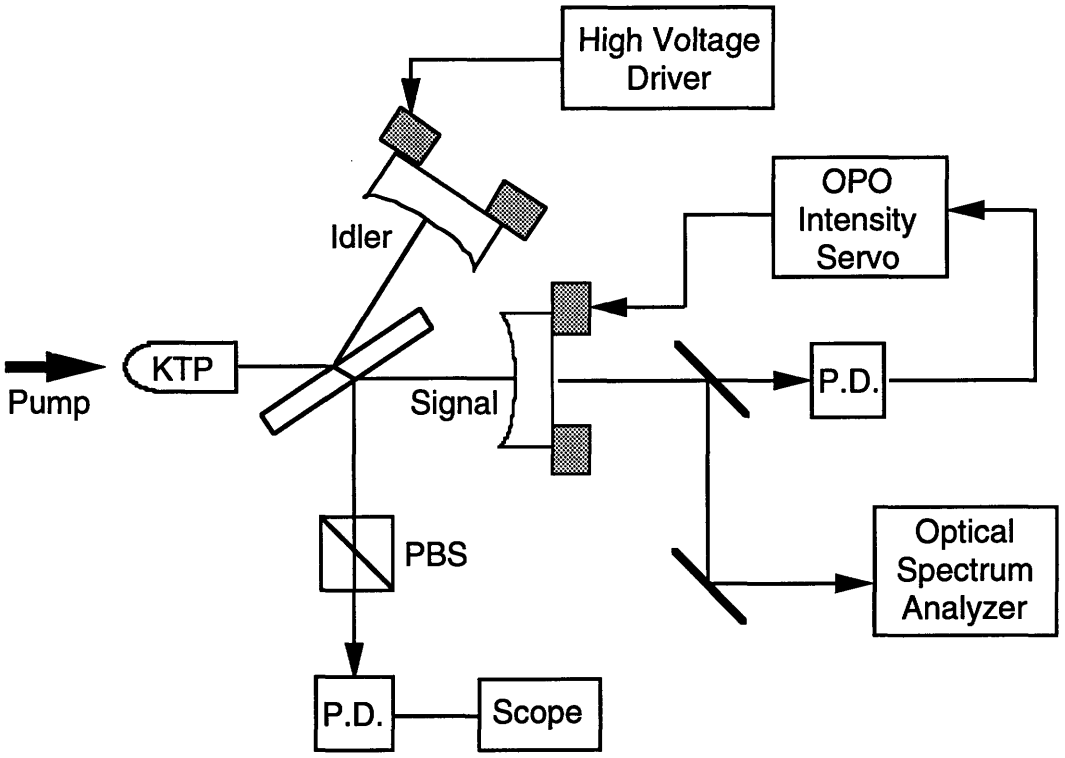

Figure 8-3: Schematic diagram of the setup of the DCDRO experiment. The transmitted idler and reflected signal fields from the polarizer plate can be selectively measured with the use of a polarizing beam splitter. (PBS, polarizing beam splitter; P.D., photodetector)

matched KTP crystal was the same crystal used in the monolithic cavity DRO, but refurbished with different specifications. The type-II geometry permitted the orthogonally polarized outputs to be separated with a PBS, even at frequency degeneracy. The angle cut for this crystal was $\theta = 90°$ and $\phi = 25.3°$ for operations near frequency degeneracy. One end of the crystal was polished flat and antireflection coated for for both 1.06 μm and 531 nm to minimize loss and reflectivity. The other end, which served as the pump input port, had a 40-mm radius of curvature and a coating of maximum reflection at 1.06 μm and ~5% reflection at 531 nm.

Polarizer-Plate Assembly

The polarizer was a 1-mm-thick dielectrically coated fused silica plate that was designed to operate near Brewster angle. The front surface was coated for maximum reflection for the *s*-ray, and the back surface was not AR coated. As a result, most of the *s*-polarization light was reflected off the front surface of the plate and it had a low loss. The *p*-polarization had a higher loss as it was transmitted through the plate and multiple reflections occurred. It was critical for the incident angle on the plate to be exact so that the transmitted and reflected rays have minimum losses.

A special bracket and rotation stage assembly was used to adjust the incident angle for maximum efficiency. An open rectangular aluminum mounting bracket was fabricated to hold the plate. The bracket was 2-mm thick with two nylon screws on the side to fasten the plate. The tension of the two screws was only hand-tightened so that the plate would not be stressed by over-tightening. The bracket was set perpendicularly on a Newport's mini-rotation stage for angular adjustment. With this mounting assembly, we were able to adjust the angular tilting of the polarizing plate in both vertical and horizontal directions. The angular adjustment of the plate was essential for minimizing the DCDRO's threshold.

Mirrors

The *p*-polarized (horizontal) signal was transmitted through the polarizing plate (PP) and resonated in the signal cavity formed by the crystal and the output coupler. The

s-polarized (vertical) idler was reflected off the front surface of PP and resonated in the idler cavity formed by the crystal and the high reflector (HR). Since the threshold was related to the product of the signal and the idler total losses, it could be minimized by reducing the loss of just one cavity. Given that the PP loss was lower for the s-ray, we minimized the idler cavity loss by using a high reflector to form the idler cavity.

We designed our DCDRO with a single-pass pump configuration to reduce pump resonance. The signal cavity output coupler (p-ray) had a 0.5% transmission at 1.06 μm and a measured 2% reflection at 531 nm. The idler cavity mirror was high reflection coated for 1.06 μm and a measured 15% reflection at 531 nm. Both mirrors were located $\sim$24 mm from the flat side of the crystal. The DCDRO cavity had a nominal free spectral range of $\sim$3.7 GHz.

Our primarily interest in the DCDRO was its tuning characteristics by the use of two independent cavity-length controls. We, therefore, did not implement temperature and E-field tuning in the DCDRO, nor did we try to minimize the output intensity noise.

Cavity Construction

The components of the DCDRO were attached to a thick aluminum base for better mechanical stability. The two mirrors were attached to PZT stacks, each with a separate high-voltage driver, for independent cavity-length controls. Each PZT-mounted mirror was attached to a Newport flexure mirror mount, which in turn was attached to the aluminum base block. We incorporated flexure mounts in our design because it was supposed to be mechanically more stable than the usual spring-loaded mirror mount, and it provided the necessary though limited angular adjustment for the cavity alignment.

Component	Horizontal Polarization [%]	Vertical Polarization [%]
Crystal (round-trip)	0.7	0.57
High reflector	0.1	0.1
Output coupler (0.5%)	0.7	0.7
Output coupler (0.75%)	1.0	1.0

Table 8.1: Measured crystal and mirrors losses at 1.06 μm for horizontal and vertical polarizations.

Polarizing plate (single trip)	Horizontal (Signal) Polarization [%]	Vertical (Idler) Polarization [%]
Reflectivity	0.07	99.97
Transmissivity	99.47	0.029

Table 8.2: Measured reflectivity and transmissivity at 1.06 μm of the polarizing plate.

8.4 Experimental Observations

8.4.1 DCDRO Cavity Loss Measurements

A diode-pumped YAG laser at 1.064 μm was coupled into the DCDRO cavity through the 0.5% output coupler to assist the DCDRO alignment and to estimate cavity losses (Fig. C-1). Tables 8.1–8.3 show various measured component losses at 1.064 μm and 531 nm at two polarizations. The signal and idler round-trip losses for the DCDRO were 2.46% and 0.73%, respectively. The corresponding losses for a 2-element SCDRO using the same KTP crystal and a 0.75% output coupler were 1.7% and 1.57% (Table 8.4).

The values of these losses were deduced from cold cavity finesse measurements of various combinations of the optical elements. In particular, careful consideration was required in measuring the reflectivity of the polarizer plate for the s-ray, as the reflectivity depended critically on the incident angle. Our approach for this measurement was to first optimize the threshold of the DCDRO when it was operating, so that the polarizer plate and the high reflector were properly aligned at the op-

Component	Reflectivity [%]	Transmissivity [%]
Crystal (curved-end)	5	92
High reflector	15	-
Output coupler	2	-
Polarizer	33.7	55.4

Table 8.3: Measured reflectivity and transmissivity for the vertically polarized 531 nm pump beam for DCDRO components.

Cavity	Signal [%]	Idler [%]	Loss Product [10^{-4}] (Signal $\times$ Idler)
DCDRO	2.46	0.73	1.8
SCDRO	1.7	1.57	2.67

Table 8.4: Summary of DCDRO and SCDRO measured total power losses at 1.06 μm.

timized angle[1]. We then blocked the pump beam, replaced the KTP crystal with a mirror with known losses, and coupled the vertically polarized (s-ray) YAG laser beam through the known mirror port into the cavity formed by the known mirror, the polarizer plate and the high reflector (Fig. 8-4). The mirror we used as our known mirror was a 0.75% transmission output coupler. The alignment was done by adjusting the mirror and the YAG steering mirrors, but not the polarizer plate and the high reflector. The finesse of this 3-element cavity was measured with a photodetector placed behind the high reflector to detect the leakage power. Once the finesse was obtained, the polarizer plate reflectivity was deduced from the known mirror and the high reflector losses.

8.4.2 Threshold

The minimum threshold we have obtained for our DCDRO was 66 mW. For diagnostic purposes, we have constructed a 2-element SCDRO with the same KTP crystal for

[1]A procedure for aligning the DCDRO for minimum threshold was established and it is presented in Appendix C.

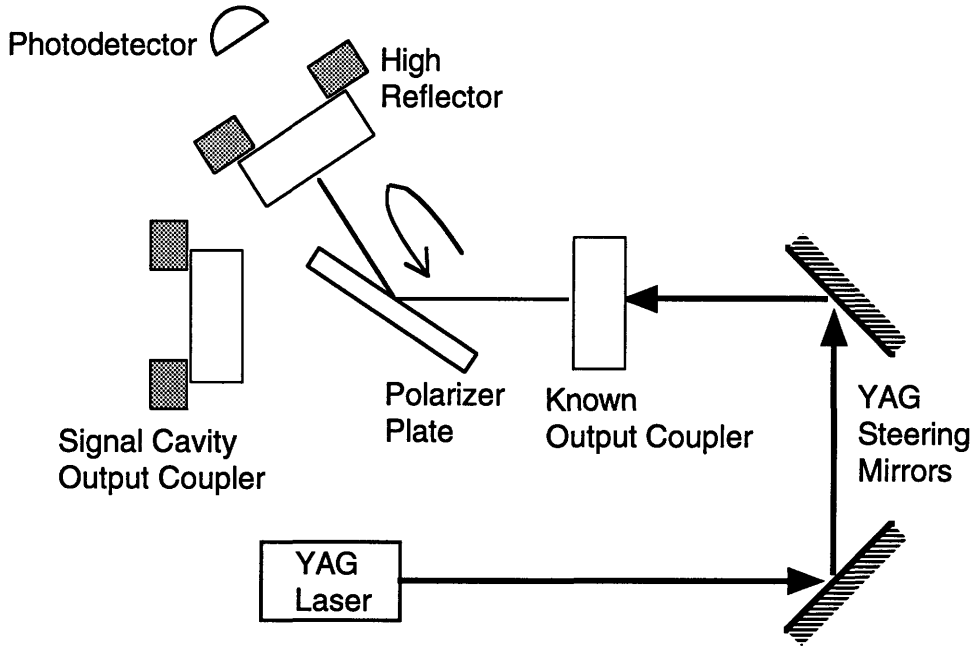

Figure 8-4: Schematic diagram of the polarizer plate s-ray reflectivity measurement. In place of the KTP crystal, a mirror with known losses was used to form a 3-element optical cavity. The signal-cavity output coupler did not play any role in this measurement

threshold comparison. The 2-element SCDRO used a 0.75% output coupler and a double-pass pump configuration. The measured threshold for this SCDRO was 40 mW.

The DCDRO had a higher threshold even though its loss product was smaller than that of the SCDRO, as listed in Table 8.4. One possible explanation for the higher threshold was the use of a single-pass pump configuration in the DCDRO, as compared with the double-pass configuration in the SCDRO. As discussed in Section 4.5.1, a double-pass configuration would increase the effective crystal length and lower the threshold by a factor between 2 to 4. The lower threshold might be an indirect evidence for the benefits of a double-pass configuration. The threshold reduction factor between the two DROs was estimated to be about 2.5, using the above measured threshold and loss values.

With about 65% increase in the threshold, we extended the PZT-tuning range from ~0.5 nm in a SCDRO to ~125 nm in a DCDRO when pumped at two times threshold, more than 250 fold. The slight increase in threshold was insignificant compare to the gain in extending the PZT-tuning range.

8.4.3 PZT-Length Scan

There were two different modes of PZT-scanning in our DCDRO operations: independent cavity scanning and simultaneous scanning. In the independent-scanning mode of operation, only one of the cavity lengths was scanned while the other cavity was kept fixed. In the simultaneous-scanning mode, both cavity lengths were scanned by two function generators simultaneously. The scan rate of the two function generators was identical and the relative phase-angle offset between them was adjustable. For our experiment, we set their phase difference to π so that they scanned in opposite directions.

Independent Cavity Scan

In the independent-scanning mode, the experimental observations were identical for signal-cavity scanning and for idler-cavity scanning. The following discussion applies to both independent signal-cavity scanning and idler-cavity scanning. Figure 8-5 and 8-6 show the observed output power for independent signal-cavity scanning and independent idler-cavity scanning, respectively.

The PZT scanning characteristics of our DCDRO were similar to those of the SCDROs, except that the adjacent mode separation was larger (Fig. 8-7b). As we scanned the cavity length, a number of 15–30 modes were excited and IR outputs were observed. Like the SCDRO, the doubly-resonant condition could only be maintained over a PZT scanning distance of ~0.5 nm in this mode of operation. Unlike the SCDRO, the resonance peaks occurred at a wider separation of ~10–20 nm, compared with ~5 nm in the SCDRO (Fig. 8-7a). As discussed in Section 8.2.3, the wider separation was the result of scanning of one of the cavity lengths and the resonance mode spacing depended on the mismatch of the two optical path lengths.

If the bias of the non-scanning cavity was slowly varied, the whole cluster would appear to move across the screen (Fig. 8-8). The moving of the modes, and hence the output frequency, was necessary to compensate for the change in cavity length in the non-scanning cavity. The output power would increase as the mode moved from one end of the profile toward the center. The direction of the movement depended on the direction the bias was applied. The frequency tuning range of a mode was estimated from the distance that mode traveled. The maximum PZT tuning range observed when pumped at two times threshold was ~125 nm, which corresponded to ~1 GHz.

Simultaneous Cavity Scan

For the simultaneous-scanning mode, the two cavities were scanned at the same frequency but in opposite directions. In this mode of operation, the doubly-resonant condition could be maintained over a much wider range. Figure 8-9 shows the DCDRO output power that was continuously scanned over a PZT-scanning range of

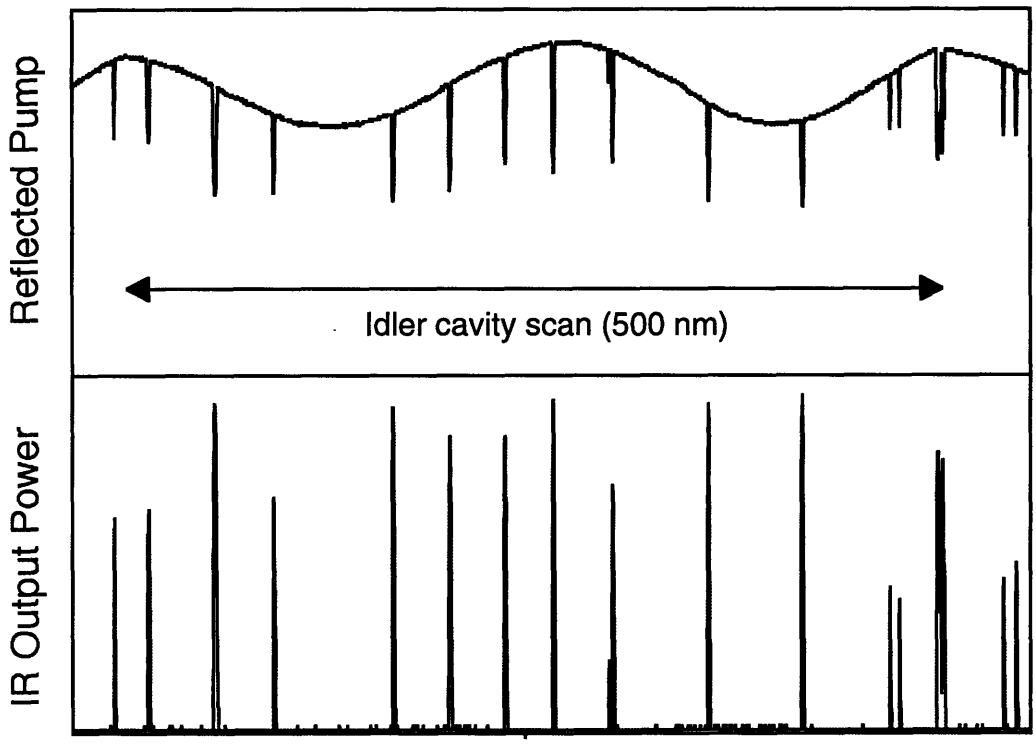

Figure 8-5: DCDRO PZT-scanning traces of detected output power and reflected pump power. Idler-cavity length was scanned and signal-cavity length was fixed. The idler-cavity scanning distance was about 500 nm. (Arbitrary vertical scale.)

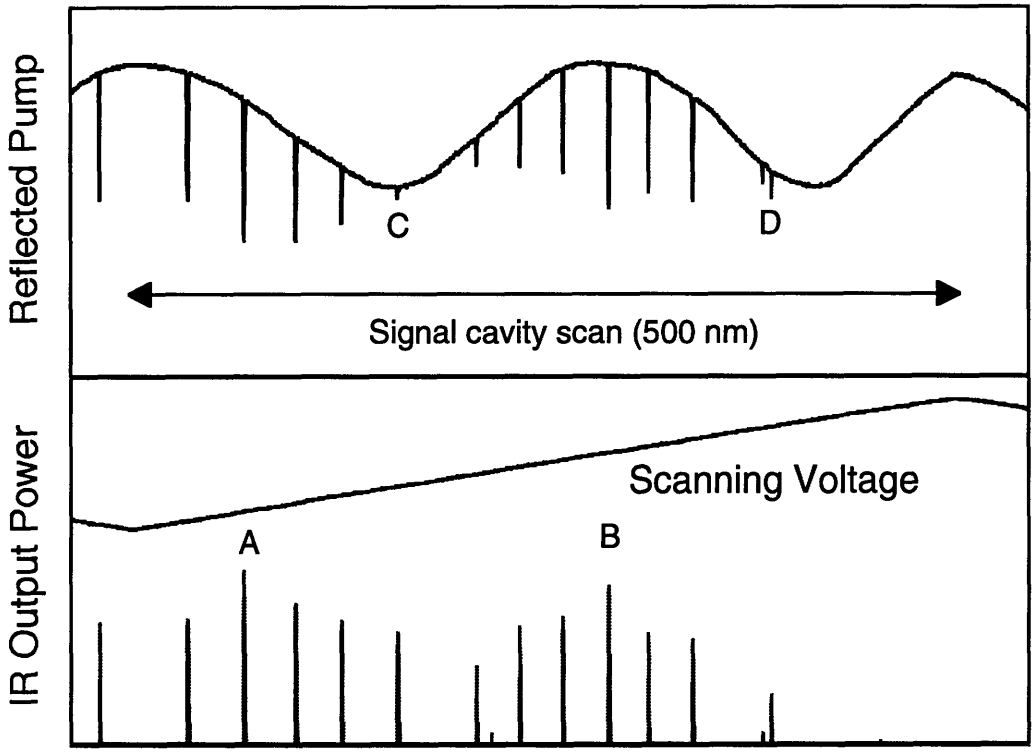

Figure 8-6: DCDRO PZT-scanning traces of detected output power and reflected pump power. Note that peak output powers at A and B do not correspond to minimum reflected pump power at C and D (slowly varying envelope). Signal-cavity length was scanned and idler-cavity length was fixed. (Arbitrary vertical scale.)

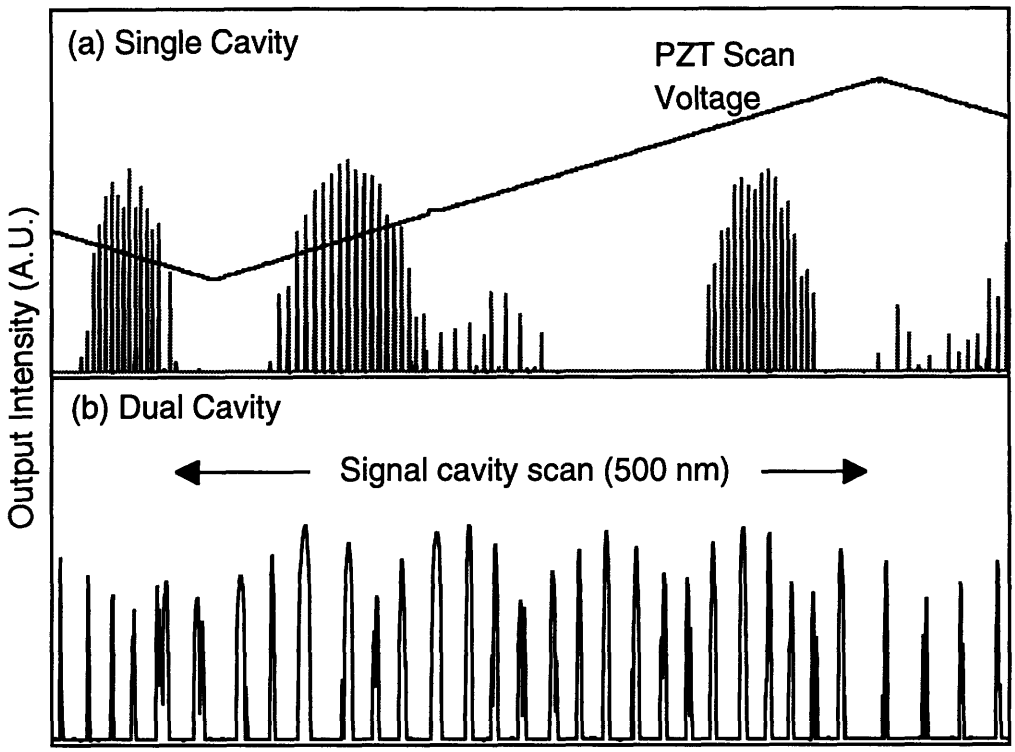

Figure 8-7: Traces of IR output power from a single-cavity and a dual-cavity DRO. (a) Typical cluster modes trace of a single-cavity DRO. (b) Trace of DCDRO detected IR power with the signal-cavity length scanning while the idler-cavity length was fixed. (Arbitrary vertical scale.)

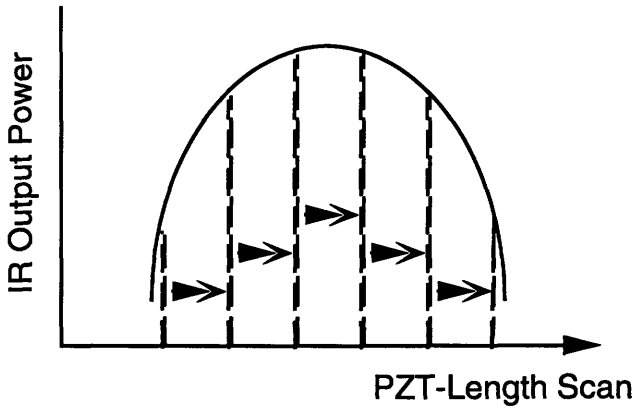

Figure 8-8: Sketch illustrating the moving DCDRO mode as one cavity was scanned and the other one was manually biased.

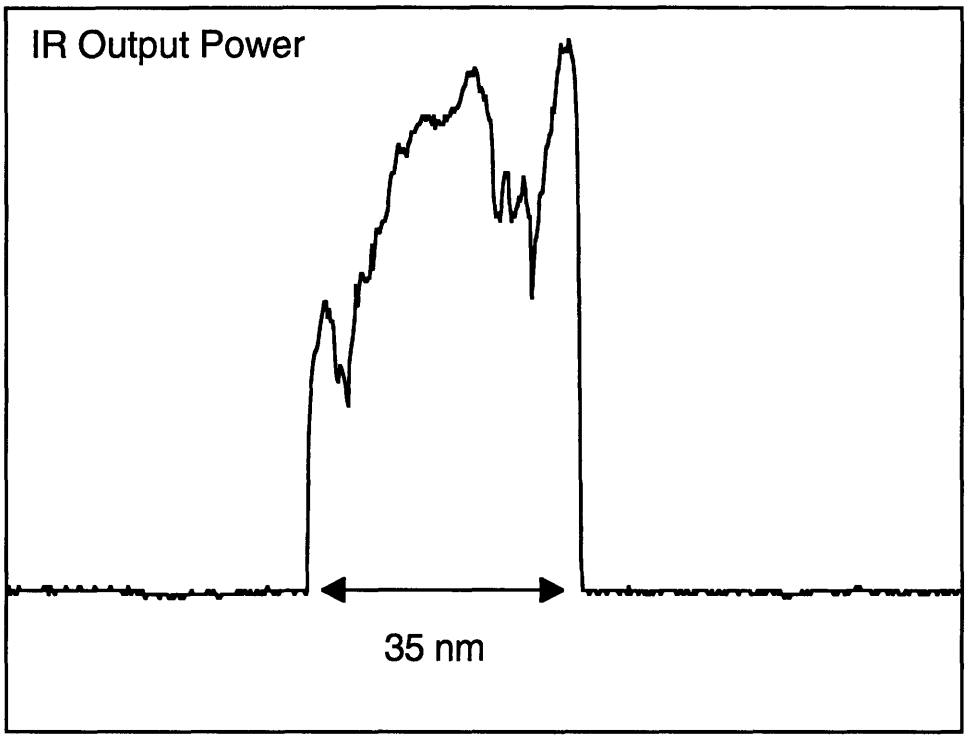

Figure 8-9: Trace of detected IR power when the signal- and the idler-cavity lengths were scanned at the same frequency but in opposite directions.

35 nm, which corresponded to a frequency tuning range of 260 MHz.

Servo-Controlled Operation

To demonstrate hands-free frequency tuning operations, we slowly scanned the idler cavity with a function generator while the signal cavity was controlled by the intensity servo. As the idler cavity was scanned, the output intensity changed accordingly. The servo compensated for the intensity change by adjusting the signal cavity length to maintain the double-resonance condition. With the cavity length under servo control, the output frequency was monitored on an 8-GHz optical spectrum analyzer and a continuous tuning range of ~600 MHz was observed (Fig. 8-10).

The DCDRO was not as stable as expected, even with our semi-rigid cavity design. The DCDRO output intensity was not stable under free-running conditions and

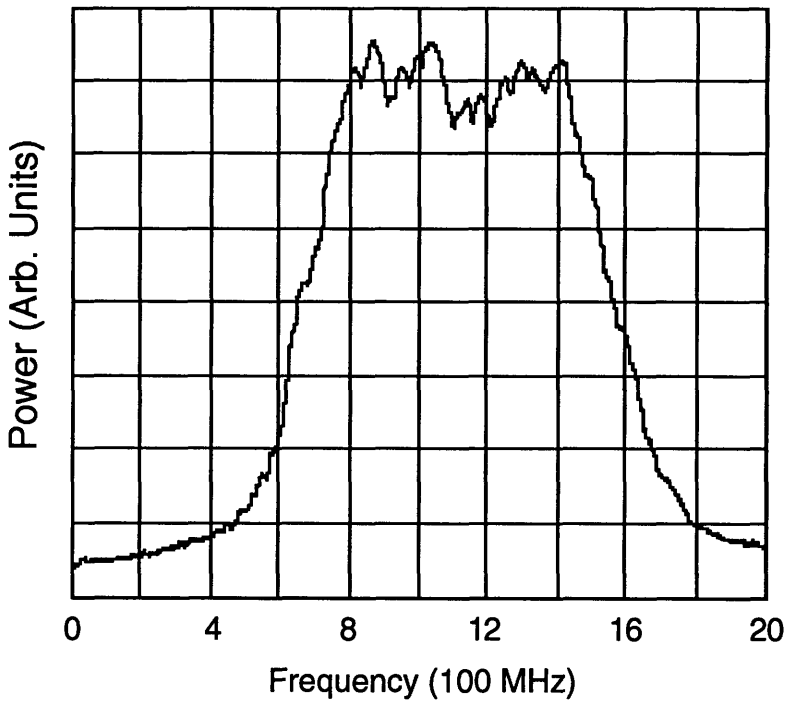

Figure 8-10: Trace of optical spectrum analyzer output showing a DCDRO continuous frequency tuning range of 600 MHz under intensity-locked conditions.

external servo control was required for cw operations. With the intensity servo, the peak-to-peak intensity noise was about 20%.

We believed that the instability was a result of two design faults. First, the polarizing plate and the mounting bracket might be vibrating, because neither of them was securely bolted down to any supporting structure. The plate was only held in place by two nylon screws that pushed against the side of the plate, and the 2-mm thick mounting bracket might not be rigid enough against environment vibrations. Secondly, the flexure mounts was not as stable as expected. As a result, the DCDRO cavity was very susceptible to environmental noise.

8.5 DCDRO Model and Observation

With independent cavity-length controls, we expected our DCDRO PZT-tuning to be continuously tunable over a free spectral range, if not as wide as the phase-matching

bandwidth of the KTP crystal. However, the observed maximum PZT range was only 125 nm, or about 1 GHz in the output frequency. This unexpected limitation motivated us to theoretically examine the tuning characteristics of the DCDRO. We have done a comprehensive theoretical study of the DCDRO to better understand its tuning behavior and the factors that lead to the limited tuning range. Detailed derivation for the DCDRO threshold and output power is presented in Appendix B. These effects have been experimentally studies and verified. Our theoretical calculations for the frequency tuning range was 140 nm, within 10% of the experimental observed value of ~125 nm.

8.5.1 Theory Model

We use plane-wave equations in our study to calculate the threshold and the output power as a function of the PZT tuning. The basic model is a double-pass pump configured DCDRO with arbitrary reflectivities and transmissivities for the cavity elements. The three major effects that we incorporated into our model are pump resonance, polarizer leakage, and polarization axis misalignment between the crystal and the polarizer.

The three effects can be selectively turned on or off for studying their individual or combined contributions. The depolarization effect can be turned off by setting the depolarization angle to zero ($\theta = 0$), while the pump resonance and the polarizer leakage can be turned off by setting the corresponding reflectivity and transmissivity to zero.

Secondary effects, such as phase mismatch (Δk), are also included in our calculations, but their contributions are found to be negligible. The final equations are implemented and plotted using the mathematics package Maple-V on a Pentium-processor-based PC.

8.5.2 Pump Resonance Effect

Theory

The pump resonance effect is caused by the nonzero reflectivities of the mirror coatings. Since the IR output power depends on the internal circulating pump power, the output power is modulated as the internal pump field is resonantly enhanced or reduced. The weak resonance effect is shown to be the dominating factor in limiting the tuning range of the DCDRO.

The pump resonance effect is modeled as two low-finesse pump cavities that are coupled through the polarizer plate. Figure 8-11 shows a series of theoretical plots of reflected pump power. Each plot shows a different idler-cavity biasing location, while the signal cavity is scanned. The shifting of the resonance peaks from one trace to the next indicates that the two cavities are coupled. The internal pump power, therefore, depends on both the signal and the idler cavity lengths. The reflectivities values used for the plots are those measured in our experiment and are listed in Table 8.3 (p. 184).

Figure 8-12 shows the calculated threshold and output power for the DCDRO as a function of the cavity scan. The theoretical plots include only the pump resonance effect, and the two cavity lengths are scanned at the same rate in opposite directions. The predicted frequency tuning range in Fig. 8-12 is ~170 nm.

Experimental Observations

Due to imperfect mirror coatings, the two resonant cavities for the pump field were coupled. Figure 8-5 and 8-6 show time traces of detected IR power and reflected pump power as the signal (idler) cavity was scanned and the idler (signal) cavity was kept at a fixed bias. The reflected pump modulations in both traces indicate that both cavities are resonating the pump field. Their cavity finesses were estimated to be less than 1. We have also experimentally observed the shifting of the resonance peaks in the reflected pump power, as predicted in Fig. 8-11.

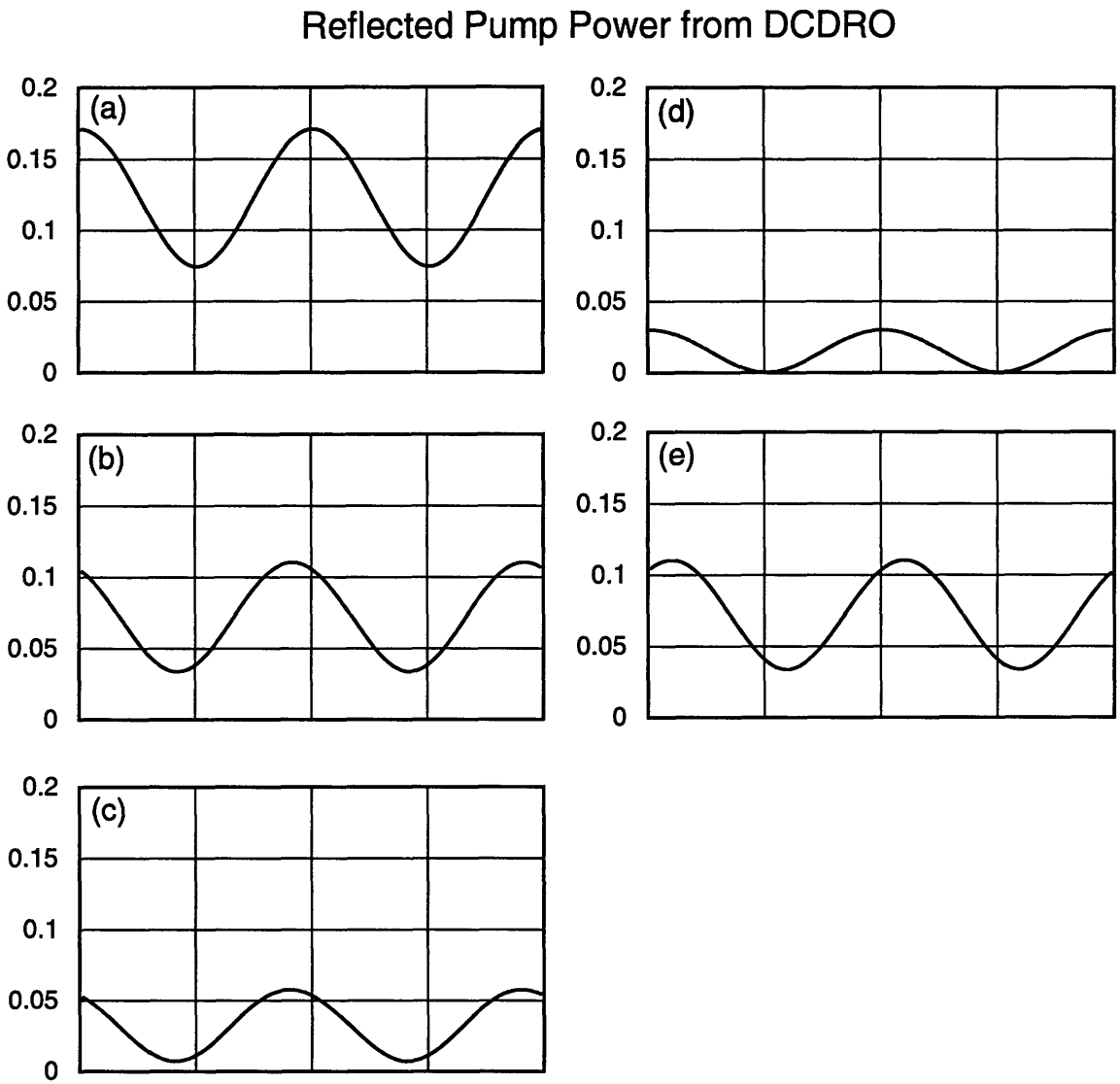

Figure 8-11: Series of theoretical plots of fractional reflected pump power (reflected power / input power) from DCDRO. Each plot shows a different idler-cavity biasing location, while the signal-cavity is scanned. The horizontal separation between two maxima or minima is one free spectral range. Horizontal span is from -2π to 2π. The idler biases are (a) π; (b) $\pi/2$; (c) $\pi/4$; (a) 0; (a) $-\pi/2$. Reflectivity values used in the plots are in Table 8.3.

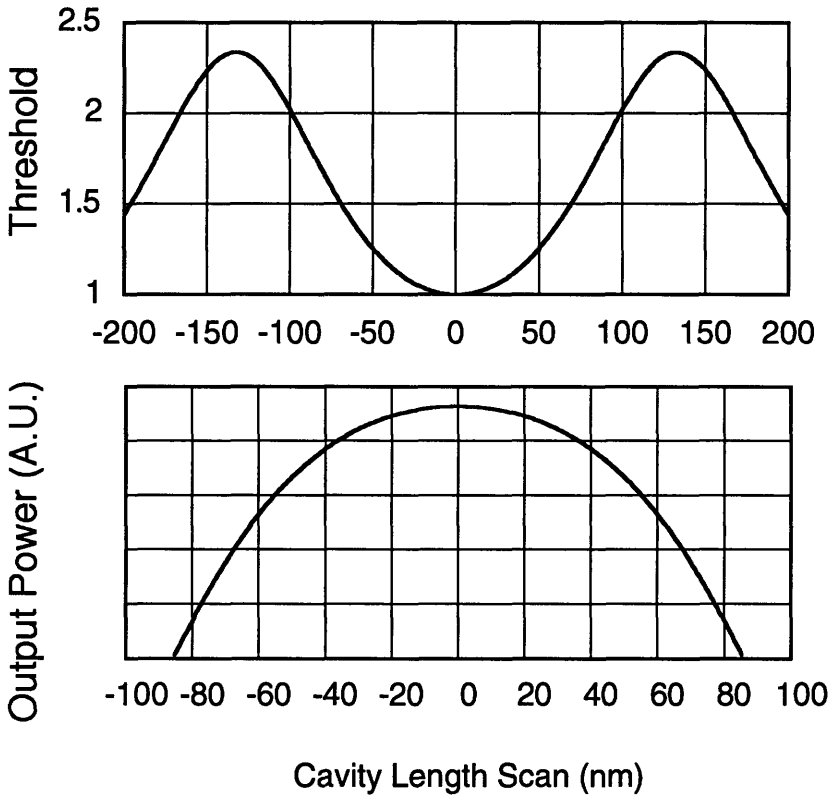

Figure 8-12: Theoretical plots of DCDRO threshold and output power as a function of cavity length scan with pump resonance effect. Threshold plot is normalized to the minimum threshold value of the same plot. Pump power for the output power plot is at 1.5× minimum threshold. Reflectivity values used in the plots are in Tables 8.1–8.3.

8.5.3 Leakage Effect

Theory

The leakage effect is caused by the finite polarization isolation ratio of the polarizer plate. A small percentage of the vertically polarized idler is transmitted into the signal (horizontal) cavity and similarly a small amount of the horizontally polarization signal is reflected into the idler (vertical) cavity. The two high finesse (~300) IR cavities are coupled through the polarizer plate.

The coupling between the two cavities modifies the finesse of the individual cavity finesses. In other words, the finesse of the signal cavity is a function of the idler cavity length, and vice versa. For example, if the idler cavity is on resonance, the effective cavity loss for the signal cavity is decreased due to the leakage into the resonant idler cavity. Figure 8-13 shows a theoretical calculation of the signal-cavity finesse as a function of idler cavity length. The decoupled signal cavity finesse is 255, and the coupled cavity has a peak-to-peak deviation of 30. The corresponding maximum and minimum losses for the signal-cavity are 2.6% and 2.3%. The reflectivities values used for the plots are listed in Tables 8.1 and 8.2.

The leakage effect on the DCDRO threshold is not as significant as the pump resonance effect. Our calculations show that its contribution to the limited tuning range is about 20% of the pump resonance effect. The tuning range is reduced from 170 nm, with only the pump resonance effect, to 140 nm when both effects are taken into account.

Experimental Observations

We have observed the variation of the signal-cavity finesse values as the idler-cavity length was biased at different PZT positions. A horizontally polarized YAG laser beam was injected into the DCDRO cavity through the signal-cavity's output coupler to measure its finesse, as sketched in Fig. 8-14. A photodetector was placed behind the KTP crystal to measure the resonance peaks as the signal-cavity was scanned. The idler cavity was then manually biased to different PZT positions to demonstrate

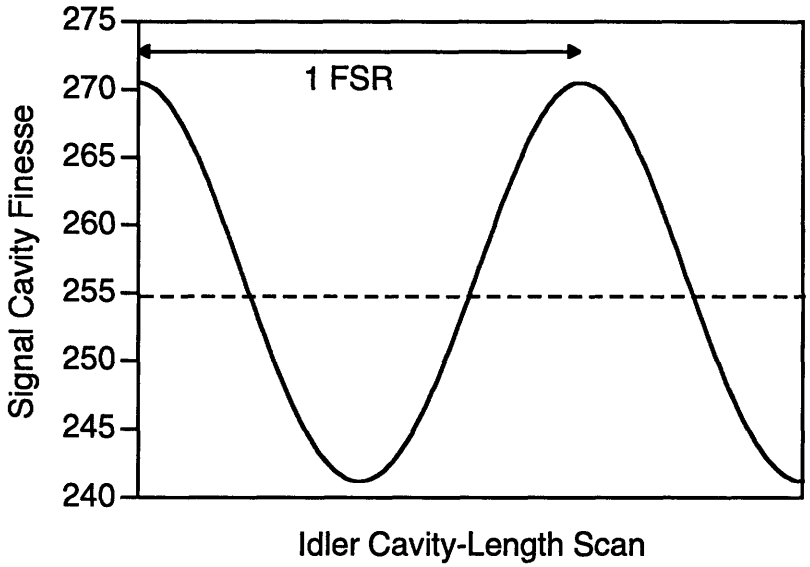

Figure 8-13: Theoretical plot of the signal-cavity finesse vs. idler-cavity length scan. Solid curve: signal-cavity finesse varies as a function of idler cavity-length for coupled cavities. Dotted curve: signal cavity's finesse is constant if the high reflector of the idler cavity is blocked. The signal cavity finesse is maximized (270) when the idler cavity is on resonance. The separation between the two maxima is one free spectral range of the idler cavity.

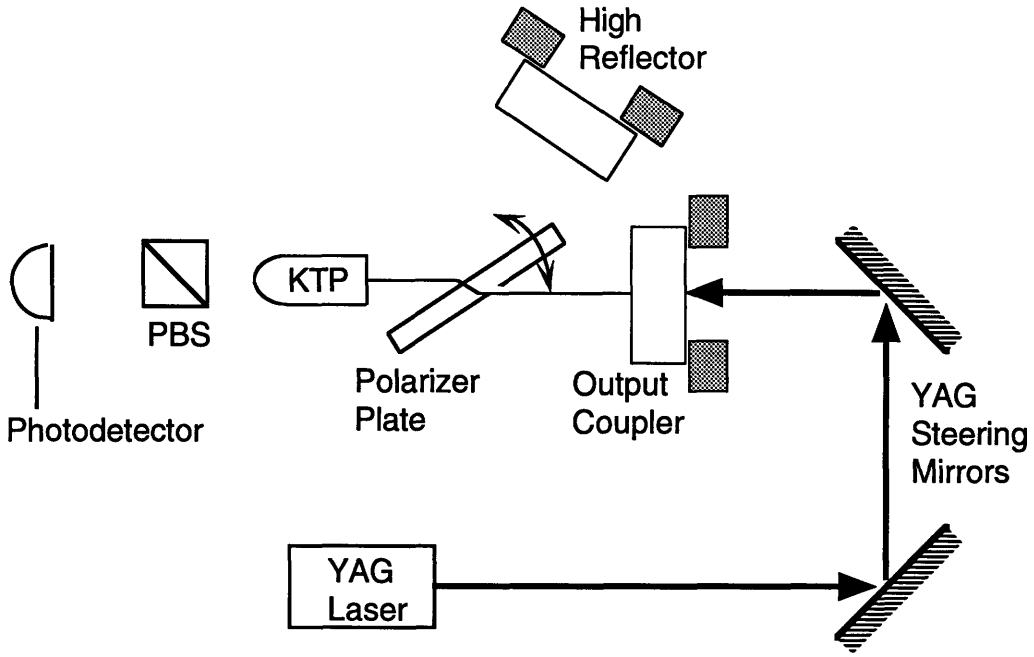

Figure 8-14: Schematic of DCDRO and associated alignment optics for measuring the signal-cavity finesse.

the coupling of the two cavities. The finesse values varied continuously between a maximum of ~283 to a minimum of 235. Figure 8-15 shows two traces of the measured resonance peaks of the DCDRO, thus confirming the coupling of the two IR cavities.

8.5.4 Depolarization Effect

Theory

The depolarization effect is caused by the slight angular misalignment between the crystal's optical axes and the polarizer axes, as illustrated in Fig. 8-16. Like the leakage effect, the depolarization effect couples the two IR cavities through the polarizer. Unlike the leakage effect, the depolarized light is effectively lost and no longer involved in the parametric interaction.

The distinction between the leakage and the depolarization effects is the transfer of signal and idler power from one polarization to the other. In the leakage effect, the

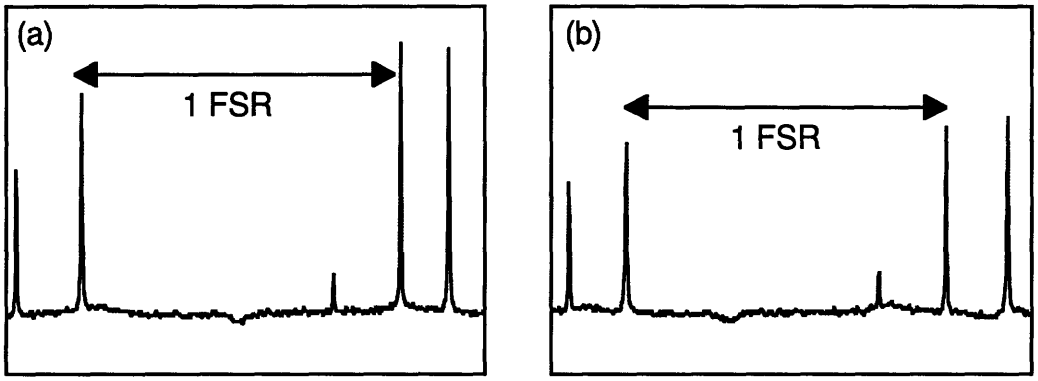

Figure 8-15: Resonance peaks of DCDRO signal-cavity finesse measurement. (a) Measured finesse is 283; Idler-cavity length is biased to enhance the signal-cavity finesse. (b) Measured finesse is 235; Idler-cavity length is biased to reduce the signal-cavity finesse.

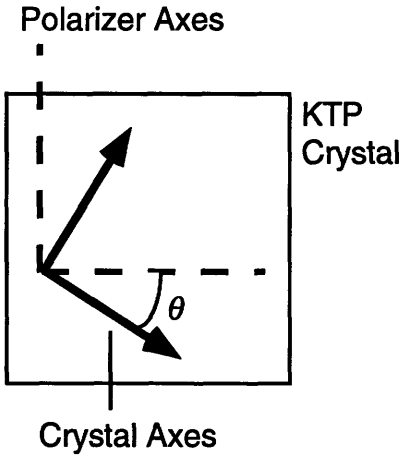

Figure 8-16: Graphical illustration of the depolarization angle θ between the crystal's optical axes and the polarizer axes.

polarizations of the signal and the idler fields remain unchanged after being leaked into the other cavity. On the other hand, in the depolarization effect, part of the horizontally polarized signal field is converted into vertical polarization and is resonated in the idler cavity. Similarly, part of the vertically polarized idler field is converted into horizontal polarization and is resonated in the signal cavity. The cavity that resonates the depolarized light is referred as the secondary cavity. The depolarized fields are not correctly phase matched and, therefore, they are effectively lost.

The depolarization loss is most significant when the depolarized light is resonant with the secondary cavity. For example, when the idler cavity is on resonance relative to the depolarized signal most of the signal power in the signal cavity is transferred to the depolarized signal field in the idler cavity. Such a loss in internal IR power would cause the threshold to increase dramatically, and as a result, the DCDRO stops oscillation. The depolarized fields may not be optimally coupled into the other cavities due to walk off or misalignment. Therefore, there might exist more than one resonance peak for the depolarized light per free spectral range as non-TEM_{00} modes are brought into resonance. The same power transfer process also applies to the idler field.

The amount of depolarization depends on the offset between the crystal axes and polarizer axes. The smaller the depolarization angle θ, the smaller are the effects. Figure 8-17 shows a series of calculated threshold traces at different depolarization angles. The effect becomes negligible as $\theta \leq 0.1°$.

We have done a simple calculation to predict the consequences of depolarization when the depolarized light is on resonance. We want to find out the relationship between two adjacent depolarized mode pairs. If the depolarized signal-frequency (idler-frequency) mode is on resonance in the idler (signal) cavity, can the adjacent depolarized signal-frequency (idler-frequency) mode also be on resonance?

We consider two adjacent signal-idler mode pairs with frequencies $f_{1,2}$ and wave number (number of half wavelengths) $m_{1,2}$ for the first pair and $f'_{1,2}$ and $m'_{1,2}$ for the

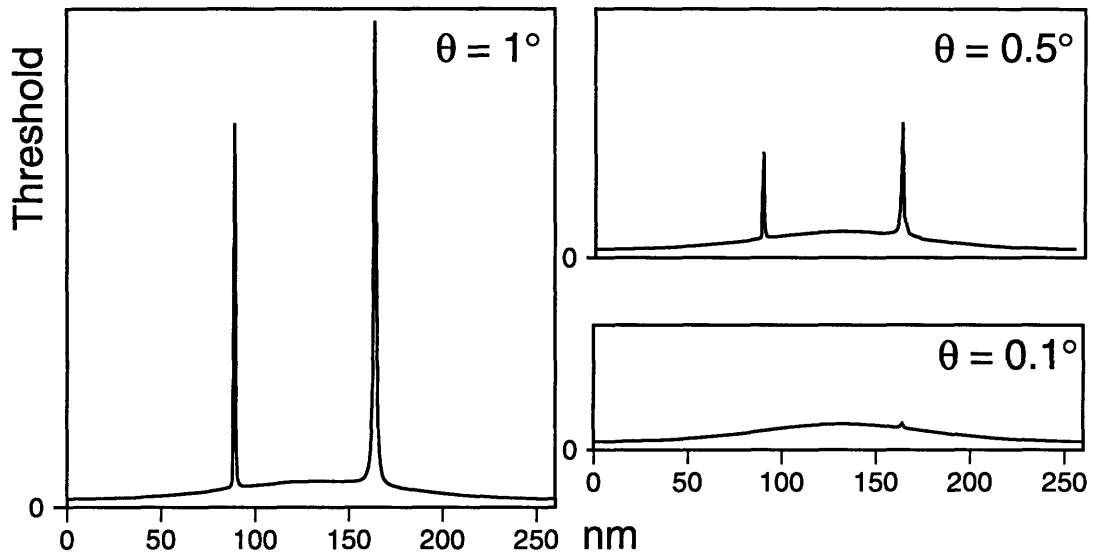

Figure 8-17: Series of theoretical plots showing DCDRO's threshold vs. cavity-length scan at three different depolarization angles θ. The signal and idler cavity lengths are scanned simultaneously in opposite directions as discussed in Sect. 8.4.3. At $\theta = 1°$ the dramatic rise in threshold is $\sim 20\times$ the nominal value. At $\theta = 0.1°$ the rise is negligible. (Vertical scale: identical arbitrary scale in all plots.)

second pair. The frequency f_i and the cavity length l_i are related by

$$f_i = \frac{m_i c}{2l_i}. \tag{8.7}$$

Assuming that the depolarized signal (subscript 1) field in the idler (subscript 2) cavity is on resonance for the first mode pair so that

$$l_2 = n_1 \frac{\lambda_1}{2}, \tag{8.8}$$

where n_1 is an integer. We can then write for the adjacent mode pair, for a fixed l_2,

$$l_2 = p \frac{\lambda_1'}{2}, \tag{8.9}$$

where p is a real number. The sum-frequency constraint,

$$f_1 + f_2 = f_1' + f_2',$$

can be rewritten into

$$\begin{aligned} \frac{n_1}{2l_2} + \frac{m_2}{2l_2} &= \frac{p}{2l_2} + \frac{m_2'}{2l_2}, \\ n_1 + m_2 &= p + m_2', \end{aligned}$$

with the use of Eqs. (8.7)–(8.9). Since n_2, m_1, and m_2 are integers (number of half wavelengths), p must also be an integer. Therefore, if the secondary cavity is on resonance for any one mode of the depolarized signal field, then all other depolarized signal modes are also on resonance. The same discussion applies to the depolarized idler mode.

Since the threshold increases dramatically when the depolarized field is on resonant with the secondary cavity, the consequence is that at certain cavity length positions for the secondary cavity, the DCDRO stops generating output power. The limitation on the DCDRO tuning range imposed by the depolarization effect can be easily removed by reducing the angular mismatch between the crystal and polarizer axes.

Experimental Observations

We have experimentally observed the transfer of internal IR power from one polarization to the other under test conditions. An experiment similar to the one performed for the leakage effect was carried out. As in the leakage experiment, a horizontally polarized YAG laser beam was injected into the DCDRO cavity through the signal-cavity's output coupler, as sketched in Fig. 8-14. A photodetector and a polarizing beam splitter were placed behind the KTP crystal to measure the transmitted horizontal power. The idler cavity was then scanned and the signal cavity was manually biased to bring the injected YAG beam into resonance. Figure 8-18a shows a trace of the detected horizontal power that was transmitted through the KTP crystal. The

two dips in the trace indicate a drop in the internal IR horizontal power. The larger dip on the left was the TEM_{00} mode and the smaller dip on the right was the non-TEM_{00} mode of the idler cavity. From the size of the dip relative to the averaged detected power, we estimated the depolarization angle θ was $\sim 0.9°$.

As discussed in previous sections, the two cavities were also coupled through the polarizer leakage, and it was not possible to study each of these two effects individually. As seen in Fig 8-18, the detected IR power is modulated due to the polarizer leakage. A theoretical plot (Fig. 8-18b) is shown for comparison showing the depolarization effect and the leakage effect. Reflectivity values used in preparing the theoretical plot are listed in Tables 8.1–8.3 and a depolarization angle $\theta = 0.9°$ is used.

We have also observed the abrupt drop in DCDRO output power caused by the resonant effect of the secondary cavity. For example, with the signal (idler) cavity scanning and the idler (signal) cavity fixed, a number of signal-idler mode pairs were excited as shown in Figs. 8-5 and 8-6. But at certain idler (signal) cavity PZT positions where the depolarized signal (idler) field was on resonance in the idler (signal) cavity, the DCDRO would abruptly stop generating outputs. No IR output power were detected. The width of these PZT positions was estimated to be about 1 nm from the experimental observation. The depolarization effect that led to this sudden drop in output power would limit the PZT-tuning range to one free spectral range of the cavity since the resonance peaks were separated exactly by one free spectral range. But fortunately, the depolarization effect can be eliminated by improving the alignment of the depolarization offset angle.

8.5.5 Combined Effects

In our DCDRO tuning experiment, it was not possible to study each of the three effects individually. The three effects together limited the PZT-tuning range of our DCDRO to 125 nm.

The pump resonance effect was the dominant effect. The leakage effect contribution was secondary and amounted to about 20% of the overall range. The depolar-

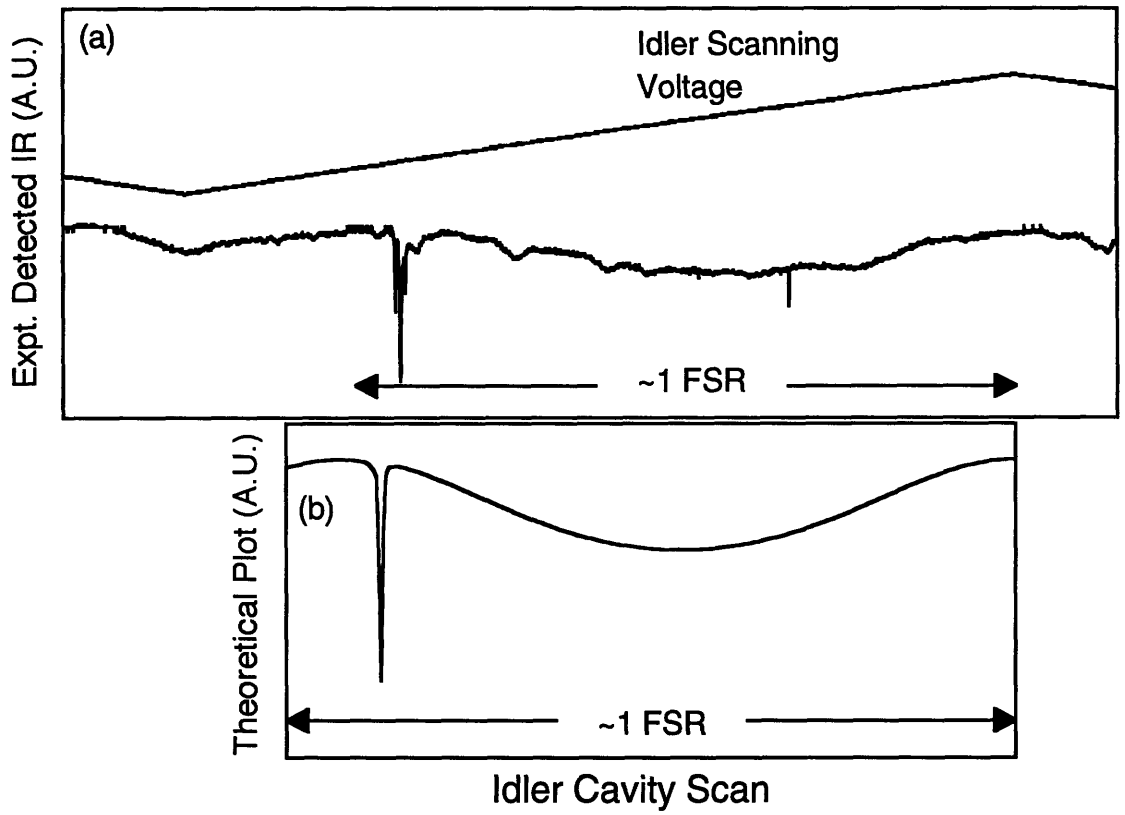

Figure 8-18: (a) Trace of detected signal-cavity horizontal power vs. idler cavity-length scan showing the depolarization effect and the leakage effect. (b) Trace of theoretical plot predicting the two effects correctly. Reflectivity values used in the theoretical plot are listed in Tables 8.1–8.3 and depolarization angle $\theta = 0.9°$. (Horizontal span is about one free spectral range of the idler cavity.)

ization effect was dramatic, but was negligible most of the time. It only affected the output when the secondary cavity was on resonance. We, therefore, only needed to consider pump-resonance effect and leakage effect for the overall PZT-tuning range.

With the two effects combined, our calculated tuning range of 140 nm, which is based on quantities (such as reflectivities and losses) measured independently, is within 10% of the experimentally observed 125 nm. Figure 8-19 shows series of calculated DCDRO threshold plots with individual effects turned on or off. Figure 8-20 shows the DCDRO output power as a function of PZT cavity-length change. The width of the output power is the PZT-tuning range. The thick trace is for the pump-resonance effect only and the lighter trace includes both effects.

8.5.6 Secondary Effects

We have also considered secondary effects such as "dynamic" phase mismatch and dispersion. "Dynamic" phase mismatch refers to the deviation from the optimal phase-matching condition as we frequency tuned the DCDRO away from the maximum output power conditions. Its contribution can be estimated by considering the phase-mismatch condition,

$$\begin{aligned} \Delta k &= \frac{n_p}{\lambda_p} - \frac{n_1}{\lambda_1} - \frac{n_2}{\lambda_2}, \\ \delta(\Delta k) &= (n_2 - n_1)\frac{\delta f_1}{c}, \end{aligned}$$

where c is the speed of light. With a frequency tuning range of $\sim$1 GHz (δf_1) and a crystal length $d = 9.5$ mm, the fractional increase in threshold due to "dynamic" phase mismatch, calculated using Eq. (5.2), is 5.9×10^{-7}.

The total contributions of "dynamic" phase mismatch and dispersion account for $\leq$1% on the limited tuning range and are neglected from our calculations.

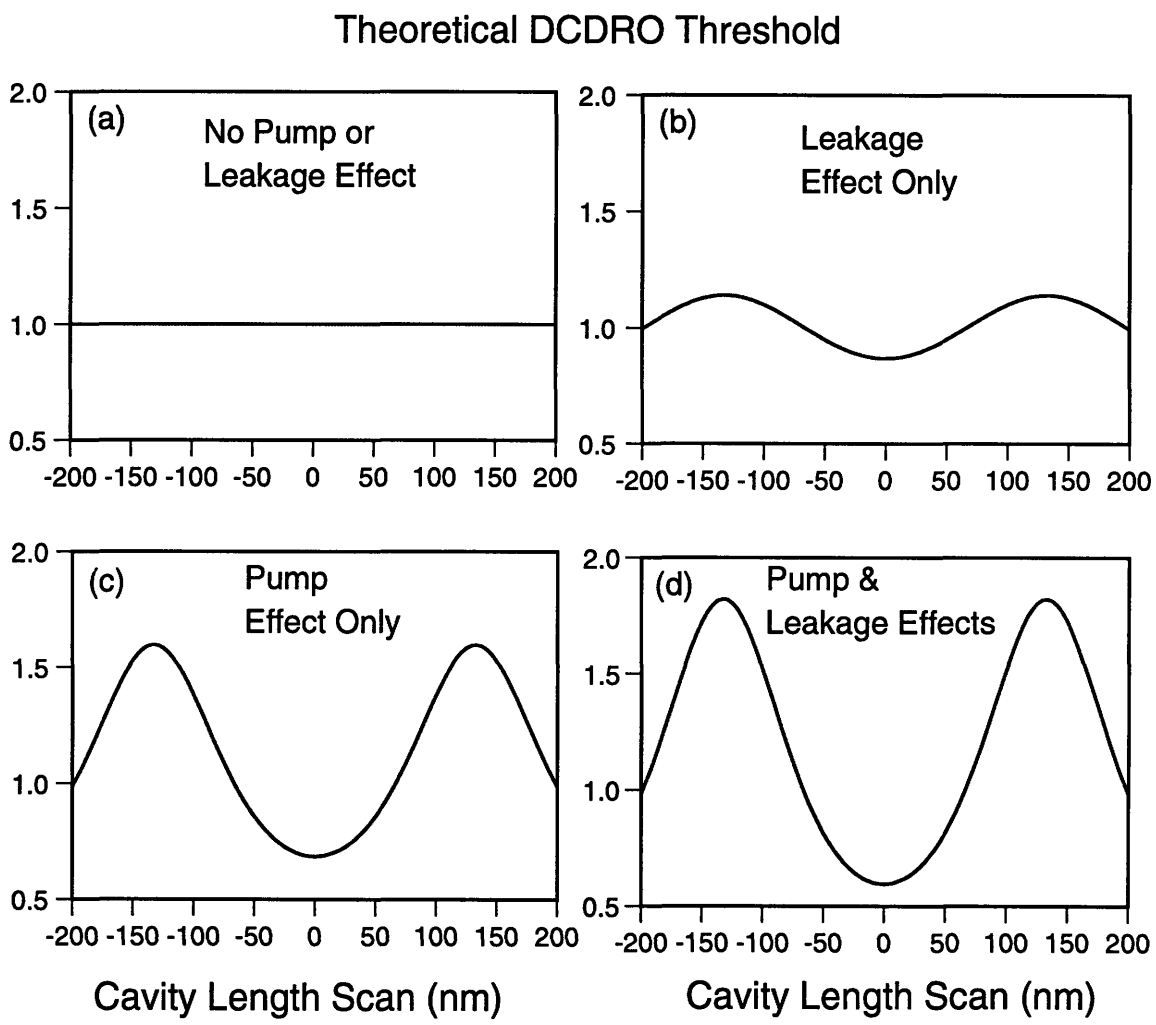

Figure 8-19: Series of theoretical plots of DCDRO's threshold vs. cavity-length scan with individual effects turned on and off. (a) No pump or leakage effect: the constant threshold indicates a continuous tuning range over the entire PZT range. (b) Leakage effect only: the threshold is slightly modulated. (c) Pump effect only: the threshold modulation is larger than (b) indicating a larger contribution to the range limitation. (d) Pump and leakage effects: the combined effect has the largest modulation. (Vertical scales for all plots are normalized to the constant threshold value in (a).)

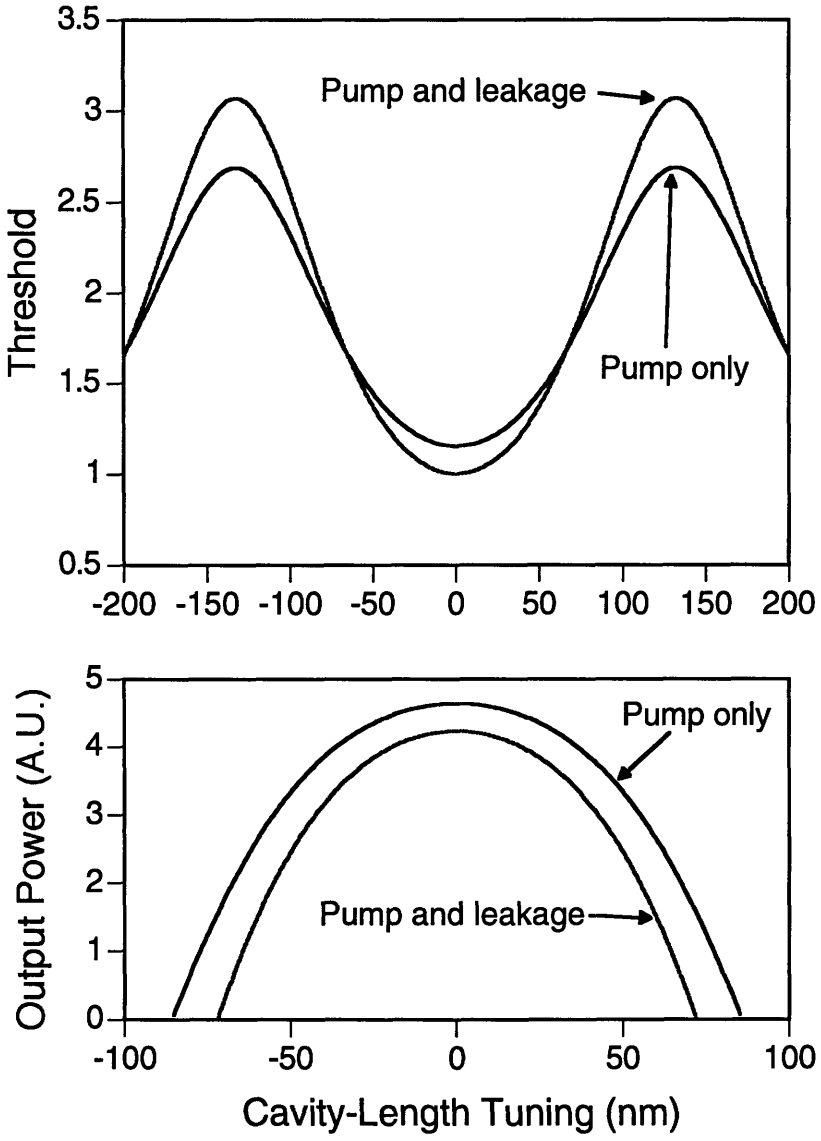

Figure 8-20: Theoretical plots of DCDRO's threshold and output power vs. PZT tuning showing the different effects on tuning ranges. With only pump resonance, the modulation in threshold is smaller and the tuning range is wider. With pump resonance and polarizer leakage, the threshold modulation in larger and the tuning range is narrower. Pump threshold plots are normalized to minimum threshold value of the pump-resonance-only trace.

8.6 Summary

We have constructed a dual-cavity DRO and investigated its PZT tunability. Our DCDRO had an observed PZT-tuning range of ~1 GHz, which was primarily limited by the pump resonance effect. Without using any adjustable parameters, our simple theory predicts a frequency tuning range of 140 nm, within 10% of the experimentally observed range of 125 nm. The theory not only predicts the tuning range of our DCDRO, but also provides insights into the design of future generations of DCDRO.

By separating the two outputs into their own resonant cavities, a number of cavity parameters, such as cavity lengths and internal losses, can be adjusted independently. In particular, pump laser noise contribution to the OPO quantum noise spectra can be eliminated with matched signal and idler losses so that the spectra can be more precisely measured. Also, the PZT-tuning range is much wider in a dual-cavity design than in a single-cavity design so that wideband continuous frequency tuning can be readily accessible.

However, our DCDRO is a first generation design and a few improvements are needed before we can use the DCDRO for further experiments. The two major issues are mechanical stability and frequency tunability. Our semi-rigid design is not as stable as expected. Better mechanical stability can be achieved with better mechanical support for the polarizer plate and the use of high quality flexure mounts.

The continuous frequency tuning range is only limited by the phase-matching bandwidth of the crystal. It should be possible to extend the tuning range if the above-discussed effects are minimized. Depolarization effect can be eliminated if the angular misalignment is adjusted to less than 0.1°. Better mirror coatings would improve the weak pump resonance effect and widen the range. However, leakage from the polarizer is the most difficult to eliminate because there is no perfect polarizer. One possibility is to separate the signal and the idler beams using the walk-off of the KTP crystal. However, such a design would require an extended cavity length which might be more susceptible to vibrations.

Our experiments with a first generation DCDRO has provided us with the nec-

essary framework for future design improvements. The DCDRO as a widely tunable optical frequency source should find many new applications in the fields of high resolution spectroscopy and metrology.

Chapter 9

Summary

In this thesis, we have investigated the noise behavior of a type-II phase-matched potassium titanyl phosphate (KTP) optical parametric oscillator (OPO). The necessary frequency tuning technique and beat-note frequency stabilization technique were developed for a first measurement of the OPO beat-note phase noise. The pump laser intensity noise to beat-note phase noise transfer function was also characterized as part of our quantum noise experiment.

We have constructed and experimented with three different doubly resonant OPO (DRO) cavity designs to evaluate their mechanical stability and frequency tunability. The three DRO designs were the monolithic cavity, the 2-element cavity and the 3-element cavity.

The monolithic design was mechanically stable but lacked some of the tuning elements. The monolithic DRO had a small confocal parameter for lower-threshold operations, but we observed an undesirable bistable behavior in which the DRO oscillated stably between two different sets of modes. The onset of oscillation was, however, not predictable.

The 2-element DRO had all of the four tuning elements built into the design, but the cavity was not stable under free-running conditions and an intensity servo loop was required for cw operations. Under servo-locked conditions, the peak-to-peak output intensity noise was 16%. We observed a discrete angle tuning range of ± 1.5 THz for the 2-element DRO, with a continuous temperature tuning range of

0.5 GHz.

Our best results were obtained from the 3-element DRO. Due to its superior mechanical design, in which no spring-loaded mount was used, the 3-element DRO was the most stable among the three and had the widest tuning range. The peak-to-peak intensity noise was 16% under free-running conditions and was 0.6% rms under intensity-locked conditions. The observed angle tuning range was ± 3 THz. Our 2- and 3-element DROs have shown excellent frequency tunability and output intensity stability, thus demonstrating the possibility of using the cw DRO as a tunable frequency source in applications of high-resolution spectroscopy and optical frequency metrology.

The next step in our DRO phase noise experiment was to stabilize the output beat-note frequency. We phase-locked the beat notes of the 2- and 3-element DROs to a stable microwave reference. The beat-note, as observed on a rf spectrum analyzer, was tightly phase locked to the reference with the beat-note linewidth limited by the measurement resolution of the spectrum analyzer. From the measured phase noise spectrum, the residual phase noise density for the 2-element DRO was estimated to be 0.2 mrad/$\sqrt{\text{Hz}}$ and the noise density for the 3-element DRO was 0.3 mrad/$\sqrt{\text{Hz}}$. One motivation of our DRO studies was to use the DRO as part of the proposed frequency chain [41, 43] with several DROs being cascaded in series or in parallel. Our frequency division (phase-locking) experiment has shown that the phase noise of the DRO outputs can be suppressed by the phase-locking servo, thus demonstrating optical frequency division and the feasibility of using DROs in an optical-microwave frequency chain.

With the DRO output intensity and beat-note frequency stabilized, the beat-note signal was demodulated to give the in-phase and the quadrature-phase signals; the in-phase noise was the amplitude noise and the quadrature-phase noise was the phase noise of the beat-note signal. The two quadrature noise power spectra were measured directly on a rf spectrum analyzer. The pump laser intensity to beat-note noise transfer characteristics were measured by amplitude modulating the pump laser field before it entered the DRO . With our carefully designed setup and our

newly developed frequency tuning and stabilization techniques, we have made the first measurement of the DRO beat-note phase noise spectrum.

A simple theoretical model was developed to help us better understand our experimental results. Our calculation was a first-order approximation for the set of three-wave mixing nonlinear coupled differential OPO equations. The calculation included cavity detuning, signal-idler loss mismatch and excess pump noise effects for a more realistic description of the experiment.

We found that our theoretical calculation agreed reasonable well with the noise characteristics of the signal-idler sum-intensity spectrum and the beat-note in-phase spectrum. These two spectra were found to have similar behavior, as predicted by our calculation. The measured and calculated shape and slope of the pump AM to in-phase (sum-intensity) transfer function were in good agreement.

However, our theory broke down when we tried to described the quadrature-phase noise behavior. There was major disagreement between the observed and calculated quadrature-phase spectra and the pump intensity to output noise transfer characteristics. We have observed more quadrature-phase noise power than our theoretical model predicts. The reason for the observed excess quadrature-phase noise power was the presence of excess pump intensity and phase noise. We measured the pump laser intensity and phase noise spectra and found that the pump laser has a large amount of excess noise power at low frequencies. The observed pump laser phase noise spectrum and the observed quadrature-phase spectrum have similar spectral profile as the pump laser phase noise was directly coupled to the quadrature-phase spectrum.

Another possible explanation for the discrepancy was that our first-order calculation was inadequate. Since our calculation was a first-order approximation, the calculation was only valid when the fluctuating terms were small. The approximation broke down when the pump field was amplitude modulated strongly or in the presence of large excess pump noise, where the fluctuating terms were no longer small. In our first-order calculation, we neglected to include higher-order term contributions which might be significant. In such a case, our experiment has shown the need for a more

complete theory to give the correct description.

Further experimental and theoretical studies are required to determine the exact cause for the discrepancy between the observed and the calculated spectra. Such a future experimental framework was laid with our dual-cavity DRO.

We have constructed and investigated the properties of a dual-cavity DRO (DC-DRO), which paved the foundation for future experiments. With the signal and the idler fields resonating in their own cavities, the signal and the idler cavity parameters can be varied independently, thus overcoming some of the constraints in a single-cavity design.

One immediate advantage is the increased cavity-length tuning range. Our DC-DRO has an observed cavity-length tuning range of $\sim$1 GHz that was limited by the weak pump resonance. By using better coating optics, we should be able to extend the tuning range to more than a few GHz's and be ultimately limited by the phase-matching bandwidth of the crystal.

The dual-cavity design also allows better signal-idler loss matching. The addition of lossy element(s) in one of the cavities would enable us to vary the internal loss continuously until the two cavity losses are identical. With perfectly balanced cavity losses, the pump laser noises do not contribute to the beat-note spectrum and the phase noise can be measured more precisely even in the presence of excess pump noise.

Appendix A

OPO Quantum Noise Spectra Derivation

In this Appendix, we derive the quantum intensity and frequency noise spectra of an OPO. We consider a cw doubly resonant OPO with arbitrary detuning and losses for the signal and idler fields. The effects of excess pump intensity noise and phase noise are also included in the calculation. However, perfect phase matching, $\Delta k = 0$, is assumed because a non-zero value affect only the threshold of oscillation but not the qualitative behavior of the OPO.

We take a semiclassical approach for our analysis. Classical field equations are used for the steady-state large-signal analysis to solve for the threshold condition and the internal fields. We then recast our equations in the quantum regime for small-signal analysis. The classical field variables become quantum mechanical operators, and the proper noise operators are added. A linearized set of small-signal solutions is found and the commutation relations are calculated to obtain the sum-intensity noise and phase noise spectra.

A.1 Large-Signal Analysis

The classical field equations for three-wave mixing in an OPO are

$$\begin{aligned} \dot{A}_p &= -\kappa_p A_p - \chi A_1 A_2 + \sqrt{2\kappa_p}\, E_p, \\ \dot{A}_1 &= -(\kappa_1 - i\Delta_1) A_1 + \chi A_p A_2^*, \\ \dot{A}_2 &= -(\kappa_2 - i\Delta_2) A_2 + \chi A_p A_1^*, \end{aligned} \tag{A.1}$$

where χ is the nonlinear coupling constant, A_i is the internal field mode, and κ_i is the field total loss rate. $E_p = e_p \exp(i\theta_p)$ is the input pump field with e_p^2 being the pump power in unit of photons-per-second and θ_p is the pump phase angle. The subscripts p, 1, and 2 refer to the pump, signal, and idler, respectively. The cavity detunings for the signal and the idler fields are defined by

$$\Delta_i = \omega_i - \omega_i^c, \qquad\qquad i = 1, 2,$$

where ω_i^c is the cavity resonance frequency for the mode i. Since we have assumed a single-pass pump configuration, the pump field is always on resonance with $\Delta_p = 0$.

To solve for the steady-state solution, we write $A_i = r_i \exp(i\phi_i)$ and set the time derivative of A_i to zero ($\dot{A}_i = 0$). After some algebra, the following relations are obtained :

$$\tan\theta_\Delta \equiv \Delta_1/\kappa_1 = \Delta_2/\kappa_2, \qquad \pi/2 > \theta_\Delta > -\pi/2, \tag{A.2}$$

$$\theta_\Delta = \phi_1 + \phi_2 - \phi_p, \tag{A.3}$$

$$r_p = \sqrt{\kappa_1\kappa_2 + \Delta_1\Delta_2}/\chi, \tag{A.4}$$

$$r_i = C/\sqrt{\kappa_i}, \qquad i = 1, 2, \tag{A.5}$$

$$e_p \cos(\theta_\Delta + \phi_p - \theta_p) = \tilde{e_p}\left(1 + C^2/2\tilde{e_p}^2\right), \tag{A.6}$$

$$e_p \sin(\theta_\Delta + \phi_p - \theta_p) = \tilde{e_p}\left(\Delta_1/\kappa_1\right), \tag{A.7}$$

where the minimum threshold,

$$\tilde{e_p} = \frac{\sqrt{\kappa_1 \kappa_2}}{\chi} \sqrt{\frac{\kappa_p}{2}},$$

is at zero detuning ($\Delta_1 = \Delta_2 = 0$). By solving Eqs. (A.6) and (A.7) simultaneously, we obtain

$$C^2 = 2\tilde{e_p}^2 \left[\sqrt{F_p - (\Delta_1/\kappa_1)^2} - 1 \right], \tag{A.8}$$

where $F_p = (e_p/\tilde{e_p})^2$ is the number of times the OPO is pumped with respect to the minimum threshold. The signal and idler output powers, in photon-per-second unit, are given by

$$P_i = \frac{2\gamma_i}{\kappa_i} C^2,$$

where γ_i is the field output coupling loss rate. Equation (A.2) is the detunings of the signal and idler fields normalized to their respective total loss rates. It imposes a strict relationship between the signal and idler detunings, suggesting that they cannot be arbitrarily set; otherwise, oscillation cannot occur.

A.2 Small-Signal Analysis

To calculate the quantum noise of an OPO, Eqs. (A.1) are modified to include the vacuum noise fluctuations and the field variable A_i becomes a quantum mechanical operator. The quantum Langevin equations for the three waves inside the OPO are

$$\begin{aligned}
\dot{A}_p &= -\kappa_p A_p - \chi A_1 A_2 + \sqrt{2\kappa_p}\, E_p + \sqrt{2\kappa_p}\, u_p, \\
\dot{A}_1 &= -(\kappa_1 - i\Delta_1) A_1 + \chi A_p A_2^\dagger + \sqrt{2\gamma_1}\, u_1 + \sqrt{2(\kappa_1 - \gamma_1)}\, v_1, \\
\dot{A}_2 &= -(\kappa_2 - i\Delta_2) A_2 + \chi A_p A_1^\dagger + \sqrt{2\gamma_2}\, u_2 + \sqrt{2(\kappa_2 - \gamma_2)}\, v_2,
\end{aligned} \tag{A.9}$$

where u_i and v_i are the vacuum input modes associated with output coupling and internal losses. Their nonzero correlations are

$$\langle u_i(t)\, u_j^\dagger(t') \rangle = \langle v_i(t)\, v_j^\dagger(t') \rangle = \delta_{ij} \delta(t - t')$$

in the time domain, or

$$\langle u_i(\omega)\ u_j^\dagger(\omega')\rangle = \langle v_i(\omega)\ v_j^\dagger(\omega')\rangle = 2\pi\delta_{ij}\delta(\omega-\omega')$$

in the frequency domain.

The small-signal analysis is calculated by writing the internal field variable A_i as

$$\begin{aligned} A_i &= r_i(1+a_i)e^{i\phi_i} \\ &= r_i(1+\mu_i+i\psi_i)e^{i\phi_i}, \end{aligned} \tag{A.10}$$

where r_i and ϕ_i are the classical mean field amplitude and phase angle, μ_i is the normalized small-signal amplitude fluctuation, and ψ_i is the small-signal phase fluctuation.

$$\mu_i = \frac{1}{2}(a_i + a_i^\dagger) \qquad \text{and} \qquad \psi_i = \frac{1}{2i}(a_i - a_i^\dagger)$$

where a_i is the annihilation operator. The classical mean-field amplitude and phase angle are constants of time and any fluctuation is contained within the operators μ_i and ψ_i. The small signal equations are obtain by substituting Eq. (A.10) into Eqs. (A.9) keeping only first order terms in u_i and v_i. For example, the small signal pump equation is given by

$$\begin{aligned} &\dot{\mu_p} + i\dot{\psi_p} = \\ &\quad -\kappa_p(1+\mu_p+i\psi_p) - \frac{\chi r_1 r_2}{r_p}(1+\mu_+ + i\psi_+)e^{i\theta_\Delta} + \frac{\sqrt{2\kappa_p}}{r_p}e_p e^{i(\theta_p-\phi_p)} + \frac{\sqrt{2\kappa_p}}{r_p}u_p e^{i\phi_p}, \end{aligned} \tag{A.11}$$

where we have defined

$$\begin{aligned} \mu_\pm &= \mu_1 \pm \mu_2, \\ \psi_\pm &= \psi_1 \pm \psi_2. \end{aligned}$$

Here, μ_+ is the summed intensity fluctuation and ψ_- is the phase difference fluctuation between the signal and the idler fields. Our goal is to derive expressions for μ_+ and

ψ_-, and using these expressions to calculate their power spectra. With Eqs. (A.4) and (A.5), we can rewrite

$$\frac{\chi r_1 r_2}{r_p} e^{i\theta_\Delta} = \kappa_p(\alpha_r + i\alpha_i), \tag{A.12}$$

where

$$\alpha_r = \frac{\sqrt{F_p - (\Delta_1/\kappa_1)^2} - 1}{1 + (\Delta_1/\kappa_1)^2} \quad \text{and} \quad \alpha_i = \frac{\alpha_r \Delta_1}{\kappa_1}.$$

Note that

$$\frac{\alpha_i}{\alpha_r} = \tan\theta_\Delta.$$

The small-signal solution therefore yields

$$\frac{\sqrt{2\kappa_p}}{r_p} e_p e^{i(\theta_p - \phi_p)} = \kappa_p + \frac{\chi r_1 r_2}{r_p} e^{i\theta_\Delta}, \tag{A.13}$$

We define the real and imaginary parts of the vacuum input modes,

$$\mu_i^u = \frac{1}{2}(\tilde{u}_i + \tilde{u}_i^\dagger) \qquad \text{and} \qquad \psi_i^u = \frac{1}{2i}(\tilde{u}_i - \tilde{u}_i^\dagger), \tag{A.14}$$

where

$$\tilde{u}_i = u_i e^{-i\phi_i}, \qquad\qquad i = 1,\ 2,\ p.$$

Substituting Eq. (A.13) back into the pump field equation (Eq. (A.11)) gives

$$\dot{\mu_p} + i\dot{\psi_p} = -\kappa_p\mu_p - i\kappa_p\psi_p - \kappa_p(\alpha_r + i\alpha_i)(\mu_+ + i\psi_+) + \frac{\sqrt{2\kappa_p}}{r_p}(\mu_p^u + i\psi_p^u). \tag{A.15}$$

The real and imaginary parts of Eq. (A.15) give the equations of motion for the internal pump field amplitude and phase:

$$\begin{aligned}
\dot{\mu_p} &= -\kappa_p\mu_p - \kappa_p(\alpha_r\mu_+ - \alpha_i\psi_+) + \frac{\sqrt{2\kappa_p}}{r_p}\mu_p^u, \\
\dot{\psi_p} &= -\kappa_p\psi_p - \kappa_p(\alpha_r\psi_+ + \alpha_i\mu_+) + \frac{\sqrt{2\kappa_p}}{r_p}\psi_p^u.
\end{aligned}$$

It is more convenience to work in the frequency domain for spectral calculations. The

above time-domain equations are Fourier transformed using

$$F(\omega) = \frac{1}{2\pi}\int_{-\infty}^{\infty} dt\, f(t)e^{i\omega t}, \tag{A.16}$$

to obtain the frequency-domain equations,

$$\begin{aligned}
(\kappa_p - i\omega)\mu_p(\omega) &= -\kappa_p\alpha_r\mu_+(\omega) + \kappa_p\alpha_i\psi_+(\omega) + R_p(\omega), &\text{(A.17)}\\
(\kappa_p - i\omega)\psi_p(\omega) &= -\kappa_p\alpha_r\psi_+(\omega) - \kappa_p\alpha_i\mu_+(\omega) + \Lambda_p(\omega). &\text{(A.18)}
\end{aligned}$$

Here,

$$\begin{aligned}
R_p(\omega) &= \frac{\sqrt{2\kappa_p}}{2r_p}\left(\tilde{u}_p(\omega) + \tilde{u}_p^{\dagger}(-\omega)\right), &\text{(A.19)}\\
\text{and}\quad \Lambda_p(\omega) &= \frac{\sqrt{2\kappa_p}}{2ir_p}\left(\tilde{u}_p(\omega) - \tilde{u}_p^{\dagger}(-\omega)\right), &\text{(A.20)}
\end{aligned}$$

are the amplitude-quadrature and the phase-quadrature noise of the pump field, respectively. Assuming that the pump intensity noise and the pump phase noise are not correlated, their nonzero correlations are

$$\begin{aligned}
\langle R_p(\omega)R_p(\omega')\rangle &= 2\pi\frac{\kappa_p^2\alpha_r}{2C^2}h^R(\omega)\delta(\omega+\omega'), &\text{(A.21)}\\
\langle \Lambda_p(\omega)\Lambda_p(\omega')\rangle &= 2\pi\frac{\kappa_p^2\alpha_r}{2C^2}h^{\Lambda}(\omega)\delta(\omega+\omega'). &\text{(A.22)}
\end{aligned}$$

h^R and $h^{\Lambda} \geq 1$ are the pump intensity and the pump phase noise factors. For a shot-noise-limited pump, h^R and h^{Λ} equal 1.

Similarly, we follow the same procedure as in the derivation of the pump field equations to obtain for the signal (A_1) and the idler (A_2) time-domain field equations,

$$\begin{aligned}
\dot{\mu_1} &= \kappa_1\mu_p - \kappa_1\mu_- + \Delta_1\psi_p - \Delta_1\psi_+ + \frac{\sqrt{2\gamma_1\kappa_1}}{C}\mu_1^u + \frac{\sqrt{2\kappa_1(\kappa_1-\gamma_1)}}{C}\mu_1^v,\\
\dot{\psi_1} &= -\Delta_1\mu_p + \Delta_1\mu_- + \kappa_1\psi_p - \kappa_1\psi_+ + \frac{\sqrt{2\gamma_1\kappa_1}}{C}\psi_1^u + \frac{\sqrt{2\kappa_1(\kappa_1-\gamma_1)}}{C}\psi_1^v,\\
\dot{\mu_2} &= \kappa_2\mu_p + \kappa_2\mu_- + \Delta_2\psi_p - \Delta_2\psi_+ + \frac{\sqrt{2\gamma_2\kappa_2}}{C}\mu_2^u + \frac{\sqrt{2\kappa_2(\kappa_2-\gamma_2)}}{C}\mu_2^v,
\end{aligned}$$

$$\dot{\psi}_2 = -\Delta_2\mu_p - \Delta_2\mu_- + \kappa_2\psi_p - \kappa_2\psi_+ + \frac{\sqrt{2\gamma_2\kappa_2}}{C}\psi_2^u + \frac{\sqrt{2\kappa_2(\kappa_2-\gamma_2)}}{C}\psi_2^v.$$

The equations of motion for the summed and differential signal-idler fluctuations are,

$$\begin{aligned}
\dot{\mu_+} &= \dot{\mu_1} + \dot{\mu_2} &&= \kappa\mu_p - \delta\mu_- + \Delta\psi_p - \Delta\psi_+ + R_+, \\
\dot{\mu_-} &= \dot{\mu_1} - \dot{\mu_2} &&= \delta\mu_p - \kappa\mu_- + \beta\psi_p - \beta\psi_+ + R_-, \\
\dot{\psi_+} &= \dot{\psi_1} + \dot{\psi_2} &&= -\Delta\mu_p + \beta\mu_- + \kappa\psi_p - \kappa\psi_+ + \Lambda_+, \\
\dot{\psi_-} &= \dot{\psi_1} - \dot{\psi_2} &&= -\beta\mu_p + \Delta\mu_- + \delta\psi_p - \delta\psi_+ + \Lambda_-.
\end{aligned}$$

Here, we have defined the following variables to simplify the algebra,

$$\kappa = \kappa_1 + \kappa_2, \tag{A.23}$$

$$\delta = \kappa_1 - \kappa_2, \tag{A.24}$$

$$\Delta = \Delta_1 + \Delta_2, \tag{A.25}$$

$$\beta = \Delta_1 - \Delta_2. \tag{A.26}$$

It should be noted that because of the normalized-detuning constraint (Eq. (A.2)), the newly defined variables must satisfy

$$\frac{\delta}{\kappa} = \frac{\beta}{\Delta}.$$

Also, the R's and the Λ's are defined as,

$$\begin{aligned}
R_i^u &= \sqrt{\frac{\gamma_i}{\kappa_i}}\,\mu_i^u = \frac{1}{2}\sqrt{\frac{\gamma_i}{\kappa_i}}\,(\tilde{u}_i + \tilde{u}_i^\dagger), \\
R_i^v &= \sqrt{1-\frac{\gamma_i}{\kappa_i}}\,\mu_i^v = \frac{1}{2}\sqrt{1-\frac{\gamma_i}{\kappa_i}}\,(\tilde{v}_i + \tilde{v}_i^\dagger), \\
R_\pm &= \frac{1}{\sqrt{2}C}\left[(\kappa+\delta)(R_1^u + R_1^v) \pm (\kappa-\delta)(R_2^u + R_2^v)\right], \\
\Lambda_i^u &= \sqrt{\frac{\gamma_i}{\kappa_i}}\,\psi_i^u = \frac{1}{2i}\sqrt{\frac{\gamma_i}{\kappa_i}}\,(\tilde{u}_i - \tilde{u}_i^\dagger),
\end{aligned} \tag{A.27}$$

$$\Lambda_i^v = \sqrt{1-\frac{\gamma_i}{\kappa_i}}\,\psi_i^v = \frac{1}{2i}\sqrt{1-\frac{\gamma_i}{\kappa_i}}\,(\tilde{v}_i - \tilde{v}_i^\dagger),$$
$$\Lambda_\pm = \frac{1}{\sqrt{2}\,C}\left[(\kappa+\delta)(\Lambda_1^u + \Lambda_1^v) \pm (\kappa-\delta)(\Lambda_2^u + \Lambda_2^v)\right].$$

The complete set of nonhomogeneous coupled equations for the OPO internal-field amplitudes and phases are

$$\begin{aligned}
(\kappa_p - i\omega)\mu_p &= -\kappa_p\alpha_r\mu_+ + \kappa_p\alpha_i\psi_+ + R_p, \\
-i\omega\mu_+ &= -\delta\mu_- + \kappa\mu_p + \Delta\psi_p - \Delta\psi_+ + R_+, \\
(\kappa - i\omega)\mu_- &= \delta\mu_p + \beta\psi_p - \beta\psi_+ + R_-, \\
(\kappa_p - i\omega)\psi_p &= -\kappa_p\alpha_r\psi_+ - \kappa_p\alpha_i\mu_+ + \Lambda_p, \\
(\kappa - i\omega)\psi_+ &= \kappa\psi_p + \beta\mu_- - \Delta\mu_p + \Lambda_+, \\
-i\omega\psi_- &= -\delta\psi_+ + \delta\psi_p + \Delta\mu_- - \beta\mu_p + \Lambda_-.
\end{aligned}$$

As a reminder, the μ's are the field amplitude operators and the ψ's are the field phase operators. We rewrite the above set of equations in matrix form to solve for the variables μ's and ψ's.

$$M\begin{pmatrix} \mu_p \\ \mu_+ \\ \mu_- \\ \psi_p \\ \psi_+ \\ \psi_- \end{pmatrix} = \begin{pmatrix} R_p \\ R_+ \\ R_- \\ \Lambda_p \\ \Lambda_+ \\ \Lambda_- \end{pmatrix},$$

where the matrix M is

$$\begin{pmatrix} \kappa_p - i\omega & \kappa_p\alpha_r & 0 & 0 & -\kappa_p\alpha_i & 0 \\ -\kappa & -i\omega & \delta & -\Delta & \Delta & 0 \\ -\delta & 0 & \kappa - i\omega & -\beta & \beta & 0 \\ 0 & \kappa_p\alpha_i & 0 & \kappa_p - i\omega & \kappa_p\alpha_r & 0 \\ \Delta & 0 & -\beta & -\kappa & \kappa - i\omega & 0 \\ \beta & 0 & -\Delta & -\delta & \delta & -i\omega \end{pmatrix}.$$

The coupled equations are readily solved by inverting M. If we write

$$N = M^{-1} = \begin{pmatrix} N_{11} & \cdots & N_{16} \\ \vdots & \ddots & \vdots \\ N_{61} & \cdots & N_{66} \end{pmatrix}, \tag{A.28}$$

then the signal-idler phase difference fluctuation (ψ_-) and sum intensity fluctuation (μ_+) are given by

$$\psi_- = N_{61}R_p + N_{62}R_+ + N_{63}R_- + N_{64}\Lambda_P + N_{65}\Lambda_+ + N_{66}\Lambda_-, \tag{A.29}$$

$$\mu_+ = N_{21}R_p + N_{22}R_+ + N_{23}R_- + N_{24}\Lambda_P + N_{25}\Lambda_+ + N_{26}\Lambda_-. \tag{A.30}$$

A.3 External Noise Measurement

Before we can proceed with our calculation, we need to specify the detection method in the experiment. Different detection schemes may require different modeling. We used direct detection to measure the phase noise between the signal and the idler with a rf spectrum analyzer. As in the phase-locking experiment, the emerging signal-idler field $E(t)$ was detected with a high-speed photodetector to generate a photocurrent $I(t)$. The ac photocurrent was split into two parts for beat frequency stabilization and noise measurement (Fig. A-1). The first part was input to the PLL to phase lock the signal-idler beat signal at 30 MHz and the second part was demodulated with a local oscillator (LO) at 30 MHz that was phase locked to the LO of the PLL. The

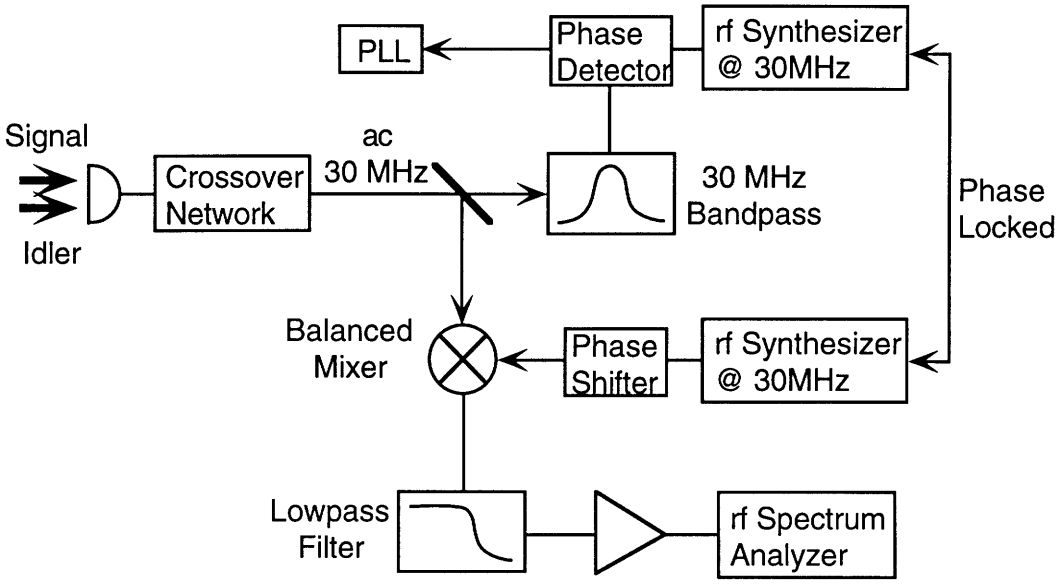

Figure A-1: Electronic setup of the phase noise measurement experiment.

demodulated beat-note signal was low-pass filtered and amplified and input to a rf spectrum analyzer for noise spectrum measurement. The LO and the PLL 30-MHz reference signals were phase locked together to eliminate any systematic drifts. The phase of the LO could be adjusted to give the in-phase ($x(t)$) or the quadrature-phase ($y(t)$) of the beat note signal.

The total electric field $E(t)$ emerging from the cavity is

$$\begin{aligned} E(t) &= \sqrt{2\gamma_1}\, r_1(1+\mu_1+i\psi_1)e^{-i(\omega_1 t-\phi_1)} + \sqrt{2\gamma_2}\, r_2(1+\mu_2+i\psi_2)e^{-i(\omega_2 t-\phi_2)} \\ &\quad -u_1 e^{-i\omega_1 t} - u_2 e^{-i\omega_2 t} - u_3 e^{-i(2\omega_1-\omega_2)t} - u_4 e^{-i(2\omega_2-\omega_1)t}. \end{aligned}$$

The image-band vacuum modes, u_3 and u_4, are included in order to give the correct shot-noise level [38]. Retaining second-order μ_i and ψ_i product terms, the ac and dc components of the photocurrent $I(t)$ are then given by

$$\begin{aligned} I_{dc}(t) &= 2\left(\frac{\gamma_1}{\kappa_1}+\frac{\gamma_2}{\kappa_2}\right)C^2 + 4\left(\frac{\gamma_1}{\kappa_1}\mu_1+\frac{\gamma_2}{\kappa_2}\mu_2\right)C^2 \\ &\quad + 2C^2\left(\frac{\gamma_1}{\kappa_1}(\mu_1^2+\psi_1^2)+\frac{\gamma_2}{\kappa_2}(\mu_2^2+\psi_2^2)\right) - \sqrt{8}\,C\left(\sqrt{\frac{\gamma_1}{\kappa_1}}\,\mu_1^u + \sqrt{\frac{\gamma_2}{\kappa_2}}\,\mu_2^u\right), \end{aligned}$$

$$
\begin{aligned}
I_{ac}(t) &= 2C^2\sqrt{\frac{\gamma_1\gamma_2}{\kappa_1\kappa_2}}\,(1+\mu_+ + i\psi_- + \mu_1\mu_2 + \psi_1\psi_2 + i(\mu_2\psi_1 - \psi_2\mu_1))\,e^{-i(\omega_{12}t-\phi_{12})} \\
&\quad - \sqrt{\frac{2\gamma_1}{\kappa_1}}\,C(\tilde{u}_2^\dagger + \tilde{u}_3)e^{-i(\omega_{12}t-\phi_{12})} - \sqrt{\frac{2\gamma_2}{\kappa_2}}\,C(\tilde{u}_1 + \tilde{u}_4^\dagger)e^{-i(\omega_{12}t-\phi_{12})} \\
&\quad + \text{hermitian conjugate},
\end{aligned}
$$

where

$$
\tilde{u}_3 = u_3 e^{-i(2\phi_1-\phi_2)} \quad \text{and} \quad \tilde{u}_4 = u_4 e^{-i(2\phi_2-\phi_1)}.
$$

The quantum efficiency of the photodetector and the electron charge is set to 1 for convenience. The shot-noise level is given by,

$$
S_0 = 2\left(\frac{\gamma_1}{\kappa_1} + \frac{\gamma_2}{\kappa_2}\right)C^2.
$$

The demodulated lowpass-filtered in-phase and quadrature-phase of the photocurrent $I_{ac}(t)$ are

$$
\begin{aligned}
\text{in-phase} : x(t) &= \frac{1}{\tau}\int_0^t d\tau\, I_{ac}(\tau)\cos(\omega_{12}\tau - \phi_{12}), \\
\text{quadrature-phase} : y(t) &= \frac{1}{\tau}\int_0^t d\tau\, I_{ac}(\tau)\sin(\omega_{12}\tau - \phi_{12}),
\end{aligned}
$$

A.4 Quadrature-Phase Noise Spectrum

The quadrature-phase of the demodulated photocurrent $y(t)$ is

$$
\begin{aligned}
y(t) &= 2C^2\sqrt{\frac{\gamma_1\gamma_2}{\kappa_1\kappa_2}}\,(\psi_- - \mu_1\psi_2 + \psi_1\mu_2) \\
&\quad + \sqrt{\frac{2\gamma_1}{\kappa_1}}\,(\psi_2^u - \psi_3^u)C + \sqrt{\frac{2\gamma_2}{\kappa_2}}\,(\psi_4^u - \psi_1^u)C \qquad \text{(A.31)} \\
&\approx 2C^2\sqrt{\frac{\gamma_1\gamma_2}{\kappa_1\kappa_2}}\,\psi_- + \sqrt{\frac{2\gamma_1}{\kappa_1}}\,(\psi_2^u - \psi_3^u)C + \sqrt{\frac{2\gamma_2}{\kappa_2}}\,(\psi_4^u - \psi_1^u)C, \qquad \text{(A.32)}
\end{aligned}
$$

and its power spectrum, normalized to shot-noise level, is obtained from

$$
S_y(\omega) = \frac{1}{S_0}\int_{-\infty}^{\infty} d\tau \langle y(\tau)y(0)\rangle e^{i\omega\tau}
$$

$$= \frac{1}{S_0}\int_{-\infty}^{\infty}\frac{d\omega'}{2\pi}\langle Y(\omega)Y(\omega')\rangle,$$

where $Y(\omega)$ is the Fourier transform of $y(t)$, $Y(\omega) = \mathcal{F}\{y(t)\}$. Equation (A.32) is obtained by retaining only the first order terms in Eq. (A.31). The remaining task is to carry out the algebraic calculation with the use of correlation relations to obtain the quadrature-phase noise spectrum. For our linearized calculation, we ignore the second-order terms to obtain

$$\begin{aligned}
S_y(\omega) &= \frac{4C^2}{S_0}\frac{\gamma_1\gamma_2}{\kappa_1\kappa_2}\Big\{\kappa_p^2\alpha_r\left(h^R|N_{61}|^2 + h^\Lambda|N_{64}|^2\right) \\
&\quad + (\kappa_1^2+\kappa_2^2)\Big(|N_{62}|^2 + |N_{63}|^2 + |N_{65}|^2 + |N_{66}|^2 \\
&\qquad\qquad - 2\Im\{N_{62}N_{65}^*\} - 2\Im\{N_{63}N_{66}^*\}\Big) \\
&\quad + 2(\kappa_1^2-\kappa_2^2)\left(\Re\{N_{62}N_{63}^*\} + \Re\{N_{65}N_{66}^*\} - \Im\{N_{62}N_{66}^*\} - \Im\{N_{63}N_{65}^*\}\right)\Big\} \\
&\quad + 2\left(\frac{\gamma_1}{\kappa_1}+\frac{\gamma_2}{\kappa_2}\right)\frac{C^2}{S_0} \\
&\quad - 4\frac{\gamma_1\gamma_2}{\kappa_1\kappa_2}\frac{C^2}{S_0}\kappa_2\left(\Re\{N_{65}-N_{66}\} - \Im\{N_{62}-N_{63}\}\right) \\
&\quad - 4\frac{\gamma_1\gamma_2}{\kappa_1\kappa_2}\frac{C^2}{S_0}\kappa_1\left(\Re\{N_{65}+N_{66}\} - \Im\{N_{62}+N_{63}\}\right), \qquad \text{(A.33)}
\end{aligned}$$

where $\Re$ and $\Im$ refer to the real and imaginary part of the relevant quantities. If we examine the phase diffusion noise spectrum (Eq. (A.33)) more carefully, we can trace each term back to its origin. The variable ψ_i^u (Eq. (A.14)) arises from the vacuum mode variable u_i, its interaction with itself ($\langle\psi_i^u(\omega)\psi_i^u(\omega')\rangle$) gives rise to the shot-noise level. The terms $h^R|N_{61}|^2$ and $h^\Lambda|N_{64}|^2$ are the transferred pump intensity- and phase-noise. The last four terms originate from the signal-idler phase difference ($\psi_-(\omega)$) and vacuum noise interactions ($\psi_i^u(\omega)$), i.e. $\langle\psi_i^u(\omega)\psi_-(\omega')\rangle$.

A.5 In-Phase Noise Spectrum

The in-phase signal of the demodulated photocurrent $x(t)$ is

$$\begin{aligned} x(t) &= 2C^2\sqrt{\frac{\gamma_1\gamma_2}{\kappa_1\kappa_2}}\,(1+\mu_+ + \mu_1\mu_2 + \psi_1\psi_2) - \sqrt{\frac{2\gamma_1}{\kappa_1}}\,(\mu_2^u + \mu_3^u)C - \sqrt{\frac{2\gamma_2}{\kappa_2}}\,(\mu_4^u + \mu_1^u)C \\ &\approx 2C^2\sqrt{\frac{\gamma_1\gamma_2}{\kappa_1\kappa_2}}\,(1+\mu_+) - \sqrt{\frac{2\gamma_1}{\kappa_1}}\,(\mu_2^u + \mu_3^u)C - \sqrt{\frac{2\gamma_2}{\kappa_2}}\,(\mu_4^u + \mu_1^u)C. \end{aligned}$$

Since we are interested in the noise spectrum, we only need to consider the fluctuating terms of the in-phase signal,

$$\Delta x(t) = 2C^2\sqrt{\frac{\gamma_1\gamma_2}{\kappa_1\kappa_2}}\,\mu_+ - \sqrt{\frac{2\gamma_1}{\kappa_1}}\,(\mu_2^u + \mu_3^u)C - \sqrt{\frac{2\gamma_2}{\kappa_2}}\,(\mu_4^u + \mu_1^u)C.$$

The algebra is much simplified in the special case of zero detuning ($\Delta_1 = \Delta_2 = 0$). We do not believe that detuning affects the noise spectrum significantly. The correlations needed to calculate the in-phase spectrum were worked out by Wong *et al.* in Ref. [44]. With reference to their calculation, the in-phase power spectrum is calculated as

$$\begin{aligned} S_x(\omega) &= \frac{1}{S_0}\int_{-\infty}^{\infty}\frac{d\omega'}{2\pi}\langle\Delta x(\omega)\Delta x(\omega')\rangle \\ &= 2\frac{C^2}{S_0}\left\{\frac{\gamma_1\gamma_2}{\kappa_1\kappa_2}\frac{1}{|D|^2}\left[(\kappa_p^2+\omega^2)\left((\kappa^2+\delta^2)(\kappa^2+\delta^2+\omega^2) - 4\kappa^2\delta^2\right)\right.\right. \\ &\qquad \left.\left. + 2\epsilon\kappa_p^2 h^R(\omega)|\kappa^2 - \delta^2 - i\kappa\omega|^2\right] \right. \\ &\quad \left. + \left(\frac{\gamma_1}{\kappa_1} + \frac{\gamma_2}{\kappa_2}\right) \right. \\ &\quad \left. - 2\frac{\gamma_1\gamma_2}{\kappa_1\kappa_2}\Re\left\{\frac{(\kappa_p - i\omega)(\kappa^2 - \delta^2 - i\kappa\omega)}{D}\right\}\right\}, \end{aligned}$$

$$\begin{aligned} \epsilon &= \sqrt{F_p} - 1, \\ D &= (\kappa^2 - \delta^2)\kappa_p\epsilon - \omega^2(\kappa_p + \kappa) - i\omega\left[\kappa\kappa_p(\epsilon+1) - \omega^2\right]. \end{aligned}$$

A.6 Intensity Noise Spectrum

The intensity noise spectrum is also calculated in the special case of zero detuning. Since the constant term in I_{dc} does not contribute to the intensity noise spectrum, we only need to consider the fluctuating terms :

$$\begin{aligned}\Delta I_{dc} &= 4\left(\frac{\gamma_1}{\kappa_1}\mu_1 + \frac{\gamma_2}{\kappa_2}\mu_2\right)C^2 - \sqrt{8}\,C\left(\sqrt{\frac{\kappa_1}{\gamma_1}}\,\mu_1^u + \sqrt{\frac{\kappa_2}{\gamma_2}}\,\mu_2^u\right), \\ &= 4C^2\left(\Gamma\mu_+ + g\mu_-\right) - \sqrt{8}\,C\left(R_1^u + R_2^u\right),\end{aligned}$$

with

$$\begin{aligned}\Gamma &= \frac{1}{2}\left(\frac{\gamma_1}{\kappa_1} + \frac{\gamma_2}{\kappa_2}\right), \\ g &= \frac{1}{2}\left(\frac{\gamma_1}{\kappa_1} - \frac{\gamma_2}{\kappa_2}\right).\end{aligned}$$

The intensity noise spectrum is then obtained from

$$\begin{aligned}S_x(\omega) &= \frac{1}{S_0}\int_{-\infty}^{\infty} d\tau \langle \Delta I_{dc}(\tau)\Delta I_{dc}(0)\rangle e^{i\omega\tau} \\ &= \frac{1}{S_0}\int_{-\infty}^{\infty} \frac{d\omega'}{2\pi}\langle \Delta I_{dc}(\omega)\Delta I_{dc}(\omega')\rangle.\end{aligned}$$

A.7 List of Correlations

$$\begin{aligned}\langle R_i^u(\omega)R_j^u(\omega')\rangle &= \frac{1}{4}\frac{\gamma_i}{\kappa_i}\delta_{ij}2\pi\delta(\omega+\omega'), \\ \langle R_i^v(\omega)R_j^v(\omega')\rangle &= \frac{1}{4}\left(1-\frac{\gamma_i}{\kappa_i}\right)\delta_{ij}2\pi\delta(\omega+\omega'), \\ \langle \Lambda_i^u(\omega)\Lambda_j^u(\omega')\rangle &= \frac{1}{4}\frac{\gamma_i}{\kappa_i}\delta_{ij}2\pi\delta(\omega+\omega'), \\ \langle \Lambda_i^v(\omega)\Lambda_j^v(\omega')\rangle &= \frac{1}{4}\left(1-\frac{\gamma_i}{\kappa_i}\right)\delta_{ij}2\pi\delta(\omega+\omega'), \\ \langle R_\pm(\omega)R_\pm(\omega')\rangle &= \frac{\kappa^2+\delta^2}{4C^2}2\pi\delta(\omega+\omega'), \\ \langle R_\pm(\omega)R_\mp(\omega')\rangle &= \frac{\kappa\delta}{2C^2}2\pi\delta(\omega+\omega'),\end{aligned}$$

$$
\begin{aligned}
\langle \Lambda_{\pm}(\omega)\Lambda_{\pm}(\omega')\rangle &= \langle R_{\pm}(\omega)R_{\pm}(\omega')\rangle, \\
\langle \Lambda_{\pm}(\omega)\Lambda_{\mp}(\omega')\rangle &= \langle R_{\pm}(\omega)R_{\mp}(\omega')\rangle, \\
\langle R_i^u(\omega)\Lambda_j^u(\omega')\rangle &= -\frac{1}{4i}\frac{\gamma_i}{\kappa_i}\delta_{ij}2\pi\delta(\omega+\omega'), \\
\langle R_i^v(\omega)\Lambda_j^v(\omega')\rangle &= -\frac{1}{4i}\left(1-\frac{\gamma_i}{\kappa_i}\right)\delta_{ij}2\pi\delta(\omega+\omega'), \\
\langle R_{\pm}(\omega)\Lambda_{\pm}(\omega')\rangle &= -\frac{\kappa^2+\delta^2}{4iC^2}2\pi\delta(\omega+\omega'), \\
\langle R_{\pm}(\omega)\Lambda_{\mp}(\omega')\rangle &= -\frac{\kappa\delta}{2iC^2}2\pi\delta(\omega+\omega').
\end{aligned}
$$

Appendix B

Dual-Cavity DRO Tuning Calculation

B.1 Introduction

In this appendix, we derive the equations that are used to predict the frequency tuning range of the dual-cavity DRO (DCDRO). The threshold and the output power of the DCDRO are calculated as a function of the cavity length changes. Our calculation includes three different effects: pump resonance, polarizer leakage and polarization axis misalignment between the crystal and the polarizer. These effects can be individually selected in our final equations so that their individual and combined contributions to the reduction of the tuning range can be examined.

B.2 Model and Assumptions

We use the plane-wave approximation for the DRO three-wave mixing equations with the following assumptions:

- arbitrary reflectivities and transmissivities for all optical surfaces at input and output wavelengths;
- high finesse IR cavities (~300);

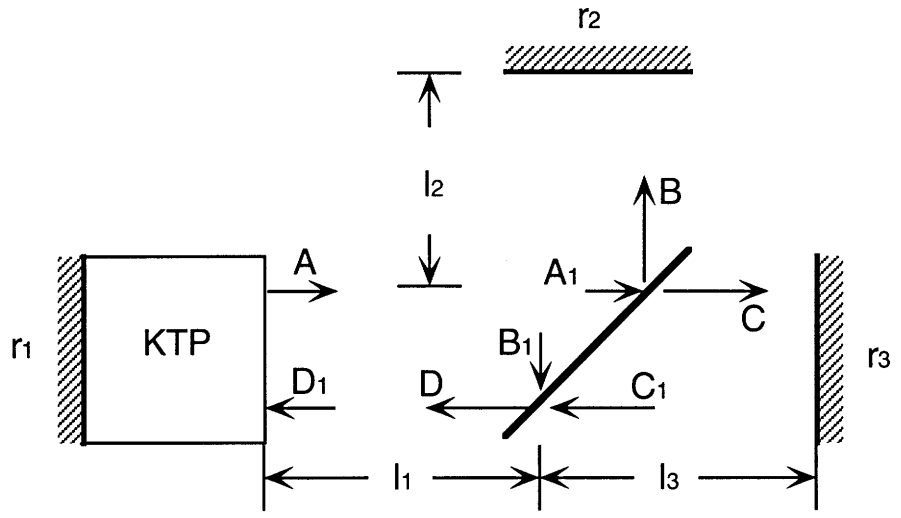

Figure B-1: Sketch of DCDRO showing internal IR fields (A–D). r_1, r_2 and r_3 are the mirror surfaces.

- angular misalignment between crystal and polarizer axes;
- depolarized light is not correctly phase matched;
- "dynamic" phase mismatch and dispersion are not included.

Figure B-1 shows a sketch of a DCDRO illustrating various reflecting surfaces and internal fields. With reference to Fig. B-1, we shall label the optical cavity formed by the crystal's front surface (r_1) and the output coupler r_3 as the signal cavity, and the cavity formed by the crystal front surface (r_1), the polarizer, and the high reflector r_2 as the idler cavity. The horizontally polarized field resonating in the signal cavity is referred as the signal, and the vertically polarized field resonating in the idler cavity is referred as the idler.

Because of the polarization axes misalignment, there are a total of five different internal modes that we need to keep track of. In addition to the usual pump, signal and idler fields, there are the depolarized signal (vertical) and idler (horizontal) fields. Table B.1 summaries the five modes, their polarizations and their variable names.

Mode	Polarization	Variable Name
Pump	Vertical	E_p
Signal	Horizontal	E_s
Idler	Vertical	E_i
Depolarized Signal	Vertical	ϵ_s
Depolarized Idler	Horizontal	ϵ_i

Table B.1: Summary of the five DCDRO internal mode polarizations and variable names.

B.3 Calculation

B.3.1 Outline of Procedure

The basic procedure of the derivation is to follow the internal fields for one round trip in the dual cavities to workout the polarization transfer functions for the two polarizations. We then apply the boundary conditions by requiring that the initial and final fields are identical after one round trip. In the case of the normal pump, signal and idler fields, the boundary conditions include the increase or decrease in field amplitude from the parametric interaction. In the case of the depolarized fields, because of phase mismatch, the boundary condition is simply the self-consistency requirement without any parametric interaction.

The five equations obtained for the five field modes inside the DCDRO can be further reduced to three coupled equations for the pump, the signal and the idler by using the self-consistency requirement again. The resulting set of three coupled equations describes the three waves inside the cavity and contains all the information. The threshold and output power equations are then obtained by solving this set of coupled equations.

With reference to Figure B-1, we define the following variables and nomenclature for our derivation:

- r_{1s} and r_{1i} are the field reflectivities of the coated crystal mirror surface for the signal and the idler fields, respectively;

- r_2 is the field reflectivity of the idler-cavity (vertical polarization) high reflector;
- r_3 is the field reflectivity of the signal-cavity (horizontal polarization) output coupler;
- t_{kp} and r_{kp} are the field transmissivity and reflectivity of mirror k for the vertically polarized pump field, where $k = 1, 2, 3$;
- 's' and 'i' in subscript or superscript denote variables associated with the signal and the idler fields, respectively.
- t_k and r_k are the field transmissivity and reflectivity of the polarizer plate for the polarization k, where $k = v$ for vertical polarization and $k = h$ for horizontal polarization;
- t_{pp} and r_{pp} are the field transmissivity and reflectivity of the polarizer plate for the vertically polarized pump field;
- $(\hat{i}, \hat{j})$ are the unit vectors representing the horizontal and vertical polarization axes of the polarizer;
- $(\hat{i}', \hat{j}')$ are the unit vectors representing the optical axes defined by the KTP crystal;
- θ is the depolarization angle between the unit vectors $\hat{i}$ and $\hat{i}'$.

The two sets of unit vectors $(\hat{i}, \hat{j})$ and $(\hat{i}', \hat{j}')$ are related by

$$\begin{aligned} \hat{i} &= c\hat{i}' - s\hat{j}', \\ \hat{j} &= s\hat{i}' + c\hat{j}', \end{aligned}$$

where $c = \cos\theta$ and $s = \sin\theta$.

B.3.2 Derivation

The total internal field inside the DCDRO can be written as the sum of the normal signal (E_s) and idler (E_i) fields and the depolarized signal (ϵ_s) and idler (ϵ_i) fields,

$$\vec{A} + \vec{a},$$

where

$$\begin{aligned} \vec{A} &= E_s\hat{i}' + E_i\hat{j}', \\ \vec{a} &= \epsilon_i\hat{i}' + \epsilon_s\hat{j}'. \end{aligned}$$

We first consider the normal signal and idler fields ($\vec{A}$) by propagating E_s (horizontal polarization) and E_i (vertical polarization) through the dual cavities for one round trip, and then for the depolarized fields $\vec{a}$.

The field $\vec{A}$ propagating from the KTP crystal's flat surface toward the right is given by (Fig. B-1)

$$\vec{A} = E_s\hat{i}' + E_i\hat{j}'.$$

After propagating a distance of l_1 to the polarizer plate, the signal and the idler fields acquire phase shifts of $e^{-i\delta_1^s/2}$ and $e^{-i\delta_1^i/2}$ to become

$$\vec{A_1} = E_s e^{-i\delta_1^s/2}\hat{i}' + E_i e^{-i\delta_1^i/2}\hat{j}'.$$

The field $\vec{A_1}$ is split by the polarizer plate into $\vec{B}$ and $\vec{C}$, where

$$\vec{B} = -r_h\left(E_s c e^{-i\delta_1^s/2} - E_i s e^{-i\delta_1^i/2}\right)\hat{i} - r_v\left(E_s s e^{-i\delta_1^s/2} + E_i c e^{-i\delta_1^i/2}\right)\hat{j},$$

and

$$\vec{C} = -it_h\left(E_s c e^{-i\delta_1^s/2} - E_i s e^{-i\delta_1^i/2}\right)\hat{i} - it_v\left(E_s s e^{-i\delta_1^s/2} + E_i c e^{-i\delta_1^i/2}\right)\hat{j}.$$

Note that we have switched from the primed basis (crystal's axes) to the unprimed

basis (polarizer axes).

After reflecting off mirrors r_2, r_3, $\vec{B}$ and $\vec{C}$ become

$$\begin{aligned}
\vec{B}_1 &= r_2 r_h \left(E_s c e^{-i(\delta_1^s/2+\delta_2^s)} - E_i s e^{-i(\delta_1^i/2+\delta_2^i)}\right)\hat{i} \\
&\quad + r_2 r_v \left(E_s s e^{-i(\delta_1^s/2+\delta_2^s)} + E_i c e^{i(\delta_1^i/2+\delta_2^i)}\right)\hat{j}, \\
\vec{C}_1 &= -i r_3 t_h \left(E_s c e^{-i(\delta_1^s/2+\delta_3^s)} - E_i s e^{-i(\delta_1^i/2+\delta_3^i)}\right)\hat{i} \\
&\quad - i r_3 t_v \left(E_s s e^{-i(\delta_1^s/2+\delta_3^s)} + E_i c e^{-i(\delta_1^i/2+\delta_3^i)}\right)\hat{j}.
\end{aligned}$$

Here, $\delta_{2,3}^{s,i}$ are the phase shifts gained by the signal and idler fields after traveling distances $2l_2$ and $2l_3$ in the two legs of the dual-cavity. The phase gained by the two frequencies of the same polarization in the same leg of the cavity need not be equal because of dispersion. As an estimate, assuming the frequency difference (Δf_d) between the two outputs is 1 GHz, the phase difference seen by the two frequencies is

$$\begin{aligned}
\delta^s - \delta^i &= \frac{\Delta f_d \alpha l_c \pi}{\lambda/2}, \\
&\approx 9.0 \times 10^{-3},
\end{aligned}$$

where α is the dispersion coefficient ($\sim 1.6 \times 10^{-16}$ Hz^{-1}), l_c is the crystal length (9.5 mm), and λ is the output wavelength ($\sim$1.062 μm).

$\vec{B}_1$ and $\vec{C}_1$ recombine at the polarizer plate and travel leftward to give $\vec{D}_1$ at the flat surface of the crystal,

$$\begin{aligned}
\vec{D}_1 &= \left[r_3 t_h^2 \left(E_s c e^{-i(\delta_1^s+\delta_3^s)} - E_i s e^{-i(\delta_1^i+\delta_3^i)}\right) - r_2 r_h^2 \left(E_s c e^{-i(\delta_1^s+\delta_2^s)} - E_i s e^{-i(\delta_1^i+\delta_2^i)}\right)\right]\hat{i} \\
&\quad + \left[r_3 t_v^2 \left(E_s s e^{-i(\delta_1^s+\delta_3^s)} + E_i c e^{-i(\delta_1^i+\delta_3^i)}\right) - r_2 r_v^2 \left(E_s s e^{-i(\delta_1^s+\delta_2^s)} + E_i c e^{-i(\delta_1^i+\delta_2^i)}\right)\right]\hat{j}.
\end{aligned}$$

Rewriting $\vec{D}_1$ into the primed crystal axes $(\hat{i}', \hat{j}')$ gives

$$\begin{aligned}
\vec{D}_1 &= \left[E_s(m_1 c^2 + m_3 s^2) - E_i sc(m_2 - m_4)\right]\hat{i}' \\
&\quad + \left[E_s sc(m_3 - m_1) + E_i(m_2 s^2 + m_4 c^2)\right]\hat{j}',
\end{aligned}$$

where

$$
\begin{aligned}
m_1 &= r_3 t_h^2 e^{-i(\delta_1^s+\delta_3^s)} - r_2 r_h^2 e^{-i(\delta_1^s+\delta_2^s)}, \\
m_2 &= r_3 t_h^2 e^{-i(\delta_1^i+\delta_3^i)} - r_2 r_h^2 e^{-i(\delta_1^i+\delta_2^i)}, \\
m_3 &= r_3 t_v^2 e^{-i(\delta_1^s+\delta_3^s)} - r_2 r_v^2 e^{-i(\delta_1^s+\delta_2^s)}, \\
m_4 &= r_3 t_v^2 e^{-i(\delta_1^i+\delta_3^i)} - r_2 r_v^2 e^{-i(\delta_1^i+\delta_2^i)}.
\end{aligned}
$$

We now consider the depolarized signal ϵ_s (vertical polarization) and the depolarized idler ϵ_i (horizontal polarization) fields, as with the normal signal and idler fields. The depolarized field $\vec{a}$ propagating from KTP crystal's flat surface toward the right is given by

$$\vec{a} = \epsilon_i \hat{i}' + \epsilon_s \hat{j}'. \tag{B.1}$$

Following the same procedure, the leftward traveling depolarized field at the crystal surface ($\vec{d_1}$) is given by

$$
\begin{aligned}
\vec{d_1} &= \left[\epsilon_i(m_2c^2 + m_4s^2) - \epsilon_s sc(m_1 - m_3)\right]\hat{i}' \\
&\quad + \left[\epsilon_i sc(m_4 - m_2) + \epsilon_s(m_1s^2 + m_3c^2)\right]\hat{j}'.
\end{aligned} \tag{B.2}
$$

Since the parametric interaction does not involve the depolarized signal (ϵ_s, vertically polarized) and the depolarized idler (ϵ_i, horizontally polarized), the depolarized fields must recover itself after one round trip. Equating all the horizontally polarized ($\hat{i}'$) idler fields (subscript i) in Eqs. B.1–B.2, we obtain

$$
\begin{aligned}
\epsilon_i &= -r_{1s}\left[-E_i sc(m_2 - m_4) + \epsilon_i(m_2c^2 + m_4s^2)\right] e^{-i\delta_1^{i'}}, \\
\epsilon_i &= \frac{r_{1s}E_i sc(m_2 - m_4)}{e^{i\delta_1^{i'}} + r_{1s}(m_2c^2 + m_4s^2)},
\end{aligned}
$$

and similarly for the vertically polarized ($\hat{j}'$) signal fields (subscript s),

$$\epsilon_s = -r_{1i}\left[-E_s sc(m_3 - m_1) + \epsilon_s(m_1s^2 + m_3c^2)\right] e^{-i\delta_1^{s'}},$$

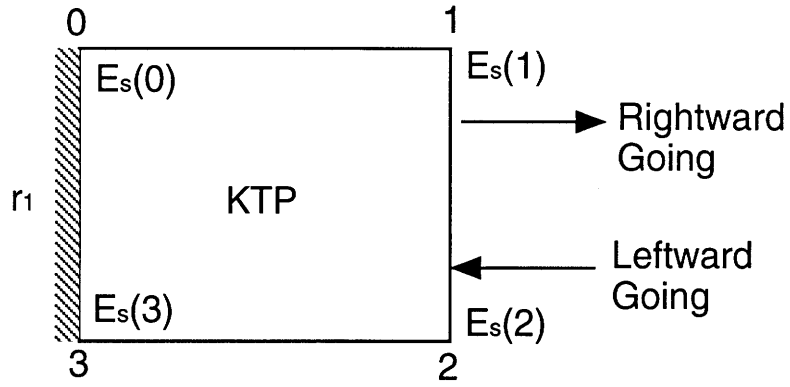

Figure B-2: A closeup look at the crystal boundary surfaces. Boundary surfaces '0' and '1' are for the rightward propagating field and '2' and '3' are for the leftward propagating fields.

$$\epsilon_s = \frac{r_{1i}E_s sc(m_1 - m_3)}{e^{i\delta_1^{s'}} + r_{1i}(m_1 s^2 + m_3 c^2)}.$$

Here, we have defined $e^{i\delta_1^{i'}}$ and $e^{i\delta_1^{s'}}$ as the phase shifts gained by the depolarized fields as they propagate through the crystal.

The total leftward propagating internal field at the crystal's flat surface is therefore

$$\begin{aligned}\vec{D}_1 + \vec{d}_1 &= -\left[E_s\alpha + \frac{E_i sc(m_2 - m_4)}{1 + r_{1s}(m_2 c^2 + m_4 s^2)e^{-i\delta_1^{i'}}}\right]\hat{i}' \\ &+ \left[\frac{-E_s sc(m_1 - m_3)}{1 + r_{1i}(m_1 s^2 + m_3 c^2)e^{-i\delta_1^{s'}}} - E_i\beta\right]\hat{j}',\end{aligned}$$

with

$$\begin{aligned}\alpha &= -\frac{m_1 c^2 + m_3 s^2 + r_{1i}m_1 m_3 e^{-i\delta_1^{s'}}}{1 + r_{1i}(m_1 s^2 + m_3 c^2)e^{-i\delta_1^{s'}}}, \\ \beta &= -\frac{m_2 s^2 + m_4 c^2 + r_{1s}m_2 m_4 e^{-i\delta_1^{i'}}}{1 + r_{1s}(m_2 c^2 + m_4 s^2)e^{-i\delta_1^{i'}}}.\end{aligned}$$

We are now ready to derive the set of three-wave mixing OPO equations. Again, since the depolarized signal and the depolarized idler fields are not correctly phase matched, they are ignored in our OPO equations. Figure B-2 shows a close-up sketch of the KTP crystal indicating the four boundary surfaces. The boundary surfaces

'0' and '1' are for the rightward traveling field and boundary surfaces '2' and '3' are for the leftward traveling fields. With reference to Fig. B-2, the signal fields at the crystal's boundary surfaces are given by

$$\begin{aligned} E_s(1) &= [E_s(0) + \chi' E_p(0) E_i^*(0)] e^{-ik_s' l_c}, \\ E_s(2) &= -\alpha E_s(1), \\ E_s(3) &= [E_s(2) + \chi' E_p(2) E_i^*(2)] e^{-ik_s' l_c}, \\ E_s(0) &= -r_{1s} E_s(3), \end{aligned}$$

where l_c is the crystal length, $k_s' = \frac{2\pi n_s}{\lambda_s}$ is the wave number for the signal mode inside the crystal, and the effective nonlinear coupling constant

$$\chi' = \chi e^{i\Delta k l_c/2} \frac{\sin(\frac{\Delta k l_c}{2})}{(\frac{\Delta k l_c}{2})}.$$

The above set of equations are solved simultaneously by keeping only the first order terms in χ'.

Similarly, we write down and solve the idler and the pump field equations at the boundary surfaces to obtain the complete set of DCDRO equations,

$$E_p(1 - r_{1p}\Gamma e^{-2ik_p' l_c}) = -r_{1p}\chi'^* E_s E_i [\Gamma e^{-2ik_p' l_c} - \alpha\beta e^{-i(k_p' + k_s' + k_i')l_c}] + it_{1p} E_p^{in}, \quad \text{(B.3)}$$

$$E_s(1 - r_{1s}\alpha e^{-2ik_s' l_c}) = r_{1s}\chi' E_p E_i^* [\alpha e^{-2ik_s' l_c} - \Gamma\beta^* e^{-i(k_p' + k_s' - k_i')l_c}], \quad \text{(B.4)}$$

$$E_i(1 - r_{1i}\beta e^{-2ik_i' l_c}) = r_{1i}\chi' E_p E_i^* [\beta e^{-2ik_i' l_c} - \Gamma\alpha^* e^{-i(k_p' - k_s' + k_i')l_c}], \quad \text{(B.5)}$$

with $(E_p^{in})^2$ being the pump input power, and

$$\Gamma = r_{3p} t_{pp}^2 e^{-i(\delta_1^p + \delta_3^p)} - r_{2p} r_{pp}^2 e^{-i(\delta_1^p + \delta_2^p)}.$$

Here, we have relabeled $E_{p,s,i}(0)$ as $E_{p,s,i}$ for a more compact form.

α, β, and Γ can be written in the form of the effective reflectivities and overall

phase shifts,

$$\begin{aligned} \alpha &= R_s e^{-i\theta_{cs}}, \\ \beta &= R_i e^{-i\theta_{ci}}, \\ \Gamma &= R_p e^{-i\theta_{cp}}, \end{aligned}$$

to simplify our calculation. Furthermore, we write

$$\begin{aligned} \phi_p &= \theta_{cp} + 2k_p' l_c, \\ \phi_s &= \theta_{cs} + 2k_s' l_c, \\ \phi_i &= \theta_{ci} + 2k_i' l_c, \end{aligned}$$

as the total round trip phase shifts for the pump, signal and idler fields, respectively. With the above definitions and the phase-mismatch equation,

$$\Delta k = k_p' - k_s' - k_s',$$

we can simplify the set of DCDRO internal field equations (Eqs. B.3–B.5) to obtain,

$$E_p(e^{i\phi_p} - r_{1p}R_p) = -r_{1p}\chi'^{*} E_s E_i[R_p - R_s R_i e^{i\psi}] + it_{1p}E_p^{in} e^{\phi_p}, \quad \text{(B.6)}$$

$$E_s(e^{i\phi_s} - r_{1s}R_s) = r_{1s}\chi' E_p E_i^{*}[R_s - R_p R_i e^{-i\psi}], \quad \text{(B.7)}$$

$$E_i(e^{i\phi_i} - r_{1i}R_i) = r_{1i}\chi' E_p E_s^{*}[R_i - R_p R_s e^{-i\psi}], \quad \text{(B.8)}$$

with $\psi = \phi_p - \phi_s - \phi_i - \Delta k l_c$.

B.4 Threshold and Output Power Equations

The threshold and power output equations are obtained by solving Eqs. B.6–B.8 simultaneously.

B.4.1 Threshold Equation

The complex conjugate of Eq. B.8 is combined with Eq. B.7 to yield for the real and the imaginary parts,

$$\Re : \cos(\phi_s - \phi_i) - r_{1i}R_i\cos\phi_s - r_{1s}R_s\cos\phi_i + r_{1i}r_{1s}R_iR_s = r_{1i}r_{1s}|\chi'|^2|E_p|^2\left[R_iR_s + R_iR_sR_p^2 - R_p(R_i^2 + R_s^2)\cos\psi\right],$$

and

$$\Im : \sin(\phi_s - \phi_i) - r_{1i}R_i\sin\phi_s + r_{1s}R_s\sin\phi_i = r_{1i}r_{1s}|\chi'|^2|E_p|^2R_p(R_i^2 - R_s^2)\sin\psi.$$

For the imaginary part, the r.h.s. contains the difference between the effective reflectivities of the idler and the signal cavities. In the case of a single-cavity DRO, with $R_i = R_s$, the imaginary part is zero. In a dual-cavity DRO, the reflectivities of the two mirrors need not be identical and, therefore, the imaginary part is not necessary zero. In our DCDRO we can approximate $R_i \approx R_s$, the imaginary part is then reduced to

$$\frac{\sin\phi_s}{\cos\phi_s - r_{1s}R_s} = \frac{\sin\phi_i}{\cos\phi_i - r_{1i}R_i}. \tag{B.9}$$

Furthermore, the round trip phase shifts $\phi_{s,i}$ are $\ll 1$ ($\phi_s \approx \phi_i \approx 0$) for a oscillating DRO so that Eq. B.9 is reduced to the familiarly signal-idler normalized-detuning equation,

$$\frac{\phi_s}{\gamma_s} = \frac{\phi_i}{\gamma_i},$$

with

$$\gamma_k = 1 - r_{1k}R_k, \qquad k = s, i.$$

B.4.2 Output Power Equation

The real part of the equation is the threshold condition for oscillation. The threshold under zero detunings conditions ($\phi_s = \phi_i = 0$) is

$$|E_p|^2 = \frac{(1 - r_{1i}R_i)(1 - r_{1s}R_s)}{|\chi'|^2 r_{1i} r_{1s}[R_i R_s(1 + R_p^2) - R_p(R_i^2 + R_s^2)\cos\psi]}. \tag{B.10}$$

The signal output power equation is obtained by solving Eq. B.8 and B.6 to eliminate E_i from the equations. After some algebra, the internal signal power equation is obtained as

$$P_s = \frac{\gamma_i}{|\chi'|^2 r_{1p} r_{1i} \mathcal{A}} \left(\sqrt{\mathcal{A}(t_{1p}^2 F - \mathcal{C}) + \mathcal{B}^2} - \mathcal{B} \right), \tag{B.11}$$

where

$$\begin{aligned}
\mathcal{A} &= (R_i^2 + R_p^2 R_s^2 - 2R_p R_s R_i \cos\psi)(R_p^2 + R_i^2 R_s^2 - 2R_p R_s R_i \cos\psi), \\
\mathcal{B} &= Re\left[(e^{i\phi_p} - r_{1p}R_p)(R_i - R_p R_s e^{i\psi})(R_p - R_s R_i e^{-i\psi})\right], \\
\mathcal{C} &= 1 + r_{1p}^2 R_p^2 - 2r_{1p}R_p \cos\phi_p, \\
F &= \frac{|E_p^{in}|^2}{|E_p|^2},
\end{aligned}$$

and F is the number of times the input power over threshold.

Appendix C

Dual-Cavity DRO Alignment Procedure

We have established a procedure for aligning the dual-cavity DRO (DCDRO). We have found that the threshold of the DCDRO is very sensitive to cavity alignment, especially the polarizer plate. The usual way of optimizing the threshold is to adjust every component of the DRO and the coupling lens in iteration while monitoring the output power. However, getting the DCDRO to oscillate from scratch could itself be an art.

The reflectivity and transmissivity of the polarizer plate depend critically and sensitively on the incident angle. The plate must be aligned correctly; otherwise, a very high threshold would result. The basic alignment procedure for the DCDRO is to adjust the polarizer's angle and the mirrors in iteration until the loss is minimized. We use a diode-pumped YAG laser for aligning the signal (horizontal polarization) cavity. The YAG beam is coupled into the cavity through the output coupler, and a photodetector is placed behind the KTP crystal to detect the leakage power. The resonance peaks and, hence the finesse of the signal cavity is monitored while adjusting the plate and the output coupler. Figure C-1 shows a schematic of the DCDRO and the YAG laser we used in the alignment.

The procedure is as follow:

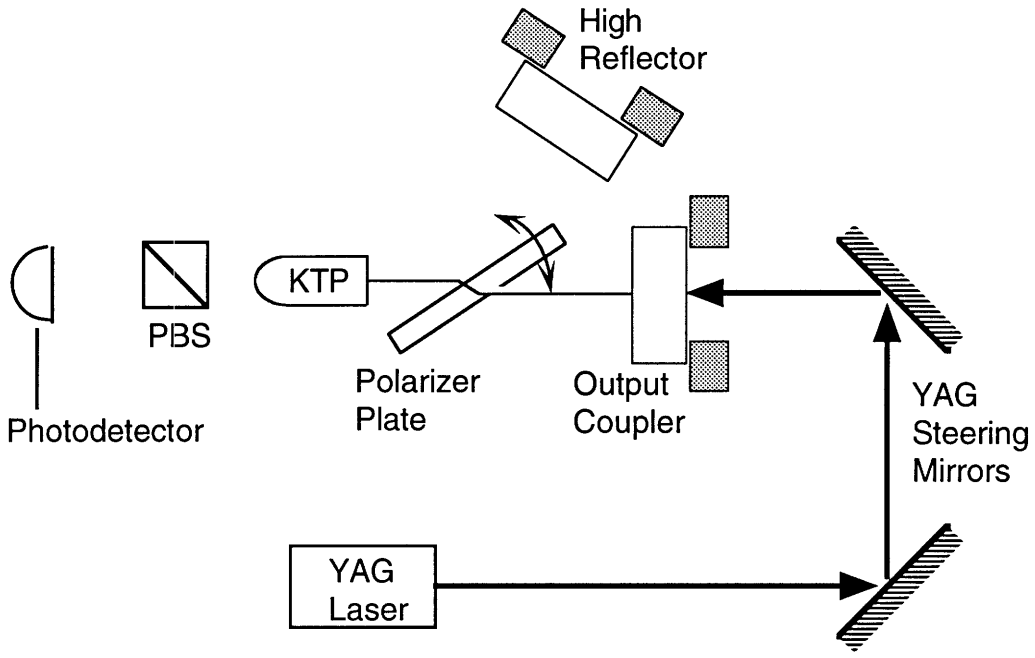

Figure C-1: Schematic of dual-cavity DRO and associated alignment optics.

1. **Minimum-threshold SCDRO alignment.** The first step is to put together a 2-element single-cavity DRO (SCDRO) using the same KTP crystal and optimize the alignment for minimum threshold. Mechanical stability is not a concern in this setup. In fact, the output coupler should be easily removable without disturbing the rest of the alignment.

   There are two reasons for optimizing the SCDRO even before we start with the DCDRO. First, there exist "sweet spots" on the KTP crystal that would yield a lower threshold than other spots on the crystal, even at about the same pump incident angle. It is easier to locate these "sweet spots" in the single-cavity configuration than in the dual-cavity configuration. Secondly, the threshold value contains valuable diagnostic information for comparing the performance and losses between the two different configurations. After we obtain the minimum threshold at a given pump incident angle, we carefully remove the single-cavity output coupler.

2. **Polarizer plate installation.** As we have mentioned, the angular alignment of

the polarizer plate is very critical. There are two angular rotations we have to align, vertical and horizontal. The horizontal rotation is for setting the Brewster angle at which the plate operates. The vertical rotation is the angular adjustment that causes the reflected pump beam to move up and down.

At this step, we align the vertical rotation with the help of the pump laser. The plate is aligned such that the reflected pump beam coincides with the incoming beam. When the incident angle is normal to the plate surfaces, the scattering loss is minimized. After we have aligned the plate for normal incident angle, we set the mini-rotation stage on which the plate is attached at an incident angle of $\sim 57°$.

3. **Mirrors installation.** The next components to be installed are the mirrors. We install the output coupler and coarse-align it using the pump beam by adjusting only the output coupler. The polarizer plate is not to be adjusted at this step. We also install the high reflector for the idler cavity at this step before we do any fine adjustment. But the high reflector should be blocked with a piece of paper once it is installed so that the idler cavity remained inactive.

4. **YAG laser alignment.** We now align the YAG laser coupling optics to couple the YAG laser beam into the DRO cavity by adjusting only the steering mirrors. The crystal, polarizer, and mirrors are not adjusted in this step. Great care should be taken that the DCDRO is not moved or perturbed in any way.

5. **Polarizer plate fine alignment.** While we monitor the signal cavity finesse with an IR detector behind the KTP crystal, we maximize the signal cavity finesse by adjusting the horizontal angular tilt of the polarizer plate, and then the YAG coupling again. The alignment should be done without adjusting the output coupler.

6. **Output coupler fine alignment.** With the YAG laser blocked and the IR detector removed, we use the pump laser to align the output coupler by adjusting only the output coupler. As in previous steps, only one component should be

adjusted at each step.

7. **Alignment iteration.** We now unblock the YAG laser and put the IR detector back behind the crystal. We then adjust the YAG coupling optics to optimize its alignment because the output coupler has been moved. We repeat steps 5 and 6 until the resonance peaks for both the YAG 1.064 μm and the pump 531 nm wavelengths are maximized. As a reminder, it is essential to have the idler-cavity high reflector blocked at all times since the two cavities are coupled.

8. **High reflector alignment.** After the polarizer and the output coupler are aligned we proceed to align the high reflector. The high reflector is coarse aligned with the use of the pump laser. In this case the output coupler should be blocked to facilitate the alignment of the idler cavity.

9. **Final adjustment.** With luck, the DCDRO should be oscillating when both cavities are unblocked and the pump power is increased. If the DCDRO does not oscillate, fine adjustments for the mirrors and pump laser input lens might be necessary. However, the polarizer plate should not be adjusted at this step. In most cases, a few minor adjustments of the mirrors and pump coupling lens should bring the DCDRO into oscillation. If the DCDRO does not start oscillating after these fine adjustments, one might need to repeat steps 4 to 9 again. Once the DCDRO is oscillating, the usual optimization procedure applies.

Appendix D

PZT-Cavity-Length Tuning

In this appendix we use a simple model to explain the PZT tuning behavior of a type-II phase-matched DRO. Consider a crystal of length d inside a cavity that has an optical length $L_i = l + dn_i$, where l is the free-space length in the cavity, n is the refractive index, and $i = 1, 2$ refers to the two orthogonal polarizations, one of them being along the crystal's z axis. Furthermore we define the free-space mode number $m_i = 2L_i/\lambda_i$, where λ_i is the vacuum wavelength for the signal or the idler with the corresponding frequency f_i.

As the cavity length is scanned, the DRO parameters change:

$$a_i \rightarrow a_i' = a_i + \Delta a_i, \tag{D.1}$$

where a denotes one of the following cavity parameters: refractive index n, cavity free-space l, optical length L, free-space mode number m, frequency f, or wavelength λ. Assuming that there is no change in the crystal temperature, d remains the same. We can easily derive the following:

$$\Delta\lambda_i = \lambda_i' - \lambda_i = -\frac{\lambda_i}{f_i'}\Delta f_i, \tag{D.2}$$

$$\begin{aligned}\Delta L_i &= m_i'(\lambda_i'/2) - m_i(\lambda_i/2) \\ &= (\lambda_i/2)[\Delta m_i - \Delta f_i(m_i'/f_i')].\end{aligned} \tag{D.3}$$

Noting that the free spectral range is given by

$$F_i = c/2L_i = f_i/m_i, \tag{D.4}$$

we can rewrite Eq. (D.3) as

$$\Delta l + d\Delta n_i = (\lambda_i/2)(\Delta m_i - \Delta f_i/F_i'). \tag{D.5}$$

For a DRO we have the additional sum-frequency constraint, so that

$$\Delta f_1 = -\Delta f_2 \equiv \Delta f. \tag{D.6}$$

For small frequency changes we assume that the crystal dispersion is linear in frequency, $\Delta n_i = \alpha_i \Delta f_i$. Retaining only first-order terms, we can rewrite Eq. (D.5) in frequency terms as

$$f_i \Delta l + [l + d(n_i + \alpha_i f_i)]\Delta f_i = (c/2)\Delta m_i. \tag{D.7}$$

By forming the sum and the difference equations of Eq. (D.7) for $i = 1$ and $i = 2$, we obtain

$$(c/2)(\Delta m_1 + \Delta m_2) = f_p \Delta l + d(n_1 - n_2 + \alpha_1 f_1 - \alpha_2 f_2)\Delta f, \tag{D.8}$$

$$(c/2)(\Delta m_1 - \Delta m_2) = (f_1 - f_2)\Delta l + [2l + d(n_1 + n_2 + \alpha_1 f_1 + \alpha_2 f_2)]\Delta f, \tag{D.9}$$

where we have made use of Eqs. (D.3) and (D.6).

For a flux-grown KTP DRO operating near frequency degeneracy at 1.0617 μm, the following parameters can be obtained from the Sellmeier equations [16]: $n_1(n_z) = 1.8305, n_2 = 1.7457, \alpha_1(\alpha_z) \sim 1.57 \times 10^{-16}\text{Hz}^{-1}$, and $\alpha_2 \sim 1.18 \times 10^{-16}\text{Hz}^{-1}$. Since

Δl is the same for both polarizations, we obtain from Eqs. (D.9) and (D.9)

$$\Delta f = (f_2\Delta m_1 - f_1\Delta m_2)[f_2/F_1 + f_1/F_2 + (2d/c)(\alpha_1 + \alpha_2)f_1 f_2]^{-1}. \tag{D.10}$$

For nearly degenerate operation $f_i \sim f_p/2$, and Eq. (D.10) can be simplified to yield

$$\Delta f = (\Delta m_1 - \Delta m_2)[2/\bar{F} + (d/c)(\alpha_1 + \alpha_2)f_p]^{-1}, \tag{D.11}$$

where

$$\bar{F} = c/(L_1 + L_2) \tag{D.12}$$

is the average free spectral range of the cavity. For $\Delta m_1 = -\Delta m_2 = 1$, we obtain

$$\Delta f = [1/\bar{F} + (d/2c)(\alpha_1 + \alpha 2)f_p]^{-1} \approx \bar{F}. \tag{D.13}$$

From Eq. (D.9) we obtain for the cavity-length spacing

$$\Delta l = d(n_1 - n_2 + \alpha_1 f_1 - \alpha_2 f_2)(\Delta f/f_p). \tag{D.14}$$

For $\Delta f = 4.3$ GHz, $f_p = 5.65 \times 10^{14}$ Hz, $d = 8$ mm, the cavity-length spacing for a resonance mode jump is $\Delta l \approx 5.9$ nm. This is in reasonable agreement with our observed value of ~4.7 nm in Fig. 5-4, within the uncertainties in the values of n_i and α_i, and in the linearity of the PZT scan. A good estimate can be obtained, in zeroth order, by ignoring the dispersion term so that $\Delta l = d(n_1 - n_2)(\Delta f/f_p)$, with only an ~10% error in the case of the KTP. This estimate is useful in designing a DRO cavity. For example, since Δf is equal to the average free spectral range of the cavity, a shorter cavity increases Δl, so that the separation between resonance peaks is wider and the DRO is easier to tune. The above calculation shows that when the DRO is tuned from one resonance peak to the next the frequencies change by one average free spectral range, the mode numbers change by one, and Δl changes by an amount much less than a wavelength.

It is also instructive to consider the cluster spacing, which is the frequency spacing

of the next mode pair that has a resonance peak at the same cavity position. This can be represented by $\Delta m_1 + \Delta m_2 = 1, \Delta m_2 = 0$, or vice versa, and $\Delta l = 0$. From Eq. (D.9) we have

$$\Delta f = (c/2d)(n_1 - n_2 + \alpha_1 f_1 - \alpha_2 f_2)^{-1} \approx 190\text{GHz} \tag{D.15}$$

Our experimental observations show that the spectral bandwidth at a fixed phase-matching angle was ~50–100 GHz. Therefore the next cluster mode would not be phase matched. This situation of unexcited cluster modes makes the type-II phase-matched KTP DRO far more stable than a type-I phase-matched DRO operating near frequency degeneracy.

It is interesting that the simple theoretical model that we have used here can also be applied to a type-I phase-matched DRO, provided second-order terms such as $(\Delta f)^2$ are included. For example, in a MgO:$LiNbO_3$ DRO operating near degeneracy, the next cluster mode spacing can be calculated to be several THz, which has been confirmed in experiments [14]. It also shows that the required cavity-length spacing for a mode jump to the next mode pair can be less than 0.1 nm, thus confirming the difficulty in maintaining stability of a type-I phase-matched DRO.

Appendix E

KTP Material Limitations

We have experienced three major KTP material problems during the course of our experiments. They are photorefractive damage, development of gray tracks, and absorption induced thermal instability.

E.1 Photorefractive Damage

Photorefractive damage of the KTP crystal leads to increased threshold and hence decreased output power. We have observed such damage in both the flux-grown and the hydrothermally grown KTP crystals. When a new crystal is first installed, it would function normally without showing any change in threshold; the output power is approximately constant at the same pump power level. After a few days of continuous operations, the threshold would increase gradually within a few hours of operation of the DRO. If the DRO is allowed to rest overnight, the threshold would usually recover to its original lower threshold value. However, the recovery is only temporary. If the DRO is to operate continuously after the initial damage, the rate of threshold increase would accelerate and the output power could drop by as much as 50%. Eventually, the DRO has to be re-aligned so that the internal fields would propagate along a new path and the original lower threshold is restored.

E.2 Development of Gray Tracks

When a dc voltage is applied across the crystal for a prolonged period of time, gray tracks would develop across the crystal parallel to the direction of the electric field[3]. Great care should be taken to minimize the amount of voltage applied, dc or ac, and to remove such voltage whenever it is not needed.

In our 2-element DRO experiment, a dc voltage of ~100 V was applied across the KTP crystal's z axis for about an hour. Visible gray tracks were developed and the DRO ceased to operate. Some of the gray tracks disappeared or lightened in color after the crystal was baked under high temperature (~80°C) for a week. We were able to operate the DRO again after the high temperature treatment, but only at an elevated threshold (~80 mW).

E.3 Absorption Induced Thermal Instability

The commonly accepted absorption coefficients for KTP are less than 1% per cm at 532 nm and less than 0.1% per cm at 1064 nm. But even at these small values, the total absorbed power can be significant.

Assuming that the DRO is pumped at 100 mW of 532-nm power and generates a combined output power of 15 mW, the internal circulating IR power is about 2 W for a 0.75% output coupler. A 8-mm crystal would absorb 1.6 mW of IR and 1 mW of pump power. Moreover, the absorption is concentrated along the beam path within the beam radii of the fields. Within such a small area, the heat diffusion to the surrounding bulk crystal, and eventually to the environment, may not be even. The localized heat may build up and relaxation would cause localized thermal cycling and would induce instability in the output power and frequencies. One way to reduce the thermal instability is to have a good thermal contact between the crystal and a large heat sink. However, since KTP is not a good thermal conductor, the improvement in thermal stability may not be significant.

Appendix F

List of Abbreviation

AM : amplitude modulation

AR : anti-reflection

cw : continuous-wave

DCDRO : dual-cavity doubly resonant OPO

DRO : doubly resonant OPO

EOM : electro-optic modulator

FFT : fast Fourier transform

FSR : free spectral range

FWHM : full width at half maximum

HR : high reflection

HR : high reflector

HWHM : half width at half maximum

KDP : potassium dihydrogen phosphate

KTP : potassium titanyl phosphate ($KTiOPO_4$)

OFCG : optical frequency comb generator

OPO : optical parametric oscillator

PBS : polarizing beat splitter

PLL : phase-locked loop

PM : phase modulation

PM : phase modulator

PP : polarizing plate

PZT : piezoelectric transducer

SA : spectrum analyzer

SCDRO : single-cavity doubly resonant OPO

SC : super cavity

SHG : second harmonic generation

SRO : singly resonant OPO

TE : thermo-electric

VCO : voltage controlled oscillator

YAG : yttrium aluminum garnet ($Y_2Al_5O_{12}$)

QWP : quarter wave plate

Bibliography

[1] Roland E. Best. *Phase-locked loops : theory, design, and applications.* McGraw-Hill, New York, 2 nd edition, 1993.

[2] J. D. Bierlein and H. Vanherzeele. Potassium titanyl phosphate: properties and new applications. *J. Opt. Soc. Am. B*, 6:622–633, 1989.

[3] P.F. Bordui, editor. *Ionic conductivity and damage mechanism in $KTiOPO_4$ crystals*, volume 1561. Proc. Soc. Photo-Opt. Instrum. Eng., 1991.

[4] B. Boulanger, J. P. Fève, G. Marnier, B. Ménaert, and X. Cabirol. Relative sign and absolute magnitude of $d^{(2)}$ nonlinear coefficients of ktp from second-harmonic-generation measurements. *J. Opt. Soc. Am. B*, 11:750–757, 1994.

[5] L. R. Brothers, D. Lee, and N. C. Wong. Terahertz optical frequency comb generation and phase locking of an optical parametric oscillator at 665 GHz. *Opt. Lett.*, 19:245–247, 1994.

[6] Eugene Butkov. *Mathematical Physics.* Addison-Wiley, New York, 1968.

[7] R. L. Byer. Optical parametric oscillators. *Quantum Electronics: a Treaties*, pages 587–702, 1975.

[8] Carlton M. Caves. Quantum-mechanical noise in an interferometer. *Phys. Rev. D*, 23:1693–1708, 1981.

[9] Yuh-Jen Chang, Paul L. Mussche, and Anthony E. Siegman. Measurement of laser quantum frequency fluctuations using a Pound-Drever stabilization system. *IEEE Journal of Quantum Electronics*, 30:1498–1504, 1994.

[10] F. G. Colville, M. J. Padgett, and M. H. Dunn. Continuous-wave, dual-cavity, doubly-resonant optical parametric oscillator. *Appl. Phys. Lett.*, 64:999, 1994.

[11] T. Debuisschert, A. Sizmann, E. Giaconino, and C. Fabre. Type-II continuous-wave optical parametric oscillators: oscillation and frequency-tuning characteristics. *J. Opt. Soc. Am. B*, 10:1668–1680, 1993.

[12] R. W. P. Drever, J. L. Hall, F. V. Kowalski, J. Hough, G. M. Ford, A. J. Munley, and H. Ward. *Appl. Phys. B*, 31:97–105, 1983.

[13] R. C. Eckardt, H. Masuda, Y. X. Fan, and R. L. Byer. Absolute and relative nonlinear optical coefficients of KDP, KD*P, BaB_2O_4, $LiIO_3$, MgO:$LiNbO_3$, and KTP measured by phase-matched second-harmonic generation. *IEEE J. Quantum Electron.*, 26:922–933, 1990.

[14] R. C. Eckardt, C. D. Nabors, W. J. Kozlovsky, and R. L. Byer. Optical parametric oscillator frequency tuning and control. *J. Opt. Soc. Am. B*, 3:646–667, 1990.

[15] C. Fabre, E. Giacobino, A. Heidmann, and S. Reynaud. Noise characteristics of a non-degenerate optical parametric oscillator - application to quantum noise reduction. *J. Phys. France*, 50:1209–1225, 1989.

[16] T. Y. Fan, C. E. Huang, B. Q. Hu, R. C. Eckardt, Y. X. Fan, R. L. Byer, and R. S. Feigelson. Second harmonic generation and accurate index of refraction measurements in flux-grown $KTiOPO_4$ crystal. *Appl. Opt.*, 26:2390–2394, 1987.

[17] Floyd Martin Gardner. *Phaselock techniques.* Wiley, New York, 2 edition, 1979.

[18] J. A. Giordmaine and R. C. Miller. *Phys. Rev. Lett.*, 14:973, 1965.

[19] J. A. Giordmaine and R. C. Miller. *Appl. Phys. Lett.*, 9:298, 1966.

[20] A. A. Godil, A. S. Hou, B. A. Auld, and D. M. Bloom. *Opt. Lett.*, 16:1765, 1991.

[21] R. Graham and H. Haken. The quantum-fluctuations of the optical parametric oscillator. *Zeitschrift für Physik*, 210:276–302, 1968.

[22] A. Heidmann, R. J. Horowicz, S. Reynaud, E. Giacobino, C. Fabre, and G. Camy. *Phys. Rev. Lett.*, 59:2555, 1987.

[23] Murray Sargent III, Marlan O. Scully, and Jr. Willis E. Lamb. *Laser Physics.* Addison-Wesley, New York, 5 edition, 1987.

[24] Special issue on squeezed states of the electromagnetic field. *J. Opt. Soc. Am. B*, 4:1450–1741, 1987.

[25] Special issue on optical parametric oscillation and amplification. *J. Opt. Soc. Am. B*, 10:1656–1791, 1993.

[26] M. Kourogi, K. Nakagawa, and M. Ohtsu. *IEEE J. Quantum Electron.*, 29:2693, 1993.

[27] B. Y. Lee, T. Kobayashi, A. Morimoto, and T. Sueta. *Conference on Laser and Electro-Optics, 1991 OSA Technical Digest Series*, 10:146, 1991.

[28] D. Lee and N. C. Wong. Tunable optical frequency division using a phase-locked optical parametric oscillator. *Opt. Lett.*, 1:13–15, 1992.

[29] K. W. Leong, N. C. Wong, and J. H. Shapiro. Nonclassical intensity correlation from a type I phase-matched optical parametric oscillator. *Opt. Lett.*, 1990.

[30] Kin Wai Leong. Intensity quantum noise reduction with an above-threshold optical parametric oscillator. *M.I.T.*, 1991.

[31] L .A. Lugiato, C. Oldano, C Fabre, E. Giacobino, and R. J. Horowicz. Bistability, self-pulsing and chaos in optical parametric oscillators. *Il Nuovo Cimento*, 10:959–977, 1988.

[32] C. D. Nabors, R. C. Eckardt, W. J. Kozlovsky, and R. L. Byer. Efficient, single-axial-mode operation of a monolithic MgO:$LiNbO_3$ optical parametric oscillator. *Opt. Lett.*, 14:1134–1136, 1989.

[33] C. D. Nabors, S. T. Yang, T. Day, and R. L. Byer. Coherence properties of a doubly resonant monolithic optical parametric socillator. *J. Opt. Soc. Am. B*, 7:815–820, 1990.

[34] S. F. Pereira, Z. Y. Ou, and H. J. Kimble. Backaction evading measurements for quantum nondemolition detection and quantum optical tapping. *Physical Review Letters*, 72:214–217, 1994.

[35] M. D. Reid and P. D. Drummond. Quantum correlations of phase in nondegenerate parametric oscillation. *Physical Review Letters*, 60:2731–2733, 1988.

[36] F. Reif. *Fundamentals of statistical and thermal physics.* McGraw-Hill, New York, 1965.

[37] J. H. Shapiro. *Lecture notes for 6.453: Optical detection and communication.* MIT, MIT, 1982.

[38] J. H. Shapiro. *IEEE J. Quantum Electron.*, 21:237, 1985.

[39] Y. R. Shen. *The Principles of Nonlinear Optics.* John Wiley & Sons, New York, 1984.

[40] R. E. Slusher, L. W. Hollberg, B. Yurke, J. C. Mertz, and J. F. Valley. *Phys. Rev. Lett.*, 55:2409, 1985.

[41] N. C. Wong. Optical frequency division using an optical parametric oscillator. *Opt. Lett.*, 15:1129–1131, 1990.

[42] N. C. Wong. Gravity-wave detection via an optical parametric oscillator. *Physical Review A*, 45:3176–3183, 1992.

[43] N. C. Wong. Optical frequency counting from the UV to the near IR. *Opt. Lett.*, 17:1155–1157, 1992.

[44] N. C. Wong, K. W. Leong, and J. H. Shapiro. Quantum correlation and absorption spectroscopy in an optical parametric oscillator in the presence of pump noise. *Opt. Lett.*, 15:891–893, 1990.

[45] Ling-An Wu, H. J. Kimble, J. L. Hall, and Huifa Wu. Generation of squeezed states by parametric down conversion. *Physical Review Letters*, 17:2520–2523, 1986.

[46] S. T. Yang, R. C. Eckardt, and R. L. Byer. Power and spectral characteristics of continuous-wave parametric oscillators: the doubly to singly resonant transition. *J. Opt. Soc. Am. B*, 10:1684–1695, 1993.

[47] J. Q. Yao and Theodore S. Fahlen. Calculations of optimum phase match parameters for the biaxial crystal $KTiOPO_4$. *J. Appl. Phys.*, 55:65–68, 1984.